



## Durham E-Theses

---

### *The structure of the upper mantle beneath East Africa*

Forth, Philip A.

#### How to cite:

---

Forth, Philip A. (1975) *The structure of the upper mantle beneath East Africa*, Durham theses, Durham University. Available at Durham E-Theses Online: <http://etheses.dur.ac.uk/8224/>

#### Use policy

---

The full-text may be used and/or reproduced, and given to third parties in any format or medium, without prior permission or charge, for personal research or study, educational, or not-for-profit purposes provided that:

- a full bibliographic reference is made to the original source
- a [link](#) is made to the metadata record in Durham E-Theses
- the full-text is not changed in any way

The full-text must not be sold in any format or medium without the formal permission of the copyright holders.

Please consult the [full Durham E-Theses policy](#) for further details.

THE STRUCTURE OF THE UPPER MANTLE  
BENEATH EAST AFRICA

by

Philip A. Forth

A thesis submitted for the degree of

Doctor of Philosophy

in the

University of Durham

The copyright of this thesis rests with the author  
No quotation from it should be published without  
his prior written consent and information derived  
from it should be acknowledged

Graduate Society

October 1975

## ABSTRACT

This study concerns the analysis of arrivals at the Kaptagat array in Kenya set up by the Durham University Department of Geological Sciences. The array consisted of ten short period seismometers and was sited 10 km west of the Elgeyo escarpment, which forms the western boundary of the Gregory Rift.

Onset time analysis was used to determine the slowness and azimuth of approach for teleseismic arrivals. Large deviations from the expected slowness and azimuth are found and it is shown that the major cause of these anomalies is the low velocity upper mantle which is assumed to exist beneath the Kenyan domal uplift.

A preliminary analysis of 60 teleseismic arrivals shows that the anomalies cannot be explained in terms of a single plane interface or any plane structure. It is shown that if the data is to be explained by a single boundary then the structure must thin both to the north and west of the station. The structure was thus assumed to be caused by a structure which is ellipsoidal in plan and hyperbolic in section and optimum structures were calculated for various assumed velocities.

Relative teleseismic P-wave delay time data between Kaptagat and Bulawayo, which confirms the presence of low material beneath the station, was reinterpreted on the basis of the model proposed and was found to be consistent with a depth to the bottom of the structure between 150 and 300 km.

The arrival of a phase corresponding to a reflection from the top of the proposed structure was searched for in the records from local earthquakes using velocity filtering techniques but no consistent arrival could be identified with confidence.

A preliminary study showed that the postulated seismic structure was not inconsistent with the available gravity data.

## ACKNOWLEDGEMENTS

I would like to thank Professor G.M. Brown and Professor M.H.P. Bott for the opportunity to work in the Department of Geological Sciences and the Natural Environment Research Council for a research studentship.

I would also like to thank Dr. R.E. Long for his supervision and guidance throughout the course of this research and for constructive criticism of this work.

Many of my colleagues have contributed to the final form of this thesis. In particular, I would like to thank Dr. Richard Backhouse for his generous help in the early stages of this work and Les Arnold for considerable guidance in the analysis of local earthquake records. A final word of thanks to Simon Armstrong for his patient help with innumerable computing problems.

## CONTENTS

### ABSTRACT

### ACKNOWLEDGEMENTS

CHAPTER 1.1.	THE EAST AFRICAN RIFT SYSTEM	
1.1.1.	Introduction	1
1.1.2.	Development of the East African Rift System	2
1.1.3.	Evidence for Anomalous Mantle beneath the Rift	4
1.1.4.	Theories of Formation of the Rift	7
1.1.5.	The Role of the Rift System in Global Tectonics	10
1.2.	PREVIOUS SEISMOLOGICAL STUDIES AT KAPTAGAT	
1.2.1.	Kaptagat Array Station	13
1.2.2.	Parameters Measured using Arrays	14
1.2.3.	Onset Time Analysis	15
1.2.4.	Errors	16
1.2.5.	Anomalies and their Interpretation	18
1.2.6.	Delay Times	20
1.2.7.	Summary	21
CHAPTER 2.	SEISMOLOGICAL DATA	
2.1.	The Data	22
2.2.	Velocities Expected at the Array	24
2.3.	Definition of Anomalies	25
2.4.	Analysis of Residuals and Site Corrections	27
2.5.	Corrections to Anomalies	29
CHAPTER 3	PRELIMINARY INTERPRETATION OF SEISMOLOGICAL DATA	
3.1.	Comparison of Kaptagat with other Arrays	30
3.2.	Source of the Anomaly	32
3.3.	Basic Approach to the Problem	34
3.4.	Use of Direction Cosines	35
3.5.	Restraints on Velocity	36
3.6.	Calculation of the Normal	39
3.7.	Properties of the Normals	39
3.8.	Errors	44
3.9.	Conclusions	44
CHAPTER 4.	OPTIMIZED SEISMIC MODELS	
4.1.	Introduction	46
4.2.	Choice of Form Structure	47
4.3.	Ray Tracing Procedure	50
4.4.	Optimizing Procedures	53
4.5.	Optimizing Models	53

CHAPTER 5.	P-WAVE DELAY TIMES	
5.1.	P-wave Delay Time Observations	65
5.2.	Delay Time Studies in Africa	67
5.3.	Delays Between Kaptagat and Bulwayo	68
5.4.	Methods of Interpretation	71
5.5.	Results	75
CHAPTER 6	VELOCITY FILTERING LOCAL EARTHQUAKES	
6.1.	Introduction	78
6.2.	Identification of Anomalous Phase	78
6.3.	Velocity Filtering	79
6.4.	Velocity Filtering Problems	80
6.5.	Event Selection and Processing Technique	87
6.6.	Results	91
6.7.	Discussion	92
CHAPTER 7.	GRAVITY MODELS	
7.1.	Introduction	97
7.2.	Previous Gravity Studies in East Africa	97
7.3.	Relation Between Density and Seismic Velocity	99
7.4.	Correlation Between Seismic Models and Regional Gravity Field	101
CHAPTER 8.	DISCUSSION AND CONCLUSIONS	
8.1.	Discussion of Seismic Models Presented	104
8.2.	The Relation of the Anomalous Mantle to Various Features	106
8.3.	Velocity Determination and the Shape of the Structure	111
8.4.	Conclusions	113
APPENDIX A		115
APPENDIX B		117
APPENDIX C		122
REFERENCES		126
COMPUTER PROGRAMS		

## CHAPTER 1

### SECTION 1 - THE EAST AFRICAN RIFT SYSTEM

#### 1.1.1. Introduction

The East African Rift System extends southward for some 4,000 km from its northern junction with the Red Sea and the Gulf of Aden. It stretches through Ethiopia and splits to form the Eastern and Western Rifts which converge again toward Lake Malawi (Fig. 1.1.). Apparent faulting ends toward the Limpopo river area although heat flow studies (Chapman and Pollack, 1975) indicate that rifting occurs down to  $16^{\circ}\text{S}$  while seismicity studies suggest that it may extend as far as  $24^{\circ}\text{S}$  (Fairhead and Girdier, 1969).

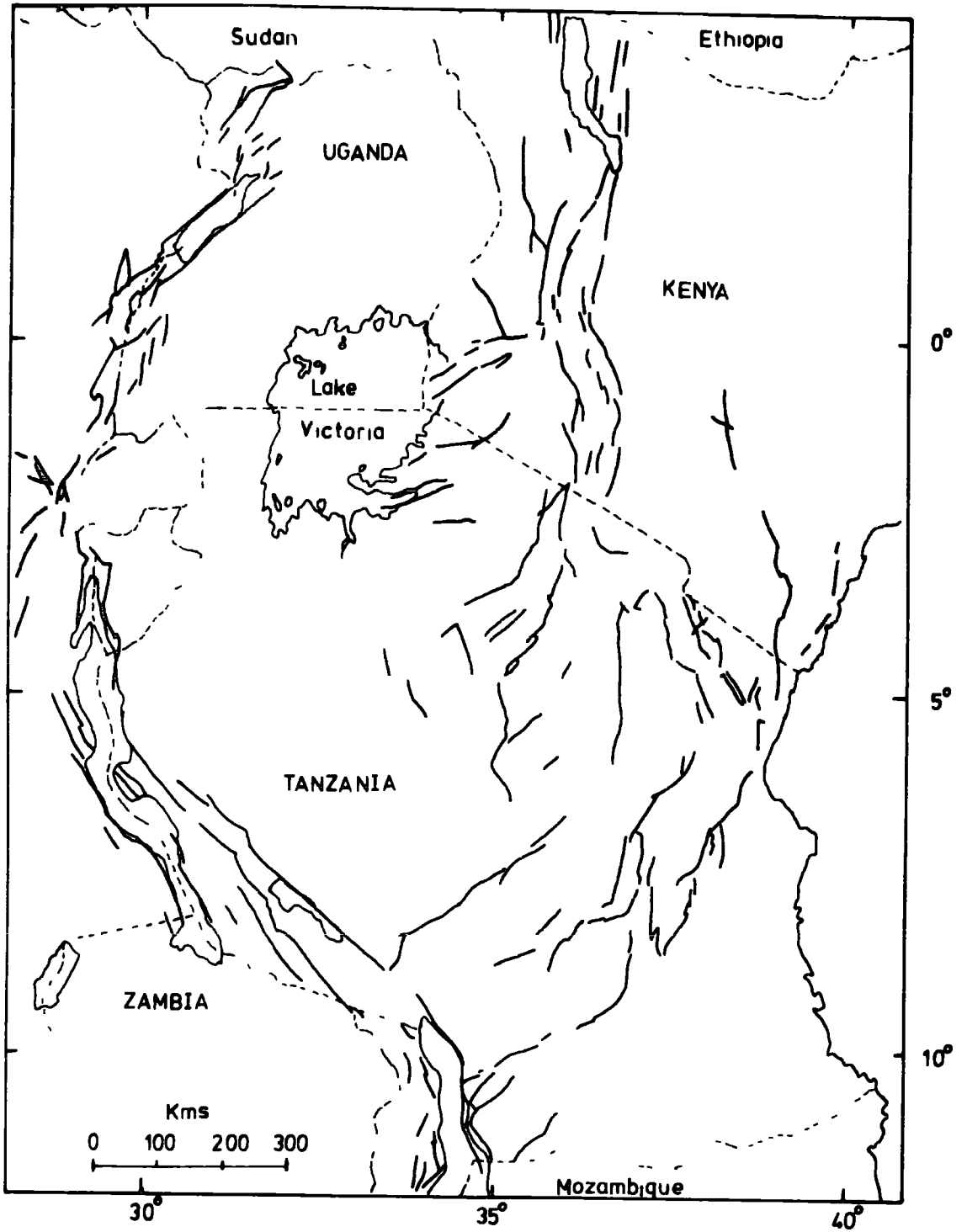
The rift, characteristically between 40 and 65 km wide, traverses two broad, elongated domal uplifts, elliptical in plan and some 1,000 km wide, in Ethiopia and Kenya and it is only here that the classic graben structures are well defined; the throws on the major faults in these regions are estimated to be as much as 4 km (Baker and Wohlenberg, 1971).

Although the rift is a north-south feature on a continental scale individual structures only rarely show this trend; the rift tends to be formed as a series of en echelon faults which effectively define a north-south structure (King, 1970).

It is now generally accepted that the rift is a tensional feature and not produced by compression as suggested by some early workers (Wayland, 1930; Bullard, 1936; Willis, 1936); the faulting has been shown by

Figure 1.1

The East African Rift System south of Ethiopia.



observation, gravity and focal mechanism studies to be preponderantly normal, not reverse, indicating extension. (Gregory, 1921; Girdler, 1964; Heiskanen and Vening Meinesz, 1958; Sykes and Landisman, 1964; Fairhead, 1968, Fairhead and Girdler, 1971.)

#### 1.1.2. Development of the East African Rift System

The basement of East Africa is formed of a complex of metamorphic and igneous rocks of Precambrian and lower Palaeozoic age. During most of the Palaeozoic, East Africa was occupied by fold mountains being eroded. Marine transgression commenced in the late Triassic-lower Jurassic in the north east of Africa and developed westward to cover Somalia, north east Kenya, most of Ethiopia and south west Arabia by the upper Jurassic. By the start of the Cretaceous Ethiopia had re-emerged and the process continued with minor interruptions and transgressions until early Tertiary (Baker et al, 1972).

The uplift in Ethiopia in the upper Eocene marks the start of the Ethiopian domal uplift and by the end of the Eocene the coast-lines of the Gulf of Aden and the Indian Ocean had been determined. At the same time as, or slightly after, the upwarping, the Trap Series fissure basalts were produced; they represent the largest single volcanic event in the history of the rift and covered 750,000 km<sup>2</sup> in Ethiopia and 30,000 km<sup>2</sup> in south west Arabia (Gass, 1970). It is estimated that the thickness reaches 4 km in northern Ethiopia (Mohr, 1967) and the total volume is assessed as 400,000 km<sup>3</sup> (Gass, 1970). The timing, in relation to doming, is disputed but Mohr (1963) claims that uplift was completed before volcanism occurred. Grasty et al (1963)

show that the flows are Eocene-Oligocene in the north and Oligocene in the south; no such early Tertiary volcanism occurred in Kenya (Logatchev et al, 1972).

There was then a period of stability (Saggerson and Baker, 1965) followed by uplifts in both Kenya and Ethiopia in the middle to late Miocene. In Kenya, the uplift was about 300 m and was accompanied by the eruption of fissure phonolites (Baker and Wohlenberg, 1970); uplift in Ethiopia has been estimated at 500 m (Merla, 1963).

There now followed another period of quiescence (Saggerson and Baker, 1965) when the uplifts were eroded until the final and most important stage of uplift began. In central Kenya the uplift was up to 1,500 m and the rift margins were warped downwards and a true graben was produced. At the same time as the start of the uplift massive eruptions of ignimbrites began in the central part of the Kenya rift sometimes filling and overflowing it (Baker and Wohlenberg, 1971). During early Pleistocene the floor of the graben was cut by dense swarms of minor faults since which time only minor faulting has occurred.

The volcanic history of the Rift is extremely complex and the present writer is not competent to deal with the problems in detail. All the rocks of the Kenyan and Ethiopian dome are alkaline with two distinct genetic series observable, one strongly alkaline and the other mildly alkaline. In both Ethiopia and Kenya the pre-rift flood basalts are more alkaline than the basalts of the rift floor, suggesting shallower melting beneath the rift than the surrounding plateaus; also the average silica content of the Kenya basalts is lower than that of those from Ethiopia

suggesting a deeper origin for the former (Green et al, 1967).

Gass (for example Gass, 1970; Gass, 1972) has argued that the domal uplift is caused by the progressive upwelling of the lithosphere-asthenosphere boundary and consequently there should be a progressive change in basalt type as rifting proceeds from alkali basalts for partial melts produced at greater depths to tholeiitic basalts on crustal separation. Harris (1969) has given evidence that this occurs but Baker et al (1972) consider that many difficulties remain on applying this theory in detail; they conclude that no satisfactory petrogenetic model yet exists but find it 'difficult to escape the conclusion' that volcanism and tectonism are dual expressions of thermal events in the asthenosphere, along an uplifted zone of crustal tension and dilation.

#### 1.1.3. Evidence for Anomalous Mantle beneath the Rift

Most explanations of the uplift, rifting and faulting (e.g. Gass, 1970; Osmaston, 1971; Artyushkov, 1973) have postulated the existence of an anomalous mantle structure beneath the rift and the evidence for this and its more detailed structure will now be discussed.

Surface wave dispersion techniques are useful for defining the average shear wave velocity distribution between two stations (Bloch et al, 1969). The Rayleigh wave dispersion curves between stations which have sampled the rift have been shown (Sundaralingham, 1971; Long et al, 1972) to be similar to those found for the rest of Africa (Gumper and Pomeroy, 1970) for shorter periods reflecting crustal structure but to have a much lower velocity for the

longer periods which reflect upper mantle structure. Knopoff and Schlue (1972) analysed the phase velocity for the path Addis Ababa-Nairobi and suggested a velocity for  $S_n$  between 4.25 and 4.45 km/sec extending to a depth of 120-200 km (compared with the average African value of 4.6-4.8 km/sec given by Gumper and Pomeroy (1970)) although the analysis of Der et al (1970) would suggest that these figures represent only mean values and not structural boundaries.

Various studies of P-wave delay times for stations close to the rift all indicate a positive delay showing that arrivals have passed through a zone of anomalously low velocity material (Lilwall and Douglas, 1970; Herrin and Taggart, 1968; Sundaralingham, 1971; Backhouse, 1972; Colley, 1973).

Gumper and Pomeroy (1970) found that  $S_n$  did not propagate across the rift north of the equator and deduced the existence of a mantle with low Q in this region (Molnar and Oliver, 1969).

In order to aid controls for gravity interpretation a seismic refraction line was shot along the rift between Lakes Hannington and Rudolf (Griffiths et al, 1971; Griffiths, 1972) and from unreversed data a high (apparent) velocity refractor (P wave velocity 6.4 km/sec) was found at a depth of 3 km with a 7.5 km/sec layer at a depth of 20 km. It was suggested that this high velocity layer could be the top of the anomalous mantle.

Banks and Ottey (1974) have attempted to define the anomalous material by its expected high conductivity and

have investigated the response to short period variations in the earth's magnetic field using arrays of magnetometers. In their report of a preliminary small scale experiment they find a region of high conductivity approximately 20 km beneath the rift floor and another approximately 100 km to the east at a depth of 100 km.

Gravity measurements in Kenya have been improving in quality and quantity with time in spite of the difficult terrain and some further detailed gravity studies are shortly expected. A broad negative Bouguer anomaly of up to -150 mgals is found over the uplifted region and superimposed on this is a lower amplitude (40-50 mgals) shorter wavelength (40-80 km) positive anomaly over the rift. The region over the uplift is in approximate isostatic equilibrium (Bullard, 1936) and this has been shown (Bott, 1965) to require a low density body at the base of the crust or within the upper mantle. All workers agree that the anomaly must be explained in terms of a low density mantle intruding into the crust where it causes the short wavelength positive anomaly but detailed interpretations vary considerably apparently because of the difficulty of assessing the influence of the low density volcanics. Baker and Wohlenberg (1971) postulate a body 10 km wide penetrating to within 1.5 km below sea level with a density contrast of 0.15 gm/cc and an anomalously low density mantle of 3.2 gm/cc. Khan and Mansfield (1971), however, assume that the 7.5 km/sec layer found by Griffiths et al (1971) represents the top of the anomalous mantle.

In summary, we may conclude that there is a wealth of evidence which shows beyond reasonable doubt that material

of anomalously low density, low velocity and low Q underlies the region of domal uplift in Kenya and Ethiopia. Further details of the structure are sparse and controversial (for example the various interpretations of the gravity anomalies) and the purpose of this work is to use seismic array data to derive further information on the shape and velocity of the anomalous body.

#### 1.1.4. Theories of Formation of the Rift

Since the development of the concept of sea floor spreading and plate tectonics theories of the formation of the rift have been framed in these terms.

The seismicity of the rift system forms a continuation of the zones of shallow seismicity associated with the mid-Indian Ridge, the Carlsberg Ridge and the Gulf of Aden (Wohlenberg, 1970) although the epicentres exhibit rather more scatter than those associated with mid-ocean ridges (Sykes and Landisman, 1964).

The most usual classification of the Rift System is as the third limb of a triple spreading centre which includes the Red Sea and the Gulf of Aden (McKenzie et al, 1970). The Red Sea is considered as a spreading centre for the Arabian and Nubian plates and the Gulf of Aden for the Arabian and Somalian plates. According to the postulates of plate tectonics (McKenzie and Parker, 1967; Morgan, 1968) the motion across the rift may be deduced if the motions across the other two spreading centres can be found.

The motion between the Arabian and Somalian plates appears to be well determined. Laughton (1966) first calculated the direction of spreading from the strike of

transform faults in the Gulf of Aden and the pole of rotation has been placed at approximately  $26.5^{\circ}\text{N}$ ,  $21.5^{\circ}\text{E}$  with an angle of rotation of  $7.6^{\circ}$  (McKenzie et al, 1970; Le Pichon, 1968).

The motion between the Arabian and Nubian plates has aroused somewhat more controversy. Early observations suggested to Girdler (1958) that only the axial trough of the Red Sea was underlain by oceanic crust but later work by Frazier (1970) and Tramontini and Davies (1969) showed that a large part of the sea was associated with oceanic crust. The first attempt to locate the pole of rotation and thus calculate the motion between the Nubian and Somalian plates was by Roberts (1969) and led to a pole for the two African plates at  $30^{\circ}\text{N}$   $47^{\circ}\text{E}$  with a rate of opening of 0.7 cm/year. This was shown to be strongly at variance with observation by Baker (1969), the most obvious contradiction being the observation that the rift decreases in width on going south.

The next calculation was by McKenzie et al (1970) who calculated the Nubian-Arabian pole from a statistical fit of the coast-lines and hence computed the Nubian-Somalian pole to be at  $8.5^{\circ}\text{S}$   $31^{\circ}\text{E}$  with a rotation angle of  $1.9^{\circ}$ . These conclusions were subject to considerable criticism. Al-Chalabi (1971) questioned the reliability of fitting contours to locate poles (although this analysis was in turn criticized by Bullard and McKenzie (1971)). Other writers (Mohr, 1970; Freund, 1970; Baker and Wohlenberg, 1970) questioned the separation predicted by the plate theory when compared with the observed crustal separation.

An alternative to the three pole system was put forward by Gass and Gibson (1969) and Baker (1969) who considered all three plates to be moving northward but at different rates so that left lateral shear had taken place along the East African Rift.

The role of plate tectonics in the East African Rift System is thus of questionable value at least in the elementary form proposed and the detailed interpretations drawn. This is suggested for several reasons; first, calculations on the location of the third pole in a three pole system depend crucially on the location of the third pole. It has been shown (Girdler and Darracott, 1972) that an error in one rotation angle of  $0.1^{\circ}$  can move the location of the African pole by  $6^{\circ}$ - $8^{\circ}$ . With the uncertainty involved in the motion of the Arabian-Nubian pole locations of the African pole are thus highly dubious. Secondly, McKenzie et al (1970) realized that the concept of characterizing the motion between plates by a single pole was a simplification. The work of Baker and Wohlenberg (1971) shows that the northern and southern regions of the Kenyan uplift have undergone a maximum crustal extension of 3 km whereas between 5 and 25 km are allowed in the central sector of the rift. Saggerson and Baker (1965) show that the vertical movements in East Africa were interspersed with long periods of stability. Clearly, these observations cannot be reconciled with the idea of two plates moving at a uniform rate about a fixed pole. Finally, it has recently been suggested (Girdler and Stiles, 1974) that the Red Sea has developed in two separate stages between 41 and 34 million years before present and from 5 million years to the present day.

Oxburgh and Turcotte (1974) have applied their theory of membrane tectonics (Turcotte and Oxburgh, 1973; Turcotte, 1974) to the formation of the Rift System. They explain the rifting as being caused by the stresses set up within the plate as Africa moves northward on an ellipsoidal earth. Their argument clearly hinges on the motion of Africa since the Tertiary and they conclude that present palaeomagnetic evidence cannot define the motion in this period adequately; they also consider that the work of Burke and Wilson (1972) which claims that the African plate has been stationary since the Tertiary is not conclusive. Until further evidence appears, their theory cannot be considered as more than interesting speculation.

#### 1.1.5. The Role of the Rift System in Global Tectonics

The place of the rift system within the realm of global tectonics has varied with time and author. Some authors such as Gass (e.g. Gass, 1972) see the rift system and the associated Red Sea and Gulf of Aden as a laboratory for the break up of a continent and the early stages of sea floor spreading, while others place rather less significance on the structure with, for example, McKenzie et al (1970) considering that the rift, although "of great interest, is not of global importance."

In considering continental rifts Le Bas (1971) has strongly emphasized that the feature of chief significance in the structure is the domal uplift and that the role of the rift valleys is not vital. It has been pointed out (Gass, 1972; Le Bas, 1971) that domal uplifts are widely distributed throughout Africa (Le Bas lists eighteen such structures). Gass goes on to suggest that a true rift zone

occurs and continental rifting begins when the areas of uplift merge and the resultant fractures overlap; a petrogenetic sequence is proposed with progressive development from continental alkali basalts in the early stages of the process to the production of oceanic tholeiites on complete crustal separation. Le Bas takes a different point of view and argues that the structures of Ethiopia and Kenya (and all other such regions of uplift) are independent and involve processes quite distinct from those involved in sea floor spreading. Murray (1970) considered that the long duration of alkaline magmatism within the rift also supports this point of view and Baker et al (1972) assert strongly, from a review of the geological evidence, that the rift system is not typical of the initial continental break up by the sea floor spreading process.

One of the aims of the present work is to investigate the connection between the two anomalous structures beneath the regions of uplift and thus compare these contrasting viewpoints.

One theory which has been put forward in earlier studies was that the present Tertiary structure is the latest phase in the history of several generations of faulting dating to the Precambrian (see for example Dixey, 1956 and McConnell, 1970). Such a suggestion has wide implications for the theory of continental drift for if a phenomenon which has its origin within the asthenosphere may be shown to have existed for a large part of geological time then relative horizontal motions between the lithosphere and asthenosphere are difficult to envisage. Recent work (King, 1970; Baker et al, 1972) has shown, however, that

the present phase of movement is independent from earlier structures which are considered to have provided a crustal grain for faulting to occur.

CHAPTER 1

SECTION 2 - PREVIOUS TELESEISMIC STUDIES AT KAPTAGAT

The present study is a development from the work of Backhouse (1972) and, as a preliminary, a brief survey of this work will be made.

The main part of the previous study concerned the measurement and analysis of teleseismic signals recorded at the seismic array station at Kaptagat, Northern Kenya.

1.2.1. Kaptagat Array Station

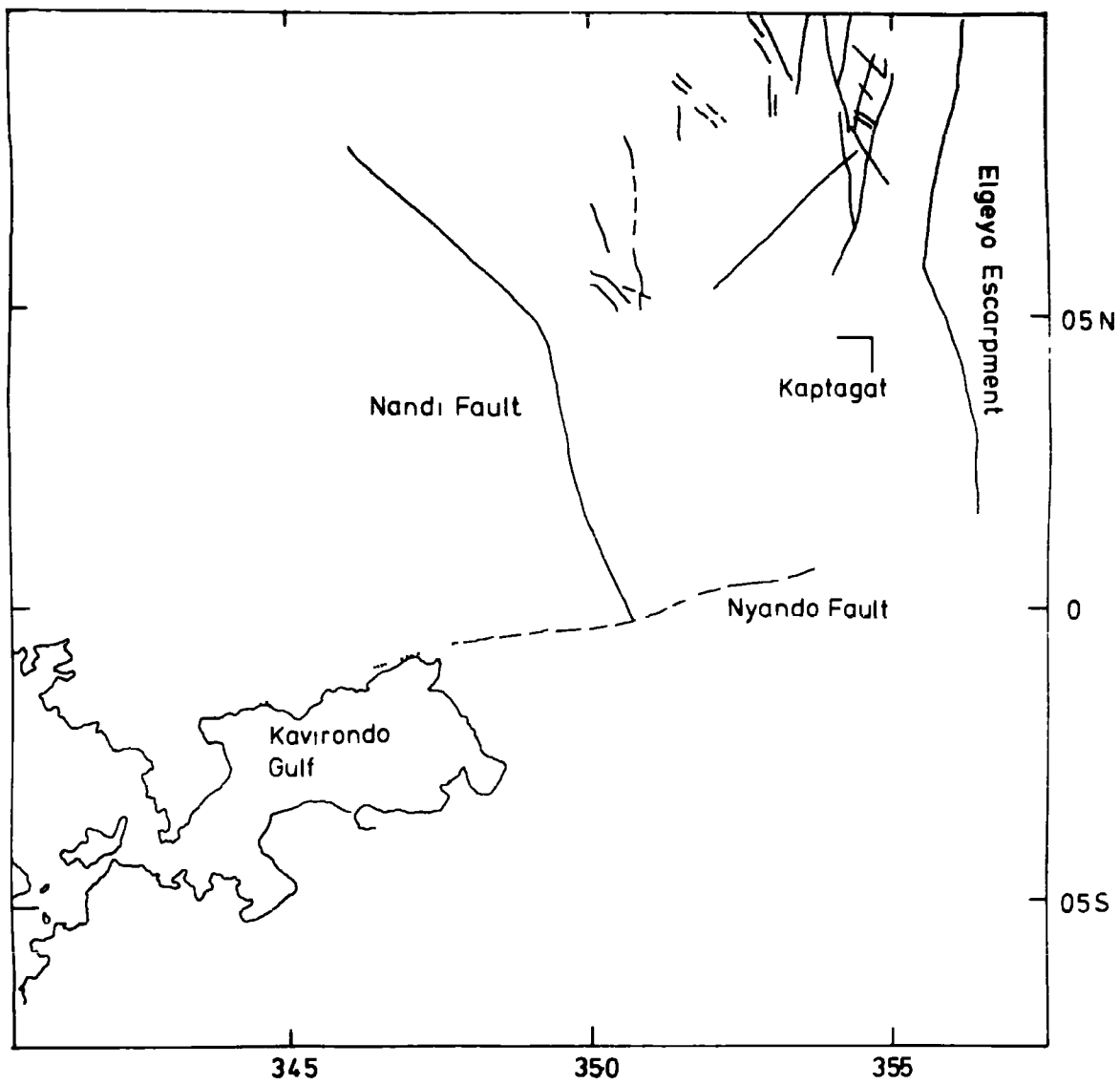
The seismic array station at Kaptagat was operated by the University of Durham Geology Department between October, 1969 and June, 1972. The purpose of the project was to investigate the structure of the crust and upper mantle beneath East Africa and to study the seismicity of the eastern and western branches of the rift and other seismically active regions such as the Kavirondo and Speke Gulf Rifts.

Kaptagat is 2,390 m above sea level on the Uasin Gishu plateau which consists of phonolite lavas dipping gently westward. There are two major lava flows and the only borehole which pierced the phonolite showed a total thickness of 144 m. As this site was 15 km south west of Kaptagat it is likely that the thickness of phonolite beneath Kaptagat is between 150 and 200 m. These lavas overlie Precambrian basement gneiss (Jennings, 1964).

The lava flows form part of the Kapsabet plateau, an upstanding block which is bounded to the east, south and west by major faults (Fig.1.2). Approximately 15 km to the east of Kaptagat lies the Elgeyo escarpment which forms

Figure 1.2.

The location of the Kaptagat array and its relation to major fault structures.



the western boundary of the Gregory Rift. The Nandi fault lies approximately 60 km to the west of the array and runs SSE after emerging from the lavas of Mount Elgon. To the south the Nyando fault, which is the northern escarpment of the Kavirondo Rift Valley, forms the southern boundary of the Kapsabet block.

The array consisted of ten Willmore Mk.II short period seismometers set vertically to two seconds period and arranged in an 'L' shape with arm dimensions of approximately 5 km. This is illustrated in Fig.1.3 and details are given in Table 1.1. The recording system was as described by Long (1968). Signals from the ten seismometers were amplified, frequency modulated and recorded on one inch, fourteen track magnetic tape at a speed of 15/160 in/sec. In addition, an internally generated binary time code and a radio signal providing Greenwich Mean Time were recorded.

#### 1.2.2. Parameters Measured Using Arrays

Waves arriving at an array from an earthquake cross it with an apparent velocity  $v_p$ . The wave will thus cross each of the seismometers in turn and the time delays incurred will be indicative of the apparent velocity and azimuth of approach.

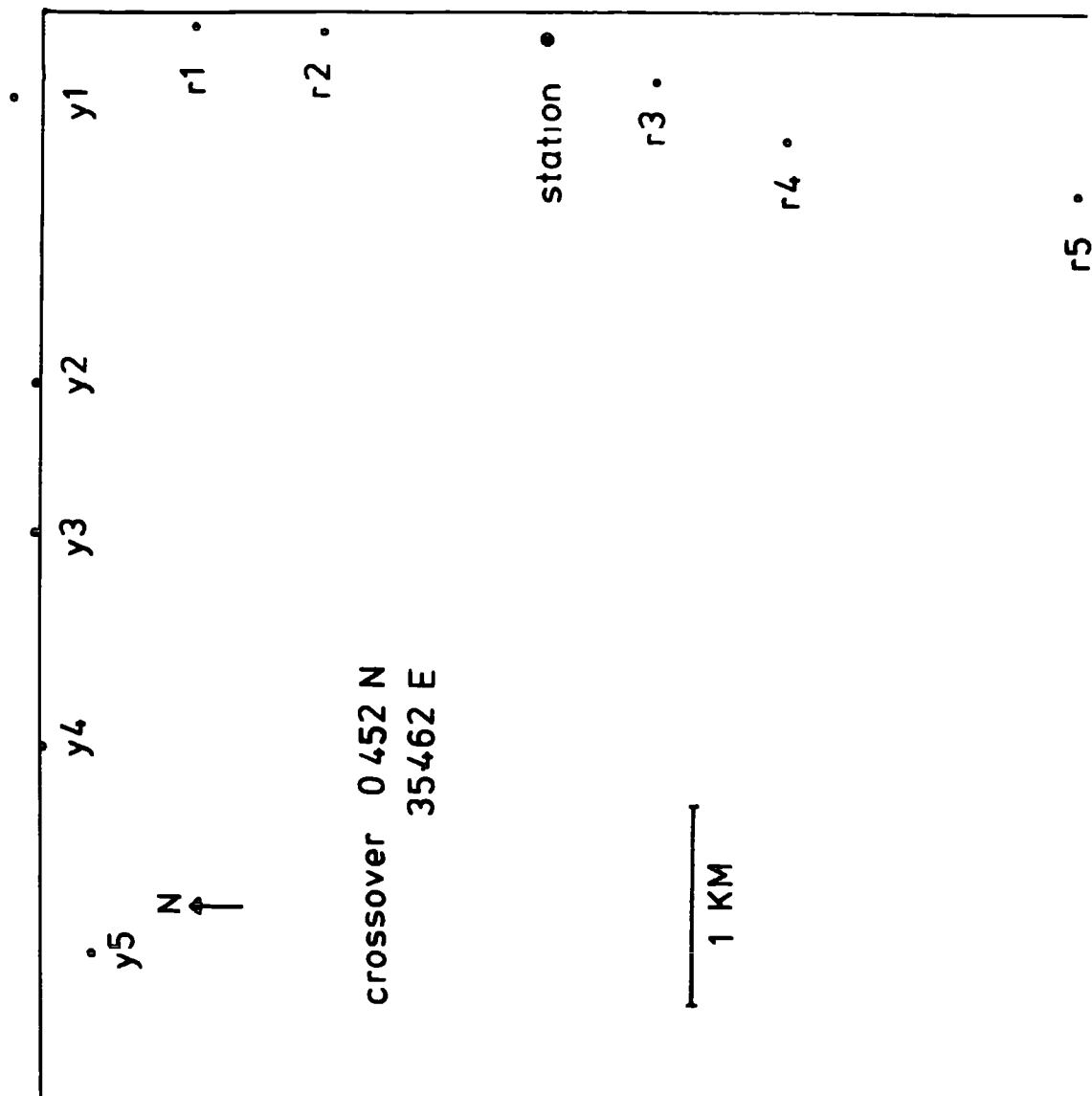
If the velocity of the wave in the medium beneath the array is  $v$  and the angle of incidence is  $i$ , then assuming a flat earth

$$v_p = \frac{v}{\sin i} \quad 1 - (i)$$

(Carpenter, 1966). For the case of plane parallel structure beneath the array  $v_p$  is a constant for the raypath as a consequence of Snell's Laws of Refraction. For a spherically

Figure 1.3

Plan of the Kaptagat array illustrating the location of the red (R) and the yellow (Y) lines of the seismometers.



crossover 0.452 N  
35462 E

N ↑

1 KM

Table 1.1

Pit Co-ordinates and Altitudes.

Pit	X <sub>1</sub> (km)	Y <sub>1</sub> (km)	Estimated Error (km)	Pit Elevation (m)
Y1	-0.446	0.166	±0.001	0.0
Y2	-1.888	0.003	±0.015	-30.0
Y3	-2.645	0.025	±0.030	-50.0
Y4	-3.720	-0.013	±0.010	-50.0
Y5	-4.750	-0.250	±0.060	-70.0
R1	-0.098	-0.766	±0.010	+10.0
R2	-0.114	-1.425	±0.020	+20.0
R3	-0.365	-3.077	±0.010	+30.0
R4	-0.663	-3.736	±0.030	+10.0
R5	-0.925	-5.200	±0.010	+30.0

symmetric earth it may be shown (Bullcn, 1965) that the phase velocity across the surface at radius  $r$  is  $v/r \cdot \sin i$  and that this is also a constant for the raypath.

The reciprocal of the phase velocity is called  $dT/d\Delta$  or slowness.

### 1.2.3. Onset Time Analysis

For an array the size of Kaptagat it is considered that onset time analysis provides the most reliable determination of velocity and azimuth (Mitchell, 1969; Corbishley, 1969).

This technique requires the relative onset times for each of the seismometers to be measured. These times enable the velocity and azimuth to be determined as is now shown.

The locations of an array of  $m$  seismometers are described by the co-ordinates  $(X_1, Y_1)$  which correspond to a distance  $R_1$  from the origin at an azimuth  $\theta_1$  (Fig.1.4). Consider a plane wavefront propagating across the array from an azimuth  $\alpha$  with velocity  $V_p$ . By equation 1-(1) the phase velocity along  $R_1$  is  $V_p / \cos(\theta_1 - \alpha)$ .

The arrival time,  $T_1$ , of the wave at  $(X_1, Y_1)$ , relative to the origin is then

$$T_1 = \frac{-R_1 \cos(\theta_1 - \alpha)}{V_p}$$

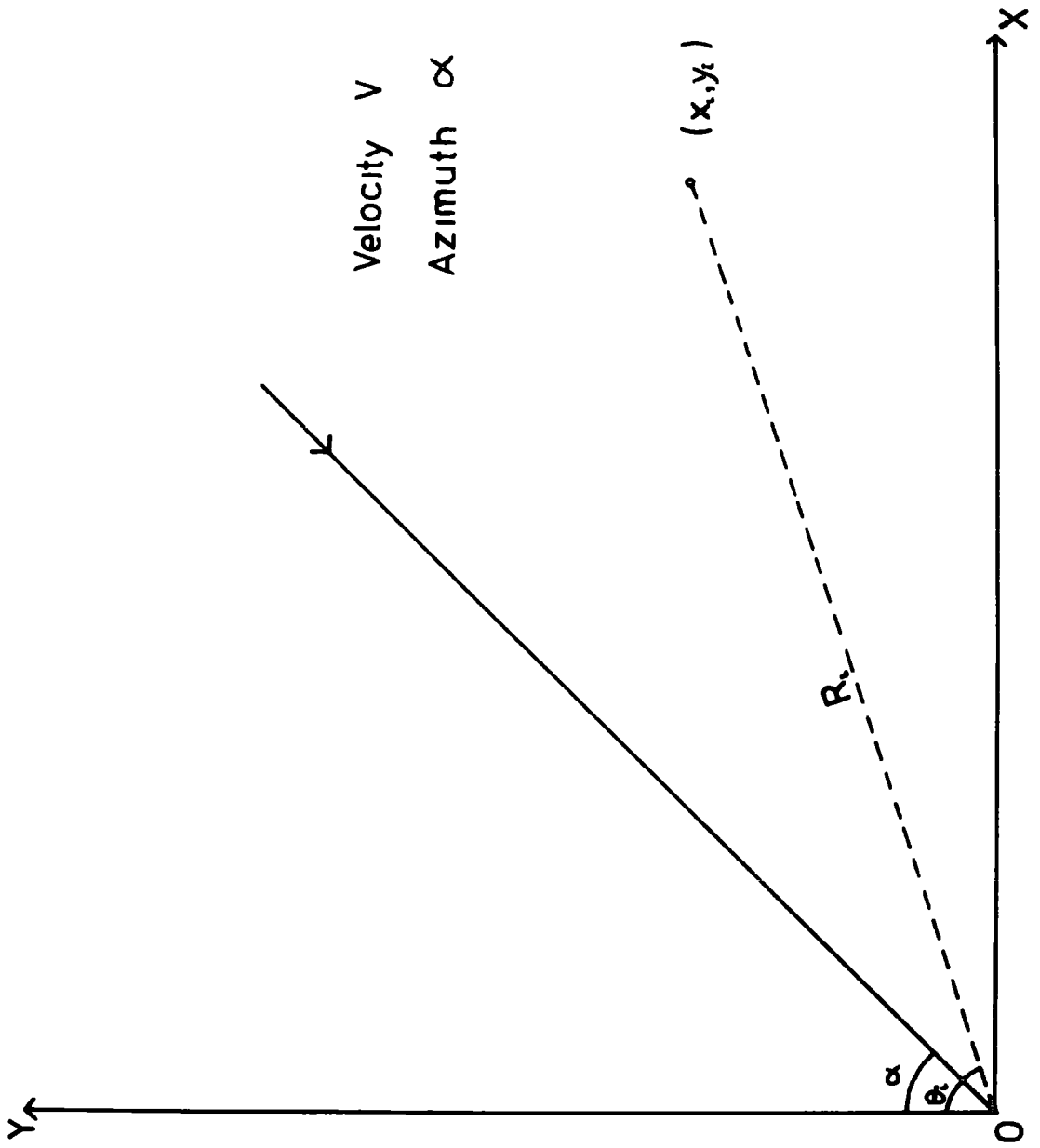
In practice the arrival time is measured relative to an arbitrary zero. If this is taken as  $t_1$  then

$$\begin{aligned} t_1 &= C + T_1 \\ &= C - \frac{R_1 \cos(\theta_1 - \alpha)}{V_p} \end{aligned}$$

where  $C$  is the time the wave crosses the origin and is a

Figure 1.4

Schematic diagram of a plane wave crossing the array.



constant for each pit.

Assuming that  $R_1$  and  $\theta_1$  are known and that the  $t_1$  are measured with errors  $\epsilon_1$  which are normally distributed then if  $m$ , the number of seismometers, is greater than three, the equations form an over-determined set of linear equations which may be solved for the quantities  $C$ ,  $\alpha$  and  $V$  by least squares applied to  $\epsilon_1$ . Full details of the solution including the estimation of confidence limits are given by Douglas (1967).

Since  $dT/d\Delta = 1/V$  the arrival time at the  $i$ th seismometer for the  $k$ th event,  $t_{ik}$  may be written

$$t_{ik} = C_k - R_i \cos(\theta_i - \alpha_k) \left( \frac{dT}{d\Delta} \right)_k + \epsilon_{ik} \quad 1-(11)$$

Corbishley (1969) showed that the most accurate method of measuring relative onset times was waveform matching (Evernden, 1953). With this technique waveforms are matched over several wavelengths and an arbitrary common point is measured on all traces.

This method has two advantages. First, because 'first breaks' are not measured events with emergent arrivals may be studied. Secondly, by matching the waveform over several wavelengths the incoherent noise within the array will be averaged out to some extent.

#### 1.2.4. Errors

Several sources of error exist in the measurements described and the assumptions made and these are now briefly reviewed.

##### 1. Plane Wavefront Approximation

In section 1.2.3 it was assumed that the wavefront crossing the array was planar. The wavefront will however

approximate to a circle of radius  $\Delta^{\circ}$ , where  $\Delta^{\circ}$  is the distance from source to station.

The maximum timing error occurs for the shortest distance considered which is  $\Delta = 20^{\circ}$ . For this distance the maximum time difference between plane and circular wavefronts is 0.7 milliseconds. As timing measurements are made to an accuracy of approximately 10 milliseconds this error is negligible.

## 2. Errors in the Location of Epicentres

The teleseismic events considered were all listed in the NOAA Preliminary Determination of Epicentre bulletins and consequently their locations and focal depths were known. Using a standard earth model 'theoretical' values of slowness and azimuth may be estimated. It is suggested (Douglas, 1967; Underwood and Lilwall, 1969; Davies and McKenzie, 1969) that earthquakes may be mislocated by approximately 25 km with a focal depth error of up to 75 km.

It is shown that this mislocation causes a maximum error in azimuth of  $0.7^{\circ}$  and in slowness of 0.1 secs/deg; the focal depth error will also cause a maximum slowness error of 0.1 secs/deg.

In the present work consideration was given to relocating the epicentres used by the Joint Epicentral Determination method (Douglas, 1967). It was not done first because these maximum errors are much smaller than the observed anomalies and, as is discussed later (section 4.2), it is not possible to interpret the anomalies to a degree influenced by these errors.

### 3. Random Reading Errors

Random errors will be introduced into the measurements at all stages of the process of recording, replaying and measuring the records. It is shown, using the theory of Kelly (1964) that the maximum reading error in slowness is 0.2 sec/deg and in azimuth less than  $2^{\circ}$ .

#### 1.2.5. Anomalies and their Interpretation

Assuming an average earth model it is possible to derive theoretical values for the slowness and azimuth expected for each event. Using these, slowness and azimuth anomalies may be defined and these form the basis of the interpretation. The data and a formal definition of the anomalies are given in the next chapter.

The anomalies observed at Kaptagat are compared with those found at other array stations (Corbishley, 1970; Niazi, 1966; Otsuka, 1966a, 1966b; Greenfield and Sheppard, 1969) and it is concluded that their dependence on azimuth and distance is similar to that found at other arrays although the magnitude of the anomalies at Kaptagat is far larger. Since at other arrays the anomalies had been interpreted as being caused by a single plane dipping interface, usually ascribed to the Moho, this was attempted with the Kaptagat data.

Thus the structure beneath Kaptagat was assumed to consist of normal crust and mantle to an unknown depth. The boundary between normal and anomalous mantle was assumed to consist of a single plane interface dipping westward which is the source of the observed anomalies; the anomalous mantle velocity was fixed at 7.5 km/sec (Griffiths et al.

1971) and various angles of dip were used to simulate the observed slowness and azimuth measurements. It was found that the large anomalies required extremely steep dips to be placed on the boundary (this will be analysed in more detail in chapter three but essentially the deviation produced by a single interface increases with the angle of incidence) and consequently certain events, notably those for shorter distances and thus making large angles of incidence to a horizontal boundary, underwent total internal reflection before achieving the necessary deviation. Consequently the model of a single interface was rejected as being unable to satisfy the data and structures containing two interfaces were proposed.

It is suggested that this rejection of a single interface was unjustified. It is always possible, within certain limits to be described in chapter three, to avoid total internal reflection by adjusting the boundary so as to reduce the angle of incidence. Since there is no fundamental reason to assume a plane boundary the most simple solution, in principle, is to postulate a curved interface between normal and anomalous mantle.

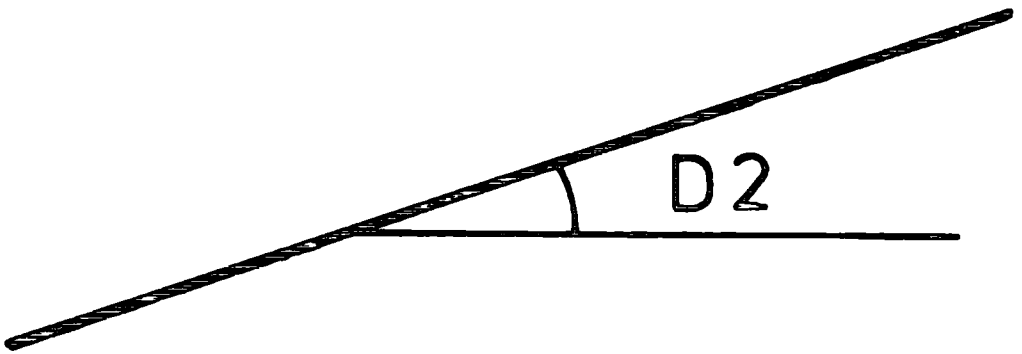
The model which was, however, assumed is illustrated in Fig.1.5. Both interfaces are assumed to lie in the same vertical plane and  $V_2$  is again maintained at 7.5 km/sec. Angles  $D_1$  and  $D_2$  are allowed to vary as is the direction of maximum thickening of the structure,  $\psi$ . An optimum solution was found when the upper surface had a dip,  $D_2$ , of  $27^\circ$  and the lower surface a dip,  $D_1$ , of  $36^\circ$  with  $\psi$   $125^\circ$  east of north. This will be referred to as model 1.

Figure 1.5

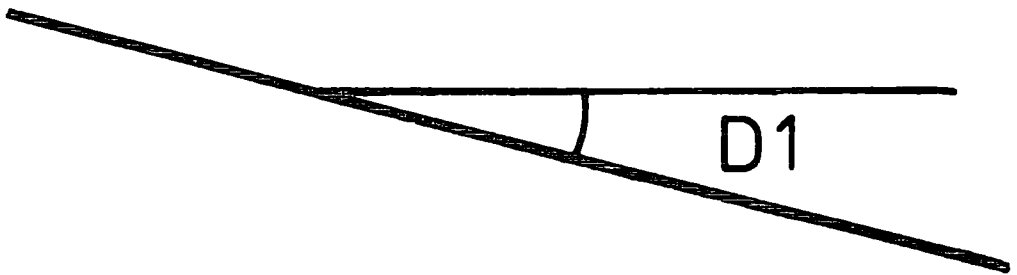
Model used in the interpretation of the array data by  
Backhouse (1972)

# KAPTAGAT

$V_3$  (km/sec)



$V_2$



$V_1$

The basic disadvantage of this model is that it increases the number of parameters needed in its definition and thus decreases the degree to which they may be determined. Thus Fig.1.6 shows a contour map of the RMSD values in the space defined by D1 and D2 with minimum RMSD of 2.03. It can be seen that the number of structures within one root mean square deviation of the minimum is vast. In particular the contours on D2 are open ended showing how poorly this interface is defined. To put the problem another way; if the structure is as postulated, the present data is unable to say anything meaningful about the dips involved.

Analysis of this model using slowness anomaly alone was then made and this gave an optimum model for an upper dip of  $26^{\circ}$ , a lower dip of  $46^{\circ}$  and with  $\psi$  at  $123^{\circ}$  east of north. Fig.1.7 shows the contour map over D1 and D2 and again the contours are open ended but the minimum RMSD is now reduced to 1.3 suggesting that slowness anomalies are more useful in this analysis.

#### 1.2.6. Delay Times

Seventy-eight measurements of delay time at Kaptagat relative to Bulawayo were made and these gave a mean delay of  $2.20 \pm 2.00$  sec where the error is the 95% confidence limit.

The delays were then analyzed in terms of a constant and azimuthally dependent term of the form

$$T_k = A + B \sin(\alpha_k + U) \quad 1-(111)$$

where  $T_k$  and  $\alpha_k$  are their delay time and azimuth of the kth event and A, B and U are constants. Using a least squares procedure on the whole data set A, B and U were evaluated to give

Figure 1.6

Contoured weighted RMSE for wedge model 1.

MODEL 1 WEIGHTED RMSD

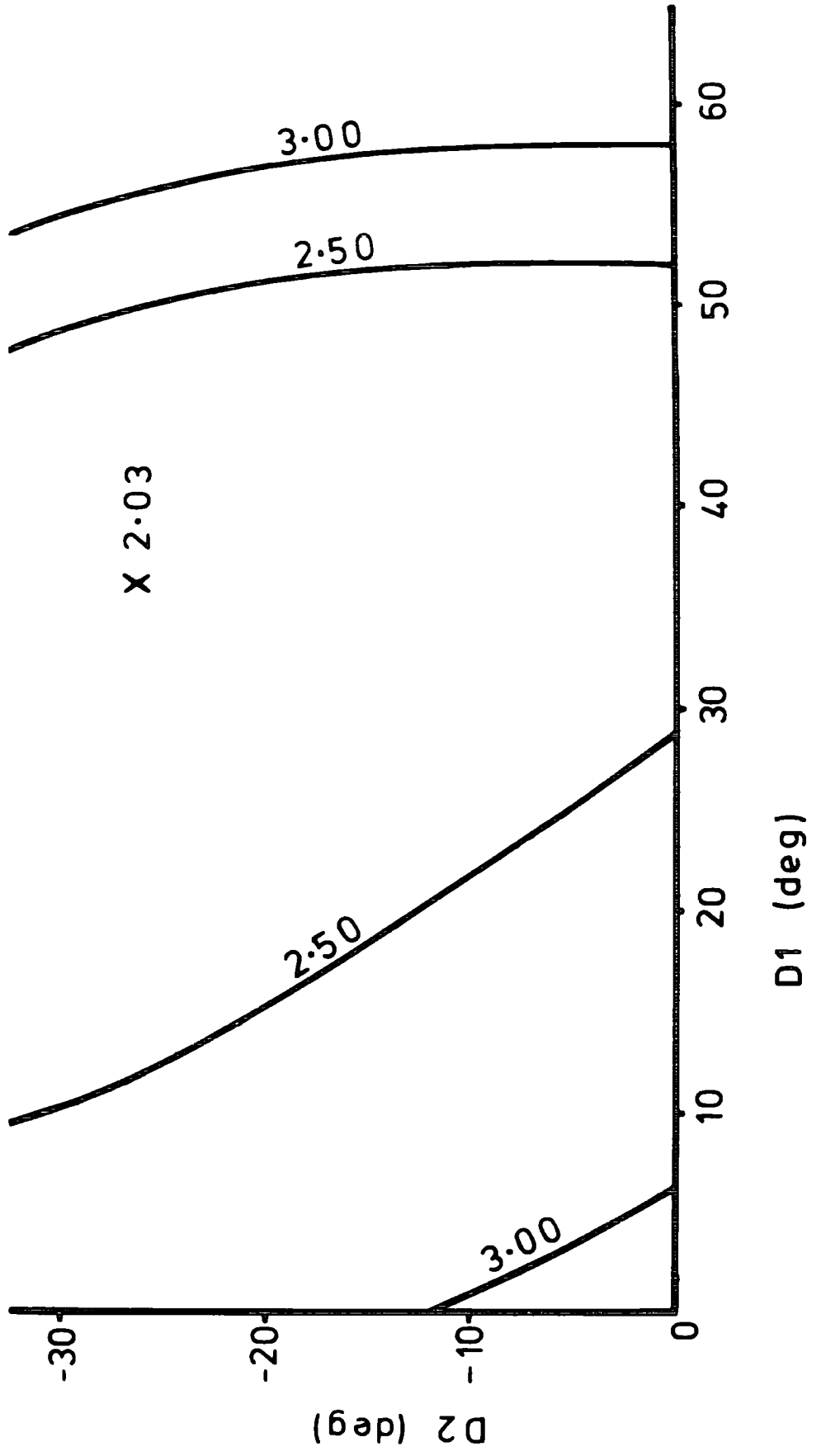
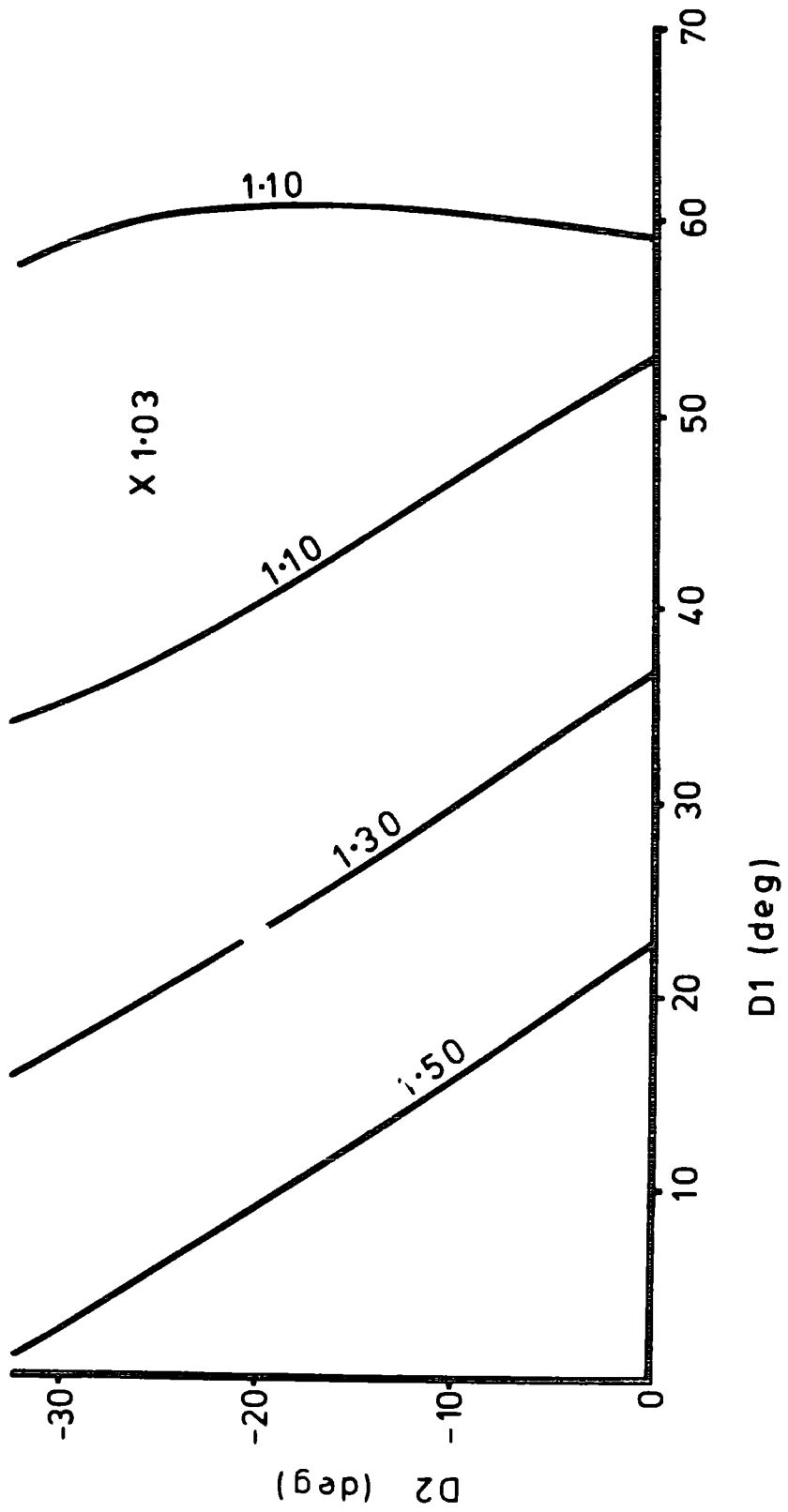


Figure 1.7

Contoured weighted RMSD for wedge model 2.

MODEL 2 SLOWNESS RMSD (sec/deg)



$$T_k = 2.36 + 0.34 \sin (\alpha_k + 284).$$

The 95% confidence limit on B is  $\pm 0.41$ .

Although detailed interpretation of these anomalies is difficult and will be considered later one point is quite clear; there is no significant variation, at the 95% confidence level, of delay time with azimuth. The delay time variation with azimuth for wedge model one is illustrated in Fig.1.8. Here the value of B in equation 1-(iii) is plotted as a function of  $V_2$ , the anomalous velocity. If the assumed anomalous velocity is 7.5 km/sec it can be seen that the expected delay time variation will have an oscillating component of amplitude 1.6 sec approximately.

In qualitative terms the model containing two steeply dipping interfaces leads to a maximum variation of delay time with azimuth which is not in agreement with observation.

Because of these problems a completely different approach to the data was developed and this is described in the present work.

#### 1.2.7. Summary

This concludes the review of the previous work in so far as it applies to the present study. Necessarily many of the details have been omitted and the techniques used have been briefly described. If further details are required the previous work should be consulted.

The final model of the upper mantle beneath the Gregory Rift proposed by Backhouse is summarized in Fig.1.9. where a cross section across the rift is shown. The structure is assumed to extend along the length of the rift both north and south from Kaptagat.

Figure 1.8

Variation in amplitude of azimuthal delay time term due to low velocity wedge model 1 with wedge velocity  $V_2$ . Hatched area gives 95% confidence limits on observed amplitude of azimuthal term (solid line). Dotted line gives the observed amplitude at angle  $\psi$  for wedge model 1.

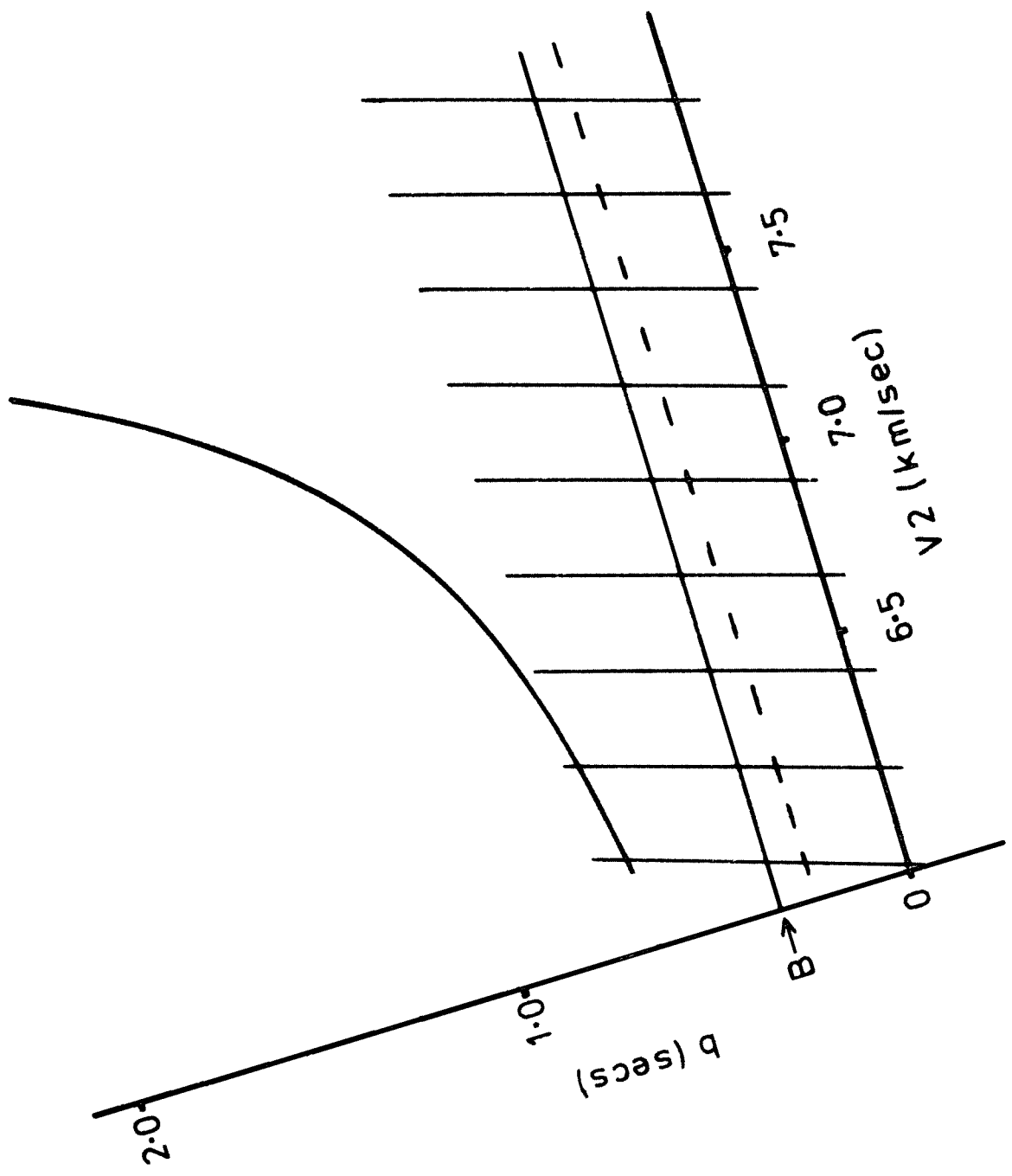
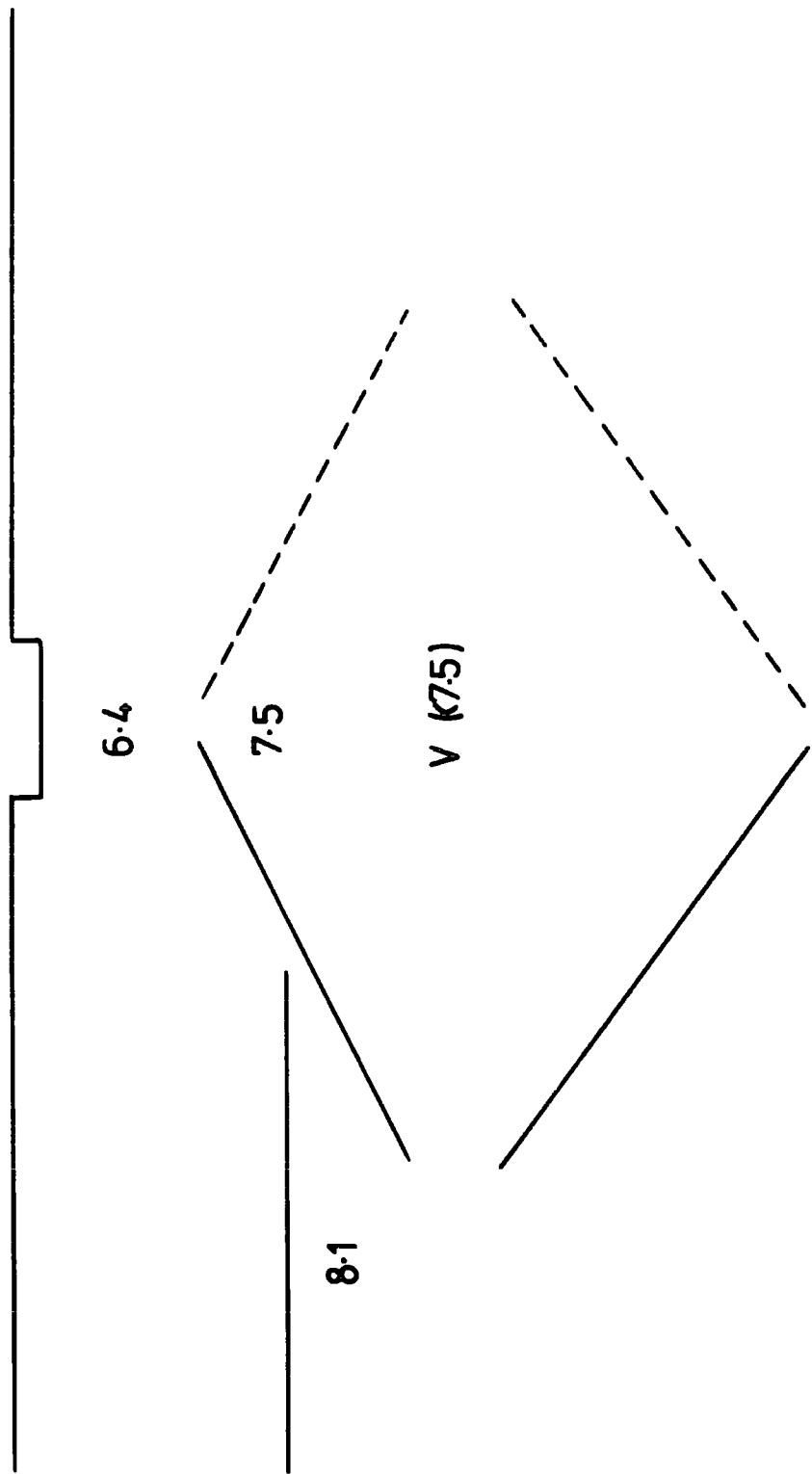


Figure 1.9

Final model of Backhouse (1972) for structure of the crust and upper mantle beneath the Gregory Rift.

GREGORY RIFT



8.2 - 8.3

CHAPTER 2

TELESEISMIC DATA

Two sets of data are presented. The first is from the previous work and will be called data set A and the second from the present work will be called data set B.

2.1. The Data

1. Data Set A

The seismic array at Kaptagat operated from October, 1969 until June, 1972 and the previous work used teleseismic data from July, 1970 until May, 1971. The main concern was for the quality of the data obtained and strict criteria had to be satisfied before an event was considered as suitable for processing. Thus the event had to be recorded with clear onsets by at least three seismometers on each arm of the array and, in fact, most of the thirty-four events used were recorded by at least eight seismometers. In addition impulsive signals were used, as Corbishley (1969) had suggested that the variation in seismometer characteristics could introduce timing errors and these would be minimized by using impulsive signals.

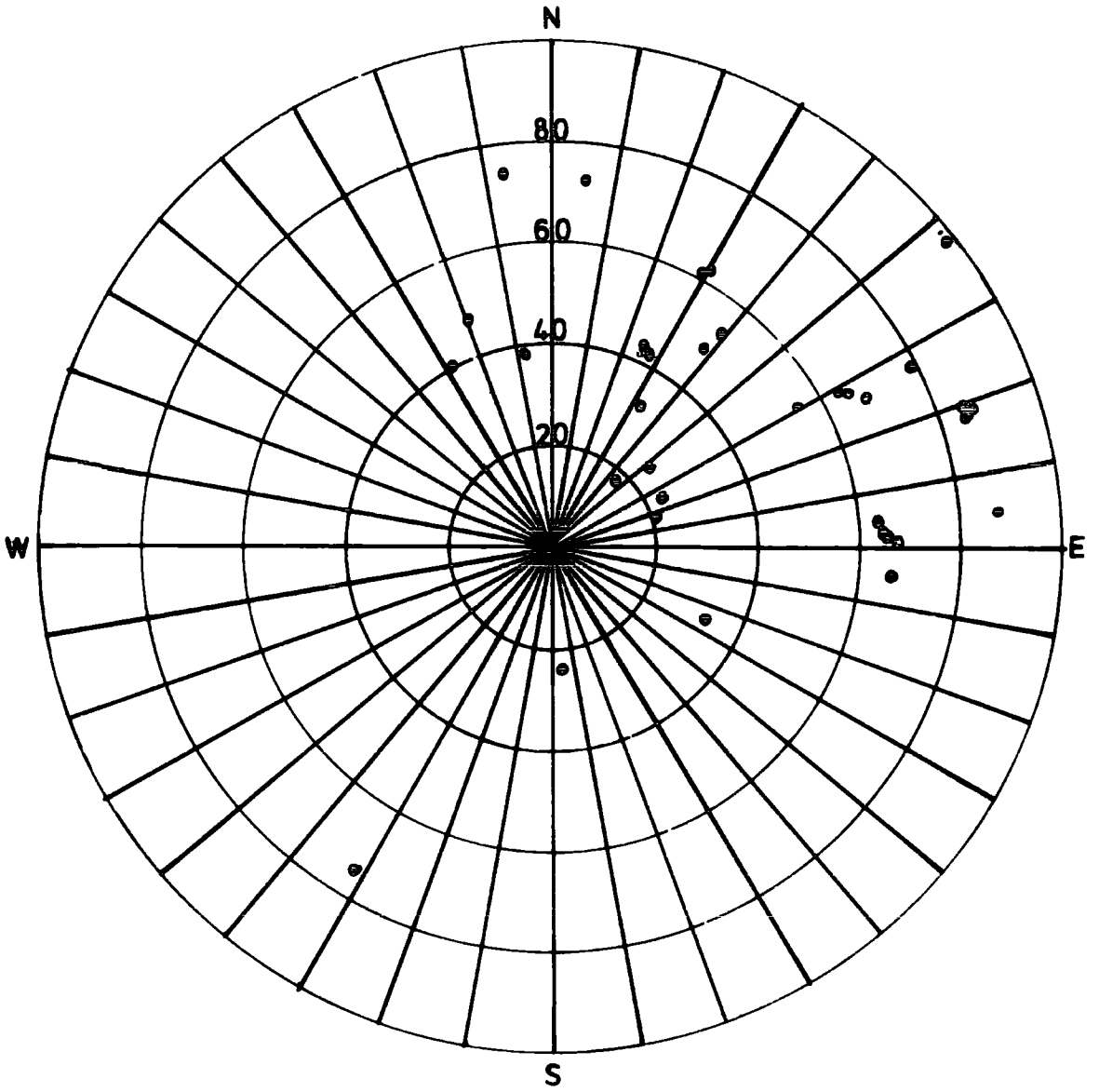
The locations of earthquakes comprising data set A are illustrated in Fig.2.1. The radial distance represents distance, in degrees, from Kaptagat and the azimuth that expected at the array from the NOAA location. It can be seen that the distribution of events is very uneven, and this may be briefly summarized

1. Azimuth  $0^{\circ}$  -  $90^{\circ}$ : Coverage is generally satisfactory representing the active areas of Southern Europe, Asia and the Far East.

Figure 2.1

Azimuth - distance plot of locations of earthquakes  
in data set A.

Data Set 'A'



2. Azimuth  $90^{\circ}$  -  $180^{\circ}$ : There are three events from Sumatra, the Mid-Indian Rise and the Mozambique Channel.

3. Azimuth  $180^{\circ}$  -  $270^{\circ}$ : There is one event from the South Sandwich Islands.

4. Azimuth  $270^{\circ}$  -  $360^{\circ}$ : There are four events from the Mediterranean, Yugoslavia, the Greenland Sea and Turkey. It may be noted that there are two events between azimuths  $120^{\circ}$  and  $330^{\circ}$ .

## 2. Data Set B

As a result of the distribution of data set A it was decided to consider all the recordings made during the experiment but to place emphasis on expanding the coverage of the data even though this would necessitate reducing the quality of the events processed. In practice it was found that three seismometers recording on each arm was usually the minimum necessary to give adequate control on velocity and azimuth. However, it was found necessary to use records with a much lower signal to noise ratio than that found on the records of data set A and on these events analogue frequency filters were used to improve the signal to noise ratio.

The pass band used depended on the signal and noise spectra but usually 0.1 Hz to 2.0 Hz was found satisfactory. Three Krohn-Hite filters were used for this work and before each event was played out it was necessary to ensure that the filtering process would not introduce any significant relative time delays into the record. Thus the event from one channel was used as input to all three filters simultaneously and the relative onset time was picked for

the same signal. No significant delays were ever found except when the filters had only recently been switched on.

The locations of the twenty-eight earthquakes comprising data set B are shown in Fig.2.2. The set still reflects the general pattern but a comparison with data set A will illustrate the improvement in data coverage.

1. Azimuth  $0^{\circ}$  -  $90^{\circ}$ : Eleven events are in this quadrant. They have been chosen to improve the distribution within the region.

2. Azimuth  $90^{\circ}$  -  $180^{\circ}$ : Seven events are in this quadrant.

3. Azimuth  $180^{\circ}$  -  $270^{\circ}$ : Four events are in this quadrant.

4. Azimuth  $270^{\circ}$  -  $360^{\circ}$ . Six events are in this quadrant.

It must, however, be emphasized that the quality of much of this data is in many cases very considerably inferior to that used in data set A.

## 2.2. Velocities Expected in the Array

Before considering the velocities actually measured consideration will be given to the velocities expected and the way these influence the accuracy of the measurements made.

From equation 1-(1) it can be seen that the phase velocity increases as the angle of incidence at the surface decreases. If the direct P-wave is considered this means that as the distance increases the phase velocity across the array also increases. If the average earth structure of Herrin et al (1968) is assumed the expected velocity as a function of distance may be calculated and this is shown in Fig.2.3.

At  $\Delta = 20^{\circ}$  the expected velocity is 9.85 km/sec and

Figure 2.2

Azimuth - distance plot of locations of earthquakes in  
data set B.

Data Set 'B'

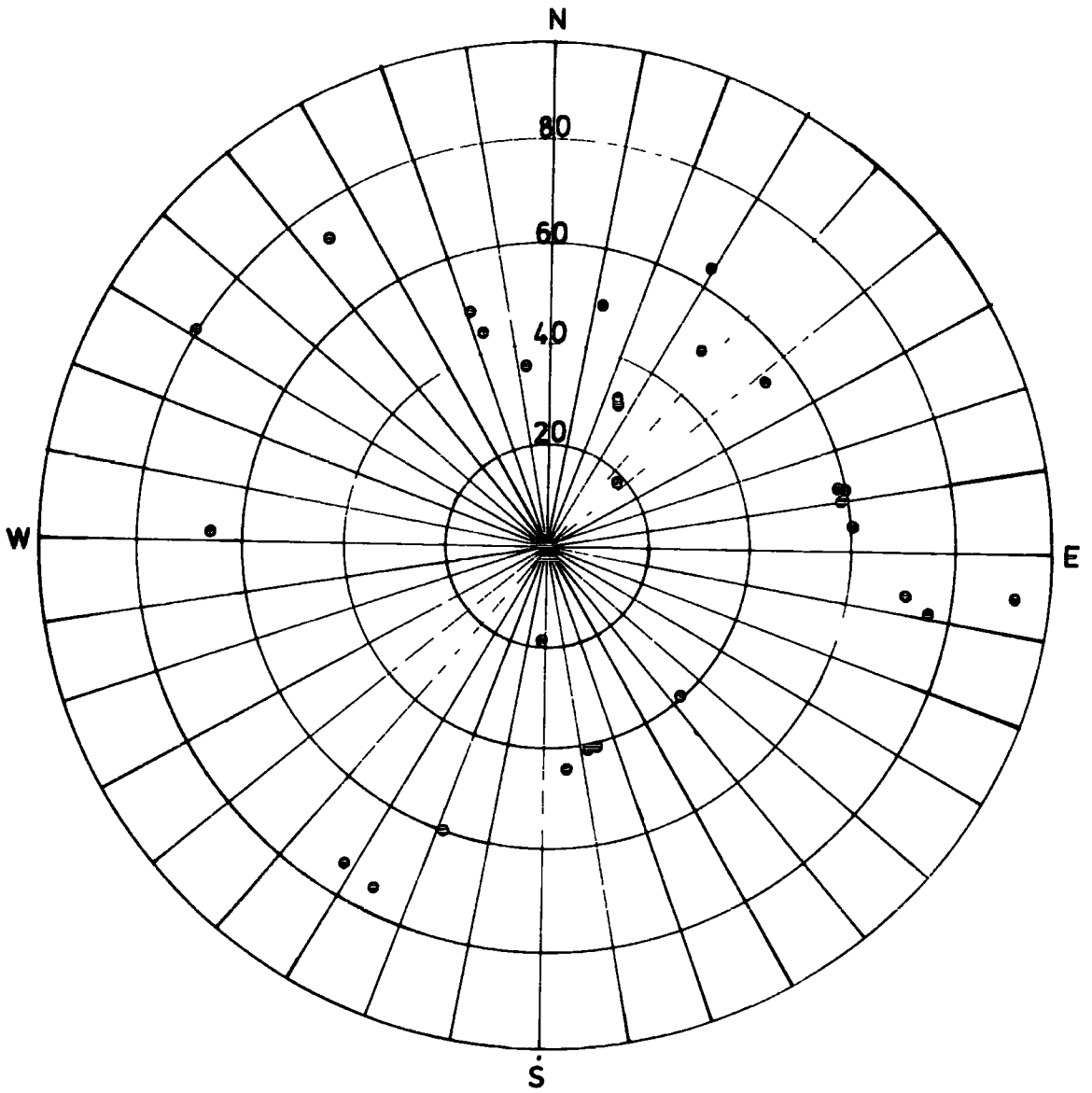
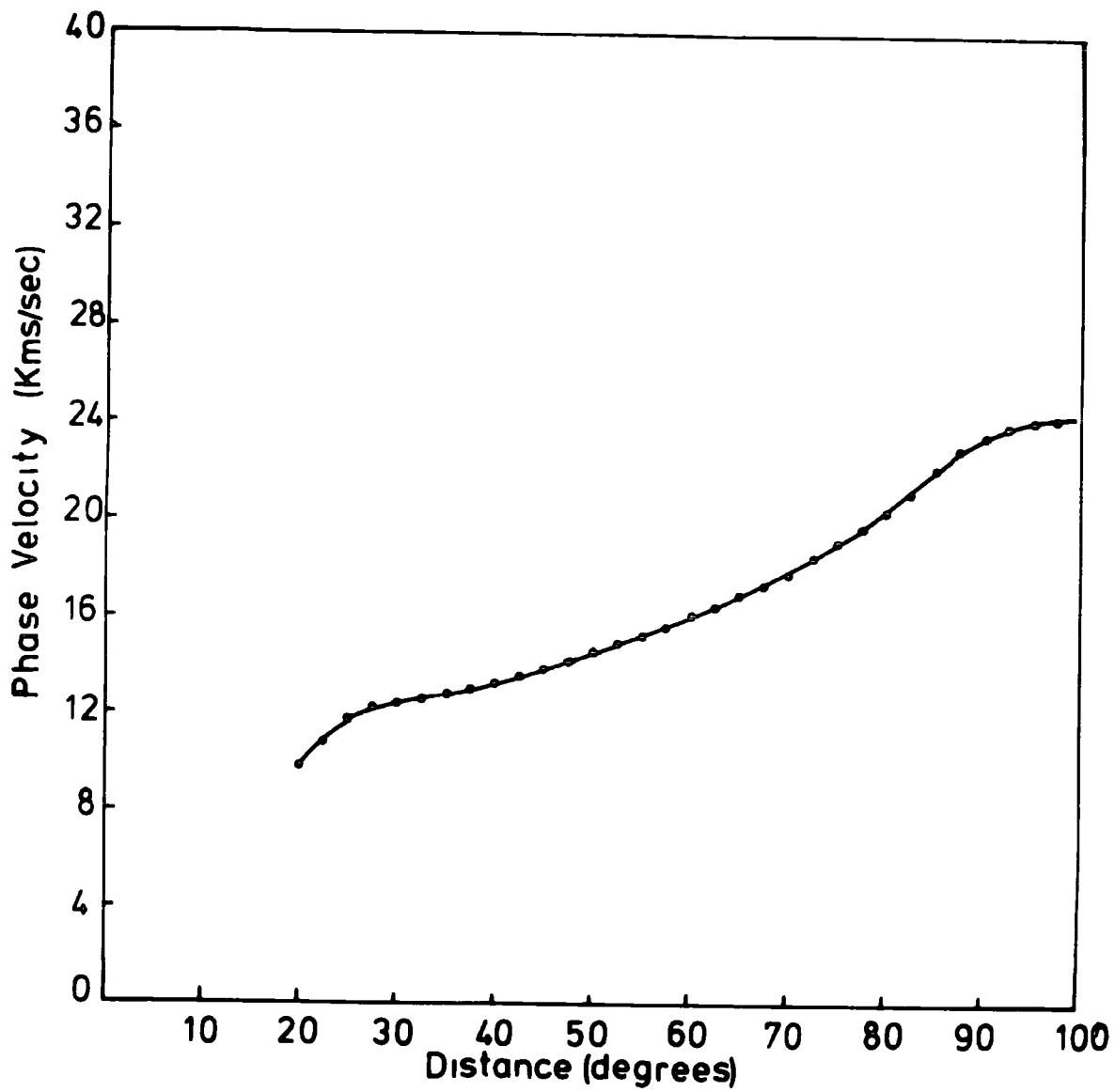


Figure 2.3

Phase velocity as a function of epicentral distance  
according to Herrin et al (1968)



taking the mean spacing of the seismometers as one kilometre the maximum delay between adjacent seismometers is 0.10 sec. When  $\Delta = 100^\circ$  the expected phase velocity is 24.36 km/sec and the maximum delay is 0.04 sec.

These figures must be considered in assessing the accuracy of the timing measurements and the resulting data. It must be recognized that for velocities of 20 km/sec and above the accuracy of the measurements approaches the average delay between seismometers.

### 2.3 Definition of Anomalies

All the events studied in both data sets were listed in the NOAA Preliminary Determination of Epicentres bulletins. When available the bulletins of ISC were used but no significant discrepancies were ever found. Thus the epicentral co-ordinates and focal depth were known subject to the errors previously discussed. The events are described by numbers of the form 3447.70; the four figure number refers to the code number used in the GEDESS computer program (Young and Gibbs, 1968) provided by the AWRE seismology group and the numbers after the decimal point indicate the year thus providing easy access to information about these events from the Durham library.

#### Calculation of Theoretical Azimuth and Slowness

The parameters measured are compared with those expected from the earth model of Herrin et al (1968).

The theoretical azimuth is taken as the great circle azimuth between station and source defined by the NOAA data; the azimuth anomaly is then defined as the difference between the azimuth measured and the great circle azimuth.

The values of slowness to be expected from the average earth model have been calculated assuming a surface focus. These may be corrected for any focal depth by application of Snell's Laws as shown in Fig.2.4. Assuming a focus within the first layer the appropriate theoretical distance for  $dT/d\Delta$  is given by

$$CDEL = DEL + h \cdot \tan i$$

where, to a good approximation,  $i$  may be calculated from

$$\frac{dT}{d\Delta} = \frac{r \cdot \sin i}{V}$$

where  $dT/d\Delta$  is that appropriate for distance DEL,  $V$  is the velocity of the layer and  $r$  is the radial distance. If the focus is in a deeper layer the ray is traced through each layer using Snell's Laws.

Generally, for a focal depth less than 50 km the correction is 0.01 sec/deg or less and the maximum correction applied was 0.11 sec/deg for an event with a focal depth of 212 km at a distance of 48.4 deg.

The slowness anomaly is then defined as the difference between the measured slowness and the theoretical slowness as calculated above.

### Anomalies

The resulting anomalies for data set A are given in Table 2.1. and those for data set B in Table 2.2. with the errors shown being the 95% confidence limits. Both sets of anomalies are plotted against the expected azimuth in Figs.2.5 and 2.6.

The errors on the anomalies are, in the main, substantial as is to be expected from high velocity signals across a

Figure 2.4

Earth structure of Herrin et al (1968) for correcting  
epicentral distance for the effect of focal depth.

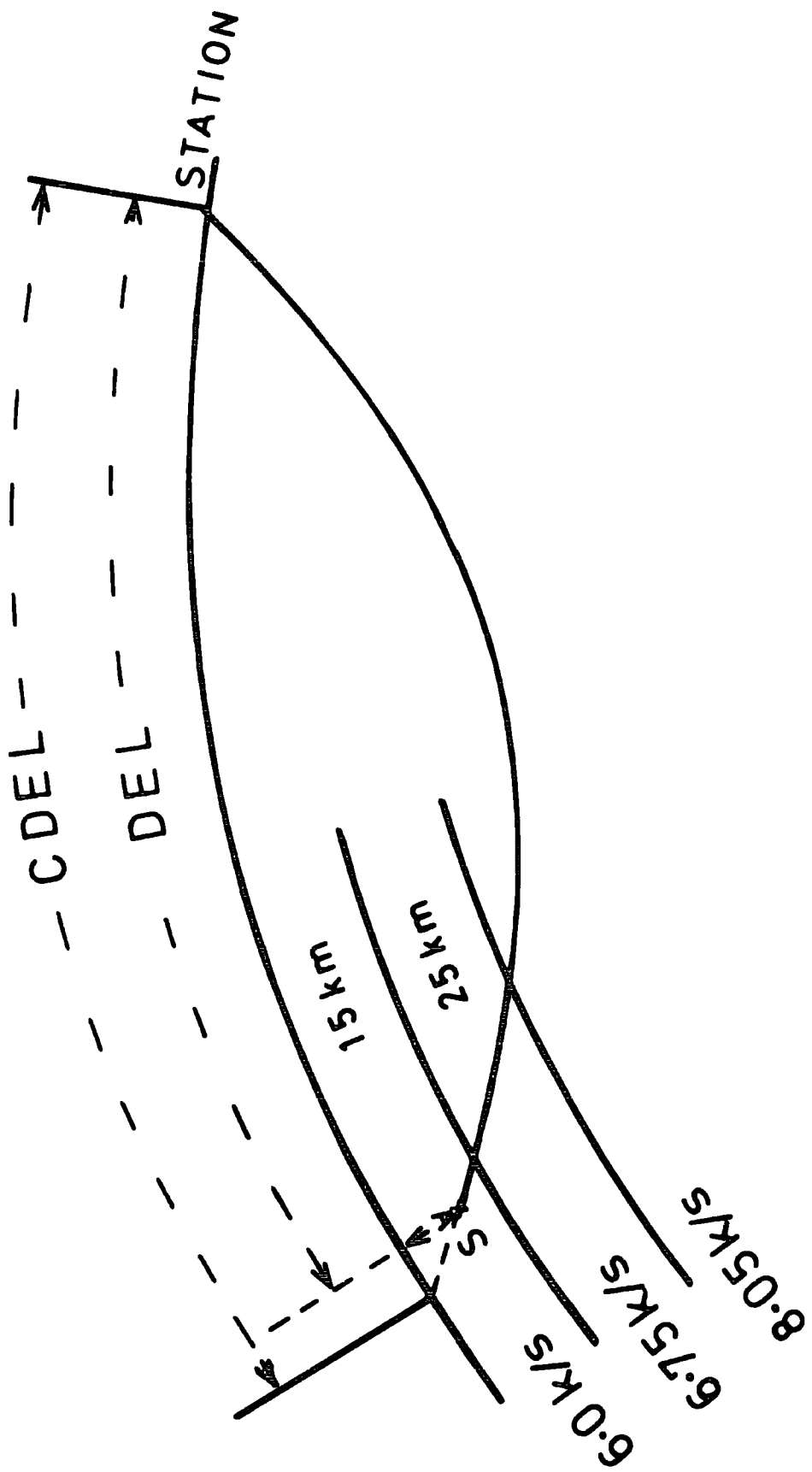


Table 2.1 Data Set A - No Pit Corrections Applied.

Event No.	Distance (degrees)	Azimuth (degrees)			Slowness (sec/deg)				
		Expected	Measured	Error	Anomaly	Expected	Measured	Error	Anomaly
3447.70	73.8	5.8	352.7	2.5	-1.1	5.65	7.56	0.27	1.68
2570.70	41.8	24.5	8.6	6.6	-15.9	8.17	9.75	1.88	1.58
1958.71	40.9	28.9	17.2	4.4	-11.7	8.24	10.20	0.64	1.96
2515.70	61.1	29.8	6.3	5.2	-23.5	6.75	7.78	0.44	1.00
1578.71	61.2	30.0	3.8	5.5	-26.2	6.78	7.78	0.52	1.00
1446.71	34.0	33.1	7.9	4.1	-5.2	8.69	13.40	0.90	4.71
3082.70	49.4	38.0	10.4	4.2	-27.6	7.61	7.72	0.48	0.11
3074.70	54.7	36.8	19.9	4.4	-18.9	7.27	9.19	0.81	1.92
1476.71	18.2	43.8	44.6	11.0	-1.2	12.08	11.23	2.14	-0.85
2997.70	23.3	50.8	40.9	6.3	-9.9	9.84	11.70	1.33	1.86
2907.70	99.7	52.6	10.3	5.2	-42.3	4.56	4.54	0.49	-0.02
2541.70	57.0	59.3	30.9	11.5	-28.4	7.09	4.99	0.96	-2.10
2574.70	63.0	60.6	35.1	9.8	-25.5	6.66	5.53	0.91	-1.13
2572.70	63.2	60.9	36.2	6.0	-24.7	6.66	5.48	0.56	-1.18
535.71	59.5	62.5	46.8	14.5	-15.7	6.91	4.54	1.17	-2.37
1624.71	67.4	65.4	39.1	11.1	-26.3	6.36	5.40	1.00	-0.96
2483.70	23.8	69.7	60.1	3.5	-9.6	9.67	9.75	0.65	0.08
1693.71	86.2	70.4	31.3	11.1	-39.1	4.87	2.65	0.48	-2.22
2471.70	24.2	70.6	65.9	2.8	-4.7	9.50	9.34	0.53	-0.16
2902.70	85.7	71.5	33.5	7.4	-38.0	4.92	4.13	0.58	-0.79
3676.70	85.8	71.7	44.1	10.4	-27.6	4.92	3.89	0.70	-1.03
2547.70	62.4	85.0	86.1	7.5	1.1	6.70	3.40	0.38	-3.30
2807.70	89.5	85.5	66.4	10.2	-19.1	4.71	2.77	0.45	-1.94
2635.70	62.6	87.3	94.3	4.3	7.0	6.69	4.01	0.34	-2.68
442.71	64.2	88.1	124.3	9.5	36.2	6.62	4.12	0.75	-2.50
3066.70	65.6	89.2	84.9	13.2	-4.3	6.49	3.69	0.71	-2.81

Table 2.1 Data Set A - continued

Event No.	Distance (degrees)	Azimuth (degrees)			Slowness (sec/deg)			Anomaly
		Expected	Measured	Error	Expected	Measured	Error	
1397.71	67.3	94.9	85.3	10.2	6.35	5.10	0.99	-1.25
3568.70	33.7	115.9	113.3	7.0	8.69	5.98	0.89	-2.71
3094.70	24.0	175.8	172.3	5.2	9.59	7.89	0.57	-1.70
2562.70	76.2	211.1	238.4	4.5	5.73	7.22	0.61	1.49
3582.70	40.1	331.6	325.3	3.6	8.29	9.50	0.55	1.21
3051.70	46.7	340.7	342.6	3.0	7.83	10.90	0.62	3.07
3527.70	75.9	352.8	351.0	6.1	5.73	7.36	0.61	1.63
1946.71	38.9	352.9	353.4	6.7	8.36	10.49	1.09	2.13

Table 2.2 Data Set B - No Pit Corrections Applied.

Event No.	Distance (degrees)	Azimuth (degrees)			Slowness (sec/deg)				
		Expected	Measured	Error	Anomaly	Expected	Measured	Error	Anomaly
4691.71	48.6	11.4	355.6	11.3	-15.8	7.68	10.52	2.64	2.84
4600.71	33.0	24.5	22.7	34.3	-1.8	8.74	10.56	0.42	1.84
533.72	61.7	30.3	356.2	14.2	-34.1	6.75	9.01	2.08	2.26
667.72	48.4	38.3	20.9	21.6	-17.4	7.61	5.86	3.33	1.25
458.70	18.8	46.8	22.1	17.0	-24.7	11.88	9.17	1.72	-2.71
455.72	55.3	52.6	15.7	27.2	-36.9	7.20	6.16	3.59	-1.04
426.72	58.3	78.3	53.6	15.2	-24.7	6.93	6.32	2.86	-0.61
4765.71	59.1	79.7	48.1	34.0	-31.6	6.92	5.37	2.09	-1.55
456.72	58.8	81.0	78.7	12.0	-2.3	6.93	4.92	3.57	-2.01
2331.71	59.5	55.6	76.7	11.9	-8.9	6.89	5.26	2.24	-1.63
2333.71	94.8	96.3	77.1	13.5	-19.2	4.58	4.99	2.25	0.41
4737.71	71.6	97.0	95.9	69.6	-1.1	5.99	3.77	2.72	-2.22
4630.71	77.0	98.7	89.9	27.0	-8.8	5.62	3.79	1.80	-1.83
499.72	39.4	138.0	147.9	51.9	9.9	8.33	4.85	1.05	-3.84
636.72	41.3	167.8	184.1	41.4	16.3	8.21	9.60	2.83	1.39
643.72	41.3	167.8	175.5	30.2	7.7	8.20	8.37	2.61	0.17
3138.70	43.8	173.6	172.4	37.5	-1.2	8.03	6.41	2.97	-1.62
4497.71	59.8	199.5	233.8	81.1	34.3	6.87	9.11	3.04	2.24
2736.70	76.5	206.3	230.7	6.7	23.9	5.67	7.28	3.13	1.61
4343.71	75.6	211.6	244.1	26.7	32.5	5.70	7.35	3.85	1.65
578.72	63.9	270.9	302.6	39.6	31.7	6.60	8.63	1.32	2.03
4342.71	79.5	300.5	312.2	45.8	11.7	5.43	10.39	4.33	4.96
3123.70	74.2	323.6	318.1	15.8	-5.5	5.84	8.67	1.00	2.83
3020.70	46.7	340.7	331.2	10.5	-9.5	7.83	9.95	2.60	2.12
2812.70	12.9	342.5	323.6	24.5	-18.9	8.09	8.09	1.92	0.00
2312.71	37.2	352.7	356.9	35.6	4.2	8.48	10.34	3.38	1.86

Figure 2.5

Observed Azimuth anomalies for data sets A and B.

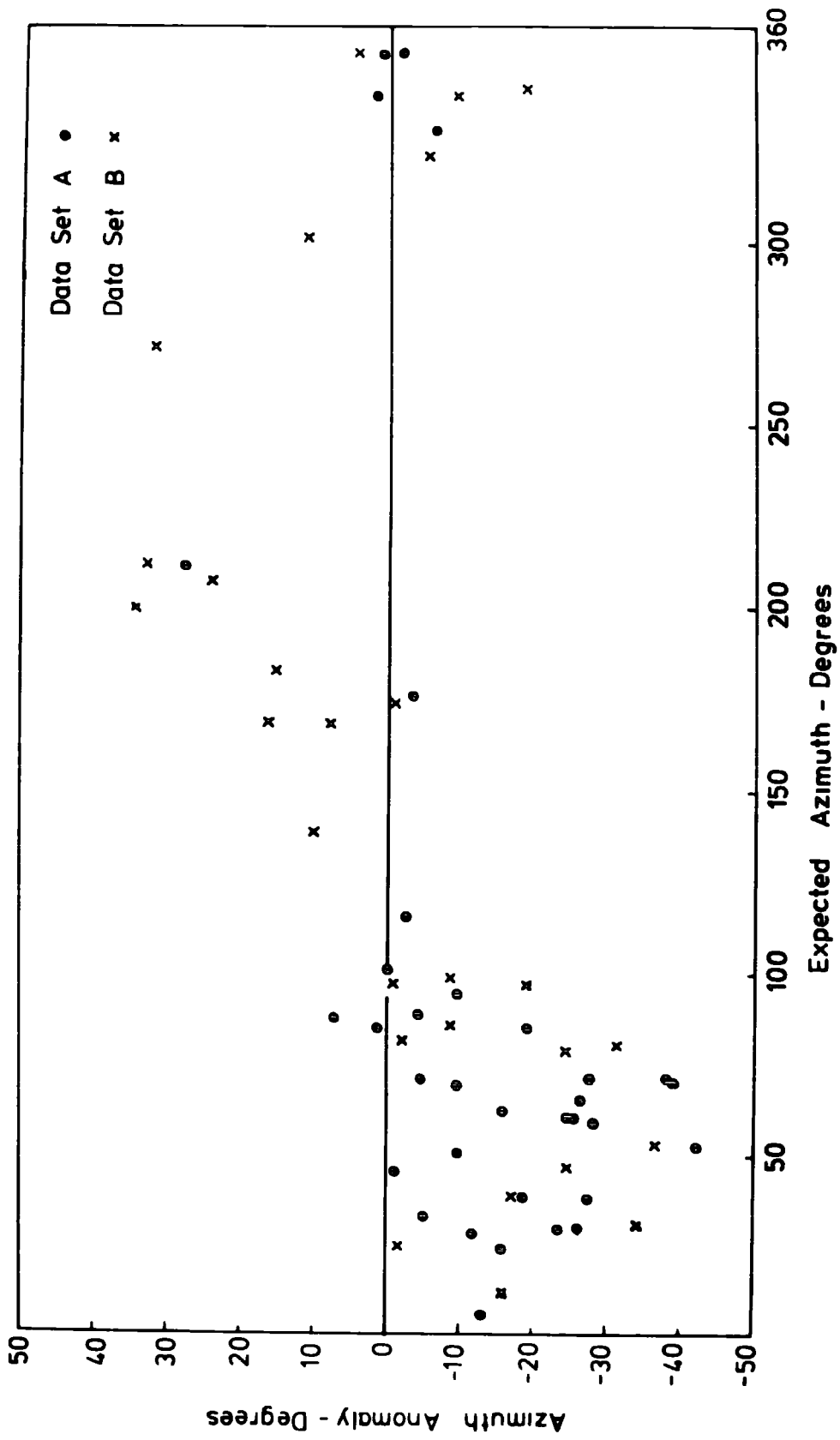
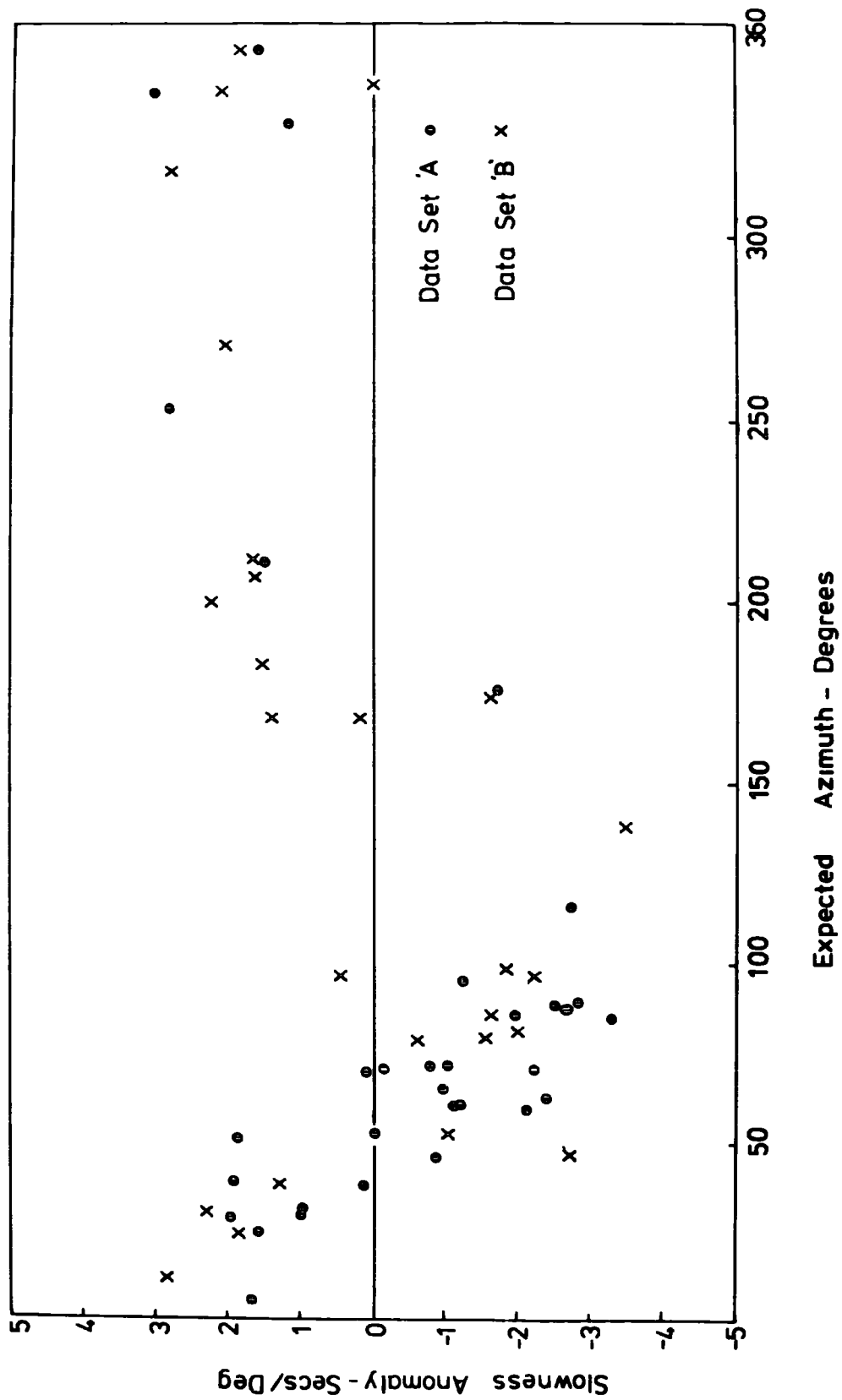


Figure 2.6

Observed slowness anomalies for data sets A and B.



small temporary array. In particular the errors on data set B are often very large. This is due, in part, to the poorer signal quality, as described previously, but also to the reduced number of seismometers usually operating thus decreasing the number of degrees of freedom in the error analysis and increasing the value of Student's t.

In spite of this the data shows a consistent variation of slowness and azimuth anomaly with azimuth. Between  $40^\circ$  and  $180^\circ$  the measured slowness is less than the theoretical value so that the waves arrive at the array more steeply than expected. From  $180^\circ$  to  $40^\circ$  in a clockwise sense the trend is apparently reversed although the majority of the data is from set B. The azimuth anomalies between  $0^\circ$  and  $100^\circ$  show a consistent deviation of the waves in an anti-clockwise sense, while between  $120^\circ$  and  $270^\circ(?)$  they are deviated in a clockwise sense. The few data points between  $290^\circ$  and  $360^\circ$  appear to have negligible azimuth anomaly.

#### 2.4 Analysis of Residuals and Site Corrections

It has been noted, in section 1.2.4., that the difference between the plane and circular wavefront caused negligible error for teleseisms. It is however possible that the wavefront at the array will have been effected on passing through inhomogeneous structures within the raypath, thus causing each seismometer to observe a different velocity and azimuth. This will be reflected in the time residuals at the pits and these residuals may be used to define pit corrections.

It was shown in section 1.2.3. that the onset time at the  $i$ th seismometer for the  $k$ th event may be written

$$t_{ik} = C_k - R_i \cos(\theta_i - \alpha_k) \left( \frac{dT}{d\Delta} \right)_k + \epsilon_{ik}$$

where  $\xi_{1k}$  is the time residual after fitting  $C_k$ ,  $\alpha_k$  and  $(dT/d\Delta)_k$  by least squares. This residual may be due to structure discussed above or simply timing and picking errors. Corbishley (1970) has analysed these residuals in terms of a constant and azimuthally dependent term of the form

$$\xi_{1k} = A_1 + B_1 \cdot \sin(\alpha_k + E_1) + r_{1k} \quad 2-(1)$$

where  $A_1$ ,  $B_1$  and  $E_1$  are constants for each seismometer,  $\alpha_k$  is the azimuth of the kth event and  $r_{1k}$  is the remaining error.

Backhouse (1972) has calculated these constants for the array using data set A by least squares criteria for the errors  $r_{1k}$  and these are shown in Table 2.3. with the associated 95% confidence limits.

The inhomogeneities may occur anywhere within the raypath but any variation in the mantle is likely to effect the whole wavefront arriving at the array and thus give rise to slowness and azimuth anomalies. Hence the structure causing the residuals is likely to be near the array.

The values of  $A_1$  are all very small which suggests that the variation of lateral structure beneath the array must be small. This agrees with the geological evidence that all the seismometers are on a substantial depth of phonolite which shows little variation in composition beneath the array (Jennings, 1964).

An azimuthal variation in the form of equation 2-(1) is an approximation to the effects of a dipping layer beneath the seismometer.  $B_1$  is dependent on the size of the dip and the phase angle  $E_1$  controls its direction.

Table 2.3

Array Site Corrections.

Pit	A <sub>1</sub> (sec)	B <sub>1</sub> (sec)	E <sub>1</sub> (degrees)
Y1	-0.005 <sub>±</sub> 0.015	0.008 <sub>±</sub> 0.017	319.8
Y2	0.016 <sub>±</sub> 0.019	0.011 <sub>±</sub> 0.022	39.9
Y3	0.029 <sub>±</sub> 0.021	0.014 <sub>±</sub> 0.024	250.7
Y4	-0.017 <sub>±</sub> 0.019	0.016 <sub>±</sub> 0.020	24.3
Y5	-0.007 <sub>±</sub> 0.011	0.008 <sub>±</sub> 0.012	205.0
R1	-0.020 <sub>±</sub> 0.012	0.008 <sub>±</sub> 0.014	174.7
R2	0.000 <sub>±</sub> 0.010	0.012 <sub>±</sub> 0.012	180.4
R3	0.011 <sub>±</sub> 0.021	0.018 <sub>±</sub> 0.022	105.8
R4	0.010 <sub>±</sub> 0.015	0.055 <sub>±</sub> 0.016	323.5
R5	-0.014 <sub>±</sub> 0.022	0.009 <sub>±</sub> 0.024	276.2

It may be seen that the  $B_1$  terms are less than 0.02 sec indicating a generally plane structure beneath the array with the expected random direction of dips indicated by the variation in the phase angle  $E_1$ .

These corrections are of the same order of magnitude as those estimated for other arrays (Corbishley, 1970).

## 2.5. Corrections to Anomalies

By equation 1-(11)

$$t_{1k} = C_k - R_1 \cos(\theta_1 - \alpha_k) \left( \frac{dT}{d\Delta} \right)_k + \epsilon_{1k}$$

and by inserting equation 2-(1)

$$t_{1k} = C_k - R_1 \cos(\theta_1 - \alpha_k) \left( \frac{dT}{d\Delta} \right)_k + A_1 + B_1 \sin(\alpha_k + E_1) + r_{1k}$$

$$t_{1k} - (A_1 + B_1 \sin(\alpha_k + E_1)) = C_k - R_1 \cos(\theta_1 - \alpha_k) \left( \frac{dT}{d\Delta} \right)_k + r_{1k}$$

A new corrected time,  $(t_{1k})_n$ , may now be defined which will correct for the structure beneath the array.

$$(t_{1k})_n = t_{1k} - (A_1 + B_1 \sin(\alpha_k + E_1))$$

and as a result

$$(t_{1k})_n = C_k - R_1 \cos(\theta_1 - \alpha_k) \left( \frac{dT}{d\Delta} \right)_k + r_{1k} \quad 2-(11)$$

Equations 2-(11) may now be solved in exactly the same way as 1-(11) and new anomalies may be defined. This has been done for data sets A and B and the resulting anomalies are shown in Tables 2.4 and 2.5.

For data set A the mean errors in slowness and azimuth have been reduced by 0.2 sec/deg and 1.6 deg respectively and for data set B the corresponding values are 0.63 sec/deg and 0.7 deg.

In all the interpretations to follow these corrected anomalies are used.

Table 2.4 Data Set A - Pit Corrections Applied.

Event No.	Distance (degrees)	Azimuth (degrees)			Slowness (sec/deg)			Anomaly	
		Expected	Measured	Error	Anomaly	Expected	Measured		Error
3447.70	73.8	5.3	352.3	3.8	-13.5	5.88	7.89	0.45	2.00
2576.70	41.8	24.5	8.6	5.2	-15.9	8.17	8.49	1.30	0.31
1958.71	40.9	28.9	17.8	4.0	-11.1	8.24	10.30	0.57	2.06
2515.70	61.1	29.8	6.2	6.9	-23.6	6.78	7.67	0.58	0.89
1578.71	61.2	30.0	2.2	2.9	-27.8	6.78	7.72	0.27	0.94
1446.71	34.0	33.1	27.0	3.1	-6.1	8.69	12.35	0.69	3.67
3082.70	49.4	38.0	11.5	1.7	-26.5	7.67	7.83	0.22	0.21
3074.70	54.7	38.3	20.0	2.9	-18.8	7.27	8.67	0.48	1.49
1476.71	18.2	45.8	42.6	9.4	-3.2	12.08	10.90	1.71	-1.18
2997.70	23.3	50.3	41.9	5.0	-8.9	9.84	11.46	1.06	1.62
2907.70	99.7	52.6	9.2	5.3	-43.4	4.56	4.18	0.46	-0.36
2541.71	57.0	59.3	32.9	10.0	-26.4	7.09	5.42	0.90	-1.66
2574.70	63.0	60.6	34.3	7.4	-26.3	6.66	5.62	0.71	-1.04
2572.70	63.2	60.9	35.3	3.4	-25.6	6.66	5.59	0.31	-1.07
535.71	59.5	62.5	46.9	12.1	-15.6	6.91	4.56	0.99	-2.35
1624.71	67.4	65.4	37.6	10.3	-27.8	6.36	5.45	0.91	-0.90
2483.70	23.8	69.7	60.3	2.4	-9.4	9.67	9.93	0.44	0.26
1693.71	86.2	70.4	29.3	13.3	-41.1	4.87	2.74	0.55	-2.14
2471.70	24.2	70.6	65.0	1.9	-5.6	9.50	9.27	0.39	-0.24
2902.70	85.7	71.5	35.9	2.3	-35.6	4.92	3.65	0.16	-1.27
3676.70	85.8	71.7	37.6	8.7	-34.1	4.92	3.62	0.48	-1.30
2347.70	62.4	85.0	93.2	4.8	-8.2	6.70	3.50	0.24	-3.20
2807.70	89.5	85.5	69.4	7.9	-16.1	4.71	2.53	0.31	-2.18
2635.70	62.6	87.3	93.8	5.1	6.5	6.69	4.28	0.43	-2.42
442.71	64.2	88.1	121.3	6.4	33.2	6.62	4.09	0.51	-2.53
3060.70	65.6	89.2	91.2	8.1	2.0	6.49	3.80	0.44	-2.71

Table 2.4 Data Set A - continued

Event No.	Distance (degrees)	Azimuth (degrees)			Slowness (sec/deg)			Anomaly	
		Expected	Measured	Error	Expected	Measured	Error		
1397.71	67.3	94.9	88.3	10.6	- 6.6	6.35	4.83	0.74	-1.52
3568.70	33.7	115.9	113.2	4.0	- 2.7	8.69	6.01	0.52	-2.62
3094.70	24.0	175.8	173.3	4.1	- 2.5	9.59	7.94	0.45	-1.64
2562.70	76.2	211.1	238.6	3.0	27.5	5.73	7.17	0.42	1.44
3382.70	40.1	331.6	325.7	2.9	- 5.9	8.29	9.67	0.42	1.37
3015.70	46.7	340.7	341.1	1.9	0.4	7.83	10.39	0.39	2.56
3527.70	75.9	352.8	351.3	3.9	- 1.5	5.73	7.56	0.41	1.83
1946.71	38.9	352.9	354.2	4.3	1.3	3.36	10.30	0.67	1.94

Table 2.5 Data Set B - Pit Corrections Applied.

Event No.	Distance (degrees)	Azimuth (degrees)			Slowness (sec/deg)			Anomaly	
		Expected	Measured	Error	Expected	Measured	Error		
4691.71	48.6	11.4	355.0	8.6	-16.4	7.68	9.98	1.83	2.30
4600.71	33.0	24.5	27.8	23.2	3.3	8.74	9.69	1.59	1.15
533.72	61.7	30.3	356.5	6.4	-33.8	6.75	9.21	0.93	2.37
667.72	48.4	38.3	34.4	9.0	-3.9	7.61	11.05	2.78	3.44
458.70	18.8	46.8	14.4	7.5	-32.4	11.88	8.83	1.03	-3.05
455.72	55.3	52.6	14.1	10.0	-38.5	7.20	6.19	0.74	-1.01
426.72	58.8	78.3	52.5	20.0	-25.8	6.93	6.26	4.83	-0.67
4765.71	59.1	79.7	50.4	63.3	-29.3	6.92	4.16	1.32	-2.76
456.72	58.8	81.0	74.7	9.5	-6.3	6.93	3.51	2.14	-3.42
2331.71	59.5	85.6	71.9	9.2	-13.7	6.89	4.66	1.17	-2.23
2333.71	94.8	96.3	74.7	9.1	-21.6	4.58	4.37	1.28	-0.21
4737.71	71.6	97.0	101.1	77.3	4.1	5.99	3.09	2.01	-1.90
4630.71	77.0	98.7	93.1	40.9	-5.6	5.62	3.61	3.40	-2.01
499.72	39.4	138.0	152.8	51.7	14.8	8.33	4.66	2.20	-3.67
636.72	41.3	167.8	184.4	49.8	16.6	8.21	9.44	3.27	1.23
643.72	41.3	167.8	175.5	40.1	7.7	8.20	8.22	2.76	0.02
3138.70	43.8	173.6	174.7	39.1	1.1	8.03	6.42	3.30	-1.61
4499.71	59.8	199.5	229.4	90.3	29.9	6.87	8.79	1.75	1.92
2736.70	76.5	206.3	229.9	7.5	23.6	5.67	6.94	2.90	1.27
4343.71	75.6	211.6	242.1	24.8	30.5	5.70	7.52	3.50	1.82
578.72	63.9	270.9	295.8	43.1	24.9	6.60	8.03	2.54	1.43
4342.71	79.5	300.5	305.6	23.5	3.1	5.43	9.42	2.56	3.99
3123.70	74.2	323.6	320.0	12.0	-3.6	5.84	8.60	0.47	2.76
3020.70	46.7	340.7	329.4	7.5	-11.3	7.83	9.32	1.83	1.49
2812.70	42.9	342.5	321.5	39.5	-21.0	8.09	7.49	2.09	-0.60
2312.71	37.2	352.7	353.5	20.0	0.8	8.48	10.65	1.78	2.17

CHAPTER 3

PRELIMINARY INTERPRETATION OF TELESEISMIC DATA

The purpose of this chapter is to propose a more general method of interpretation which will form the basis for the models proposed in the next chapter.

3.1. Comparison of Kaptagat with other Arrays

The basis for the previous interpretation of the teleseismic array data was their similarity with those found at other arrays. As examples of many such studies the following are taken:

1. Using the Warramunga Array, Australia, Cleary et al (1968) concluded that the Moho beneath the array had a dip of  $6.5^{\circ}$ .

2. Greenfield and Sheppard (1968) found that the Large Aperture Seismic Array (LASA), central Montana, U.S.A., gave maximum anomalies of nearly 1 sec/deg in slowness and  $3^{\circ}$  in azimuth.

3. Niazi (1966) using the Tonto Forest Array in Arizona found the dip on the Moho to be 'as much as  $8^{\circ}$ .'

4. Otsuka (1966) using arrays in California found a cyclic variation of anomaly with azimuth giving maximum azimuth and slowness anomalies of  $4.5^{\circ}$  and 0.6 sec/deg respectively.

(It may be remarked that these anomalies were derived with reference to Jeffreys-Bullen Tables (1940) and while these may alter details in the anomalies compared with Herrin's Tables the general trend will remain unaltered.)

In comparison, the average absolute anomaly at Kaptagat, based upon 60 events, is  $16.4^{\circ}$  on azimuth and 1.23 sec/deg on

slowness. In addition, it has been described that the present data requires a dipping interface so steep that total internal reflection occurs for some events (if the entire anomaly is to be attributed to a single interface) and that a model with a slope of  $27^{\circ}$  on the upper interface still requires a slope of  $46^{\circ}$  on the lower interface in the model of Backhouse.

This difference is not surprising since, in general, seismic arrays have been used to study the source effects of earthquakes or the properties of the path between source and receiver and consequently the effect of the structure beneath the array has been considered an unwanted feature for which corrections must be made. The aim of array location has therefore been to minimize the effect of structure beneath the array. The difference in the approach to the siting of seismic arrays between previous investigations and that being described is illustrated by Corbishley (1970) who recommended that 'seismic arrays should ideally be situated over regions that are free from elastic discontinuities, lateral variations and in areas that have low relief.' Clearly, using these criteria, Kaptagat is not an ideal site and it is suggested that the methods applied to the structure beneath other arrays are not necessarily applicable to Kaptagat.

Recent work by Aki (1973) and Capon (1974), based on the theory of wave propagation in a random medium due to Chernov (1960), has suggested that the anomalies at other arrays could be ascribed to a cause other than that of a dipping interface. The slowness anomaly at nine of the subarrays of LASA, which each consist of twenty-five

seismometers within a diameter of 7 km was calculated and found to vary considerably within each subarray. This variation was explained by a random variation in the refractive index of the crust and upper mantle to a depth of 136 km. The standard deviation of the refractive index was required to be 1.9% and the correlation distance was found to be 12 km. Thus although for LASA, which has a diameter of 300 km, this random disturbance causes 'only a small experimental error,' smaller arrays such as Kaptagat would observe a coherent waveform through such a random medium and thus observe a slowness and azimuth anomaly.

This explanation is also favoured for the observed anomalies at NORSAR (Norwegian Seismic Array) by Dahle et al (1975) after Berteussen (1975) had shown that a plane dipping interface could explain only 17.9% of the observed anomaly and only 24.3% could be explained by a single interface which was physically reasonable. (It may be noted that in spite of this, the anomalies at NORSAR had earlier been 'explained' on the basis of a Moho dipping at  $12.6^{\circ}$  (Kaneström, 1969).)

It should be emphasized that this model provides an alternative explanation for the small anomalies such as are found at other arrays whose order of magnitude was mentioned earlier and cannot be used to explain the bulk of the much larger anomalies found at Kaptagat.

### 3.2. Source of the Anomaly

The anomalies observed at the array may be caused by structure anywhere within the raypath. By using other studies it is possible to estimate the effects of various

parts of the raypath and thus decide the major source of the anomaly.

1. Structure at Source and within the Lower Mantle

It is unlikely that the source or the lower mantle could account for the major part of the anomaly since similar variations would then be expected at other arrays. Davies and Sheppard (1972) considered that the anomalies observed at LASA, after correction had been made for local structure, were caused by lateral variations in velocity structure within the mantle. This has been confirmed by Powell (1975) who found similar anomaly distributions at two array stations, LASA and Hansford, which were close enough to observe similar source and mantle structure but with sufficient separation to have differing crustal structures. Both these studies indicate that these inhomogeneities within the mantle and at source cannot be the cause of the major part of the anomalies.

2. Structure Immediately Beneath the Array

It has been shown in the analysis of residuals of travel times at the pits (section 2.4.) that there is little lateral inhomogeneity beneath the array.

3. Structure Within the Crust

Maguire and Long (1975) have shown that local and regional arrivals at Kaptagat exhibit no systematic variation of apparent velocity with azimuth thus indicating a plane parallel crustal structure beneath the array.

4. Structure Within the Upper Mantle

It is thus necessary to conclude that the source of the major part of the anomaly is the anomalous mantle material

beneath the rift which is inferred from gravity, seismic and other methods described in Chapter 1.

### 3.3. Basic Approach to the Problem

It has been suggested that the difficulty found in the interpretation of the array data by Backhouse was due to insufficient consideration of the properties of the model required to satisfy the data. The purpose of this chapter is to deduce some of the properties of the structure which are necessary to give the observed anomalies, making the simplifying assumptions that the whole of the anomaly is caused by a single interface and that the body may be characterized as having a uniform velocity.

(It may be noted that a plane interface at the bottom of the anomaly does not give rise to an azimuth anomaly but does produce a small slowness anomaly due to the deviation produced on traversing the low velocity structure. This effect is of considerable importance in considering delay times and will be discussed in greater detail in Chapter 5 where it will be shown that it can produce, at most, 5% of the observed slowness anomaly and as such may be neglected.)

It is stressed at the outset that this preliminary work does not intend to define a structure but rather to attempt to define the basic geometric properties of the model required to satisfy the data.

It was shown in section 1.2.2. that for a spherically symmetric earth both slowness and azimuth are constants for the raypath. If it is assumed that the anomaly is produced at a single interface the slowness and azimuth of the wave before entering the anomalous zone may be derived from the

'theoretical' slowness and azimuth, these parameters may also be calculated for the wave within the zone if a mean velocity for the body is assumed and in a similar manner they may be calculated on leaving the zone from the measured slowness and azimuth. The compressional velocity within the normal upper mantle varies very slowly with depth (Lehmann, 1967) so that the depth of the interface is not crucial and the estimate made for the velocity of the normal mantle will be reasonably accurate.

It will be shown that, if a velocity for the anomalous mantle is assumed, it is possible to calculate the direction of the normal to the surface which is causing the anomaly. By considering all the events in this manner it is possible to begin to build up a picture of the surface causing the anomalies. This procedure and the results obtained are now described.

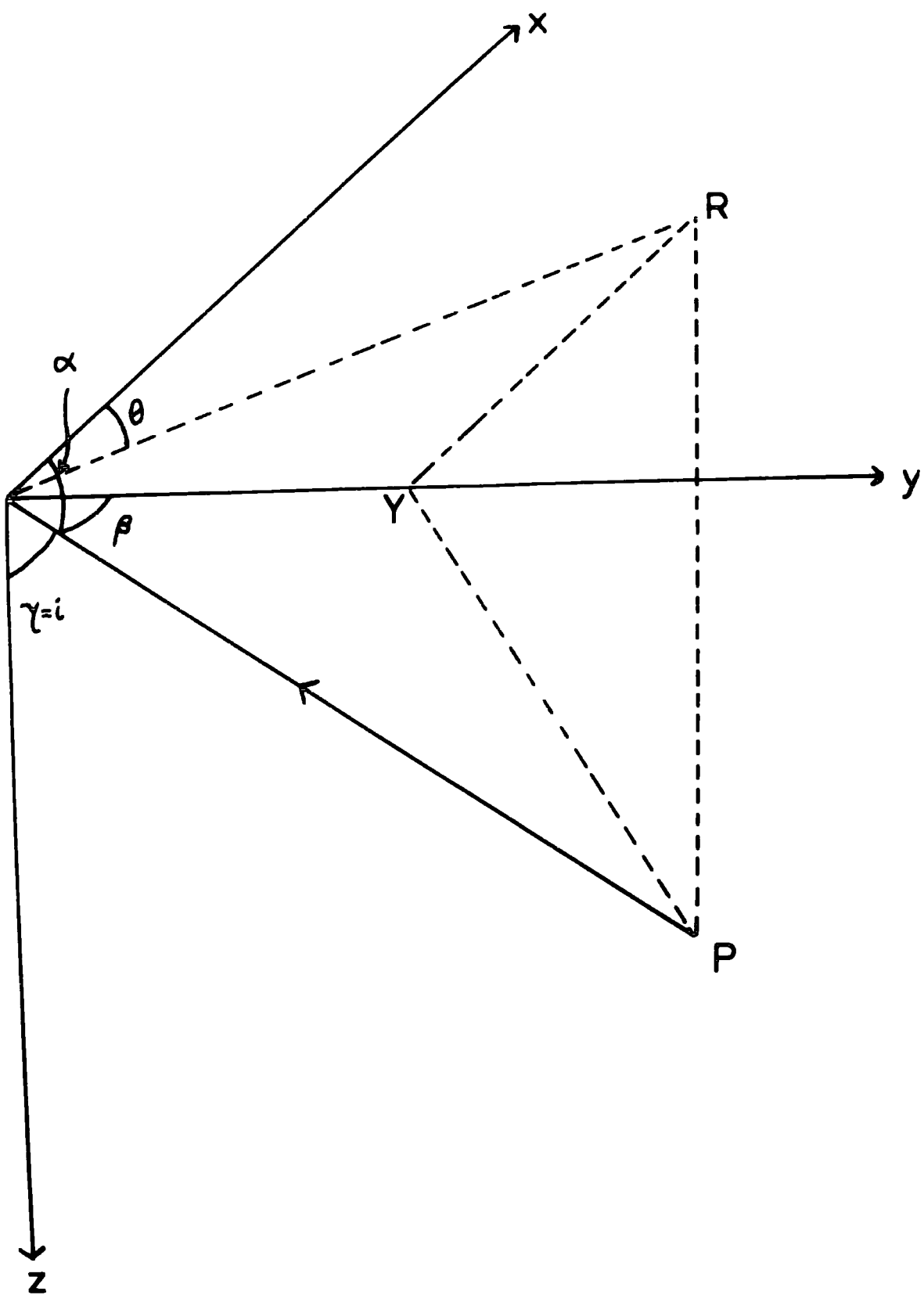
#### 3.4. Use of Direction Cosines

If the velocity in the medium beneath the array is known the angle of incidence may be calculated from the measured slowness using equation 1-(1). Thus the measurement of slowness and azimuth is equivalent to measuring the direction of approach of the wave in three dimensions and it is possible to specify this direction by defining the direction cosines relative to a co-ordinate system as shown in Fig.3.1.

The ray PO is incident at angle  $i$  to the array from an azimuth  $\theta$ . The direction cosines of the ray OP are  $\cos\alpha$ ,  $\cos\beta$  and  $\cos\gamma$  and denoted  $(l,m,n)$ . OR is the projection of OP on the xy-plane and OY the projection of OP on the line Oy.

Figure 3.1

Diagram to illustrate the use of direction cosine to describe the direction of approach of a wave.



We have

$$\sin 1 = \frac{OR}{OP}$$

$$\cos \beta = \frac{OY}{OP}$$

$$\sin \theta = \frac{OY}{OR}$$

so that

$$m = \cos \beta = \frac{OY}{OP} = \frac{OY \cdot OR}{OR \cdot OP} = \sin \theta \cdot \sin 1 \quad 3-(1)$$

similarly it may be shown

$$l = \cos \alpha = \cos \theta \cdot \sin 1 \quad 3-(11)$$

$$\text{and } n = \cos \gamma = \cos 1 \quad 3-(111)$$

the ray OP may thus be represented by the unit vector  $\hat{R}$  with components  $(\cos \theta \cdot \sin 1, \sin \theta \cdot \sin 1, \cos 1)$ .

### 3.5. Restraints on Velocity

One of the fundamental problems of the work is the dependence of structure on velocity so that it would appear that it is not possible to derive both velocity and structure using this data alone. There are however some constraints which may be applied to the velocity.

If the normal upper mantle is assumed to have a velocity of 8.1 km/sec then the direction cosines of the wave in this medium may be calculated and represented by the unit vector  $\hat{T} (t_1, t_2, t_3)$ . Similarly, assuming a velocity for the anomalous body a corresponding vector  $\hat{I} (i_1, i_2, i_3)$  may be calculated.

On passing through an interface with a velocity contrast a wave is deviated according to Snell's Laws of Refraction. If the angle of incidence is  $i$  in a medium with velocity  $V_1$  and angle of refraction is  $r$  in medium with velocity  $V_r$  then

$$\frac{\sin i}{\sin r} = \frac{v_1}{v_r} \quad 3-(iv)$$

If  $v_r > v_1$  then the deviation,  $d$ , is given by

$$d = r - i$$

As the angle of incidence increases the deviation will also increase and will reach a maximum at the critical angle,  $i_c$ , when the deviation,  $d_{max}$ , is given by

$$d_{max} = \frac{\pi}{2} - i_c \quad 3-(v)$$

This is illustrated in Fig.3.2. where the deviation is plotted against the incident angle for a velocity ratio of 0.94 and the maximum deviation is shown to be  $20.0^\circ$ .

If  $v_r$  is fixed the maximum deviation for various  $v_1$  may be calculated. This is shown in Fig.3.3. where as the velocity is decreased the maximum deviation increases.

For the problem of the low velocity upper mantle the deviation,  $\alpha$ , is given by

$$\cos \alpha = \hat{I} \cdot \hat{T} = i_1 \cdot t_1 + i_2 \cdot t_2 + i_3 \cdot t_3 \quad 3-(vi)$$

This deviation must be less than the maximum deviation possible so that

$$\cos \alpha \leq \cos d_{max}$$

By 3-(v) and 3-(vi)

$$i_1 \cdot t_1 + i_2 \cdot t_2 + i_3 \cdot t_3 \leq \cos \left( \frac{\pi}{2} - i_c \right)$$

$$i_1 \cdot t_1 + i_2 \cdot t_2 + i_3 \cdot t_3 \leq \sin i_c$$

and since  $\sin i_c = \frac{v_1}{v_r}$

$$i_1 \cdot t_1 + i_2 \cdot t_2 + i_3 \cdot t_3 \leq \frac{v_1}{v_r}$$

Thus if a velocity for the normal upper mantle is assumed an upper limit on the velocity in the low velocity medium is given by

Figure 3.2

Deviation produced by a plane wave on crossing a plane interface with velocity ratio  $0.71$  as the angle of incidence is varied.

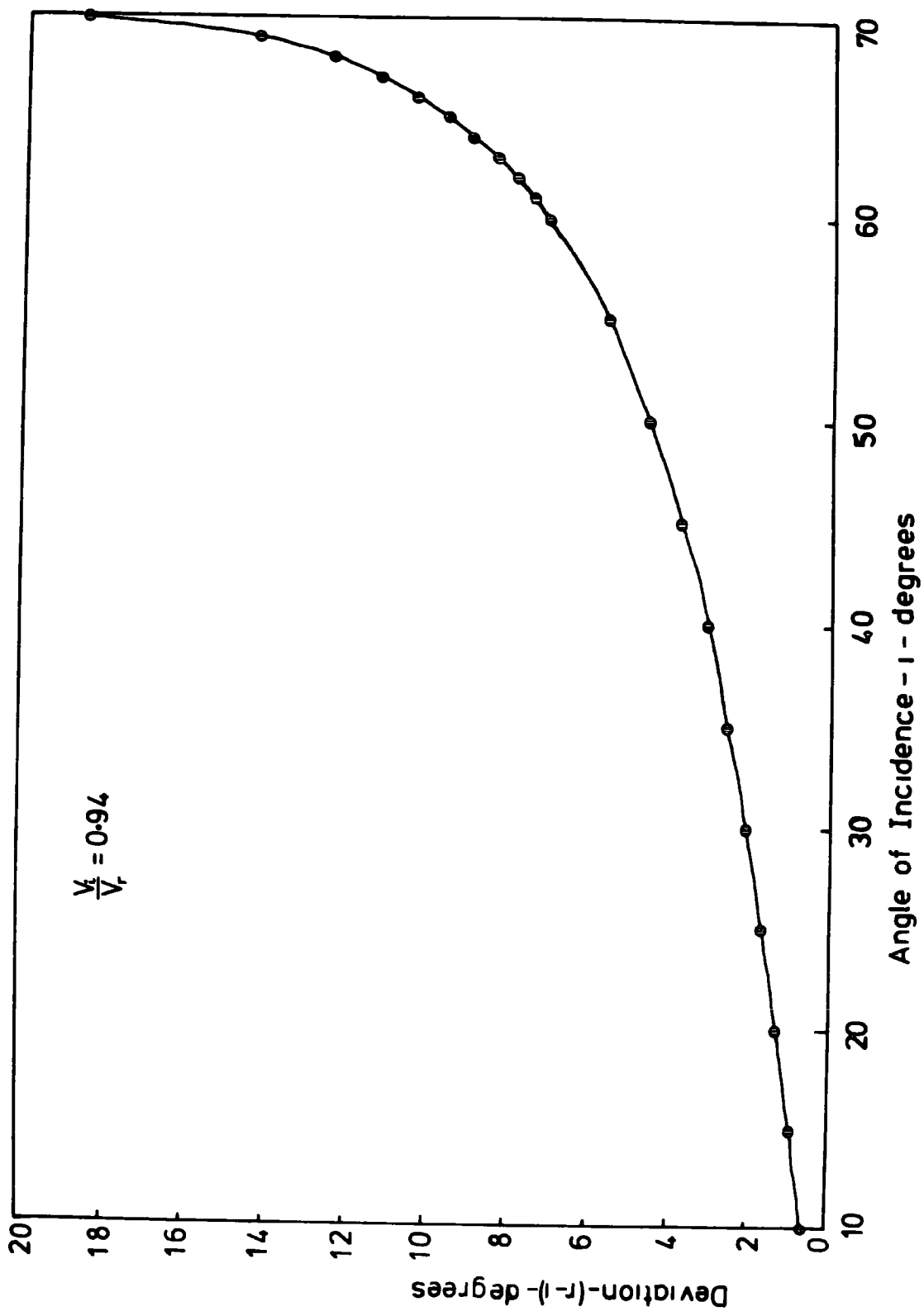
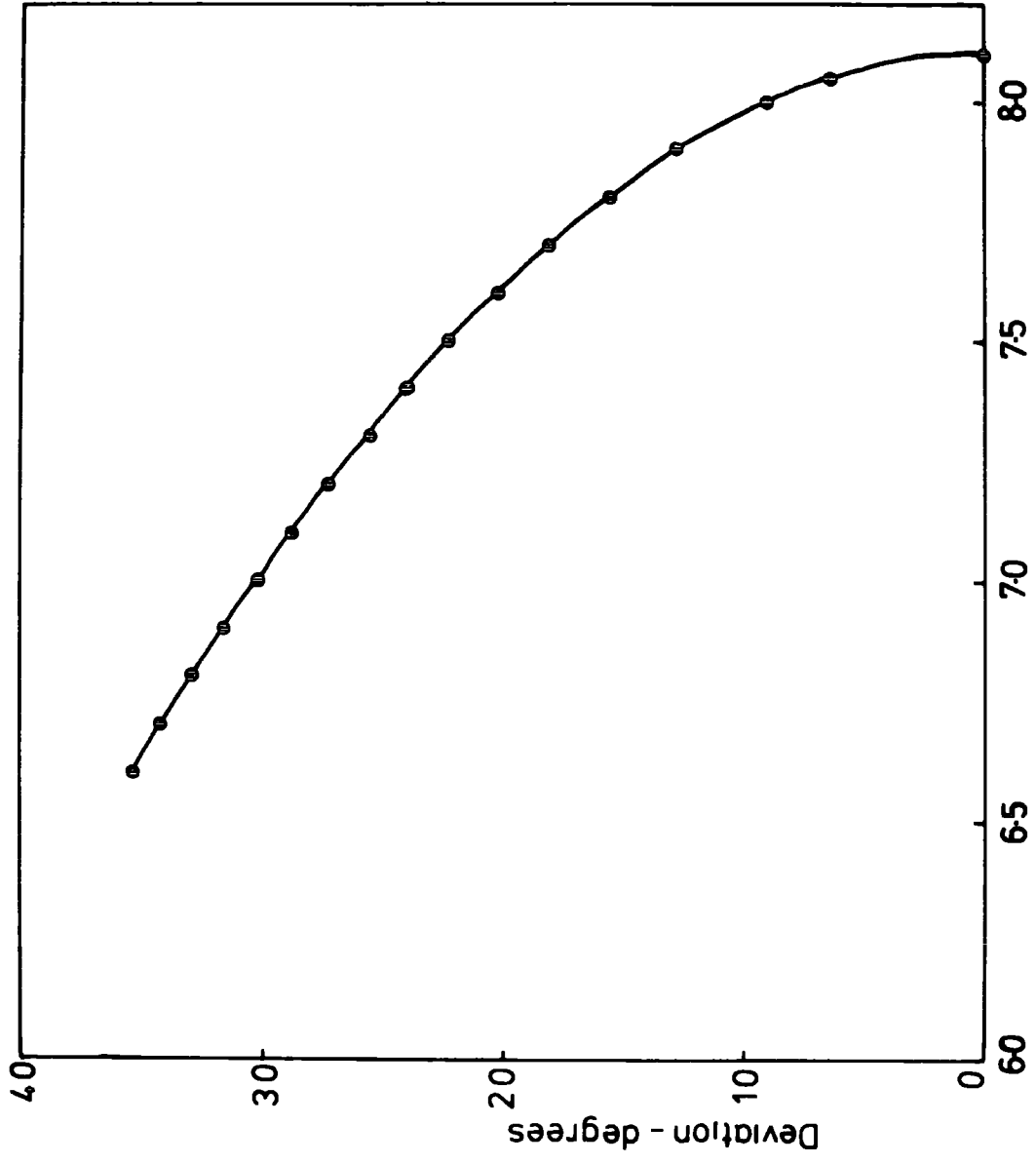


Figure 3.3

The maximum deviation that can be produced by a plane interface as  $V_1$  is varied,  $v_r$  is fixed at 8.1 km/sec



Anomalous Velocity (Kms/Sec)

$$V_r \leq \frac{V_1}{(i_1 \cdot t_1 + i_2 \cdot t_2 + i_3 \cdot t_3)}$$

Another possible restraint to place on the velocity is to limit the dip on the surface to being vertical. In this case a lower velocity may be obtained but it is sometimes the case that the theoretical deviation is exceeded before the interface becomes vertical.

In most cases the velocities obtained by the above methods are usually 7.9 km/sec or above but the lower velocities obtained are listed in Table 3.1. Method (a) refers to the theoretical limit and method (b) to the limit obtained by having a vertical interface. Where no value is given for method (b) this indicates that the theoretical maximum is reached before the surface becomes vertical. The first data group are from data set A and the second from data set B.

The extremely low values obtained for some events in data set B are probably in error but there would seem to be some justification for requiring a velocity less than 7.5 km/sec.

As this represents the upper limit on the velocity the true velocity must be considerably less than this value for any reasonable structure. It must, however, be compared with the 7.5 km/sec layer found by Griffiths et al (1971) 20 km beneath the rift with caution. First, this velocity was obtained from an unreversed line and could be an apparent velocity. Second, the concept of characterizing the zone by a particular velocity is almost certainly an oversimplification. It is most likely that the zone will have

Table 3.1

Limiting Velocities on Structure.

Event No.	Velocity (km/sec)	
	Method (a)	Method (b)
1476.71	8.00	7.55
2541.70	7.90	7.65
535.71	7.95	7.55
1693.71	7.85	7.75
2347.70	7.85	7.45
2807.70	8.00	7.75
2635.70	7.95	7.55
442.71	7.80	7.55
3066.70	7.95	7.55
1397.71	8.05	7.70
3568.70	7.90	7.35
5094.70	8.00	7.50
4342.71	7.55	-
4499.71	7.60	-
2331.71	7.95	7.55
4737.71	7.95	7.55
4765.71	7.80	7.45
456.72	7.85	7.40
499.72	7.75	7.20
533.72	7.40	-
667.72	7.45	-
458.70	7.30	7.05
3138.70	8.00	7.60

a velocity structure and what is being defined is a complicated mean velocity over all raypaths. While the refraction line may only be seeing the 'lid' of the structure the arrivals at the array will have sampled the body of the structure. This problem will be considered in more detail later.

### 3.6. Calculation of the Normal

It has been shown that the measured slowness and azimuth allow  $\hat{T}$  to be calculated and that the theoretical values define  $\hat{I}$ . The problem is then to deduce the direction cosines of the normal causing the deviation.

These may be calculated using Snell's Laws of Refraction

1. The incident ray, the refracted ray and the normal lie in the same plane.

2. The ratio of the sines of the angles of incidence and refraction equal the ratio of the velocities in the incident and refracted media.

The details of the calculation are given in Appendix A.

In order to aid representation of the normals the dip and strike of the plane with that normal have been calculated using the inverse of equations 3-(1), (11), (111) and for the rest of this chapter this representation will be used.

The normals have been calculated for various velocities of the anomalous upper mantle assuming a velocity of 8.1 km/sec for the normal mantle.

### 3.7. Properties of the Normals

Before presenting and discussing the results their

sensitivity to various parameters will be considered. For clarity, details will be given only for sample events which illustrate the general behaviour of the whole data sets.

### 1. Variation in the Anomalous Velocity

Figs.3.4. and 3.5. illustrate the behaviour of the dip and strike of the normal as the anomalous velocity is varied from 6.8 km/sec to 7.8 km/sec for seven events producing a wide variety of the dips and strikes. It can be seen that as the velocity increases, and the velocity contrast decreases, the dip on the structure required to produce the observed deviation increases; the effect of increasing the dip is, for nearly all the angles of approach covered by the data, to increase the angle of incidence and thus, from Fig.3.2., the deviation. Fig.3.5. shows that the strike of the surface is independent of the assumed velocity. This may be shown to be expected as a consequence of Snell's Laws, but since the algebra is somewhat laborious the proof is given in Appendix B.

Fig.3.4. illustrates a fundamental point which will occur constantly throughout this work and this is the dependence of the structure on velocity. The general shape of the body is not altered by changing the anomalous velocity since the strike of the interface has been shown to be independent of the velocity; rather the scale of the structure is controlled by this velocity. If the zone is characterized by a large average velocity the dips are large and the structure is small and deep while a very low average velocity will produce a large shallow structure. It may be noted that although the velocity controls the dip this does

Figure 3.4

Variation of the dip of the interface with anomalous upper mantle velocity for sample events, normal upper mantle velocity is taken as 8.1 km/sec

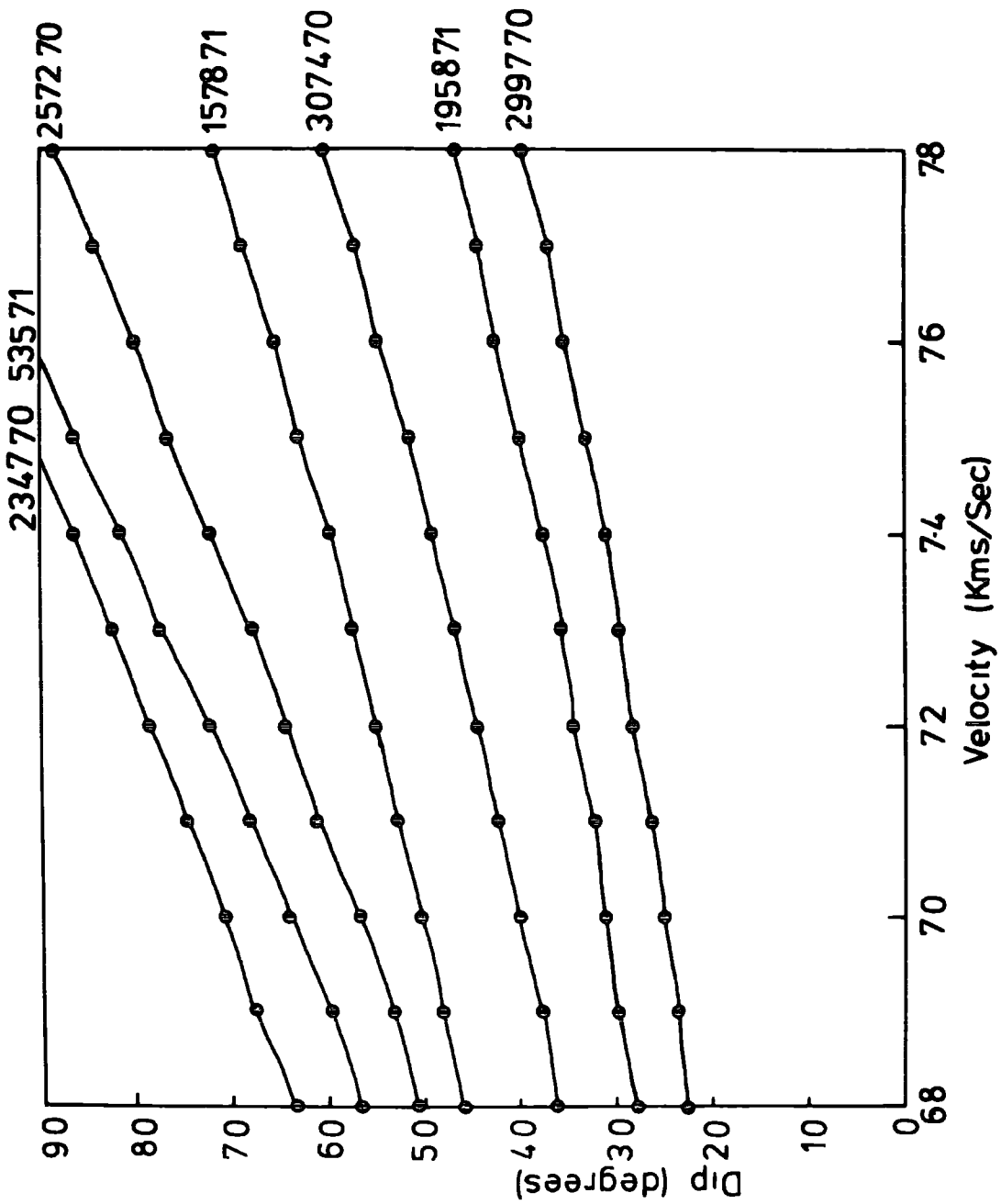
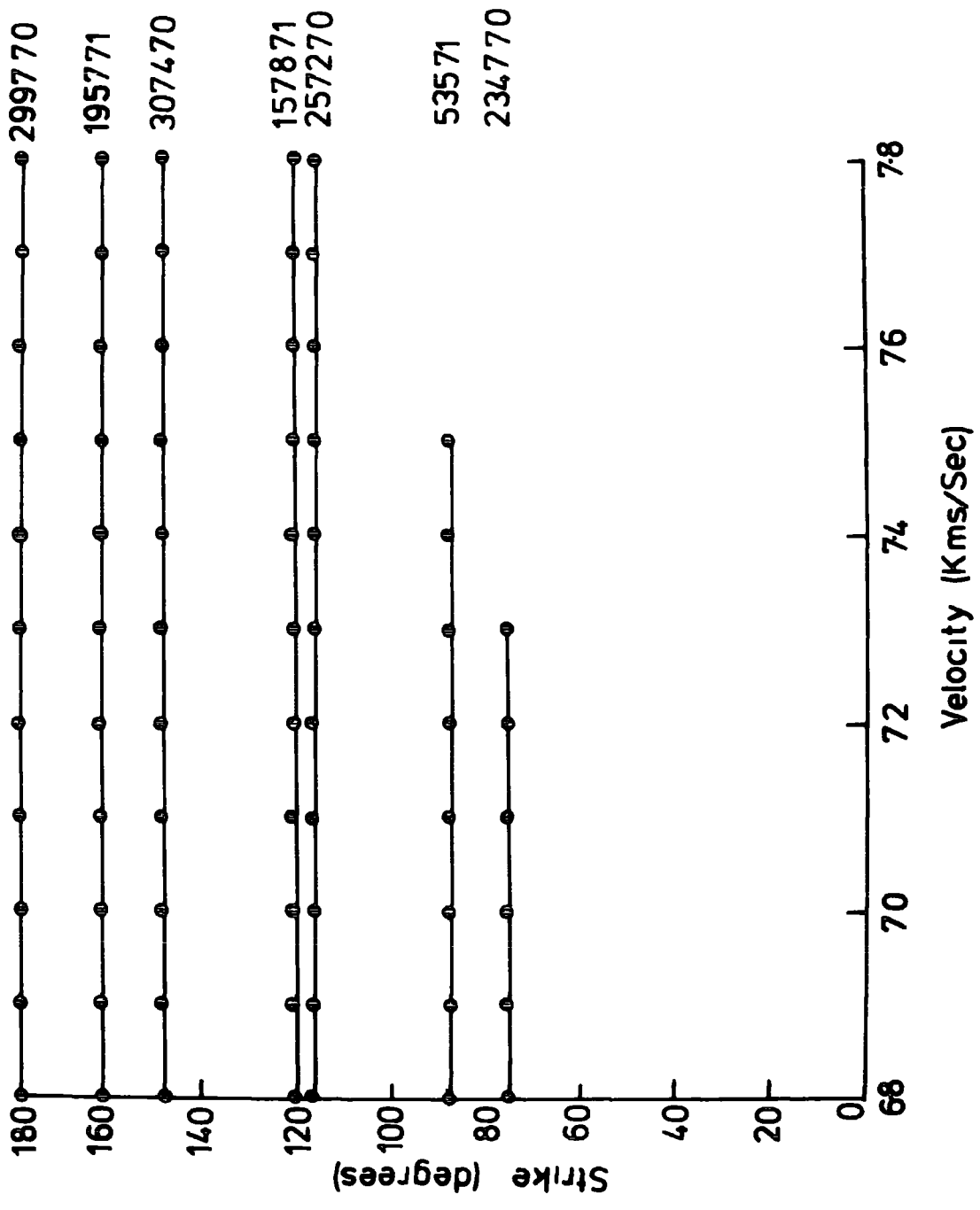


Figure 3.5

Variation of the strike of the interface with anomalous upper mantle velocity for sample events, normal upper mantle velocity is taken as 8.1 km/sec



not preclude the possibility of using this data to determine an optimum velocity (and structure) since the dip bears a non linear relationship to the velocity so that the scaling process of dip against velocity is a complex one.

## 2. Variation in Measured Parameters

Only event 3047.70 is considered in detail as all other events show similar properties. The measured velocity and azimuth have been varied between the limits defined by the 95% confidence limits and the effects on the dip and strike of the normal are shown in Figs.3.6. to 3.9.

Figs.3.6. and 3.7. show that an error of 0.6 km/sec on the measured phase velocity leads to negligible variation in the dip of the structure but to a variation in the strike of the normal of approximately  $7^{\circ}$ .

Figs.3.8. and 3.9. show that even a  $3^{\circ}$  error in the measurement of azimuth can lead to a  $4^{\circ}$  variation in the dip of the normal and a  $5^{\circ}$  variation in its strike.

It can thus be seen that, if the average errors are considered, measured errors on azimuth can lead to much more severe errors on structure, both in regard to the dip and strike of the normal, than the measured velocity errors. This is a possible explanation for the observation made by Backhouse that slowness is a more useful parameter in this study than azimuth. The second point that emerges is that the strike of the normal is very sensitive to the errors in measurement and care should thus be taken in interpreting these strikes.

(While attention has been given to errors on the

Figure 3.6

Effect of the variation of measured phase velocity on  
the dip of the interface.

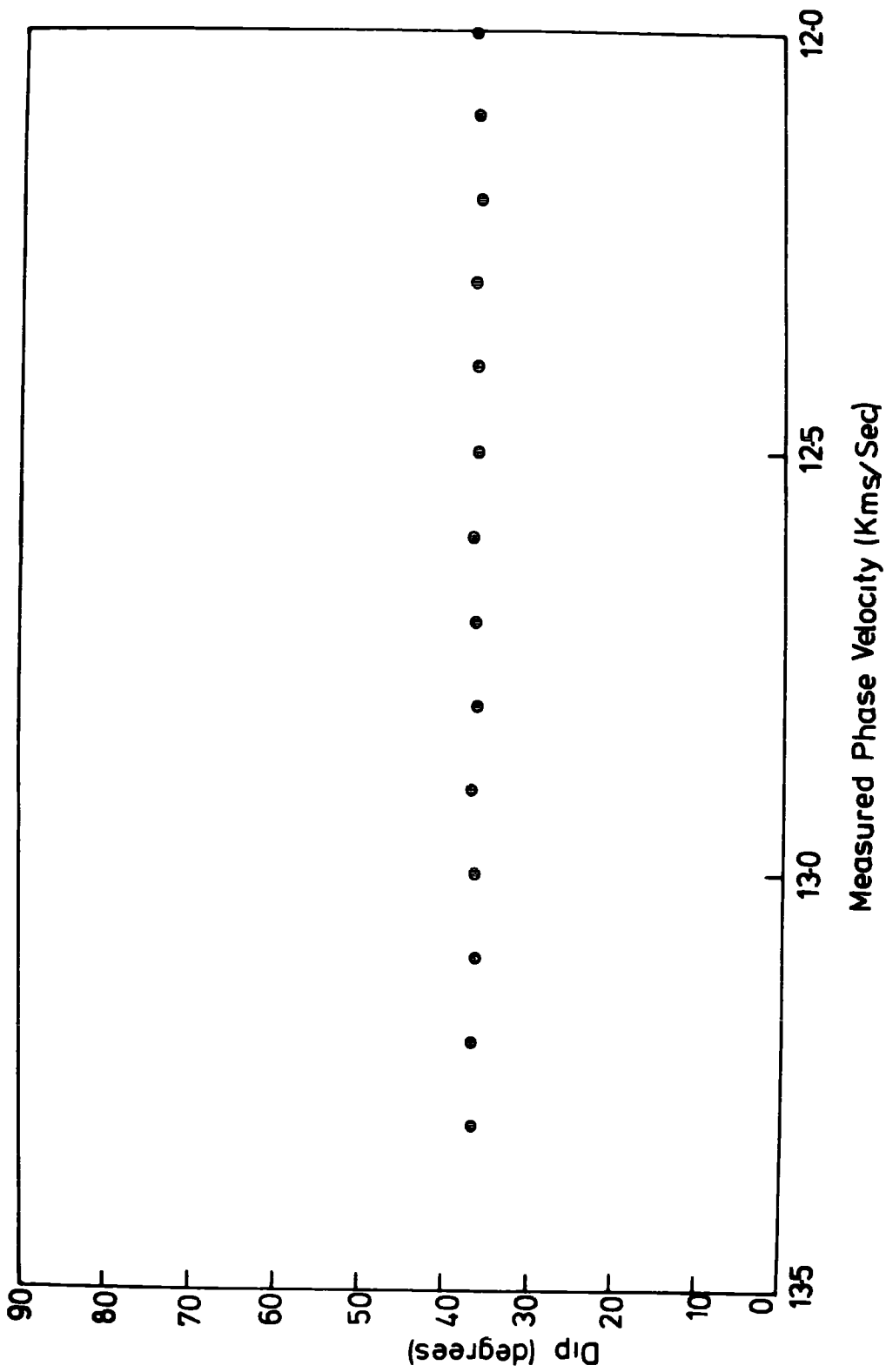
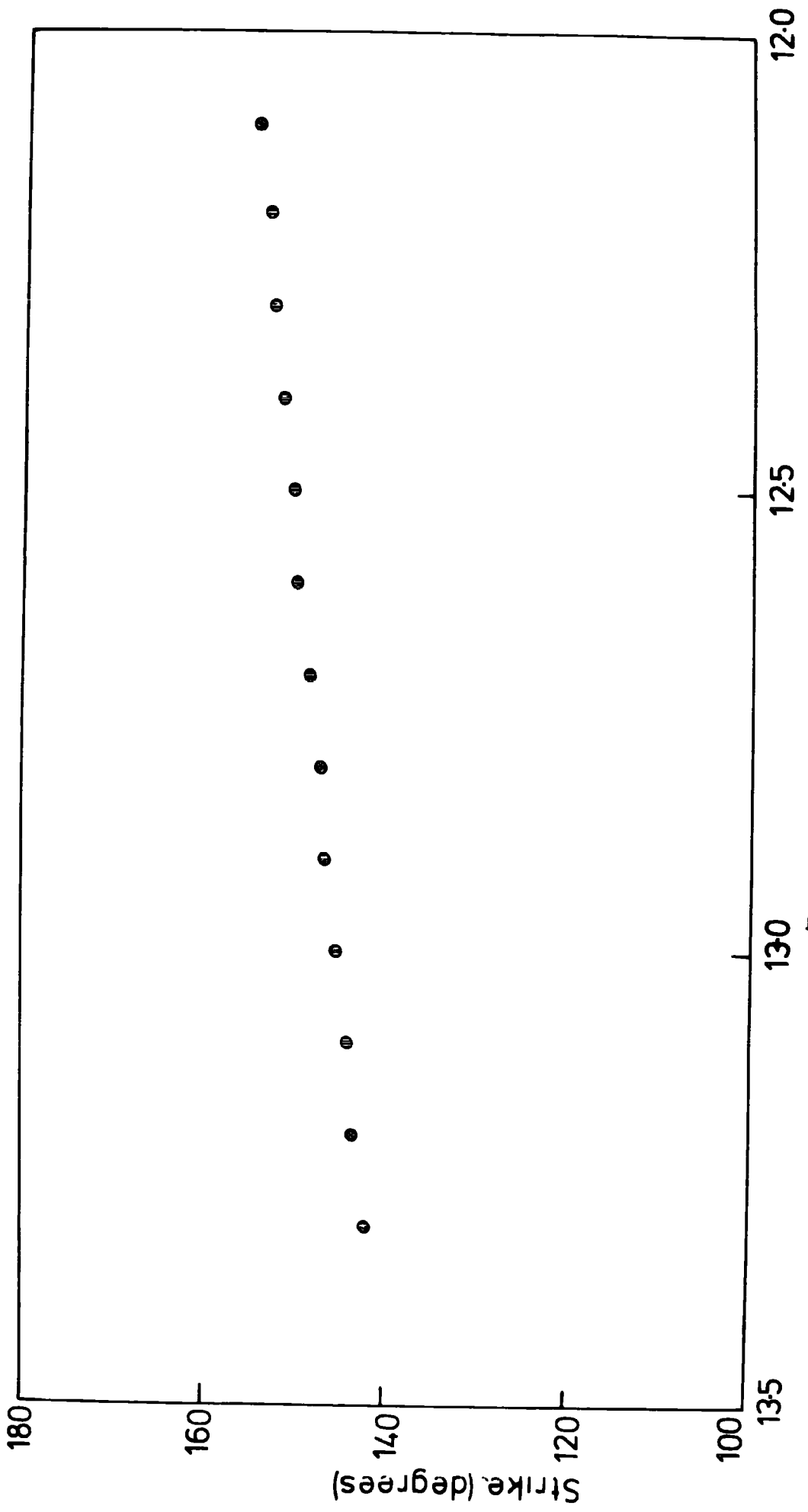


Figure 3.7

Effect of the variation of measured phase velocity on  
the strike of the interface.



Measured Phase Velocity (Kms/Sec)

Figure 3.

Effect of the variation of the measured azimuth on  
the dip of the interface.

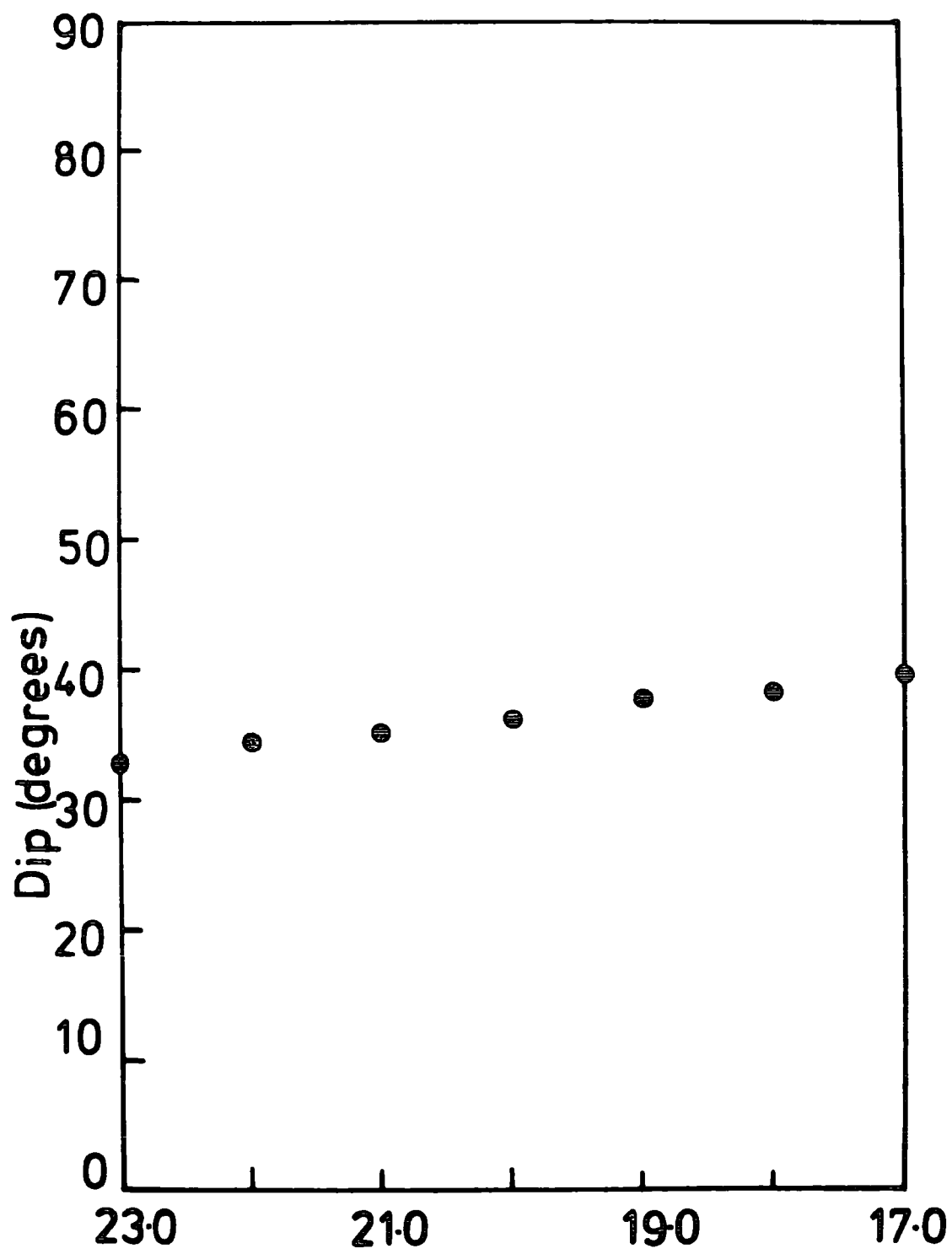
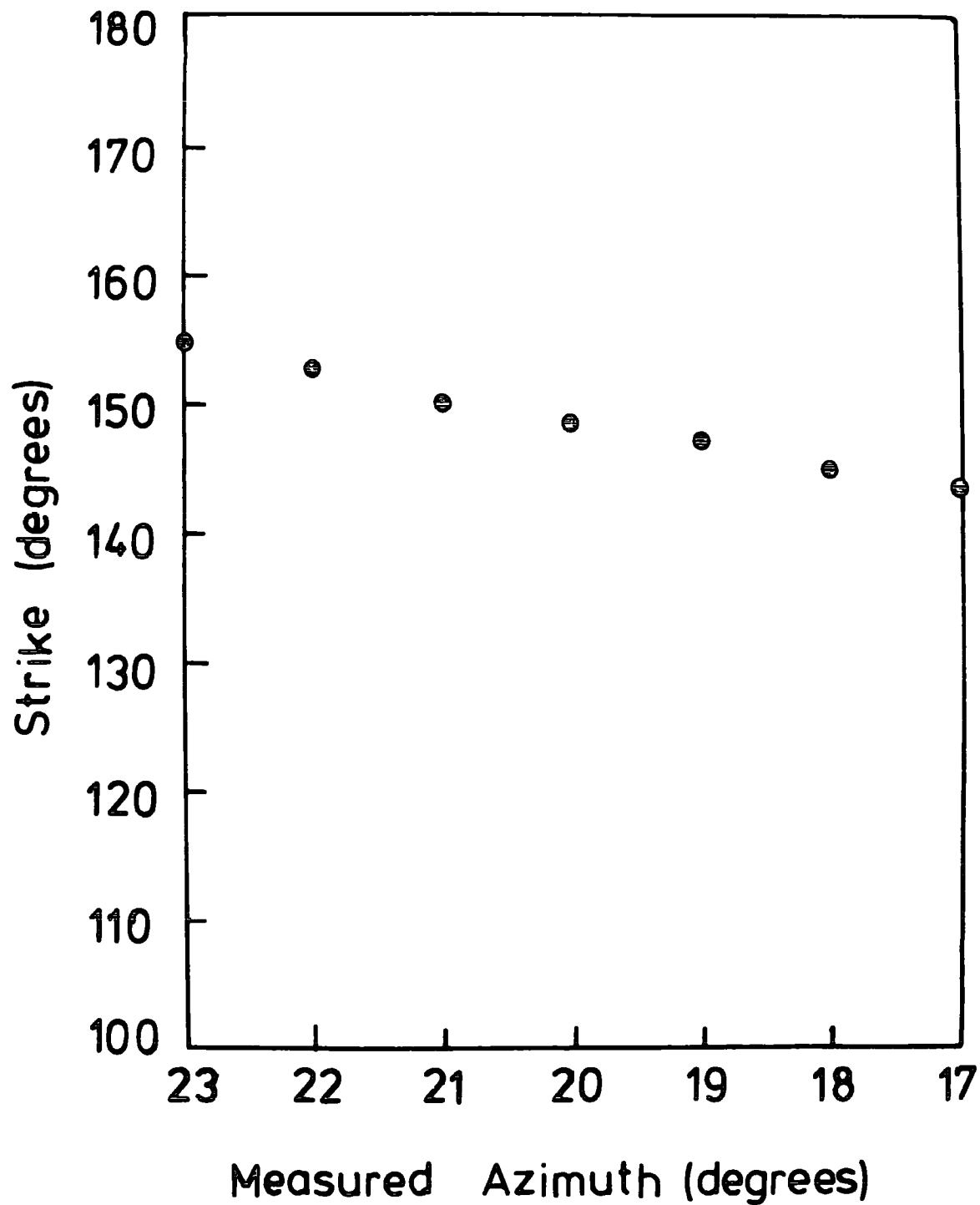


Figure 3.9

Effect of the variation of measured azimuth on the strike of the interface.



measured velocity and azimuth similar considerations will apply to errors on the theoretical velocity and azimuth; thus if anomalies occur before reaching the interface, as has been shown likely to occur, this will also produce errors in the calculated structure in a similar way to that described above.)

Fig. 3.10. shows the variation of the dip of the structure with distance for all azimuths assuming an anomalous velocity of 7.4 km/sec. Clearly the neglect of any azimuthal dependence will produce wide variations in the dips as shown but a general trend may be observed, namely that events from shorter distances appear to have encountered structures with shallow dips while events further away have met steeper dips. As the distant events approach the array at a steep angle they observe the interface near the array and thus it may be concluded that structure close to the array is characterized by a steep boundary while further away the boundary becomes shallower.

Fig. 3.11. attempts to illustrate the variation of the direction of strike of the surface. The distance of the event is plotted radially with distance decreasing outwards. Thus strikes near the centre of the plot indicate structure near Kaptagat and the azimuth is that measured at Kaptagat. It has been shown that these directions are sensitive to errors in measurement so considerable scatter may be expected. Nevertheless some trends may be observed. Those events from the east sample structure between Kaptagat and the Rift and show strikes pointing on average north. Events from azimuths between  $30^{\circ}$  and  $70^{\circ}$  show that the strike has come around to the east somewhat while events from the north show a strike

Figure 3.10

Plot of the dip of interface against the distance of the event from Kantat.

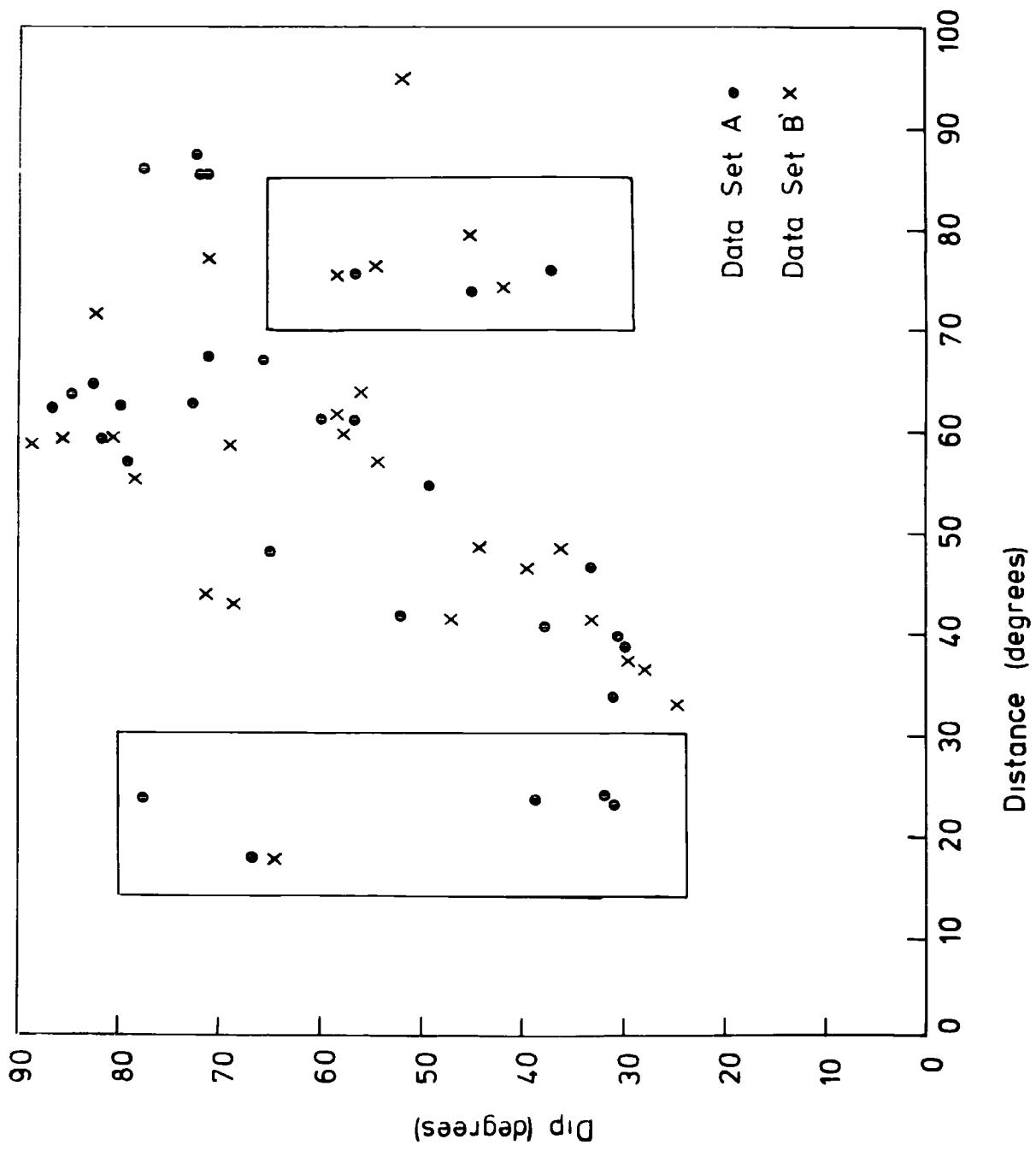
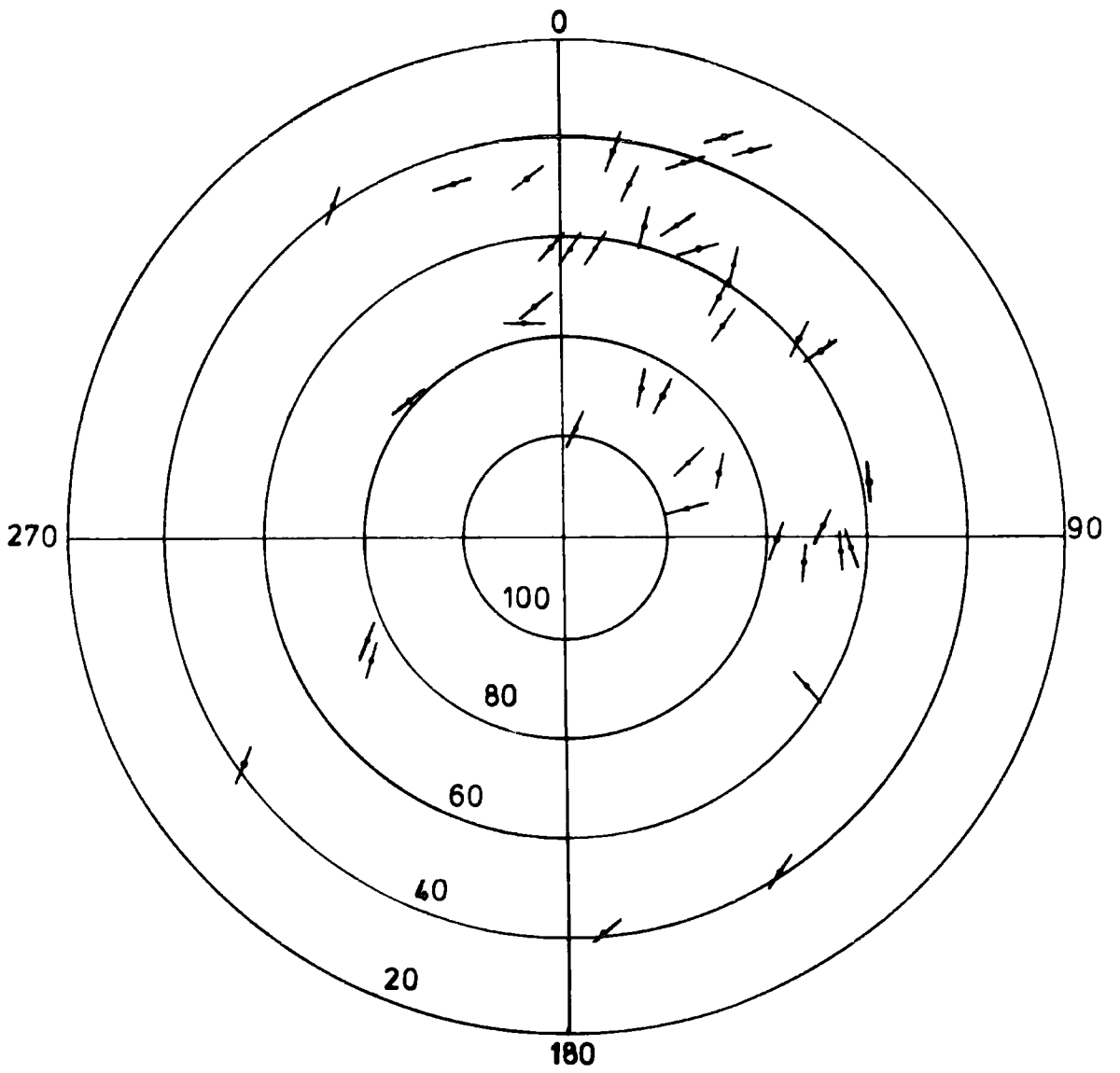


Figure 3.11

Plot of the strike of the interface against distance and the apparent azimuth of the event from Kaptagat, the distance (in degrees) decreases as the radius increases.



between north east and east. Events between  $340^{\circ}$  and  $360^{\circ}$  show a consistent eastward strike. Some events have been omitted from the diagram when several events come from the same region.

The diagrams illustrate why Backhouse's original model of a single plane dipping boundary failed. To attempt to represent the variation in dip shown by such a model must lead to large errors and as he commented the large dip required for distant events would lead to total internal reflection for nearer events where a considerably smaller dip is required. Similarly the variation in the direction of the strike of the surface indicates that the structure is truly three dimensional and while several dipping interfaces may help to solve the slowness anomalies no plane structure will ever explain the observed variation in strike direction.

Two data groups appear to be at variance with the general trend found in the dip against distance plot and are listed in Table 3.2. and indicated by rectangles in Fig.3.10.

The first group contains all events from distances less than  $30^{\circ}$  and appear to require dips greater than expected. The second group contains events in the distance range  $70^{\circ}$  to  $80^{\circ}$  and shows smaller dips than expected on the trend suggested. They are all from the west of Kaptagat and have small azimuth anomalies especially those from the north. At the present time it is difficult to exclude the possibility that these effects are due to the asymmetry of the structure which these simple, effectively two dimensional plots, cannot investigate. The methods developed in the next chapter permit a more thorough analysis of this problem and these groups will thus be considered later.

Table 3.2

Event No.	Distance (degrees)	Azimuth (degrees)		Slowness (sec/deg)	
		Expected	Measured	Expected	Measured
Group 1	2997.70	50.8	41.9	9.84	11.46
	2471.70	70.6	65.0	9.50	9.27
	2483.70	69.7	60.3	9.67	9.93
	1476.71	45.8	42.6	12.08	10.90
	3094.70	175.8	173.3	9.59	7.94
458.70	46.8	14.4	11.88	8.83	
Group 2	3527.70	352.8	351.3	5.73	7.56
	3123.70	323.6	320.6	5.84	8.60
	3447.70	5.8	352.3	5.88	7.89
	4342.71	300.5	300.6	5.43	9.42
	2736.70	206.3	219.9	5.67	6.94
	2562.70	211.1	238.6	5.73	7.17
	4343.71	211.6	242.1	5.70	7.52

### 3.8. Errors

If it is assumed that the errors in the dip and strike of the structure are reflected in the errors found in the measurements of the slowness and azimuth at the array then formal errors may be ascribed to the dips and strikes ascribed to the structure if a velocity is assumed. On assuming a velocity of 7.2 km/sec for the anomalous velocity the errors on the dips for the data are illustrated in Fig. 3.12. Where several events from the same region occur some data points have been omitted to avoid confusion. The errors on the strike of the surface are rather larger for the reason explained in the previous section and go up to as much as  $20^{\circ}$  and have an average of  $11.9^{\circ}$  in contrast to the average error of  $5.9^{\circ}$  on the dip. On some events it is not possible to derive a formal error as the deviation required by one or both of the limiting values of slowness and azimuth cannot be produced by a single interface with the velocities chosen.

These errors cannot be used to restrain the structure in any real sense because it is not possible to ascribe the whole of the measured anomaly to this single interface rather they may be considered as providing a limit to the extent to which any more detailed interpretation is meaningful.

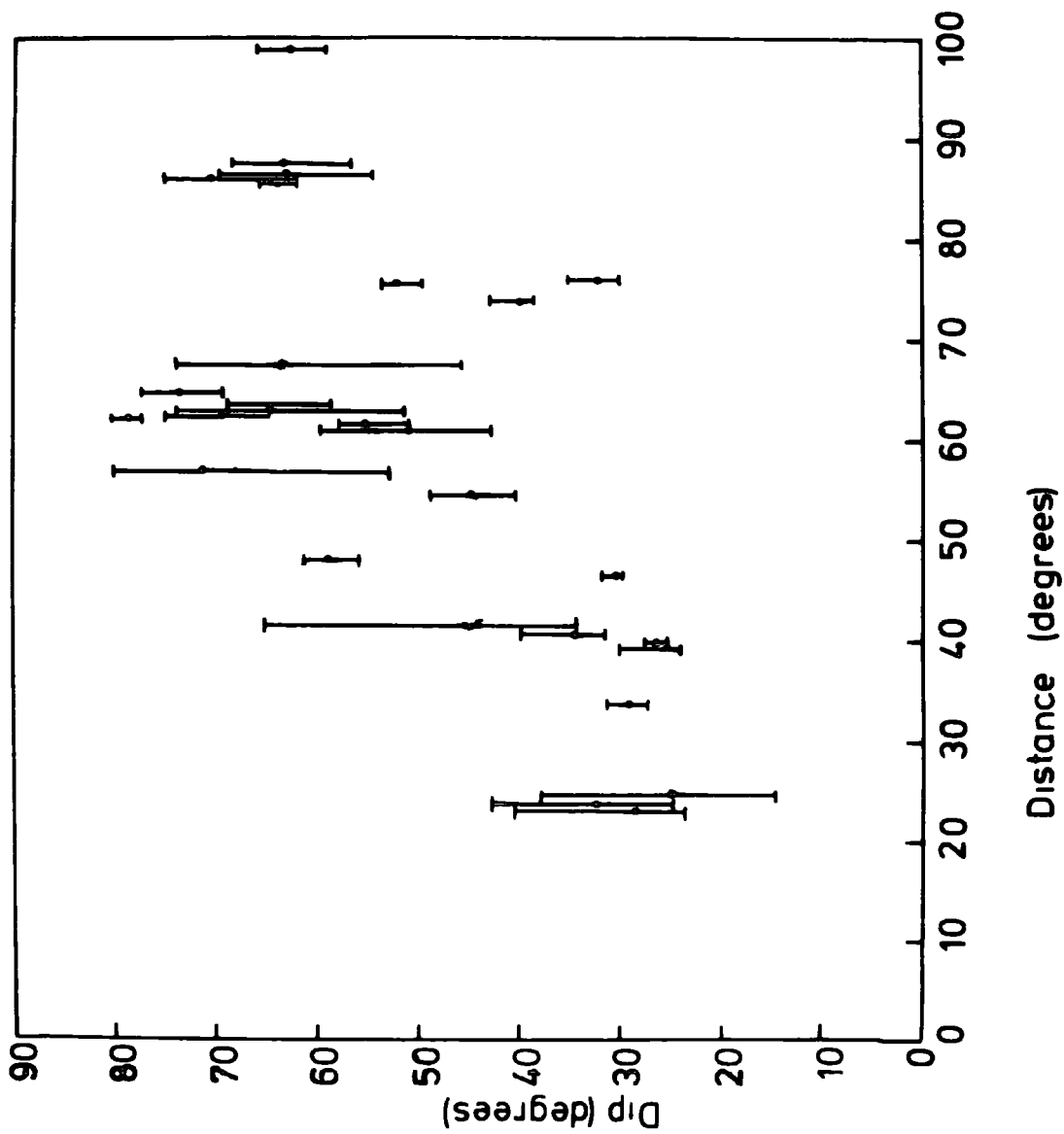
### 3.9. Conclusions

If it is assumed that the major part of the anomaly may be ascribed to a single interface the analysis has shown that we may conclude

1. The 'average' velocity in the anomalous material must be less than 7.5 km/sec.
2. Dips on the structure close to Kaptagat are required to be considerably steeper than dips on the structure further

Figure 3.12

Plot of dip of interface against distance indicating the 95% confidence limits for those events to which it is applicable.



away from Kaptagat. The structure is apparently thinning both north and west from Kaptagat.

3. The strikes of the surface for structure to the north of Kaptagat show a more easterly component than those indicative of structure to the east of Kaptagat.

4. A single plane interface cannot give a realistic interpretation of the data.

5. No plane structure, no matter how complex, can explain the observed anomalies.

These conclusions form the basis for the interpretation of the next chapter.

CHAPTER 4

OPTIMIZED SEISMIC MODELS

4.1. Introduction

The preliminary work, described in chapter 3, has indicated some of the properties of the single interface which are required to produce the anomalies which have been measured. This method, however, does have some severe limitations.

First, although the dip and strike of the structure are known, as is its direction from Kaptagat, the depth of the interface is not known. Moreover, because the velocity gradient within the upper mantle is so small, there does not appear to be any way of putting a constraint on the depth using the present method. Secondly, there will be errors on the dip and the strike calculated from the anomalies which have been estimated and shown to be considerable (section 3.8). It is thus desirable to derive a surface which effectively smoothes out these irregularities. Thirdly, from a more practical point of view, it is very difficult to visualize a structure in three dimensions which is defined by the dips and strikes at various points. The difficulty found in representing the results of the last chapter satisfactorily illustrates this problem.

In order to overcome these problems the surface will be described by a function  $f(x,y,z) = 0$ . Rays will then be traced from Kaptagat through this structure and the anomalies produced will be compared with those measured. By adjusting the constants of the function a surface which produces the minimum difference between the observed and the calculated

anomalies may be found.

By deriving a surface which best fits the data in a least squares sense the random errors which have been introduced into the measurements will be smoothed. Also, if it is assumed that the anomalous structure approaches the surface beneath the rift (whether the 1.5 km beneath sea level suggested by Baker and Wohlenberg (1971) or the 20 km beneath the surface suggested by Khan and Mansfield (1971)) control on the depth will be much improved. Effectively the structure is being located at one point and the data extrapolated from this point using a best fitting model.

#### 4.2. Choice of Form of Structure

Three points influenced the choice of the form of the function  $f(x,y,z) = 0$ :

1. The function may be chosen to be as complicated as desired. As the number of parameters required to describe the surface increases the accuracy with which they may be determined will decrease as the amount of data available is limited. From a more practical point of view the complexity of ray tracing through such a structure is increased and the computer resources required consequently increased.

2. If the structure is made so complicated as to allow rapid variations of the surface it is possible that the simple plane wave theory may no longer be valid. For example, Berteussen (1975), in attempting to derive a structure for the Moho beneath NORSAR, decided that a polynomial above the third order would produce such a detailed map of the structure that plane wave theory would not be applicable.

3. The extent to which the structure may be defined is limited by four factors:

(1) The accuracy of the array measurements. This has already been discussed in section 1.2.4.

(11) The effect of the anomalies introduced by various parts of the raypath. Although it has been shown that these cannot be the major cause of the anomalies they will produce perturbations. Consequently, it is impossible to tell if perturbations in the anomaly pattern represent structural complexities within the anomalous mantle or inhomogeneities within the rest of the raypath.

(111) The assumption of a uniform velocity within the anomalous body is almost certainly a simplification. Unless there is a better control of the velocity within the structure detailed structural considerations are meaningless.

(iv) Although it has been assumed that the bottom of the anomaly is effectively flat it is probable that some part of the anomaly is caused by structure other than the upper interface with the normal mantle.

It was thus decided to take a model which illustrated the two trends which were found in the preliminary interpretation.

(1) In cross section a steep slope is required for structure near the surface and a gentler slope is required at greater depths.

(11) In plan between Kaptagat and the rift the structure appears to run approximately northwards but further north the structure seems to trend to the east.

These features may be modelled by an expression of the form

$$f(x,y,z) = \frac{x^2}{a^2} + \frac{y^2}{b^2} - \frac{z^2}{c^2} - 1 = 0 \quad 4-(1)$$

where the z-axis points vertically downwards and x- and y- axes are in the plane of the surface. Thus in cross-section the function is a hyperbola and in plan is an ellipse. The orientation of the axes in the x-y plane is allowed to vary as is the location of the co-ordinate system. As has been described it was planned to place some restraint on the location of the co-ordinate system so as to make the structure cut the surface beneath the rift but initially it was allowed to vary. The structure is thus described completely by six parameters - a,b,c, the co-ordinates of the origin and the orientation of the co-ordinate system - for a fixed velocity within the anomalous upper mantle.

Three properties of the function  $f(x,y,z)$  are of importance in considering the structure

(i) The variation in dip provided by the hyperbolic form  $(x^2/a^2) - (z^2/c^2) = 1$  is small beyond the region  $|x| > 2a$ . However, the total range of gradient provided by the three dimensional form of  $f(x,y,z)$  is much larger. It was decided to retain the simplicity of the function rather than assume a form which provided a more rapid variation of gradient. If it was found that this function could not provide sufficient variation in dip a more complex function could be used.

(ii) The hyperbola  $(x^2/a^2) - (z^2/c^2) = 1$  tends to the straight line  $x = z(a/c)$  for  $|x| \gg a$  and  $|z| \gg c$ . Clearly this is physically unrealistic. As long as this is recognized it will cause few difficulties and may be used to advantage. Thus if a particular group of events appears to cross the structure as defined by  $f(x,y,z) = 0$  this could

indicate that the structure needs to be made shallower in this particular region.

(111) One of the criticisms made of the final model of Backhouse was the poor resolution on the parameters describing the structure. That model was defined by three parameters while the present one is defined by six so that the problems of resolution are likely to be even worse. However, this fails to recognize that Backhouse's final model was not based on any consideration of the data whereas the present model has been defined so that it does possess the general properties required to fit the data and thus it is possible to hope for somewhat better resolution.

#### 4.3. Ray Tracing Procedures

Procedures for tracing rays through complex geological structures using plane wave theory have been given by several authors although they often tend to be somewhat specialized in their approach.

Sattlegger (1965) treated the case of refraction through a two dimensional model with any number of dipping interfaces. Although it was considered that the method could be extended to three dimensions quite easily the computer time required was described as very long. Otsuka (1966) developed an elegant method for calculating slowness anomalies as a result of transmission through an arbitrary number of plane interfaces but did not deal with the details of the ray tracing. Sorrels et al (1971) described a method for calculating both travel time and slowness anomalies for rays passing through an arbitrary number of plane or circular interfaces for use in the analysis of anomalies associated with the LONGSHOT explosion. Finally, Shah (1973) describes a more general

method for tracing rays through an interface defined by the function  $\phi(x,y,z)$  and has included the case of transmission through a structure with a continuously varying velocity.

Shah's treatment provides the basis of the method used in the current ray tracing procedure. A detailed description of the methods are given in Appendix B and only an outline is given below. A crustal structure appropriate to Kaptagat is assumed (Long and Maguire, 1975) as is Herrin's average model for normal upper mantle (Herrin et al, 1968). The ray is traced through each layer of the crust and mantle and the location of the intersection of the ray with the anomalous surface is calculated. When this intersection occurs within the layer under consideration the ray is traced through this interface using Snell's Laws of Refraction. Since it is being assumed that the whole of the anomaly is being caused by this interface the ray will then have the same slowness and azimuth if traced back to source. Thus if the model satisfies the structure the wave in the mantle will have the same slowness and azimuth as the theoretical values calculated. The residuals are defined as the difference between the theoretical values and the calculated values and the aim is to derive a structure which will minimize these residuals.

Using this method of ray tracing total internal reflection can only occur when the intersection with the structure occurs within the crust. This occurred only rarely and its effects are investigated in more detail later but provisionally the residual was placed equal to the anomaly on occasions when this problem arose.

When the observed ray had not crossed the anomalous structure by a depth of 400 km it was assumed that the

intersection would not occur and so the residual was put equal to the measured anomaly. It seems likely that the anomaly will trend to the normal upper mantle as its depth increases so that if an intersection occurs deeper than 400 km it is unlikely to represent a realistic structure because of the asymptotic form of the hyperbola. Thus it was found that events which corresponded to depths of intersection greater than 400 km were all found to have very large residuals. This will be discussed further later in this chapter.

As the confidence to be placed on individual measurements within the data sets is to varied some method was required to define the relative importance of each event. This is necessarily a somewhat arbitrary procedure but must be related to the errors found for each of the measurements. Several methods were tried but the differences in structure so produced were never judged to be significant. It was found that the relative importance attached to the azimuth and slowness residuals was far more crucial. Backhouse remarked that slowness seemed to be a more reliable parameter than azimuth in his study and a possible explanation of this was given in section 3.6. where it was shown that the dip and strike of an interface were more sensitive to azimuth errors than slowness errors. To cater for these points the function to be minimized was given by

$$F = \sum_{i=1, n} \left[ (W_s) \frac{(S_r)_i^2}{(S_e)_i^2} + (W_z) \frac{(Z_r)_i^2}{(Z_e)_i^2} \right] \quad 4-(11)$$

where

$(S_r)_i, (Z_r)_i$  are slowness and azimuth residuals for the  $i$ th event

$(S_e)_1, (Z_e)_1$  are proportional to the errors found for the slowness and azimuth on the 1th event

$W_s, W_z$  are weights attached to the slowness data group and the azimuth data group

and  $n$  is the number of events.

$(S_e)_1$  and  $(Z_e)_1$  were maintained at a constant value for all calculations whereas  $W_s$  and  $W_z$  were varied for each optimization procedure.

#### 4.4. Optimizing Procedures

As the structure was to be described initially by six parameters a methodical search through the field defined by these parameters to find minima was considered impracticable and various optimization procedures were used.

As no reasonable starting value was known and it was possible that several fields containing minima of interest existed it was decided to use a Monte Carlo type search (James, 1968) as a preliminary to using more methodical means of finding a minimum. In this technique each parameter is given a starting value and upper and lower limits. Each time the function is calculated the parameters are chosen randomly according to a Gaussian distribution with widths equal to one half the total allowed variation. By calculating the function for a wide range of random values the 6-dimensional field may be covered in reasonable detail so that it is likely that all significant regions of minima may be found.

In order to calculate the exact minimum, to the accuracy required, a development of the method of co-ordinate variation, due to Rosenbrock (1960), was used. Starting at the initial value a set of  $n$  orthogonal vectors are defined in the

n-dimensional space formed by the n parameters defining the function using the Schmidt orthogonalization procedure. The values of the parameters are then varied in each of these directions in turn until a new minimum is found. A new set of orthogonal vectors is now defined with one of the components being the direction joining the old minimum (or starting value) to the new minimum and the process is repeated until no significant improvement is found in the function.

This method has the advantage of moving quickly toward a solution in regions quite far from the minimum and being able to cope with poorly behaved functions. Its disadvantage lies in the slowness of its convergence to an exact minimum. Since it was envisaged that the function would be badly behaved in those parts of the space where total internal reflection occurred and because of the previous considerations of the resolution available from the data so that the location of an exact minimum was meaningless this technique was considered of more use than other, more sophisticated techniques (for example Davidon (1968) or Powell (1964)) which tend to be extremely rapid when close to a minimum but are rather poorer further away from the minimum and with badly behaved functions.

The two optimizing routines, the Monte Carlo and the Rosenbrock, were available as main programs in a CERN library program (James and Roos, 1969) for use on the NUNAC IBM 360/67 and later on the IBM 370/168 and subroutines defining the function to be minimized and the input/output controls were written and are described at the end of the thesis.

4.5. Optimized Models

4.5.1. Monte Carlo Techniques

In an attempt to define areas within which an optimum solution might be found a random search was carried out over a wide range of values defining the structure. It was demonstrated in the last chapter that a variation in the anomalous velocity leads to a change in the scale of the structure and thus this velocity was set to an arbitrary value of 7.1 km/sec, as a result the field of search is reduced to six variables. The full data set of sixty events was used and the weighting factors on slowness and azimuth (equation 4-(11)) were chosen so that equal weights are, on average, given to both sets of anomalies if the weighting factors associated with the observed errors are neglected. Since the average azimuth error, as a fraction of the average azimuth anomaly, is larger than the corresponding factor for slowness this implies that the optimized function weighs rather more heavily on the slowness data, since it has been demonstrated (section 3.8.) that the structure is rather more sensitive to azimuth errors than slowness errors this is considered satisfactory.

Upper and lower limits for the parameters were chosen so as to encompass all reasonable values and starting values for the parameters were chosen at random within these limits for the eight runs which were made. Each run consisted of calculating the function to be minimized for 400 values of the parameters. A large majority of the parameter sets caused the rays for some of the events to miss the structure (i.e. to intersect at a depth greater than 400 km) and many resulted in physically unacceptable solutions (for example the

rift cutting the surface to the west of the station) but several parameter sets were obtained which resulted in low values for the function to be minimized.

It was found that several of these sets were equivalent in that they corresponded to similar structures but with the separation between rift and station increased and the depth of intersection increased. The best range of solutions was found in the region of the point

$$(a,b,c) = (103.0, 31.2, 57.3) \text{ km}$$

$$\theta = 27.0^\circ$$

$$(x,y) = (61.5, -68.7) \text{ km}$$

where a, b and c are defined in equation 4-(1);  $\theta$  is the orientation of the co-ordinate system and (x, y) indicates the location of the station. This solution assumes an average anomalous velocity of 7.1 km/sec.

This solution was used as the basis for further work and in the discussion to follow all reference to optimization procedures will refer to the Rosenbrock method.

#### 4.5.2. Investigation of the Properties of the Data Sets

It was shown in the last chapter that several events did not agree with the model that is proposed here. The behaviour of these groups is now analysed by optimizing the whole data set and observing the distribution of residuals.

The degree to which a model satisfies the observed anomalies is expressed by the percentage of the anomaly, in terms of slowness and azimuth, which it explains. This can be an unreliable indicator of the success of the optimization process since a large anomaly with a large error is not weighed very heavily in the search for a solution; nevertheless,

it does have the advantage of relating directly to the quantities measured which a description of the function being optimized does not. The final models will be examined in more detail in this respect.

The same weighting factors and starting values were used as described in the last section. The data was optimized at various fixed velocities and, as an example, the case of an assumed velocity of 6.8 km/sec is discussed. The optimum solution in this case was

$$(a,b,c) = (81.4, 29.7, 43.9) \text{ km}$$

$$\theta = 15.9^\circ$$

$$(x,y) = (88.6, -62.7) \text{ km}$$

The model produces an average azimuth residual of  $11.6^\circ$  and an average slowness residual of 0.98 sec/deg and thus accounts for 29% and 44% of the observed anomalies respectively.

Details of the solution for the second group of Table 3.2. are given as the first seven events in Table 4.1. The average slowness and azimuth residuals are 1.19 sec/deg and  $25.5^\circ$ . These seven events all come from azimuths to the west of Kaptagat (except 3447.70 which is from an azimuth of  $5.8^\circ$ ) and consequently their depths of intersection with the structure is relatively deep. The rest of Table 4.1. shows all events with a depth of intersection greater than 200 km, giving a total of 17 events. This group shows average residuals of  $17.4^\circ$  on azimuth and 1.34 sec/deg on slowness while the 43 events covering structure less than 150 km deep show average residuals of  $9.5^\circ$  and 0.81 sec/deg respectively.

Thus the events from east of Kaptagat and describing

Table 4.1 - Events Used to Control Deep Structure.

Event No.	Depth (km)	Azimuth (degrees)		Distance (degrees)	Azimuth (degrees)		Slowness (sec/deg)	
		Expected	Observed		Anomaly	Residual	Anomaly	Residual
3527.70	193.7	352.8		73.9	- 1.5	43.9	1.83	0.10
3123.70	400.0	323.6		74.2	- 3.6	- 3.6	2.76	2.76
3447.70	202.7	5.8		73.8	-13.5	31.1	2.00	0.27
4342.71	400.0	300.5		79.5	5.1	5.1	3.99	3.99
2736.70	158.7	206.5		76.5	23.6	-25.4	1.27	0.24
2562.70	214.2	211.1		76.2	27.5	-31.5	1.44	-0.42
4343.71	290.3	211.6		75.6	30.5	-37.7	1.82	-0.56
3382.70	400.0	331.6		40.1	- 5.9	- 5.9	1.37	1.37
3015.70	368.2	340.7		46.7	0.4	0.4	2.56	2.56
1946.71	400.0	352.9		38.9	1.3	1.3	1.94	1.94
533.72	248.2	30.3		61.7	-33.8	9.0	2.37	0.44
4499.72	291.8	199.5		59.8	29.9	-26.5	1.92	0.10
578.72	400.0	270.0		63.9	24.9	24.9	1.43	1.43
3020.70	400.0	340.7		46.7	-11.3	-11.3	1.49	1.49
2812.70	400.0	342.5		42.9	-21.0	-21.0	-0.60	-0.60
2312.71	400.0	352.7		37.2	0.8	0.8	2.17	2.17
4621.71	400.0	11.4		48.6	-16.4	-16.4	2.30	2.30

When the depth of intersection exceeds 400km the residual is put equal to the anomaly.

structure between the station and the rift require a different model from those events describing the deeper structure to the west of the station and consequently the 43 events are discussed below and the events controlling the deeper structure are discussed in section 4.5.4.

The optimum model for the 43 events, again at 6.8 km/sec, was

$$(a,b,c) = (88.1, 26.6, 46.6) \text{ km}$$

$$\theta = 10.1^\circ$$

$$(x,y) = (116.2, -48.9) \text{ km}$$

which differs considerably from the previous solution. The residuals are plotted against the expected azimuth in Figs.4.1. and 4.2. with the calculated 95% confidence limits (in certain cases these are omitted for clarity but this is never done when the error is smaller than the residual). The average slowness and azimuth residuals are 0.67 sec/deg and  $11.6^\circ$  respectively and on only three occasions does the slowness residual exceed the 95% confidence limit to a degree which is not acceptable in the light of the discussion on the possible source of the anomalies (section 4.2.). This occurs for events 2997.70, 458.70 and 1446.71 which are from distances of  $23.3^\circ$ ,  $18.8^\circ$  and  $34.0^\circ$ . The behaviour of the first group of events in Table 3.2. is illustrated in Table 4.2. where the dips indicated are those calculated in section 3.6. for a velocity of 6.8 km/sec, in addition event 1446.71 is included. It can be seen that several of these events are either incident to the structure beyond the critical angle or produce results which are not consistent with the model proposed.

Figure 4.1

Plot of slowness residuals against expected azimuth for  
all events east of Kaptagat.

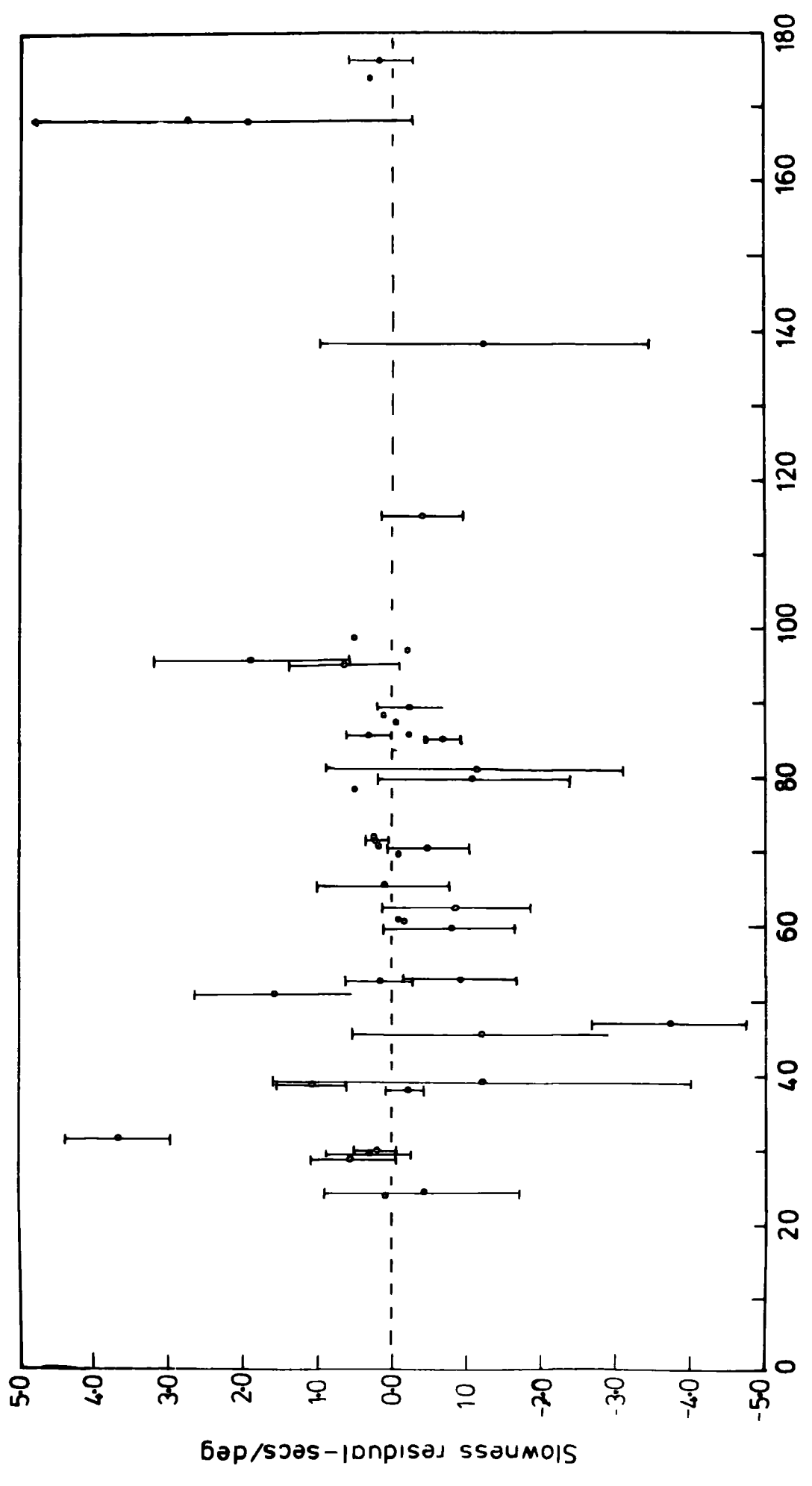


Figure 4.2

Plot of azimuth residuals against expected azimuth  
for all events east of Iaptagat.

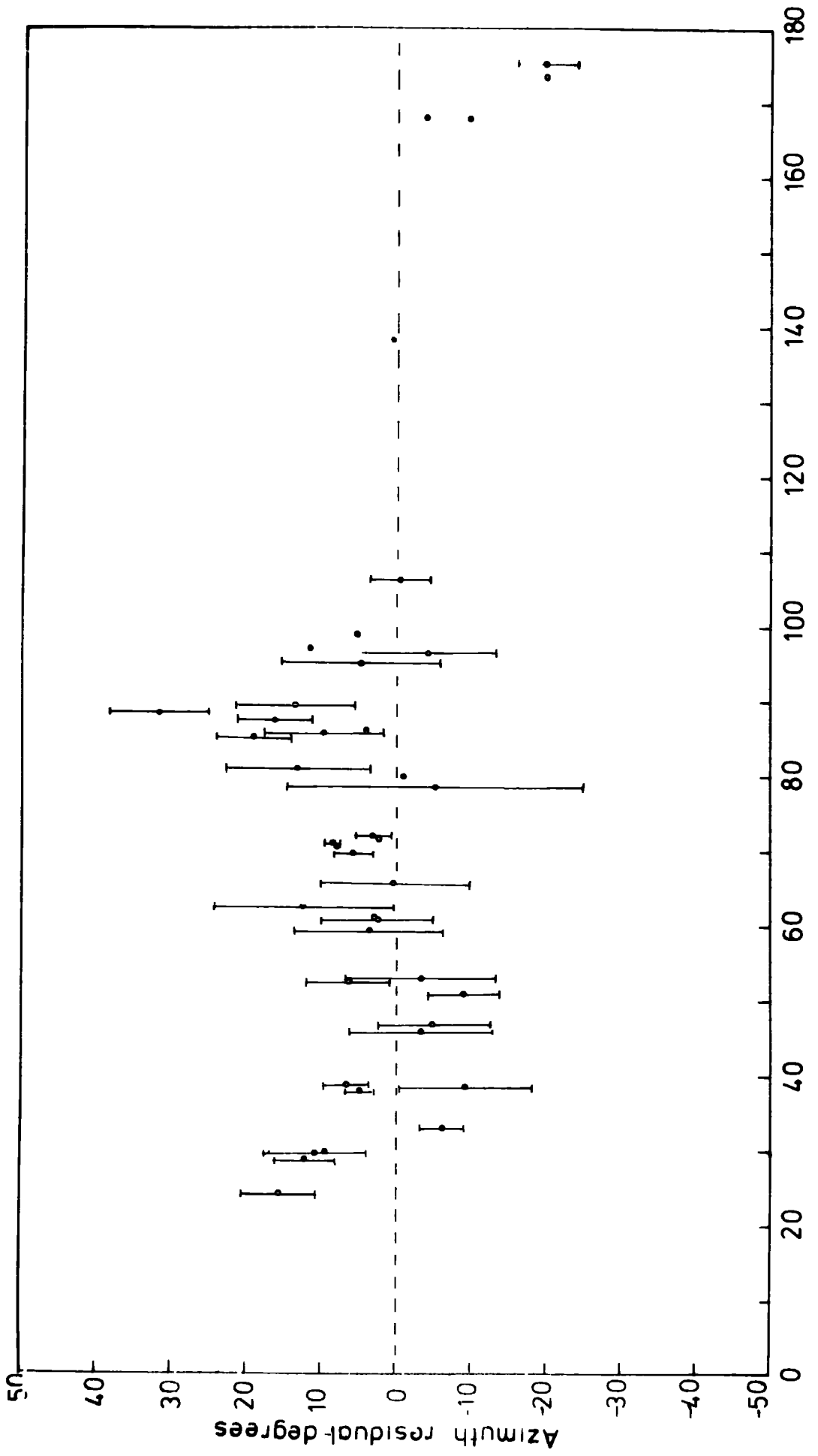


Table 4.2

Events From  $\Delta < 30^\circ$

Event No.	Azimuth Residual (degrees) ---	Slowness Residual (degrees)	Dip Required (degrees)
2997.70+	- 8.9*	1.60*	34.3
2471.70	3.6*	0.22	36.6
458.70	- 4.8	-3.70*	65.2
2483.70	5.9*	-0.07	39.7
1476.71	- 3.2	-1.18	82.2
3094.7-	-19.5*	-0.17	82.7
1446.71+	- 6.1	3.67*	32.1

\* - indicates that residual is greater than 95% confidence limit.

+ - indicates that total internal reflection occurs for this event and the residual is not equal to the anomaly.

If the behaviour of the function near the minimum is considered it will be seen that these events can have serious effects in the search for a minimum. Figs.4.3. and 4.4. show how the variation of parameters a and c near the minimum influence the value of the function being minimized. Variation of the other parameters leads to a discontinuity of the form illustrated in Fig.4.3. although it does not usually occur quite so close to the minimum. Variation of parameter c also leads to the second kind of discontinuity which occurs when c is approximately 54 km. The first kind is caused in the examples shown by event 1476.71 and is caused by total internal reflection, here it occurs exactly as the ray intersects the structure within the crust and the large deviations near the critical angle are avoided. The anomaly is large when the intersection occurs within the mantle and is reduced to the observed anomaly when it occurs within the crust. The second form of discontinuity is caused by event 2483.70 and in this case total internal reflection does not occur at the crust-mantle boundary but at shallower depths and thus large deviations are observed. Other events in this group show similar behaviour but at some distance from the present minimum. Consequently the location of the minimum is being controlled by the discontinuity rather than the shape of the curve and it was decided to omit these events from further consideration.

#### 4.5.3. Final Optimized Models

The final models for the shallow structure of the proposed anomalous body were derived using the 36 events listed in Table 4.3. The residuals obtained at an assumed velocity of 6.8 km/sec, together with the 95% confidence limits,

Figure 4.3

Dependence of the function value on parameter 'a' in  
the region of the minimum.

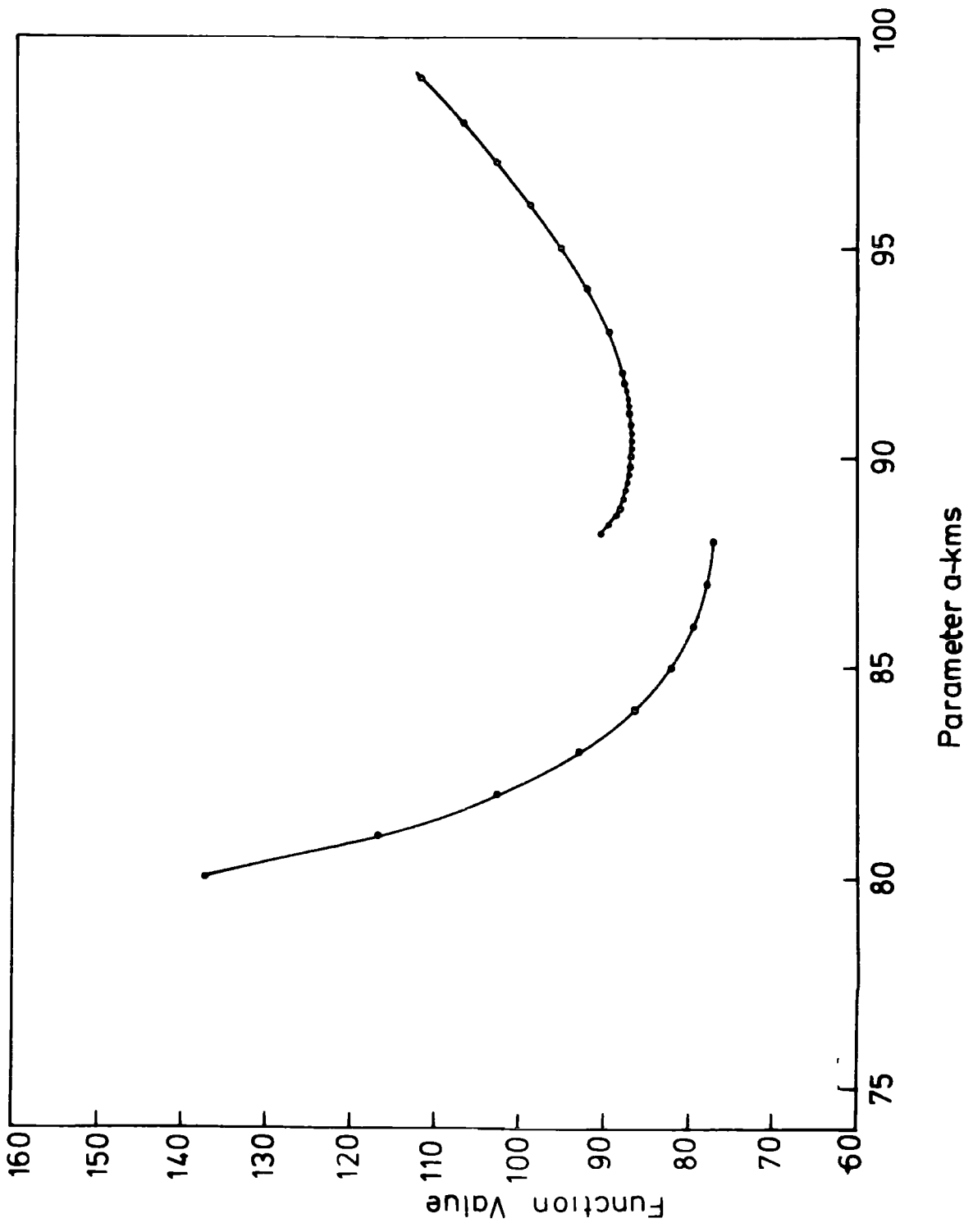


Figure 4.4

Dependence of the function value on parameter 'c' in  
the region of the minimum.

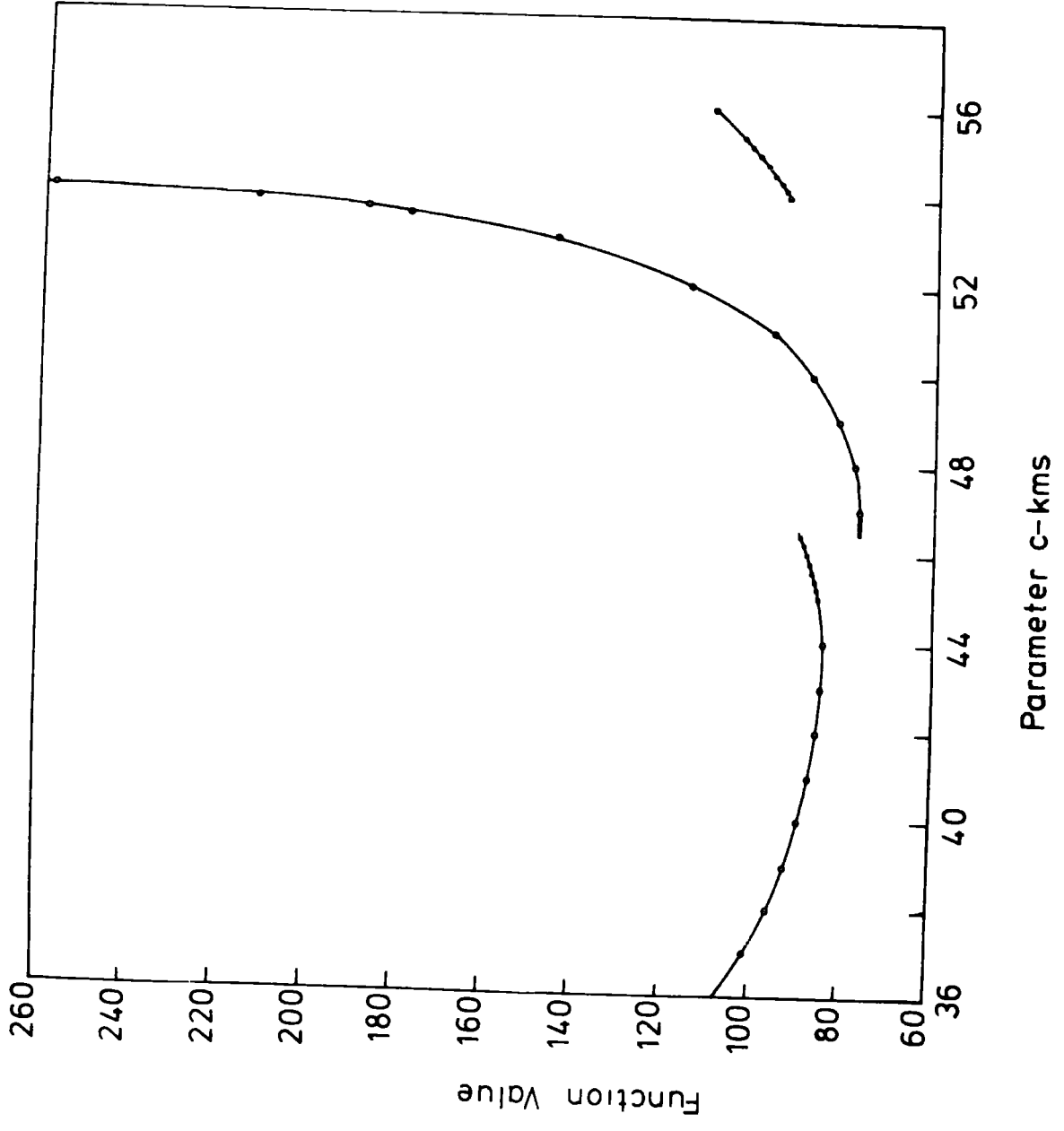


Table 4.3

Optimum Solution at 6.8km/sec

Event No.	Slowness (sec/deg)			Azimuth (degrees)		
	Anomaly	Residual	Error	Anomaly	Residual	Error
2578.70	0.31	-0.57	1.30	-15.9	15.0	5.2
1958.71	2.06	0.26	0.57	-11.1	12.5	4.0
2515.70	0.89	0.18	0.58	-23.5	10.2	6.3
1578.71	0.94	0.04	0.27	-27.8	8.0	2.9
3082.70	0.21	-0.32	0.22	-26.5	4.4	1.7
3074.70	1.49	0.95	0.48	-18.8	6.8	2.9
2907.70	-0.38	0.12	0.46	-43.4	5.3	5.3
2341.70	-1.66	-0.74	0.90	-26.4	3.8	10.0
2574.70	-1.04	-0.12	0.71	-26.3	2.6	7.4
2572.70	-1.07	-0.05	0.31	-25.6	3.0	3.4
535.71	-2.35	-0.79	0.99	-15.6	12.3	12.1
1624.71	-0.90	0.14	0.91	-27.8	0.4	10.3
1693.71	-2.14	-0.47	0.55	-41.1	7.3	12.3
2902.70	-1.27	0.24	0.16	-35.6	2.0	2.3
3676.70	-1.30	0.27	0.48	-34.1	2.9	8.7
2547.70	-3.20	-0.60	0.24	8.2	13.7	4.8
2807.70	-2.18	0.34	0.31	-16.1	9.4	7.9
2635.70	-2.42	0.06	0.43	6.5	15.8	5.1
442.71	-2.53	0.17	0.51	33.2	30.9	6.4
3066.70	-2.71	-0.17	0.44	8.1	13.0	2.0
1397.71	-1.52	0.77	0.74	-6.6	4.3	10.6
3568.70	-2.60	-0.30	0.52	-2.7	-1.1	4.0
4600.71	1.15	0.08	1.59	3.3	24.7	23.2
667.72	3.44	-1.16	2.78	-3.9	0.9	9.0
455.72	-1.01	-0.96	0.74	-38.5	-3.7	10.0
426.72	-0.67	0.63	4.83	-25.8	-5.1	20.0
4765.71	-2.76	-1.02	1.32	-29.3	-1.3	62.3
456.72	-3.42	-1.05	2.14	-6.3	12.9	9.5
2331.71	-2.23	-0.15	1.17	-13.7	3.8	9.2
2333.71	-0.21	1.98	1.28	-21.6	-4.6	9.1
4737.71	-1.90	-0.15	2.01	4.1	11.2	77.3
4630.71	-2.01	0.58	3.40	-5.6	4.8	40.9
499.72	-3.67	-1.24	2.20	11.8	-0.7	51.7
636.72	1.23	2.60	3.27	16.6	-4.8	49.8
643.72	0.02	1.89	2.76	7.7	-10.5	40.1
3138.70	-1.61	0.25	3.30	1.1	-20.3	59.1

are also listed in the table and are illustrated in Figs.4.5. and 4.6. (Again for clarity some confidence limits are omitted.) The optimum solution was

$$(a,b,c) = (83.0, 29.7, 48.2) \text{ km}$$

$$\theta = 8.8^\circ$$

$$(x,y) = (97.8, -55.3) \text{ km}$$

which differs considerably from the previous solution. The average slowness and azimuth residuals are now 0.59 sec/deg and  $8.3^\circ$  respectively which account for 56% of the azimuth anomalies and 65% of the slowness anomalies. It may be noted that events such as 4765.71, which has a 95% confidence limit of  $63.3^\circ$  on azimuth, has a residual of  $1.3^\circ$  and that in general those events with large azimuth errors fit the model satisfactorily. Thus these events, which play a very small part in determining the optimum structure, confirm the suitability of the model in regions which otherwise could not have been considered.

Fig.4.7. shows a contour map of the surface produced by this model down to 140 km with the locations of the intersections with the raypath indicated. The area of the surface which is sampled by the data is disappointing but is a necessary consequence of being restricted to a single station and the available earthquakes.

Figs.4.8. to 4.12. show the sensitivity of the optimum model to changes in the parameters describing the structure. The y co-ordinate is the value of the dimensionless function being optimized and all figures are on the same vertical scale except for parameter 'b' which has a y-scale one half as sensitive. It can be seen that the structure is well defined but that the station may be moved 10 km in any

Figure 4.5

Plot of slowness residuals against expected azimuth  
for data set controlling shallow structure.

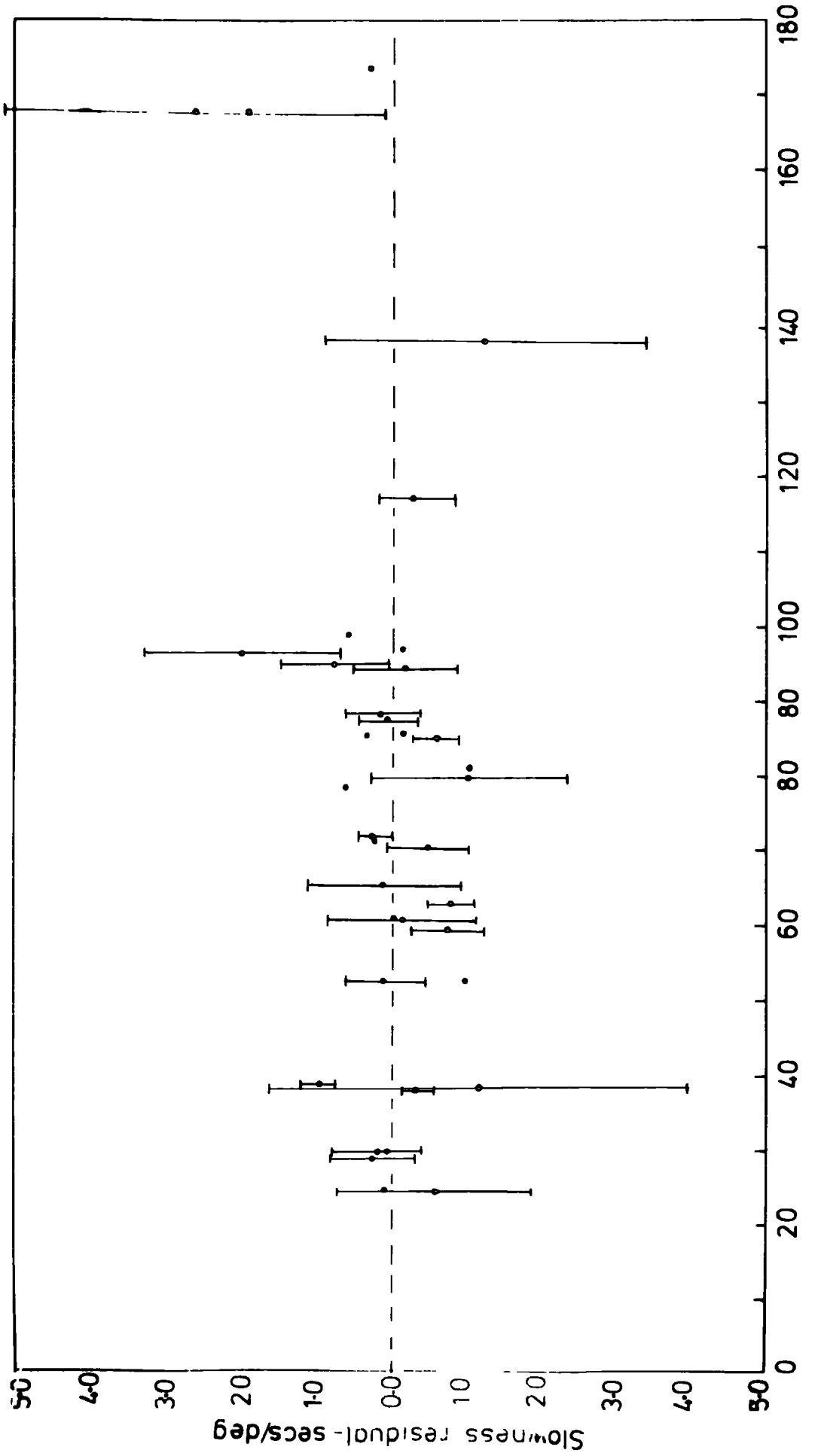


Figure 4.6

Plot of azimuth residuals against expected azimuth  
for data set controlling shallow structure.

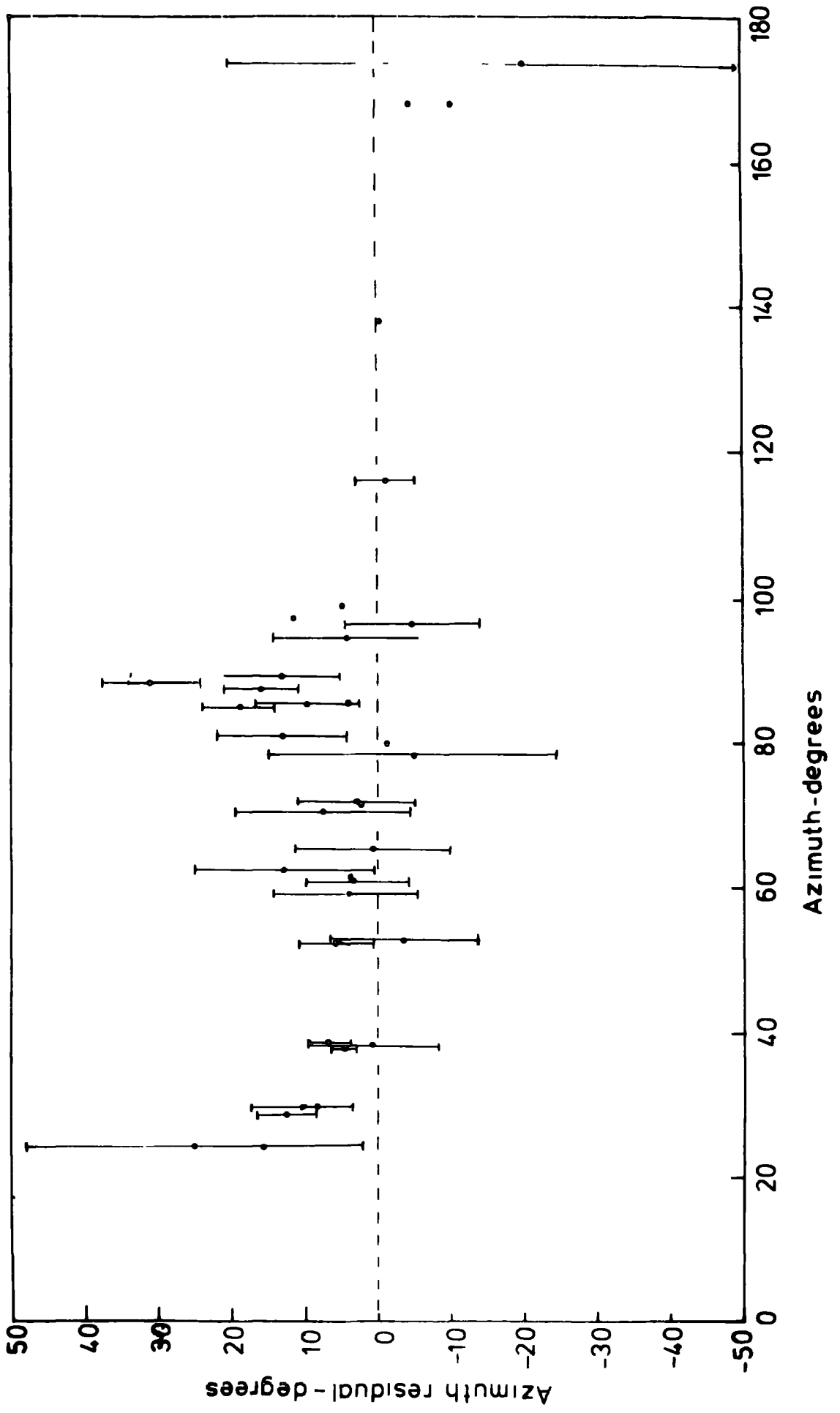
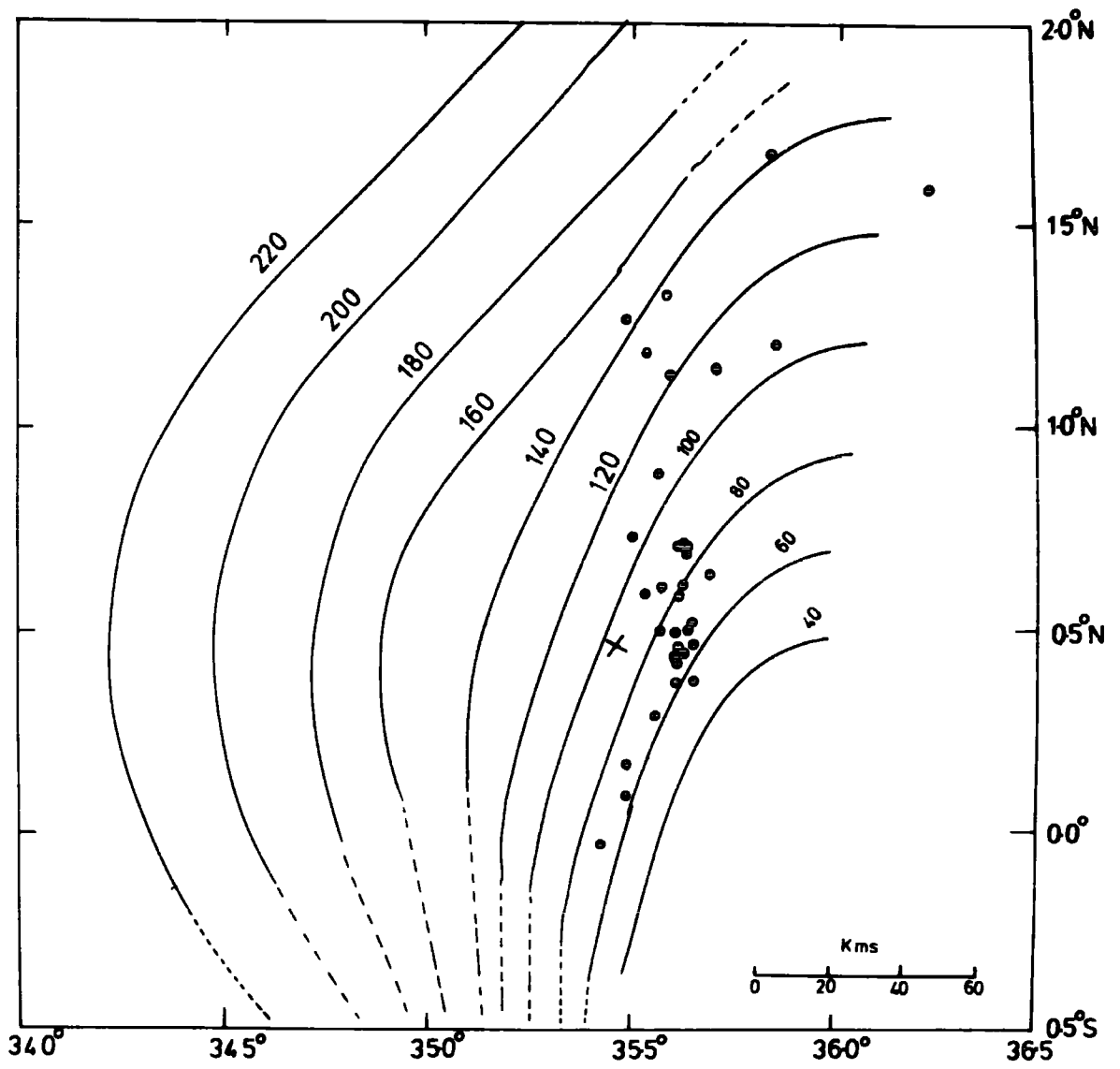


Figure 4.7

A contour map of the upper surface of the anomalous upper mantle for an assumed average velocity of 6.8 km/sec. Structure to a depth of 140 km is controlled by the optimization process described, deep structure is controlled by the extrapolation technique described in section 4.5.4. The location of the intersection of the rays is indicated for the shallow structure.



direction without significantly effecting the residuals and thus any attempt to constrain the structure by demanding that it cuts the surface a given distance from Kaptagal may only be used in a very broad sense. Finally, it can be seen that problems of total internal reflection play no part in the location of this minimum.

The effect of the variation in the velocity is most easily seen by comparing Figs.4.7. and 4.13. where the contours are shown at 20 km intervals for velocities of 6.8 km/sec and 7.4 km/sec although details of the variation in the parameters are given in Table 4.4. The model at 7.4 km/sec shows a structure with extremely steep slopes as would be expected, moreover, because the steep slopes are required for nearly all the events the x co-ordinate is minimized so as to maintain as many events as possible on the steep side of the structure. At a velocity of 6.8 km/sec the situation is reversed so that the x co-ordinate is maximized to provide a shallower slope and a greater variation in the strikes available. The orientation of the co-ordinate system,  $\theta$ , changes from  $2.0^\circ$  at a velocity of 6.7 km/sec to  $22.2^\circ$  at 7.3 km/sec. If the contours are considered, however, the strike of the structure remains approximately constant as the curve introduced by the function at low velocities has been compensated for by a change in the orientation of the axes. The function value decreases steadily with velocity although beneath 7.2 km/sec the search does not appear to reduce the azimuth or slowness residual effectively. Since the velocity proposed here is an average velocity and there are indications (Griffiths et al, 1971) that the lid of the structure has a velocity of

Table 4.4 - Dependence of Structure on Assumed Velocity

Velocity (km/sec)	a (km)	b (km)	c (km)	(degrees)	x (km)	y (km)	Av. Azimuth		Av. Slowness		Function Value
							Residual	Residual	Residual	Residual	
6.7	81.2	31.4	45.3	2.0	102.9	-53.9	7.3	0.58	0.58	28.2	
6.8	83.0	29.7	48.2	8.8	97.8	-55.3	8.3	0.59	0.59	29.6	
7.0	102.9	37.9	65.9	9.2	86.5	-57.1	8.2	0.58	0.58	30.1	
7.2	103.8	35.9	69.4	12.5	76.5	-48.9	8.9	0.69	0.69	31.2	
7.3	109.9	30.3	67.6	22.2	44.3	-47.6	9.8	0.74	0.74	46.9	
7.4	111.4	22.1	74.7	19.7	55.3	-37.8	9.1	0.84	0.84	84.5	

Figure 4.8

Dependence of the function value on parameter 'a'.

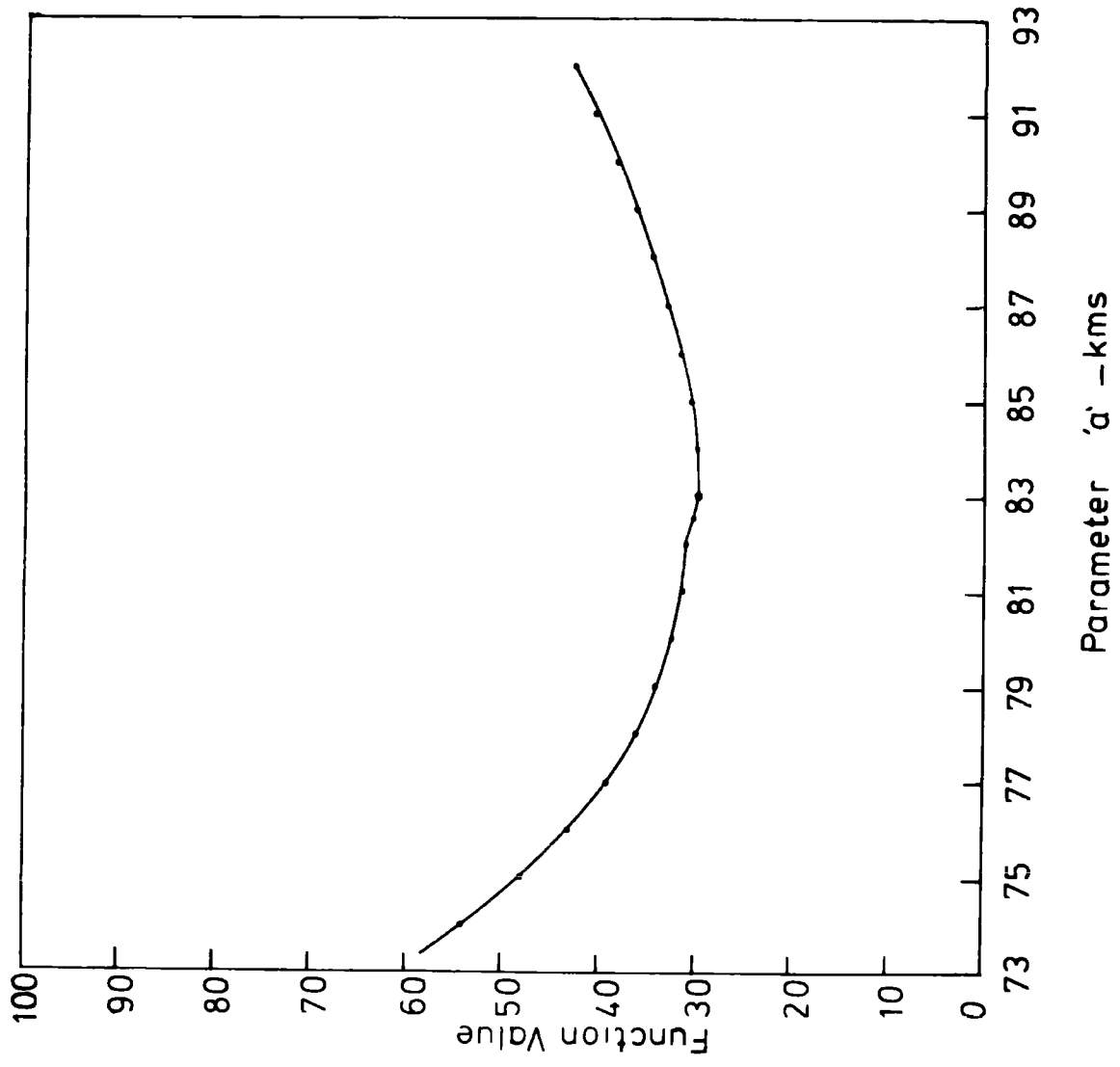


Figure 4.9

Dependence of the function value on parameter 'b'.

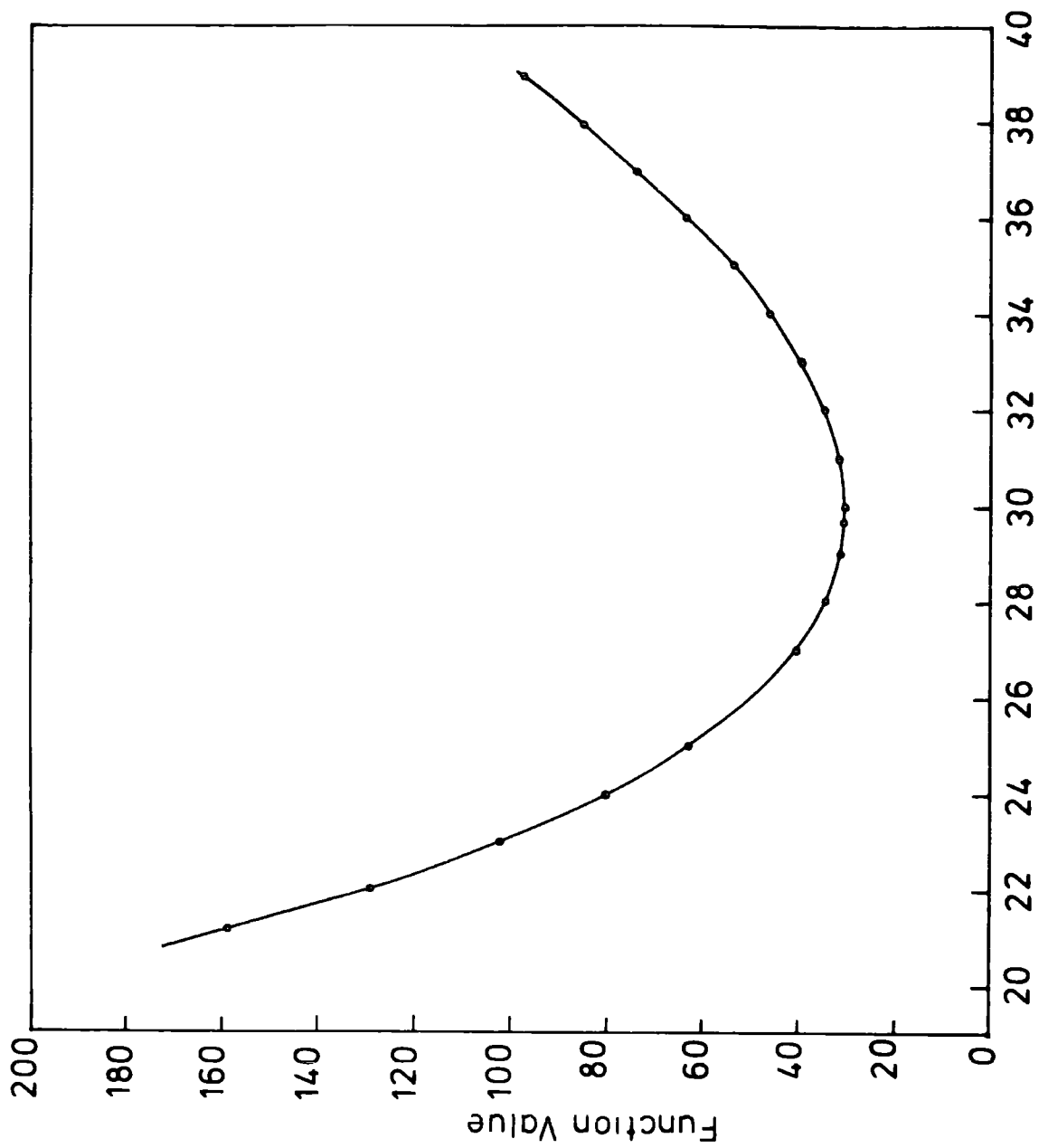


Figure 4.10

Dependence of the function value on parameter 'c'.

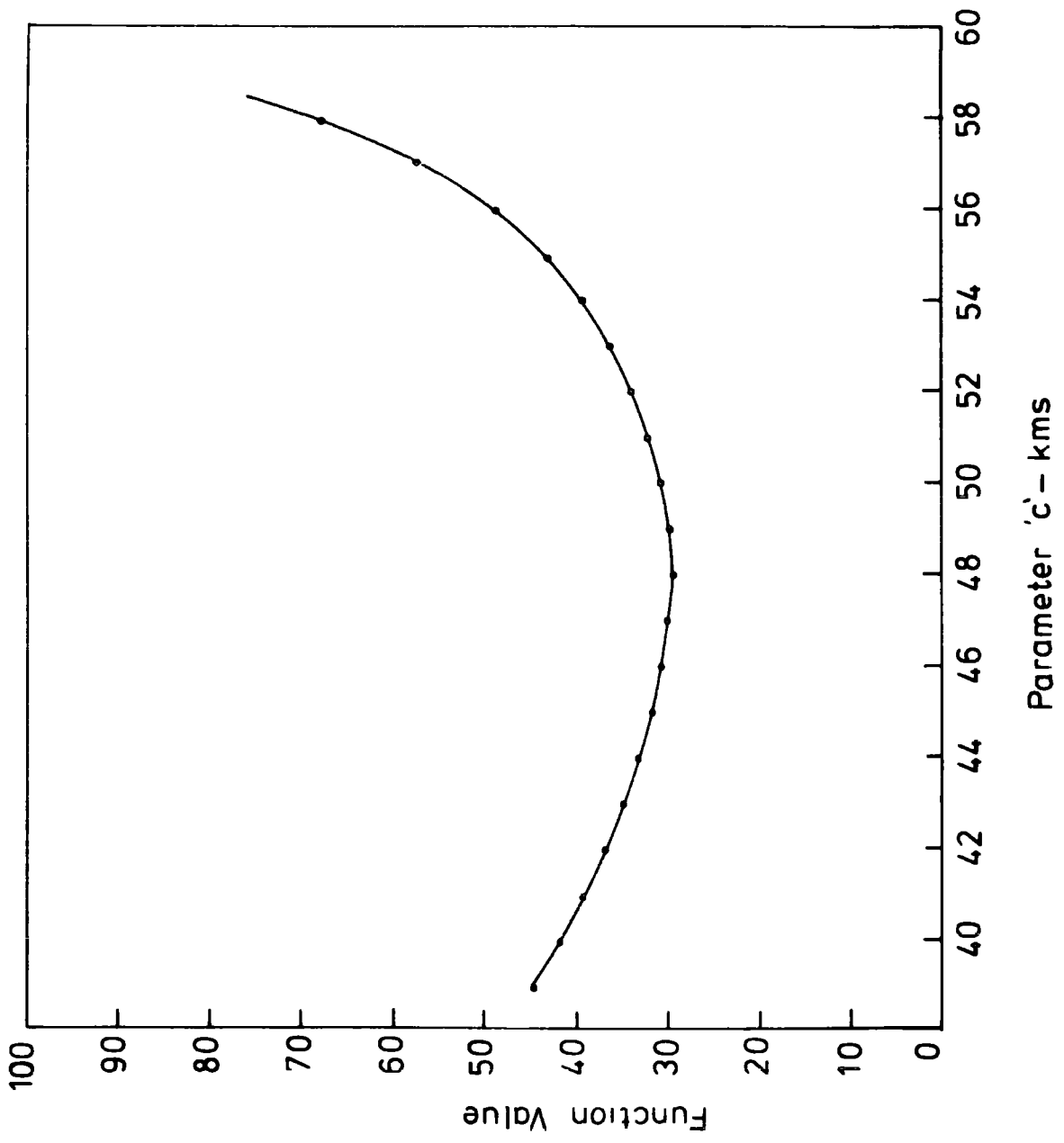


Figure 4.11

Dependence of the function value on the orientation  
of the co-ordinate system. -  $\theta$

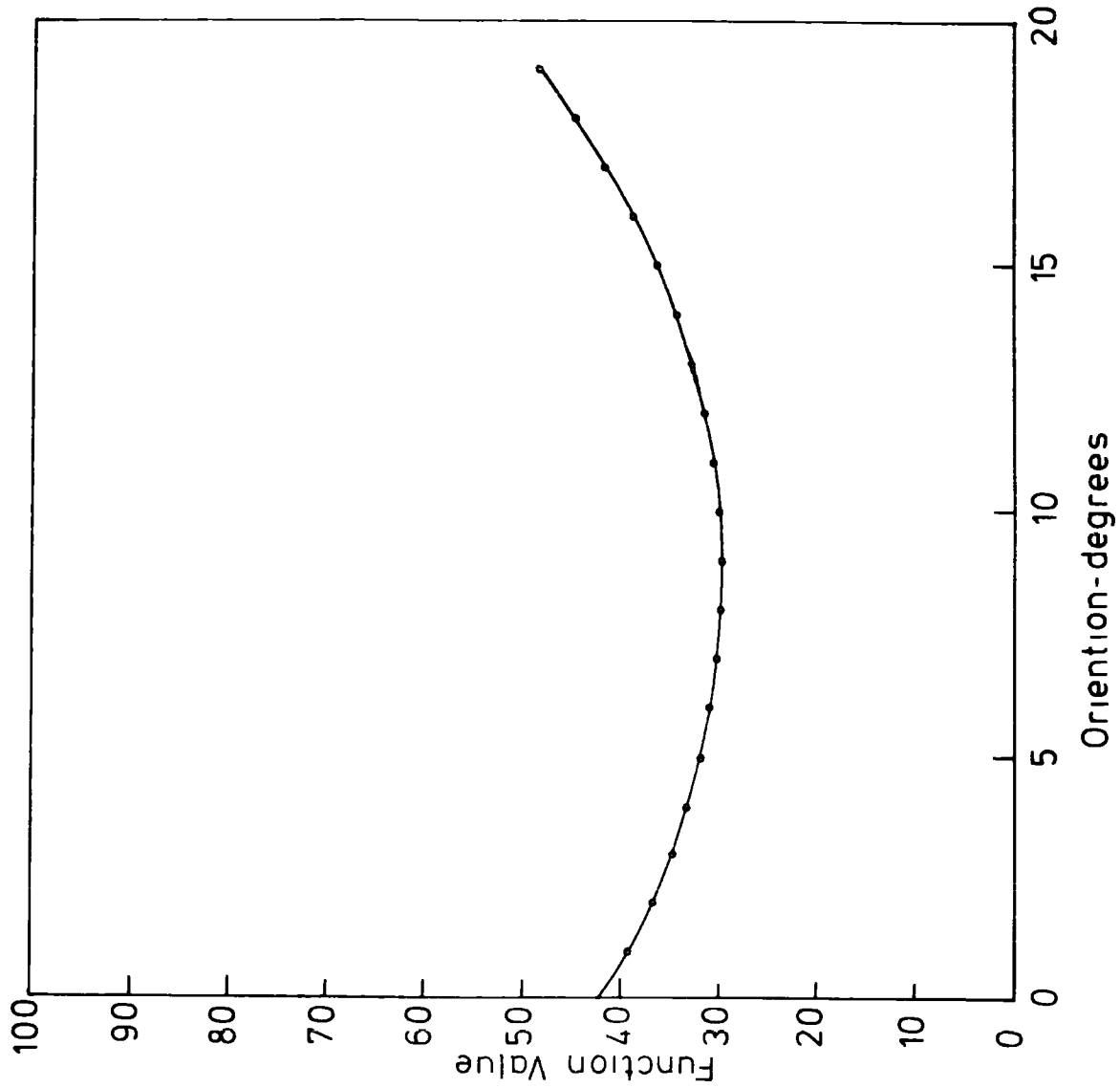
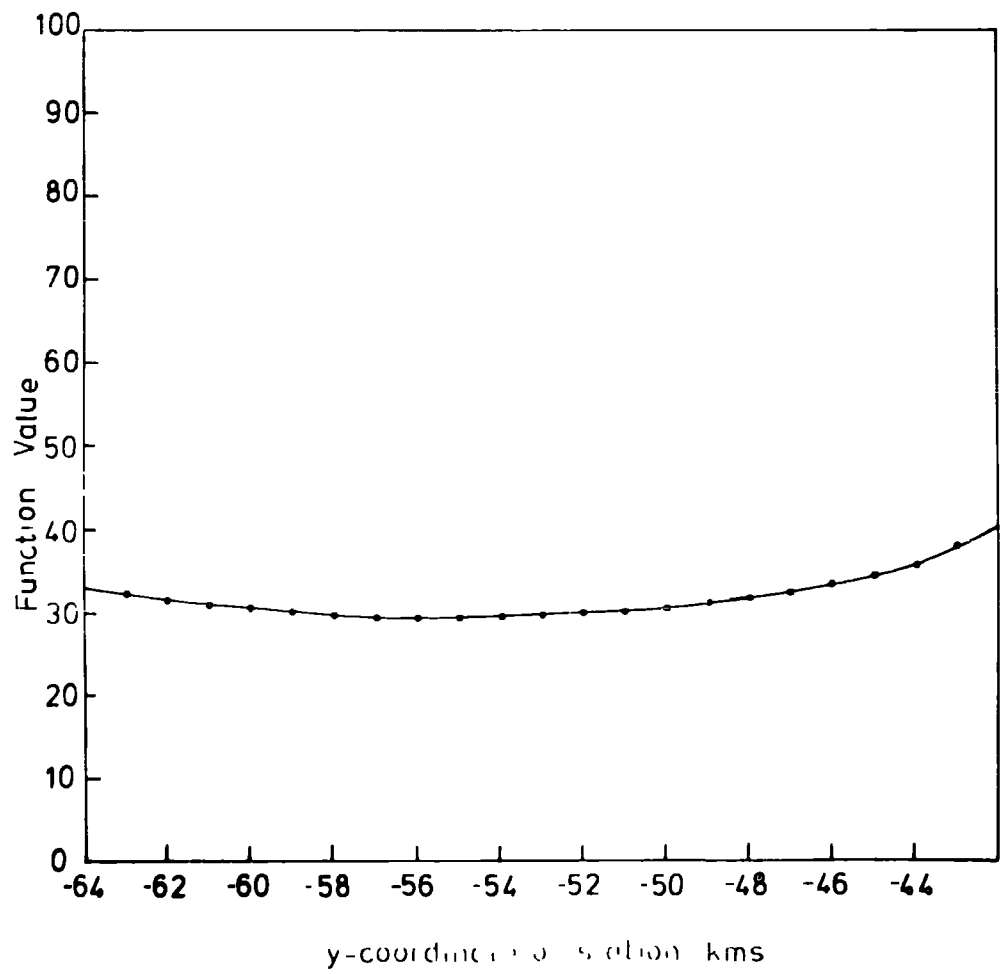
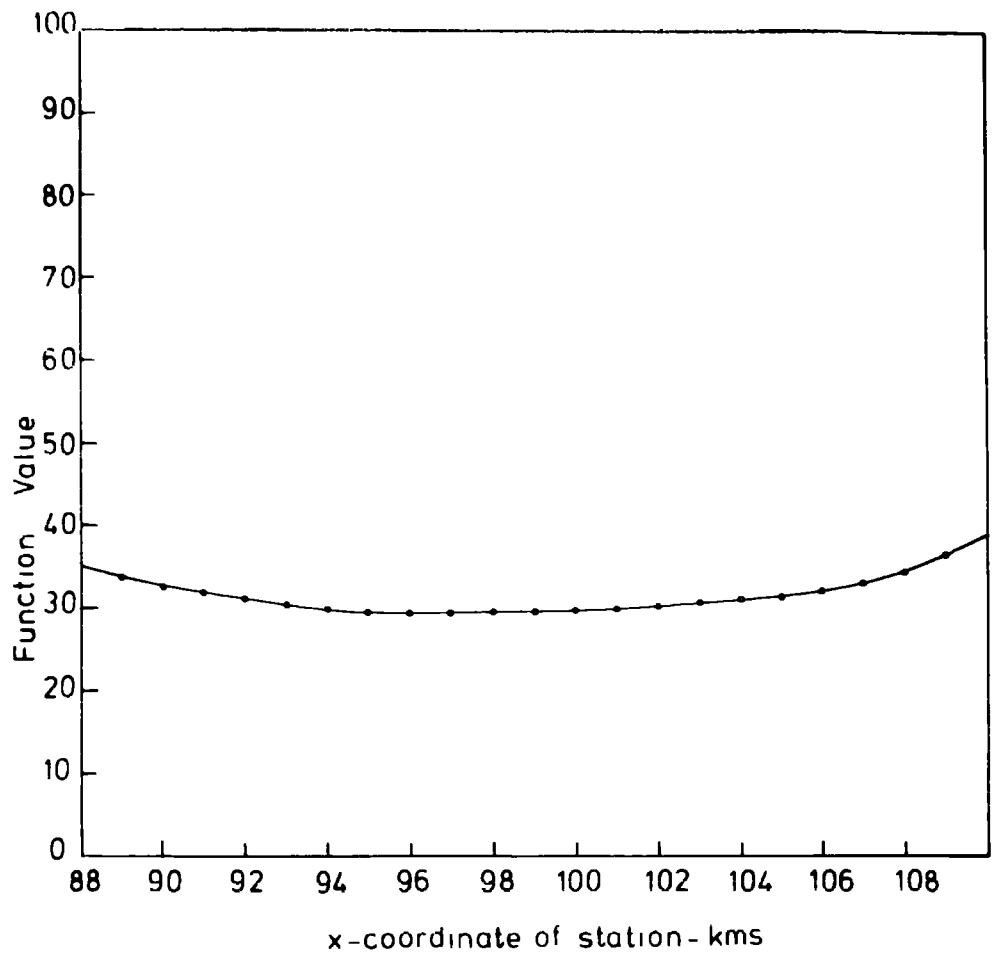


Figure 4.12

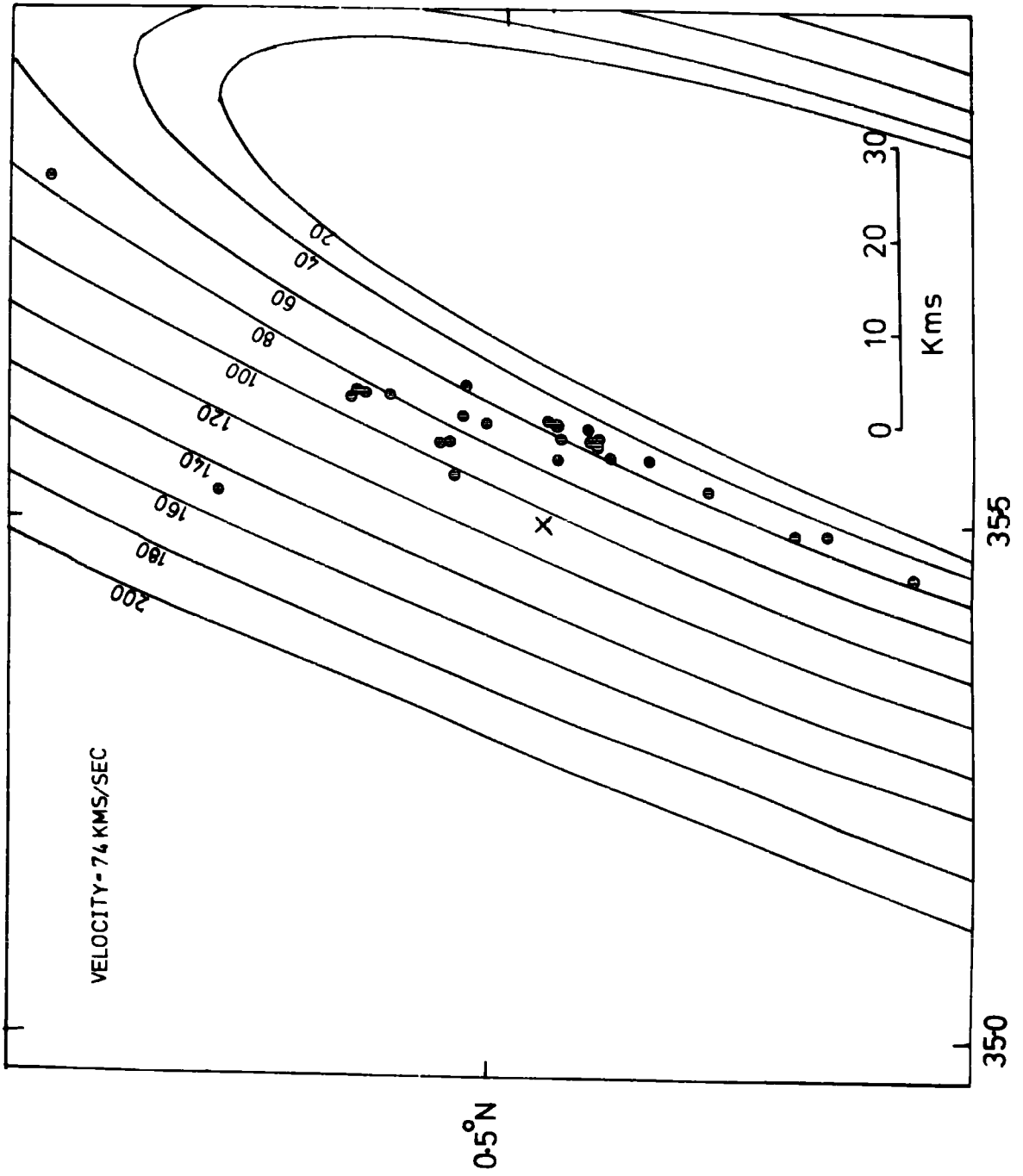
Dependence of the function value on the location  
of the co-ordinate system -  $(x,y)$ .



---

Figure 4.13

A contour map of the upper surface of the anomalous upper mantle for an assumed average velocity of 7.4 km/sec. Details are as given in Fig. 4.7.



7.5 km/sec, it is implied that the core of the structure could have an ultra-low velocity.

#### 4.5.4. Structure to the West of Kaptagat

The events arriving between azimuths of  $180^{\circ}$  and  $360^{\circ}$  (in a clockwise sense) will now be used to calculate the deeper structure of the model. The area of the surface covered by this data is extremely large and, in addition, several of the 17 events used have large errors so that the reliability of this interpretation is somewhat less than that of the last section.

The events used are listed in Table 4.5. together with their azimuths, their depths of intersection using the optimum model for the whole data set and the dips and azimuths required of the single interface to explain the anomaly at a velocity of 6.8 km/sec (section 3.6.), they are arranged in groups of approximately equal azimuths. In the first group from measured azimuths between  $350^{\circ}$  and  $355^{\circ}$  the two events with depths of intersection greater than 1,000 km have extremely shallow dips while those with shallower intersections have larger dips (unfortunately event 3527.70 does not agree with this classification; all that can be suggested is that the calculated dip is so low as to suggest that it is not caused by the structure under consideration). Thus, as the depth of the interface increases the dip decreases much more rapidly than indicated by the optimum model of the last section. Events 2812.70 and 4499.71 also do not agree with this trend, but the errors are so large that they are not significant at the 95% confidence level.

Table 4.5

Events Used in Extrapolation Procedure.

Event No.	Distance (degrees)	Azimuth (degrees)		Depth (km)	Dip (degrees)	Strike
		Measured	Expected			
2312.71	37.2	353.5	352.7	>1000	22.7	165.8
1946.71	38.9	354.2	352.9	>1000	22.0	178.6
4691.71	48.6	355.0	11.4	400.8	33.9	141.6
3447.70	73.8	352.3	5.8	187.6	33.3	141.2
3527.70	75.9	351.3	352.8	181.1	16.6	162.5
3382.70	40.1	352.7	331.6	539.3	21.0	114.8
2812.70	42.9	321.5	342.5	842.0	39.0	61.7
3020.70	46.7	329.4	340.7	372.9	27.1	119.7
578.72	63.9	295.8	270.9	550.6	46.3	169.8
3123.70	74.2	320.0	323.6	387.4	32.6	127.4
4342.71	79.5	305.6	300.5	>1000	38.9	144.3
4499.71	59.8	279.4	199.5	>1000	53.1	116.7
4343.71	75.6	242.1	211.6	>1000	47.0	112.7
2562.70	76.2	238.6	211.1	389.6	42.6	108.9
2736.70	76.5	229.9	206.3	209.8	40.3	97.4

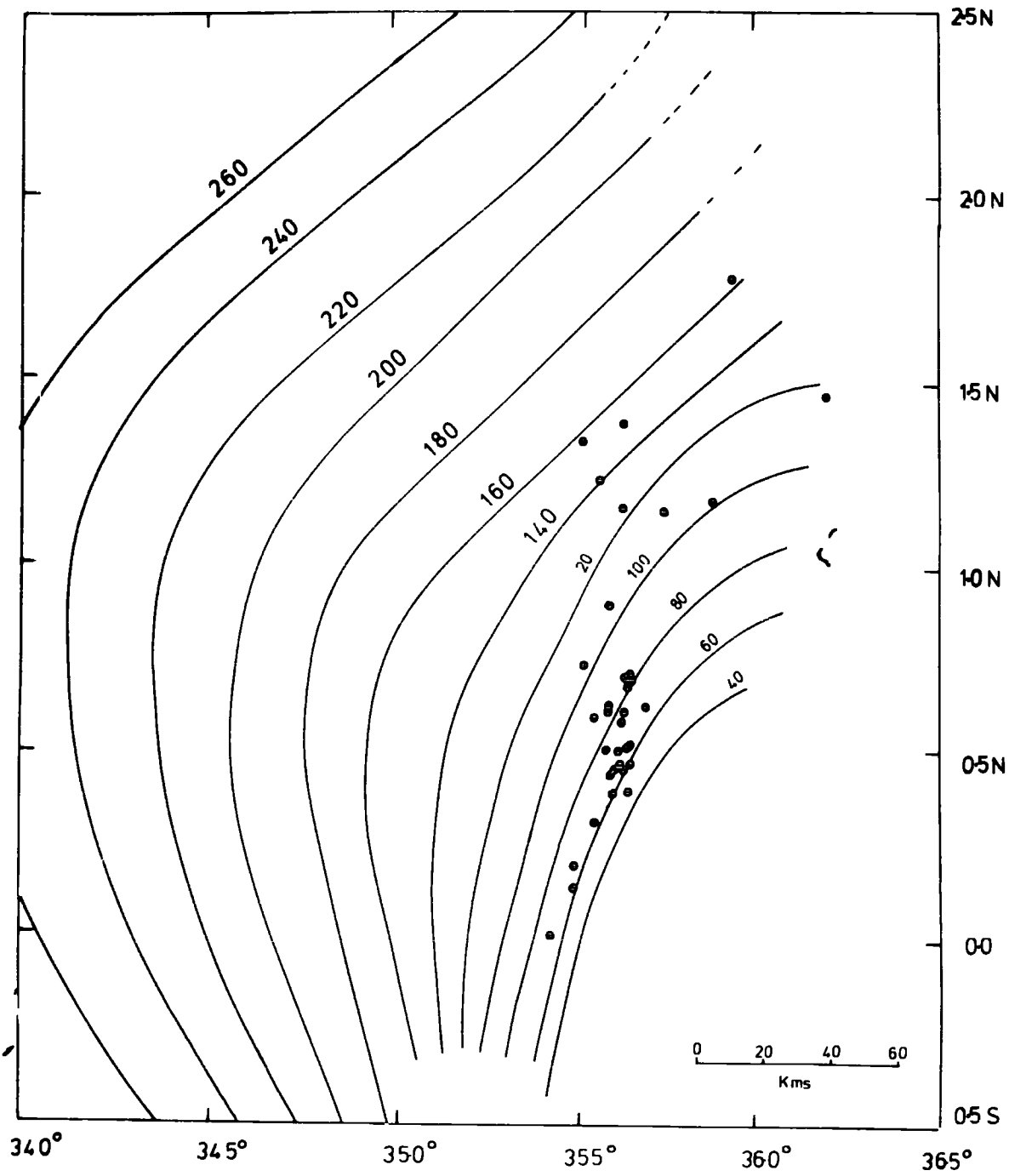
Because the data points were so sparse it was considered that an analysis of the kind performed for the shallow structure was not justified and a simple extrapolation technique was used. Each of the three azimuth groups is taken in turn, the events intersecting at the shallowest depth are traced from the station and the dips which have been calculated for that event are assumed to apply to the structure from the point of extrapolation. The point of intersection of the new structure with the ray is now calculated and this serves as a point for further extrapolation using the next deepest intersection. At the first stage in this process the strike of the surface as derived from the optimization procedure is assumed correct and at the deeper stages the strike in Table 4.5. is assumed. (As there are no data points from the shallow analysis near azimuths  $220^{\circ}$  and  $320^{\circ}$  extrapolation begins from the station.) By combining these three lines contours may be drawn to extend the structure and the results are shown in Fig.4.7. for a velocity of 6.8 km/sec and in Fig.4.14. for a velocity of 7.0 km/sec.

The full extrapolation procedure at an azimuth of  $320^{\circ}$  leads to a depth in excess of 300 km although if the errors at the 95% confidence limits are taken this produces depths of approximately 200 km and more than 400 km. It will be seen in the next chapter that the larger thicknesses are not consistent with the delay time data indicating a shallowing of the structure at least as severe as shown in Figs.4.7. and 4.14.

In conclusion, it is suggested that the structure in

Figure 4.14

A contour map of the upper surface of the anomalous upper mantle for an assumed average velocity of 7.0 km/sec. Details are as given in Fig. 4.7.



the region north east of Kaptagat is well controlled by the data and the model satisfies the measurements to the limit of their reliability at the 95% confidence level. In the region to the west of the station there is good evidence to suggest that the anomaly dips progressively more gently westward although the details of the structure are not so well restrained by the data.

CHAPTER 5

P-WAVE DELAY TIMES

5.1. P-Wave Delay Time Observations

There are two methods of detecting the consistent late or early arrival of waves at a station. The first involves the location of the earthquakes from the arrival times at various stations (the single epicentre method); this technique has been developed by Douglas (1967) to locate several earthquakes simultaneously (the joint epicentre method) and has the advantage of correcting for source bias which is known to occur (Cleary and Hales, 1966, Herrin and Taggart, 1968). The time residuals from the location are then equivalent to delay times and by averaging the residuals at a particular station the mean delay may be found.

A more simple and direct method of measuring the delay time is to compare the travel time to a set of standard travel time tables such as Jeffreys-Bullen (1940) or Herrin et al (1968).

Although the delay time is relatively simple to calculate, it is much more difficult to define where the delay is occurring within the travel path. Long and Mitchell (1970) suggested that the delay caused by structure in the crust and upper mantle beneath the station could, to a large extent, be isolated by calculating the relative delay between two stations whose separation was considerably smaller than the distance between source or stations. They expressed the travel time residual as

$$R = T_o + T_e + T_t + T_s + E$$

where  $T_o$  is caused by errors in the focal data  
 $T_e$  is caused by anomalous crust or mantle beneath  
source  
 $T_t$  is caused by errors in standard travel time tables  
 $T_s$  is caused by anomalous crust or mantle beneath  
the stations  
and  $E$  is caused by poor timing or mis-reading

The likely magnitudes of these effects, when using the relative delay technique, have been evaluated by Backhouse (1972) and are now briefly summarized.

### 1. Errors in Focal Data

Errors in timing will cancel on taking relative delays but errors on epicentral distance and focal depth will not. Using the figures of Davies and McKenzie (1969) (25 km error on location and 75 km error on focal depth) it is found that an artificial relative delay of 0.8 sec can be caused by mislocation and the focal depth error may produce an apparent delay of up to 0.7 sec.

### 2. Source Effects

Anomalies caused by source effects should to a good approximation cancel if the lateral variations of structure at source are not too rapid. In certain circumstances this is likely; for example, Davies and McKenzie (1969) suggest that the descent of cold plates of oceanic lithosphere into the hot mantle could produce a 'fast' plane and thus cause a negative delay for certain azimuths.

### 3. Errors in Travel Time Tables

Several studies have shown that residuals obtained using Herrin's Tables are smaller than those obtained with Jeffreys-Bullen Tables (Long and Mitchell, 1970, Fairhead,

1968). However most tables tend to have a similar shape and differ mainly in a small d.c. component (Lilwall and Douglas, 1970, Cleary and Hales, 1966) which should cancel on using relative delays.

#### 4. Poor Timing and Misreading

It has been suggested (Stefansson, 1967) that positive delays are caused by the loss of first arrivals in noise. By choosing only those records with good onsets this effect was considered to be small. Also it was not thought that errors due to variations in the recording or playing out of the records could be as substantial as those already discussed.

#### 5. Lateral Variations in the Lower Mantle

A further term which may be added in view of recent work is the effect of lateral variations which are found to occur within the lower mantle (Greenfield and Sheppard, 1969, Powell, 1975). While these have been shown to exist it is not yet possible to quantify their effect although the general applicability of the delay time concept shows that the effect is not, in general, large.

It can thus be seen that relative delays can be contaminated with considerable errors and this must be borne in mind when interpreting delay time data.

### 5.2. Delay Time Studies in Africa

Studies have shown that P-wave delay times associated with stations in Africa exhibit considerable variation. Using the joint epicentre method, Lilwall and Douglas (1970) obtained mean residuals for stations in Africa as shown in Table 5.1. It can be seen that Addis Ababa (AAE) and Nairobi (NAI) show positive delays of about two seconds. Lwiro (LWI), associated with the western rift, shows a smaller positive delay, while

Bulawayo (BUL) and Pretoria (PRE), associated with shield structure, show negative delays. Studies by Herrin and Taggart (1968) and Cleary and Hales (1966) show similar results and these are given in Table 5.1. Equivalent relative delays are given in Table 5.2.

Sundaralingham (1971) measured P-wave delays for several African stations relative to Bulawayo and these are listed in Table 5.2; a similar trend as described above is found. Colley (1973) found the relative delay between Kaptagat and Nairobi to be -0.43 sec and suggested that this indicated a greater thickness of anomalous material beneath Nairobi than Kaptagat. Finally, Backhouse (1972) has shown that the relative delay between Kaptagat and Bulawayo is 2.20 sec.

Two conclusions may be drawn from this data. First, although individual measurements are subject to considerable errors, the averages produce consistent results. Secondly, stations associated with shield areas in Africa give a small negative delay indicating higher than average crustal and upper mantle velocities; regions associated with the eastern rift give positive delays in the order of two seconds confirming the presence of anomalously low velocity material beneath the rift, while Lwiro on the western rift gives a smaller positive delay suggesting that this anomalously low velocity material is not so well developed beneath the western rift.

### 5.3. Delays between Kaptagat and Bulawayo

It is proposed to interpret the delay times measured by Backhouse in the light of the models proposed in chapter four. The data set consists of 78 measurements of relative delay

Table 5.1

Station Residuals for Various African Stations.

(1) Lilwall and Douglas (1970) - Joint Epicentre Method.

AAE	.20	±	0.32 (sec)
BUL	-0.53	±	0.35
LWI	0.78	±	0.37
NAL	1.88	±	0.35
PRE	-0.42	±	0.47

(11) Herrin and Taggart (1968) - Single Epicentre Method.

AAE	1.12 (sec)
BUL	-0.45
LWI	0.36
WIN	-0.99

(111) Cleary and Halos (1966) - Single Epicentre Method.

AAE	1.5 (sec)
BUL	0.0
LWI	-0.2
WIN	0.3

Table 5.2

Relative Delays Between Various African Stations.

(i) Sundarlingham (1971) - Herrins tables as standard.

$$\begin{aligned} \text{BUL} - \text{AAE} &= 2.7 \pm 0.3 \text{ (sec)} \\ \text{BUL} - \text{NAI} &= 2.3 \pm 0.3 \\ \text{BUL} - \text{LWJ} &= 1.1 \pm 0.3 \end{aligned}$$

(ii) Lilwall and Douglas (1970) - Joint Epicentre Method.

$$\begin{aligned} \text{BUL} - \text{AAE} &= 2.73 \pm 0.67 \text{ (sec)} \\ \text{BUL} - \text{NAI} &= 2.41 \pm 0.70 \\ \text{BUL} - \text{LWI} &= 1.31 \pm 0.72 \end{aligned}$$

(iii) Herrin and Taggart (1968) - Single Epicentre Method.

$$\begin{aligned} \text{BUL} - \text{AAE} &= 1.57 \text{ (sec)} \\ \text{BUL} - \text{LWI} &= 0.81 \end{aligned}$$

(iv) Cleary and Hales (1966) - Single Epicentre Method.

$$\begin{aligned} \text{BUL} - \text{AAE} &= 1.5 \text{ (sec)} \\ \text{BUL} - \text{LWI} &= 0.3 \end{aligned}$$

(v) Backhouse (1972) - Herrin's Tables as standard.

$$\text{KAP} - \text{BUL} = -2.20 \pm 2.00 \text{ (sec)}$$

(vi) Colley (1972) - Herrin's Tables as standard.

$$\text{KAP} - \text{NAI} = +0.43 \pm 0.17 \text{ (sec)}$$

between Kaptagat and Bulawayo; a mean delay of  $2.20 \pm 2.00$  sec is found with the error being the 95% confidence limit. These values have been derived relative to Herrin's travel times and corrections have been applied for the earth's ellipticity (Bullen, 1956, Young and Gibbs, 1968), the heights of both stations and also for the angle of emergence so that a vertical travel time anomaly is defined.

It has been suggested that the errors on the focal data could introduce a maximum error of 1.5 sec and the picking lists at Bulawayo are given to the nearest second thus allowing an error of 0.5 sec so that an error, at the 95% confidence level, of 2 sec although large is not unreasonable. Furthermore, the concept of classifying the structure beneath Kaptagat by a single delay time is questionable when the various models which have been proposed are considered. Each raypath sees a different part of the anomaly and the 78 measurements should, in theory, be considered individually. Thus the large apparent error could, in part, be reflecting the complexity of the structure beneath the array.

Backhouse showed that, at the 95% confidence level, there was no significant variation of delay time with azimuth if a variation of the form

$$T_k = A + B \cdot \sin(\alpha_k + U) \quad (\text{equation 1-(111)})$$

is assumed. This variation models the effects of a plane dipping interface and has been used by several authors (Herrin and Taggart, 1968; Bolt and Nuttli, 1966, Lilwall and Douglas, 1970) although it has been criticized by Davies and McKenzie (1969) who argued that a short spherical harmonic series would be more appropriate than a sinusoidal variation.

Moreover, it has been shown in chapter three that the array anomalies cannot be explained by any set of plane interfaces and the models put forward by Backhouse give rise to delays which do not vary sinusoidally with azimuth (Nuttli and Bolt, 1969). Hence the analysis should not be considered as indicative of structure but rather of the general behaviour of the data.

An analysis of the delay times caused by the wedge models was given by Backhouse and discussed in section 1.2.6., where it was shown that these models produced travel time residuals which were strongly dependent on azimuth. In these calculations, the effect of the deviation of the ray was not considered although it was decided that it could produce an increase in the delay of 0.6 sec. It will be shown that this effect cannot be disregarded and must be considered as an essential part of the calculation.

The delay times are given in Table 5.3. and in these values no correction is made for the angle of incidence of the wave. The locations of the events are shown in the azimuth-distance plots of Fig.5.1. and the same problems of distribution found with the slowness data are apparent.

As would be expected from the previous discussion (section 5.1.) individual measurements from the same region show considerable scatter. For example, events 38, 39, 40, 43, 44, 45 and 46 are all located within  $0.1^{\circ}$  of latitude and  $0.1^{\circ}$  of longitude and are all given the same focal depth of 33 km yet the delays vary between 1.3 sec (event 43) and 4.1 sec (event 44); the average delay for the group is 2.7 sec with a standard error of 0.28 sec. Consequently, it was considered necessary to divide the data into the groups

Table 5.3

Delay Time Data.

D. 1. - Delay at Kaptagat.

D. 2. - Delay at Bulawayo.

D. Total - Relative delay between Kaptagat and Bulawayo.

Event	Lat.	Long.	Delta (degrees)	Azimuth	D.1. (sec)	D.2. (sec)	D.Total (sec)	Group
1	37.55	48.98	39.0	17.2	3.7	1.5	2.2	A
2	10.83	125.39	89.8	79.2	3.1	0.8	2.4	F
3	-43.14	41.66	43.8	173.4	6.3	3.6	2.7	H
4	36.47	70.47	48.3	38.5	3.0	1.1	1.9	A
5	49.96	77.76	61.1	29.8	3.4	1.3	2.1	A
6	25.71	83.50	56.9	59.3	3.6	1.7	1.9	C
7	- 8.83	118.51	83.5	98.9	2.9	1.9	1.0	F
8	-56.01	- 27.51	75.6	211.1	5.8	1.9	3.9	G
9	29.88	77.80	55.0	39.3	2.7	-0.1	2.8	A
10	26.02	95.40	63.0	60.9	3.3	0.6	2.7	C
11	37.82	55.88	41.7	24.6	2.7	1.5	1.2	A
12	14.26	51.84	21.2	49.0	1.9	0.2	1.7	B
13	2.60	97.98	62.5	87.3	3.3	0.5	2.8	E
14	11.86	- 43.74	79.3	281.9	4.0	1.2	2.8	I
15	1.15	126.11	90.6	88.9	4.3	1.8	2.5	F
16	41.10	19.77	42.9	342.5	2.9	0.8	2.1	D
17	0.32	122.20	86.7	80.8	4.6	1.9	2.7	F
18	18.10	120.47	85.1	72.0	2.8	-0.4	3.3	F
19	- 8.02	107.39	72.2	95.5	5.2	1.5	3.7	E
20	1.80	94.56	59.1	88.2	6.0	2.4	3.7	F
21	36.58	70.11	48.2	27.9	4.3	1.1	3.2	A
22	14.83	55.76	23.1	50.0	-0.6	0.3	-0.9	B
23	37.04	71.38	49.3	38.5	3.4	2.7	0.7	A
24	49.77	78.08	61.1	30.1	2.4	1.9	0.5	A
25	0.94	100.19	64.7	89.2	3.6	1.8	1.7	E
26	- 0.57	121.83	86.4	90.6	2.2	-0.0	2.2	F
27	36.42	70.07	48.1	38.0	4.3	1.3	3.1	A
28	-23.19	37.29	23.9	175.5	5.5	3.3	2.0	H
29	-23.47	37.18	23.3	175.1	4.1	4.4	-0.3	H
30	51.12	- 29.95	74.2	323.6	2.7	0.7	2.0	O
31	-43.23	41.48	43.8	173.6	5.2	0.7	4.5	H
32	-56.92	- 27.29	75.6	216.8	5.1	1.3	3.8	G
33	34.96	13.67	39.9	131.6	4.6	2.3	2.4	D
34	- 3.59	86.16	50.8	95.0	3.3	0.0	3.3	E
35	73.32	55.15	73.8	5.8	3.5	0.9	2.6	O
36	74.62	8.41	75.8	352.8	2.4	2.3	0.1	O

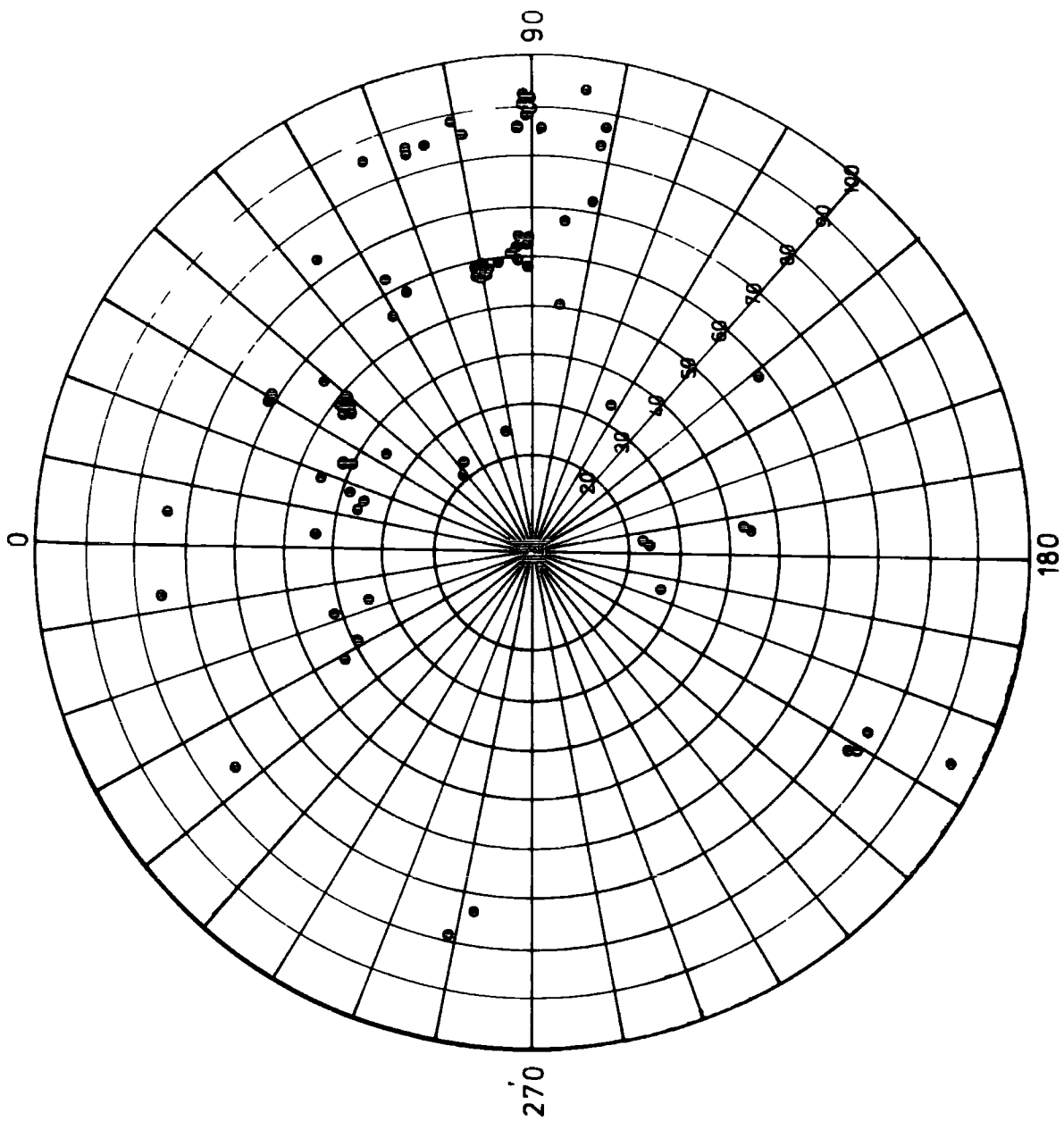
Table 5.3 - continued

Delay Time Data.

Event	Lat.	Long.	Delta	Azimuth	D.1.	D.2.	D.Total	Group
			(degrees)	(degrees)	(sec)	(sec)	(sec)	
37	7.66	- 37.60	73.1	277.8	3.4	2.3	1.1	T
38	9.06	94.02	58.9	79.8	5.1	2.1	3.0	E
39	9.02	94.02	58.9	79.8	4.9	2.6	2.3	E
40	9.11	94.04	58.9	79.7	4.2	2.2	2.0	E
41	36.77	45.13	37.2	12.9	3.4	2.7	0.7	A
42	-13.69	66.26	33.6	115.9	3.3	1.1	2.2	O
43	9.02	93.87	58.8	79.8	3.5	2.2	1.3	E
44	8.97	94.00	58.9	79.9	3.9	1.8	4.1	E
45	8.98	94.08	59.0	79.8	5.4	2.3	3.1	E
46	9.15	94.06	59.0	79.7	4.4	1.1	3.4	E
47	-40.09	80.55	58.0	140.7	1.5	0.7	0.8	O
48	18.51	120.88	85.5	71.6	3.2	-0.8	4.0	F
49	29.52	56.85	55.4	33.3	4.1	0.8	3.3	A
50	36.91	71.62	49.3	38.6	4.2	1.6	2.6	A
51	22.71	121.34	86.0	67.4	3.6	1.2	2.4	O
52	14.25	120.10	84.7	75.1	3.4	2.4	1.0	F
53	6.49	94.70	59.4	82.8	4.5	1.5	3.0	E
54	36.94	9.73	43.4	329.6	3.0	-0.1	3.7	D
55	0.70	124.93	89.5	89.3	3.8	1.3	2.6	F
56	35.90	105.49	73.6	52.7	2.5	1.2	1.3	C
57	43.78	39.15	45.3	3.9	3.6	1.8	1.8	A
58	0.04	124.49	89.0	90.0	4.0	1.0	2.9	F
59	- 6.27	130.14	94.7	96.2	2.8	1.0	1.8	F
60	2.39	94.88	59.4	87.5	4.0	0.6	3.5	E
61	43.85	54.77	46.5	19.3	4.2	1.9	2.3	A
62	- 4.25	103.37	68.0	94.7	2.6	1.1	1.4	E
63	2.02	126.46	91.0	88.0	3.0	1.4	2.5	F
64	34.10	24.01	35.4	343.6	3.2	1.5	1.7	D
65	35.06	46.92	36.1	16.1	4.7	2.4	2.4	A
66	5.72	61.24	26.3	73.0	5.5	2.5	3.1	B
67	- 7.80	122.67	87.3	97.8	2.5	0.6	1.9	F
68	1.66	126.58	90.9	88.3	2.8	-0.2	2.9	F
69	-26.02	27.94	27.3	194.9	3.1	1.2	1.9	H
70	1.28	99.10	63.7	88.1	3.4	0.9	2.5	F
71	23.76	91.76	59.2	62.5	2.4	0.9	1.5	C
72	0.65	96.84	63.4	89.5	2.2	-1.8	4.0	E
73	2.19	126.59	91.4	87.8	3.5	3.4	0.1	F
74	-63.45	- 61.22	93.4	206.6	5.1	2.6	2.5	G
75	1.48	121.28	85.8	88.6	2.9	0.0	2.9	F
76	36.56	55.63	40.5	25.3	4.3	0.6	3.6	A
77	-59.78	- 26.43	76.6	207.3	6.1	2.7	3.5	C
78	3.24	95.93	60.5	86.6	3.6	0.7	2.9	E

Figure 5.1

Locations, on a distance - azimuth plot, of events used in delay time study, locations are relative to Kaptagat.



shown in Fig.5.2., the mean values of the delays for the groups together with the standard errors and 95% confidence limits are given in Table 5.4. It can be seen that the most reliable data may be expected from groups A, C, E, F and G while the scatter on the other groups is such as to make any interpretation unconvincing. Consequently detailed interpretation will be restricted to the above five groups.

#### 5.4. Methods of Interpretation

This analysis is concerned with deriving the delay time at a single station relative to standard travel times. The structure at Bulawayo will be assumed to be that given by the AFNIC model of Gumper and Fomeroy (1970) and delays for such structures may be easily calculated.

The aim is to derive a method for calculating the delay caused by the three dimensional structures discussed in chapter four. It is proposed to illustrate the general properties of such delays with reference to simple two dimensional models in order to estimate the magnitude of various effects.

##### 1. A Plane Layer in Two Dimensions

The problem is illustrated in Fig.5.3. where a low velocity layer with velocity  $V_1$  and thickness  $L$  occurs within a medium with velocity  $V_n$ . The ray which arrives at the station  $K$  is indicated by the solid line and the broken line indicates the travel path of this ray if the layer were not present i.e. this ray travels with velocity  $V_n$ . The times  $t_2$  and  $t_2'$  refer to the travel times of the observed ray within the given layers and  $t_1$  and  $t_1'$  refer to the hypothetical undeviated ray.

Figure 5.2

Grouping of events used in delay time study, letters identify groups and numbers identify the numbers of events in each group.

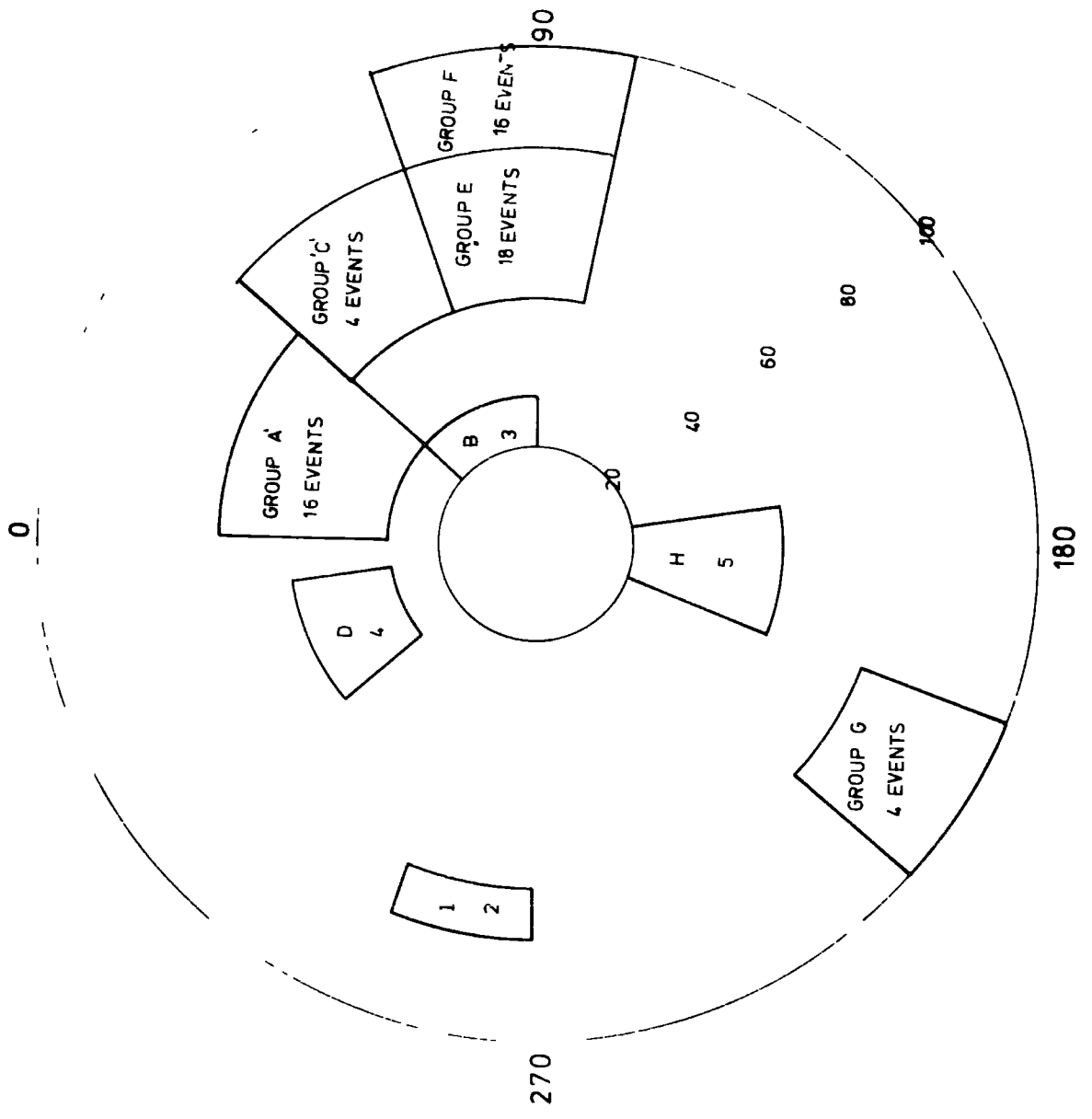


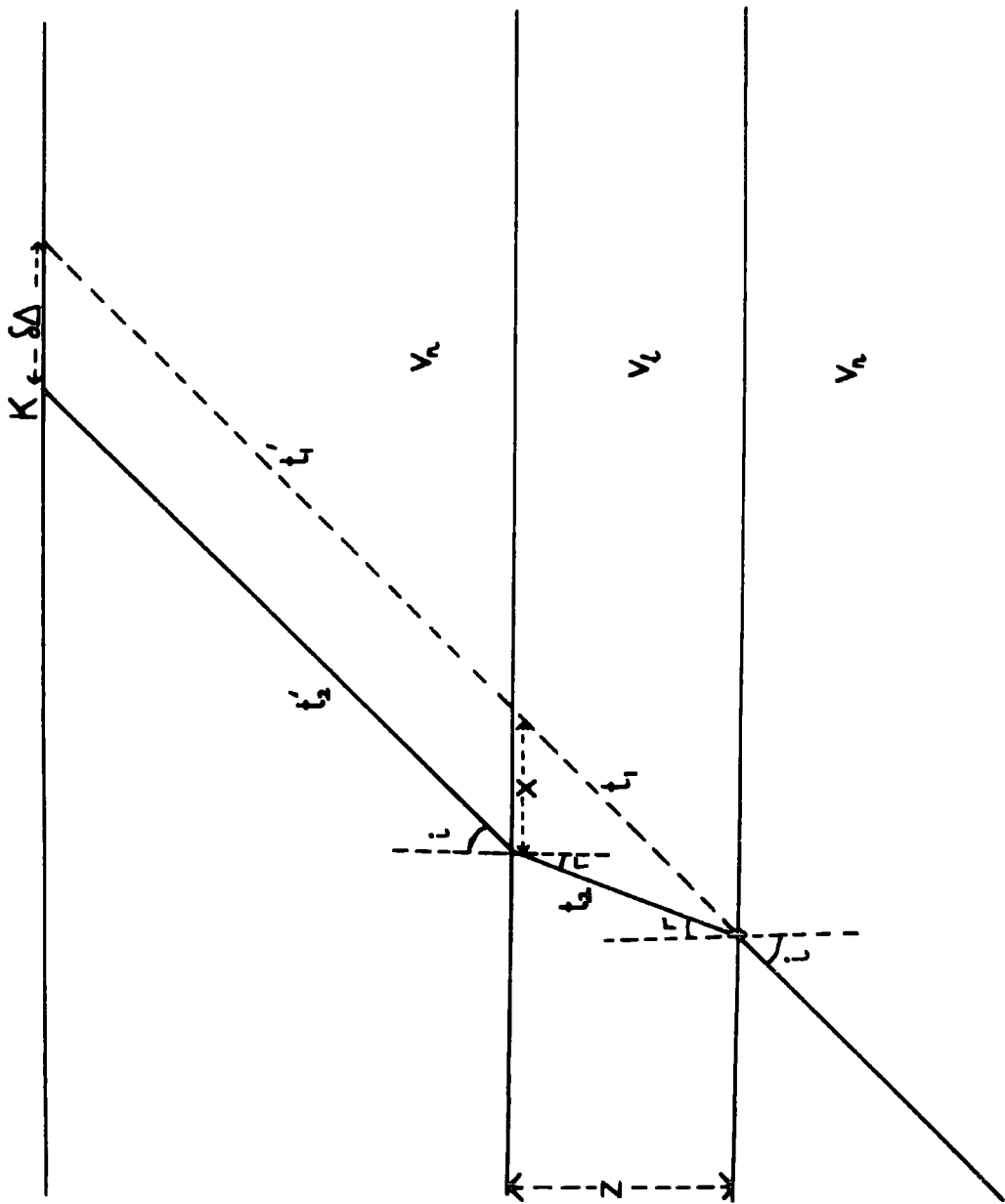
Table 5.4

Group Delay Times.

Group	No. Events	Delay (sec)	Standard Error (sec)	95% Confidence Limit (sec)
A	16	2.15	0.24	2.04
B	3	1.30	0.96	7.15
C	4	1.85	0.27	1.72
D	4	2.48	0.38	2.42
E	16	2.87	0.20	1.79
F	16	2.29	0.23	1.96
G	4	3.43	0.28	1.78
H	5	2.16	1.21	7.52
I	2	2.00	0.60	10.78

Figure 5.3

Diagram to illustrate the delay time calculation  
for the case of a plane parallel layer.



If the distance from source to detector is  $\Delta^0$  and the standard travel time and slowness are  $T$  and  $dT/d\Delta$  then the travel time from source to hypothetical detector of the wave including the broken line is

$$T' = T + \frac{dT}{d\Delta} \cdot \delta\Delta \quad 5-(1)$$

to a first approximation if  $\delta\Delta \ll \Delta$ . The travel time to the station of the actual arrival is given by

$$\left[ T + \frac{dT}{d\Delta} \cdot \delta\Delta \right] - (t_1 + t_1') + (t_2 + t_2')$$

Because plane layering is assumed

$$t_1' = t_2'$$

and since the expected travel time is  $T$  and delay  $D$  may be written

$$D = \left( \frac{dT}{d\Delta} \right) \cdot \delta\Delta + (t_2 - t_1) \quad 5-(ii)$$

and it may be shown that

$$\delta\Delta = Z \cdot (\tan i - \tan r) \quad 5-(iii)$$

$$t_2 = \frac{Z}{V_1 \cdot \cos r} \quad 5-(iv)$$

$$t_1 = \frac{Z}{V_n \cdot \cos i} \quad 5-(v)$$

whence equations 5-(ii) to 5-(v) enable the delay to be written

$$D = \left( \frac{dT}{d\Delta} \right) \cdot Z \cdot (\tan i - \tan r) + Z \left( \frac{1}{V_1 \cdot \cos r} - \frac{1}{V_n \cdot \cos i} \right) \quad 5-(vi)$$

$$= d_1 + d_2$$

$d_1$  is a deviation effect and causes the observed ray to travel via a different path than the 'theoretical' arrival and  $d_2$  represents the delay caused by a travel path within the low velocity layer.

To evaluate the relative importance of these effects consider

as an example a structure similar to that proposed for the upper mantle beneath Iceland (Tryggvason, 1964) where  $V_1 = 7.4$  km/sec,  $V_n = 8.1$  km/sec and  $Z = 200$  km. The resulting values for various distances are shown in Fig.5.4. It is clear that both terms are significant in evaluating delay times. Considering the deviation effect, an increase in distance causes a decrease in the angle of incidence and this has been shown (section 3.5.) to decrease the deviation and thus the delay associated with this term. The reverse effect is however true for the delay  $d_2$ . As the incident angle increases (distance decreases) the path length in the high velocity medium increases more rapidly than that in the low velocity medium so that the delay decreases. The net effect is that, although both terms are quite strongly distance dependent, the total effect is to produce a delay which is relatively insensitive to distance. It is worth remarking that both effects are directly proportional to  $Z$  and thus they have the same relative weight for all thicknesses.

## 2. Structures with Dipping Interfaces

It may be noted that in the previous case the ray will always be 'pulled in' by the anomalous low velocity layer and thus the actual ray will travel a deeper and longer path before entering the zone than the theoretical ray. Fig.5.5. shows that this is no longer necessarily true when dipping boundaries are considered. The effect of the first refraction is again to pull the ray inward; however, whereas in the

Figure 5.4

Delay caused by a plane parallel layer,

$d_1$  is the delay caused by the deviation of the ray

$d_2$  is the delay caused by the travel path within  
the layer

and the total delay is the sum of these terms.

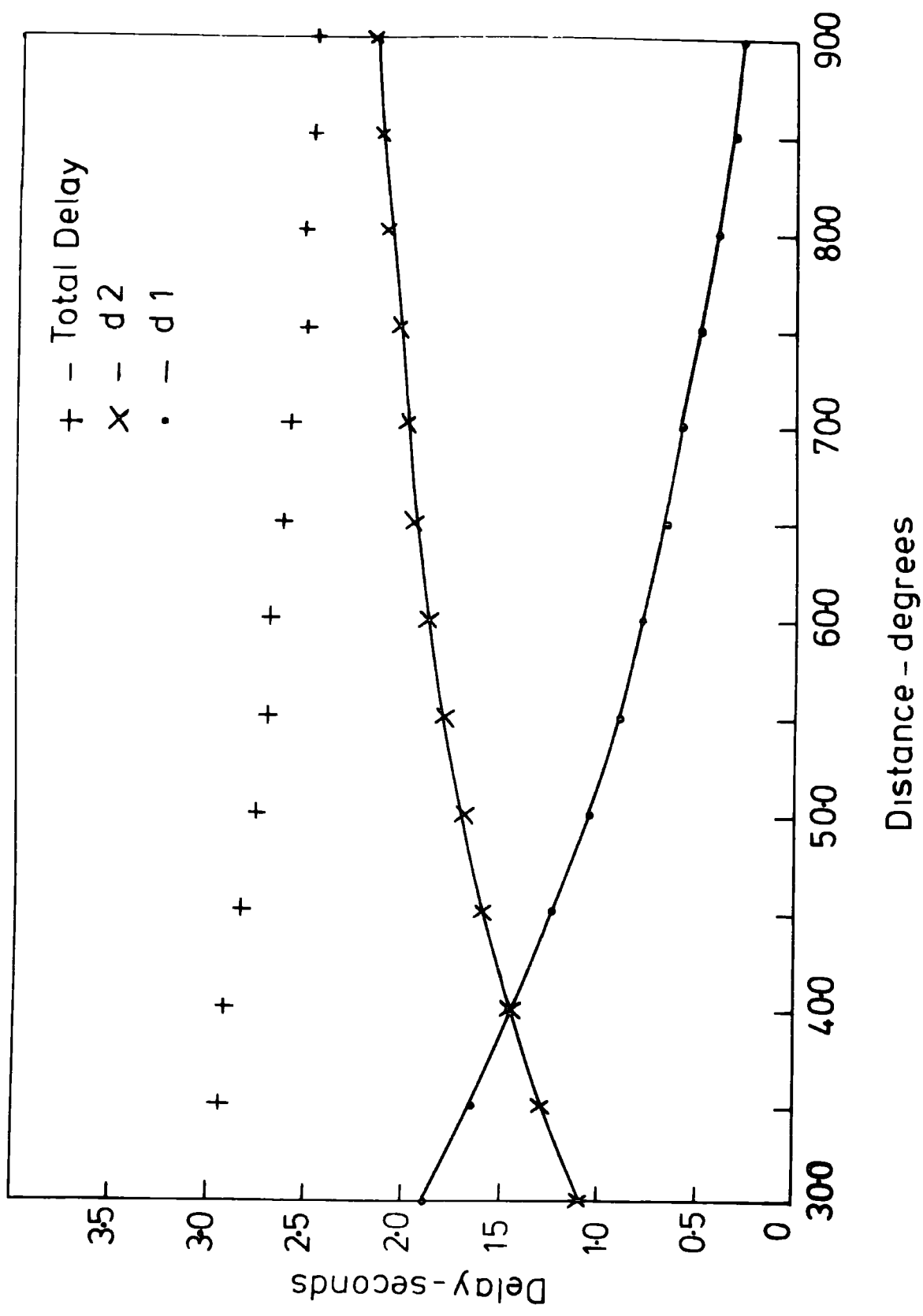
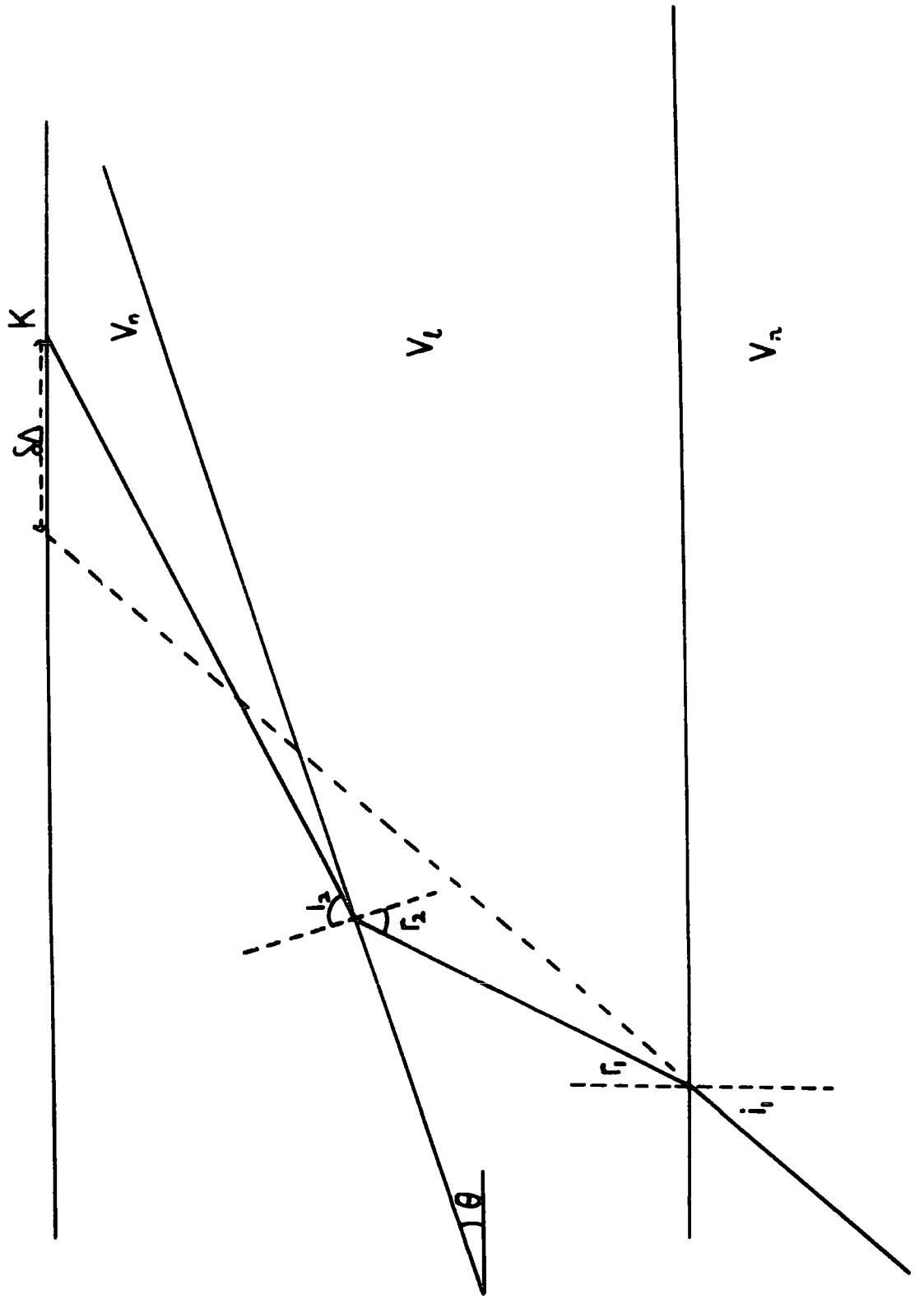


Figure 5.5

Diagram to illustrate the delay time calculation  
for the case of a single dipping interface.



previous case  $r_2 = r_1$ , we now have  $r_2 = r_1 + \theta$  where  $\theta$  is the angle of dip. Consequently  $i_2 > i_1$  and it is possible that the observed ray now takes a shallower path than the theoretical ray and equation 5-(1) now becomes

$$T = T - \left( \frac{dT}{d\Delta} \right) \cdot \delta\Delta$$

This effect could, in theory, become very large when  $i_2$  approaches  $90^\circ$  and the arrival tends to a headwave.

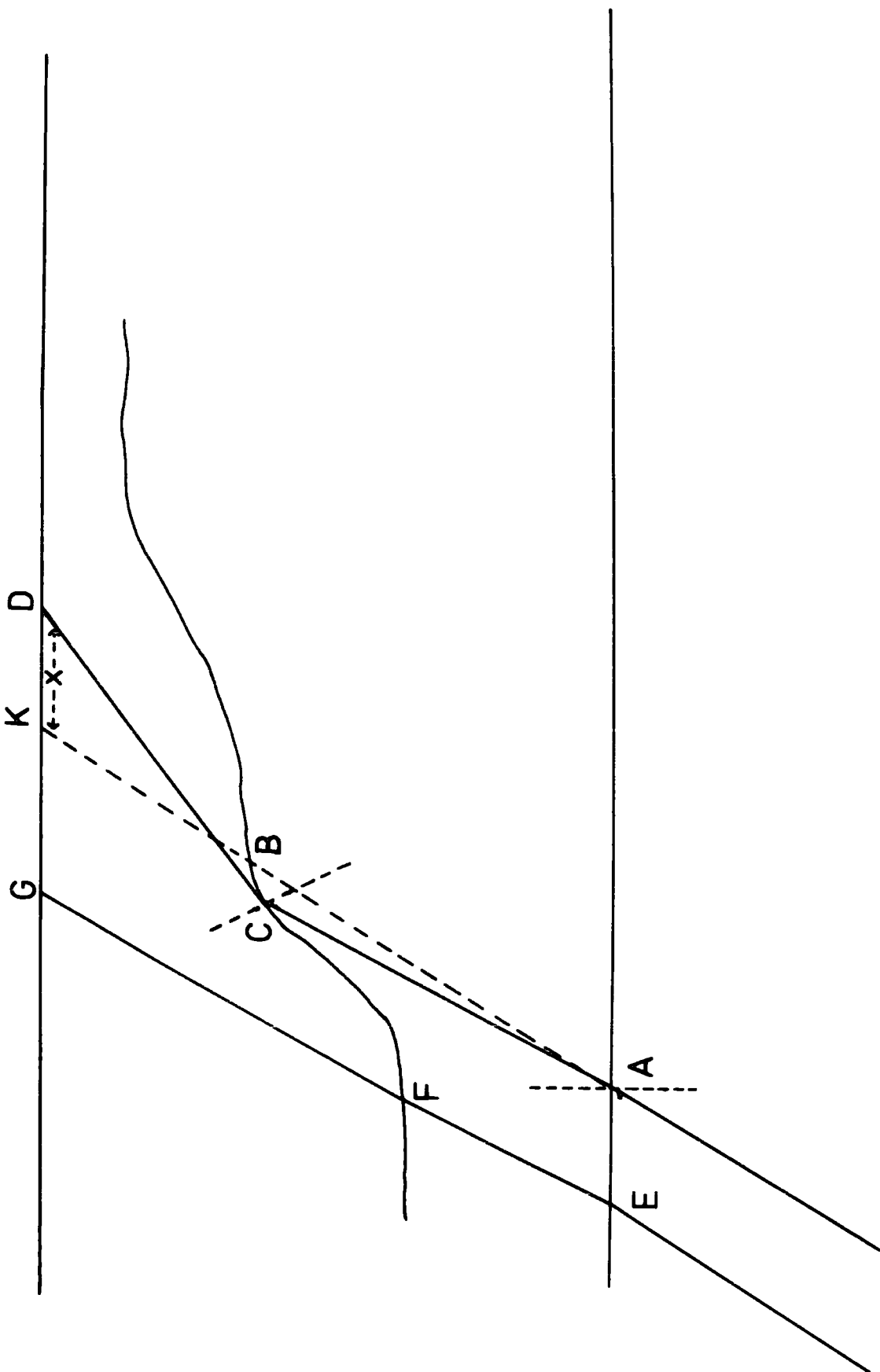
The ray tracing so far has been from the station to the source and the reverse problem is more common, given an event at distance  $\Delta$  from azimuth  $\alpha$  calculate the observed delay time. It is straightforward to calculate the point on the bottom surface at which the ray, if undeviated, hits in either of the two previous cases. The ray may be traced through the structure and the deviation  $\delta\Delta$  calculated. The whole raypath may now be shifted by this amount and the delay calculated. Unfortunately, the angle  $i$  at which the ray hits the bottom interface has now changed (it will now have a slightly different slowness) and on tracing through the structure will miss the station. The shift  $\delta\Delta'$  may be applied and the process converges very rapidly because  $i$  varies very slowly within the distance variation considered and a solution is rapidly found.

### 3. Structures with Curved Interfaces

The problem just considered becomes rather more complicated on considering curved interfaces and is illustrated in Fig.5.6. The undeviated ray passes through A and B and arrives at K. On tracing the ray through the structure it passed through A, C and D a distance  $x$  from K. The ray is therefore traced from E where  $EA = KD$  but now the angle of

Figure 5.6

Diagram to illustrate the delay time calculation  
for a single curved interface.



incidence at F will not be related to that at C. In fact, for surfaces which behave in a reasonable manner the problem is not so difficult although the iterative process required is considerably more complex.

#### 4. Structures with Curved Interfaces in Three Dimensions

The problems which have arisen in the previous cases also occur in three dimensions but they are rather more difficult to visualize. In addition the problems of refraction in three dimensions must be considered, effectively the ray will become twisted on refraction and the iteration process has to locate the station on the plane of the surface.

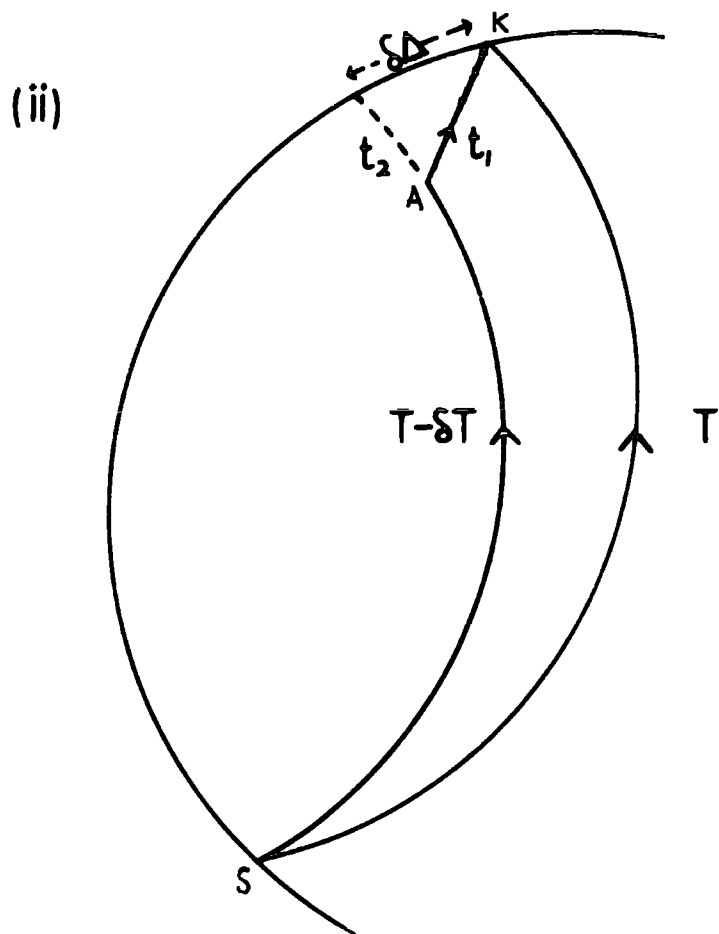
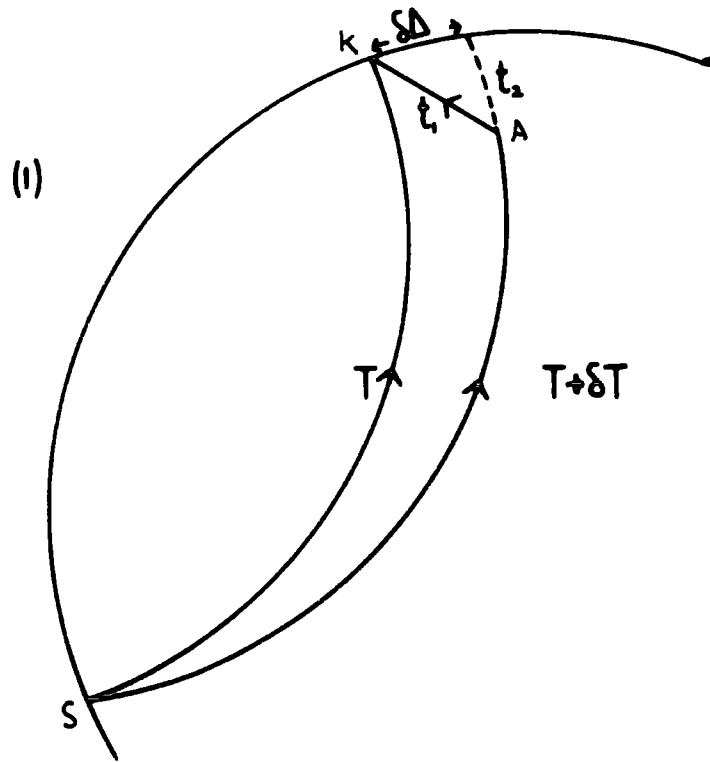
Since the data had been grouped as shown in Fig.5.2. it was decided that a full calculation using the iterative methods described was not justified and a simpler approach to the problem was made. Although it is difficult to calculate the delay for an event from a given distance and azimuth it is relatively easy to calculate the delay for an event which arrives at a station with a given slowness and azimuth. Moreover, by tracing the ray through the anomaly it is possible to calculate the point from which the ray originated. Hence, the general pattern of the delays caused by the structure may be found and compared with the overall pattern illustrated in Fig.5.2.

Equation 5-(vi) may be generalized to three dimensions quite simply with reference to Figs.5.7(1) and 5.7(11). The ray travels from S to K and the effect of the anomalous body is to deviate the ray at A. With reference to equations 5-(1) to 5-(v) the delay is given by

$$D = \pm \left( \frac{dT}{d\Delta} \right) \cdot \delta\Delta + (t_1 - t_2) \quad 5-(v11)$$

Figure 5.7

Diagram to illustrate the delay time calculation for  
the three dimensional case.



Calculation of  $\delta\Delta$  is a little more difficult in three dimensions but an approximate method is illustrated in Fig.5.8. A wave arrives at the origin O from S and its expected azimuth is  $\phi$ . The undeviated ray takes a deeper path and arrives at P(x,y) at an azimuth  $\theta$  relative to the origin. If  $|\theta - \phi| > \frac{\pi}{2}$  then the undeviated ray has a greater path length and  $\frac{dT}{d\Delta} \cdot \delta\Delta$  is positive. If  $|\theta - \phi| < \frac{\pi}{2}$  then the undeviated ray has a shorter ray path and makes a negative contribution to the delay time. Now SO and SP will be much greater than OP and  $\delta\Delta = |SP - SO|$  so to a very good approximation

$$\delta\Delta = OP \cdot \sin\left(\theta - \phi - \frac{\pi}{2}\right) \quad 5-(v111)$$

A computer program DELAY was written which calculated the delays caused by the structure proposed in chapter four and the results are now discussed.

### 5.5. Results

The purpose of these calculations is to show that the observed properties of the delay times are consistent with the models proposed on the basis of the slowness anomalies and also to attempt to put some form of constraint on the depth to the bottom of the anomalous body.

It has been shown in chapter three that, if the slowness anomalies are to be explained by a single interface, a maximum average velocity of 7.5 km/sec is allowed for the anomalous body. Assuming this velocity a maximum thickness may be determined, this velocity will also be used to illustrate the behaviour of the delay time as a function of azimuth and distance.

The optimum models derived in chapter four are used and the delay for each event within the groups is calculated

Figure 5.8

Diagram used to calculate the increase in path length  
for the three dimensional delay calculation.

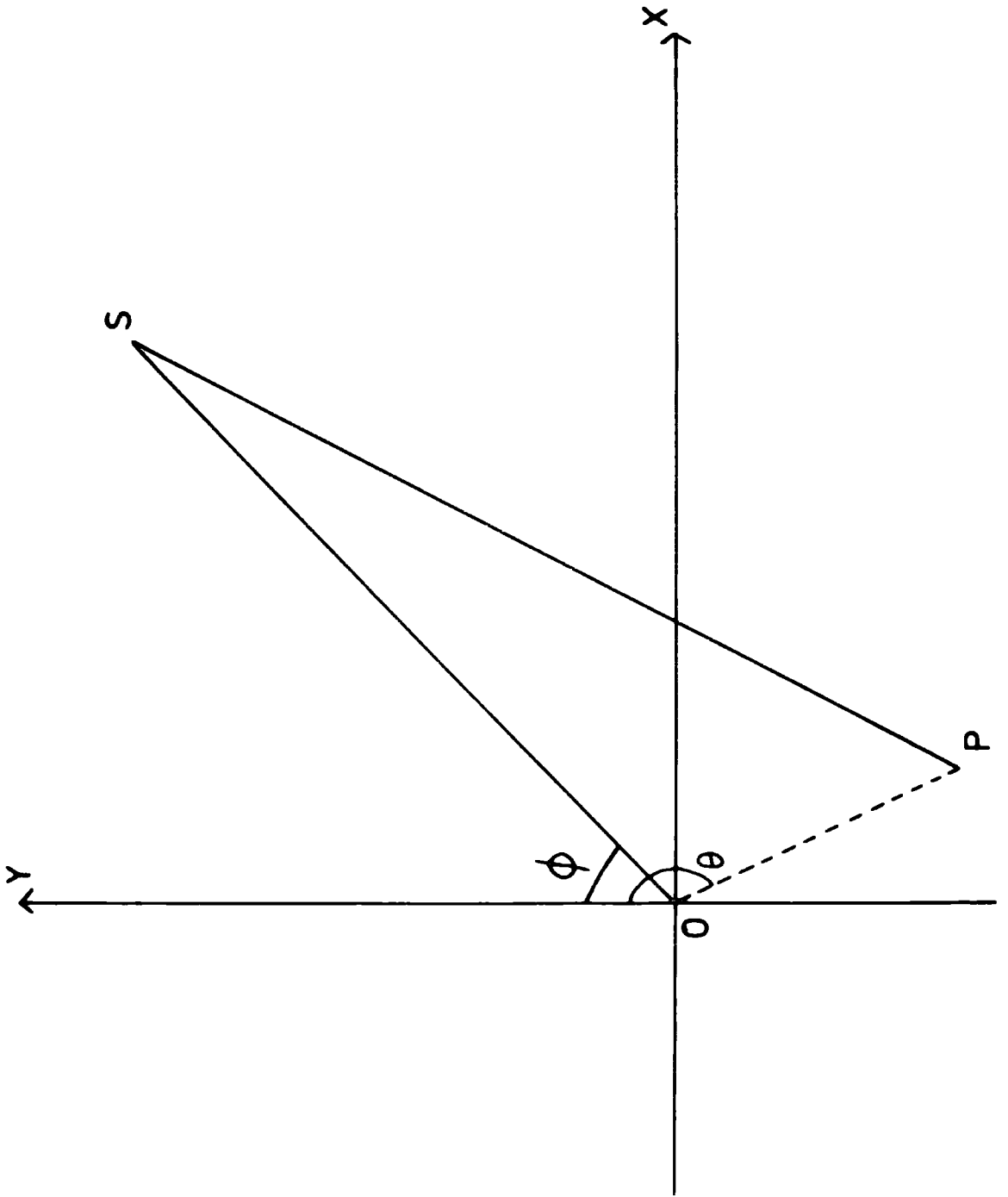


Table 5.5 - Observed and Calculated Group Delays.

<u>Velocity = 7.5 km/sec</u>		Observed Delay (sec)		Calculated Delay and Standard Error	
Group	Delay	Standard Error	60' Limit	300 km	350km
A	2.15	0.24	0.83	1.81 ± 0.07	2.68 ± 0.03
C	1.85	0.27	0.53	1.58 ± 0.07	2.26 ± 0.05
E	2.87	0.20	0.73	2.21 ± 0.06	3.06 ± 0.08
F	2.29	0.23	0.80	2.55 ± 0.03	3.44 ± 0.04

<u>Velocity = 7.3 km/sec</u>		Observed Delay (sec)		Calculated Delay and Standard Error	
Group	Delay	Standard Error	60' Limit	250 km	300km
A	2.15	0.24	0.83	1.41 ± 0.05	2.33 ± 0.03
C	1.85	0.27	0.53	1.29 ± 0.05	2.27 ± 0.11
E	2.87	0.20	0.73	2.11 ± 0.06	3.00 ± 0.07
F	2.29	0.23	0.80	2.39 ± 0.05	3.03 ± 0.02

individually, average group delays, together with apparent standard errors, are then calculated for various depths to the bottom interface. Sample results are given in Table 5.5.

The first point to note is that approximately one quarter of the observed standard error for each group can be attributed to structural complexity in the upper mantle beneath the rift. If a more realistic model were used, including a more complex velocity structure, it is likely that more of the scatter could be attributed to the anomalous mantle. Even though the scatter caused by error is now reduced it is difficult to place any meaningful restraint on the depths at the 95% confidence level but if the interpretation is reduced to the 60% confidence level useful conclusions may be drawn. At a velocity of 7.5 km/sec the maximum depth to the bottom of the anomaly is approximately 350 km and a minimum depth of somewhat less than 300 km is suggested. If the velocity is reduced to 6.8 km/sec then the optimum thickness is 160 km. a lower limit cannot be given because most rays miss such a shallow structure and a maximum depth of approximately 220 km is found.

The observed variation in delay time with azimuth is reflected in that found for the proposed model in that Group C shows lower delays than Groups A, E or F and Groups E and F show a larger delay than Group A. Although these variations are not significant at the 60% confidence level it is encouraging to find similar trends in both theory and observed delays.

Interpretation of Group G is difficult since neither the optimized model nor the extrapolated model cover this

region. Calculations made for the region between azimuths of  $90^{\circ}$  and  $180^{\circ}$  indicate that the theoretical delay increases steadily with azimuth and the delay for Group G does not appear inconsistent with the model.

This interpretation has been made at the 60% confidence level and thus conclusions are drawn with somewhat less confidence than earlier interpretations made at the 95% confidence level. Nevertheless if such limitations are accepted some important conclusions may be drawn

1. Models with steeply dipping boundaries are consistent with delay times which do not vary strongly with azimuth.

2. The models derived from teleseismic slowness data are consistent with the observed delay time data.

3. If an average velocity of 7.5 km/sec is assumed for the structure a maximum depth to the lower interface is placed at 350 km and a velocity of 6.8 km/sec produces an optimum depth of 160 km.

4. The large observed scatter may be ascribed, in part, to the structural complexities of the upper mantle beneath the rift.

In section 3.3. it was mentioned that the deviations caused by the structure and discussed in this chapter would cause the theoretical slowness to be in error. The maximum deviation found for the delays calculated was 35.3 km which may cause a maximum error in the theoretical slowness of 0.15 sec/deg at a distance of  $20^{\circ}$  and 0.01 sec/deg at a distance of  $100^{\circ}$ .

## CHAPTER 6

### VELOCITY FILTERING LOCAL EARTHQUAKES

#### 6.1. Introduction

This chapter will describe attempts made to identify a wave which has been reflected off the top surface of the structure, postulated in chapter four, in the secondary arrivals in local earthquake records. The possibility that such a phase did not exist or was of such low amplitude as to be unrecognizable was appreciated from the outset; for example, the transition between normal and anomalous mantle could occur over a distance large compared with the wavelength so that no reflections of significant amplitude would be produced or the angle of incidence to the structure could be such as to make the reflected amplitude negligible. In spite of such possibilities the attempt was made because of the importance of the data from such arrivals which when combined with the data from first arrivals from teleseisms would enable the structure to be defined with more confidence.

#### 6.2. Identification of the Anomalous Phase

A wave reflected from the interface could be identified by the following characteristics:

1. If the wave is reflected from a structure beneath the Moho it must arrive with a velocity greater than the Moho headwave and will be expected to have a velocity in excess of 8 km/sec.

2. A wave reflected from the structure will arrive with an azimuth different from that of the first arrival which is assumed to have travelled through normal crustal material (Events will be chosen which are likely to have such first arrivals).

Many of the multiply reflected and refracted arrivals will have an apparent velocity greater than 8 km/sec but if they have travelled through normal crust they should all have the same azimuth as the first arrival. Hence the most reliable indicator of the reflection was taken to be the arrival at an azimuth different from the primary azimuth; as a confirmation the velocity would be determined.

### 6.3. Velocity Filtering

Velocity and azimuth filtering techniques (Birtill and Whiteway, 1965; Whiteway, 1965) were used to search for the anomalous phase. Essentially this method involves the summation of individual seismometer channels after appropriate delays have been applied corresponding to the assumed velocity and azimuth of the arrival. Usually two partial sums are correlated and the maximum in the correlation coefficient provides a reliable estimate of the approximate velocity and azimuth although it is sensitive to signal interference and window positioning effects (King et al, 1973).

The technique was originally developed for the analysis of teleseismic signals and refinements have, in general, been concerned with the improvement of the recognition of such signals. The VESPA (Velocity Spectral Analysis) process (Davies et al, 1971) improved the velocity resolution of an event from a known azimuth and a sophisticated technique described by Capon et al (1967) effectively weighted each channel at different frequencies.

It appears that the process has not been so widely used (or so successful?) in the analysis of local earthquakes. McCamy and Meyer (1964) attempted to analyse a crustal

refraction experiment using velocity filtering techniques but found a profusion of second arrival correlations many of which could not be explained. King et al (1973) concluded that the density of arrivals for events closer than  $30^{\circ}$  made accurate resolution of velocity impossible.

#### 6.4. Velocity Filtering Problems

##### 6.4.1. Limits Imposed by the Array and Data Processing Facilities

In this section the limits imposed on the resolution of velocity and azimuth by the geometry of the array and the data processing capability will be analysed. It should be emphasized that these limits are those applicable to a plane wave crossing the array in the absence of noise and as such represent the best resolution available.

It is necessary as a preliminary to describe some of the data processing facilities, in so far as they are relevant to this study.

The velocity filtering process is carried out using a CTL Modular One computer with an 8K 16 bit word core store. The analogue array records are first digitized and store on either a fixed-head disc (for temporary use) or magnetic tape (for permanent use). The disc contains twelve fixed length files each of which provides space for approximately fourteen seconds of record digitized at 50 samples/second (or correspondingly more or less at different sampling rates) consisting of ten seismometer channels and one binary time code.

The executive, compiler and filters (programs) are within core store and the remaining room is allocated to the storage of data in time series channels. Each of the

seismograms is allocated a time series channel and the process of velocity filtering requires that positive or negative delays are applied to these channels. Consequently it is necessary to have sufficient samples in store at a given time to allow the necessary delays to be applied. It is clear that the number of samples required to be stored is directly proportional to the digitization rate.

It was found that for general use a rate of 50 samples/second allowed sufficient flexibility of operation and that 100 samples/second could be accommodated with some difficulty; any higher rate was not practicable.

In the routines available on the computer at the time of writing no interpolation is allowed between samples so that delays are applied to the nearest digit.

If a wave crosses an array with velocity  $V$  from azimuth  $\alpha$  (fig.1.4.) then the arrival time at a seismometer at  $(x_1, y_1)$  relative to a zero time at the origin is

$$t = \frac{(X_1 \cdot \sin \alpha + y_1 \cdot \cos \alpha)}{V}$$

(Carpenter, 1966).

If the seismogram is digitized at  $S$  samples/second the wave will arrive at the station at sample  $n$  where

$$\begin{aligned} n' &= t \times S \\ &= \frac{(X_1 \cdot \sin \alpha + y_1 \cdot \cos \alpha)}{V} \cdot S \end{aligned} \quad 6-(i)$$

and  $n$  is the digit nearest  $n'$ . A quantity of importance is the rate at which these digits change for each seismometer or more precisely the relative rate at which they change for

either a change in velocity or azimuth. This is given by

$$\left(\frac{\partial n'}{\partial v}\right)_\alpha = \frac{(X_1 \cdot \sin \alpha + y_1 \cdot \cos \alpha)}{v^2} \cdot S \quad 6-(11)$$

for a fixed azimuth; similarly

$$\left(\frac{\partial n'}{\partial \alpha}\right)_v = \frac{(X_1 \cdot \sin \alpha + y_1 \cdot \cos \alpha)}{v} \cdot S \quad 6-(11i)$$

for a fixed velocity.

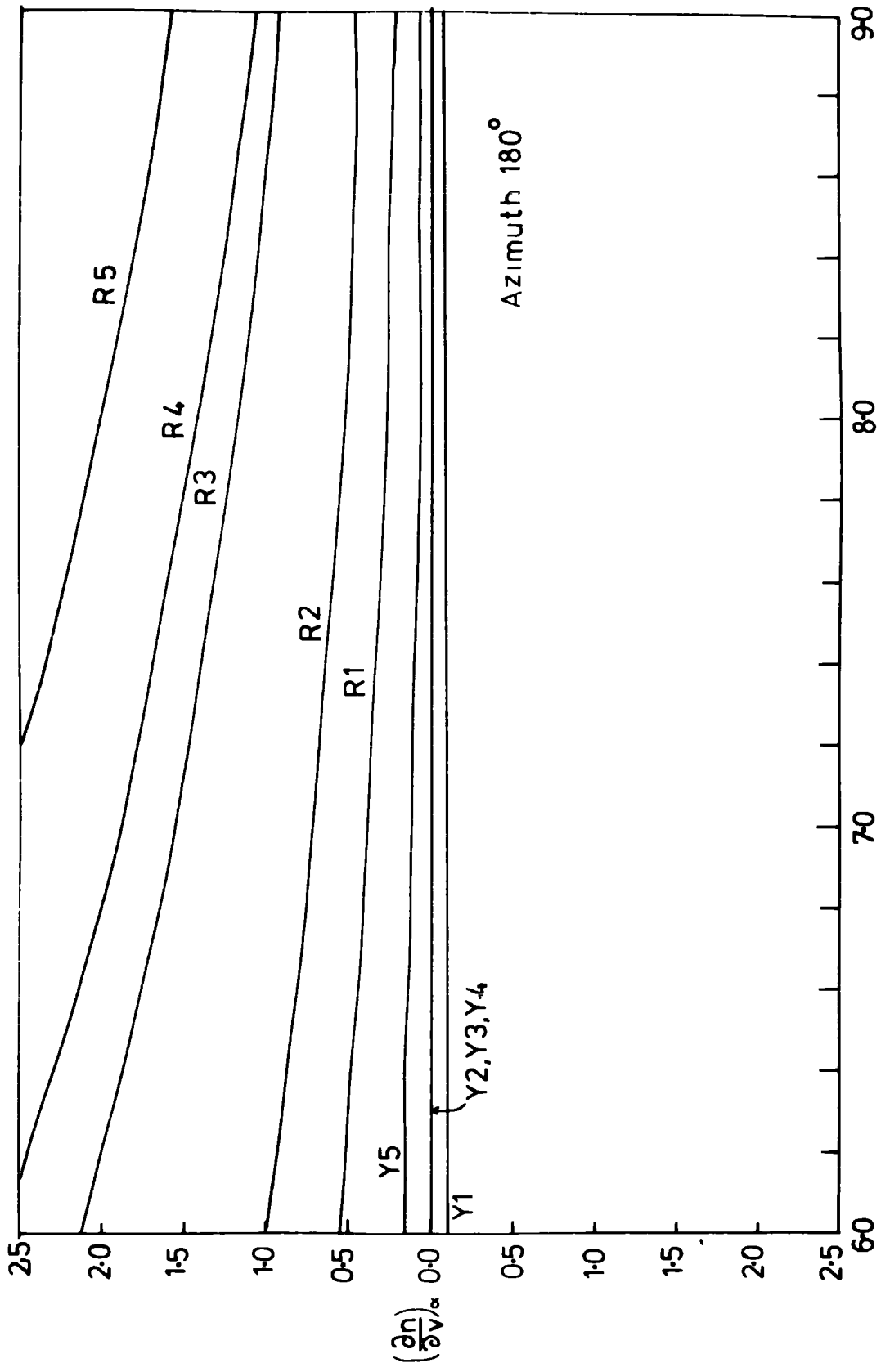
These equations enable the sensitivity of the array, to changes in both velocity and azimuth, to be determined for any velocity and azimuth. As examples Fig.6.1. shows the variation of  $\left(\frac{\partial n'}{\partial v}\right)_\alpha$  with velocity for an azimuth of  $180^\circ$  and Fig.6.2. shows the variation of  $\left(\frac{\partial n'}{\partial \alpha}\right)_v$  with azimuth for a velocity of 8 km/sec; both are calculated for a digitization rate of 25 samples/second.

Fig.6.1. enables the response in changes of velocity to be determined; it shows that the gradients for the yellow line are approximately equal throughout the velocity range considered indicating that the same samples are used to calculate the correlation at 6 km/sec as at 9 km/sec. The red line indicates a much larger variety of gradients and thus the samples change much more rapidly with velocity. It may be concluded that for a maximum variation in samples as wide a variety of gradients as possible is required. Thus similar graphs at different azimuths show that events from the south-east and north-west provide a maximum variation while events from the north-east and south-west provide a minimum variation.

Fig.6.2. shows that if a determination of azimuth is required the array is most sensitive to arrivals from the

Figure 6.1

Plot of  $(\frac{\partial n}{\partial v})_{\alpha}$ , in units of samples per km/sec, against velocity at an azimuth of  $180^{\circ}$  for the seismometers of the array.



Velocity (kms/sec)

Azimuth  $180^{\circ}$

$(\frac{dn}{dv})_{\alpha}$

R5

R4

R3

R2

R1

Y5

Y1

Y2, Y3, Y4

60

70

80

90

2.0

1.5

1.0

0.5

0.0

0.5

1.0

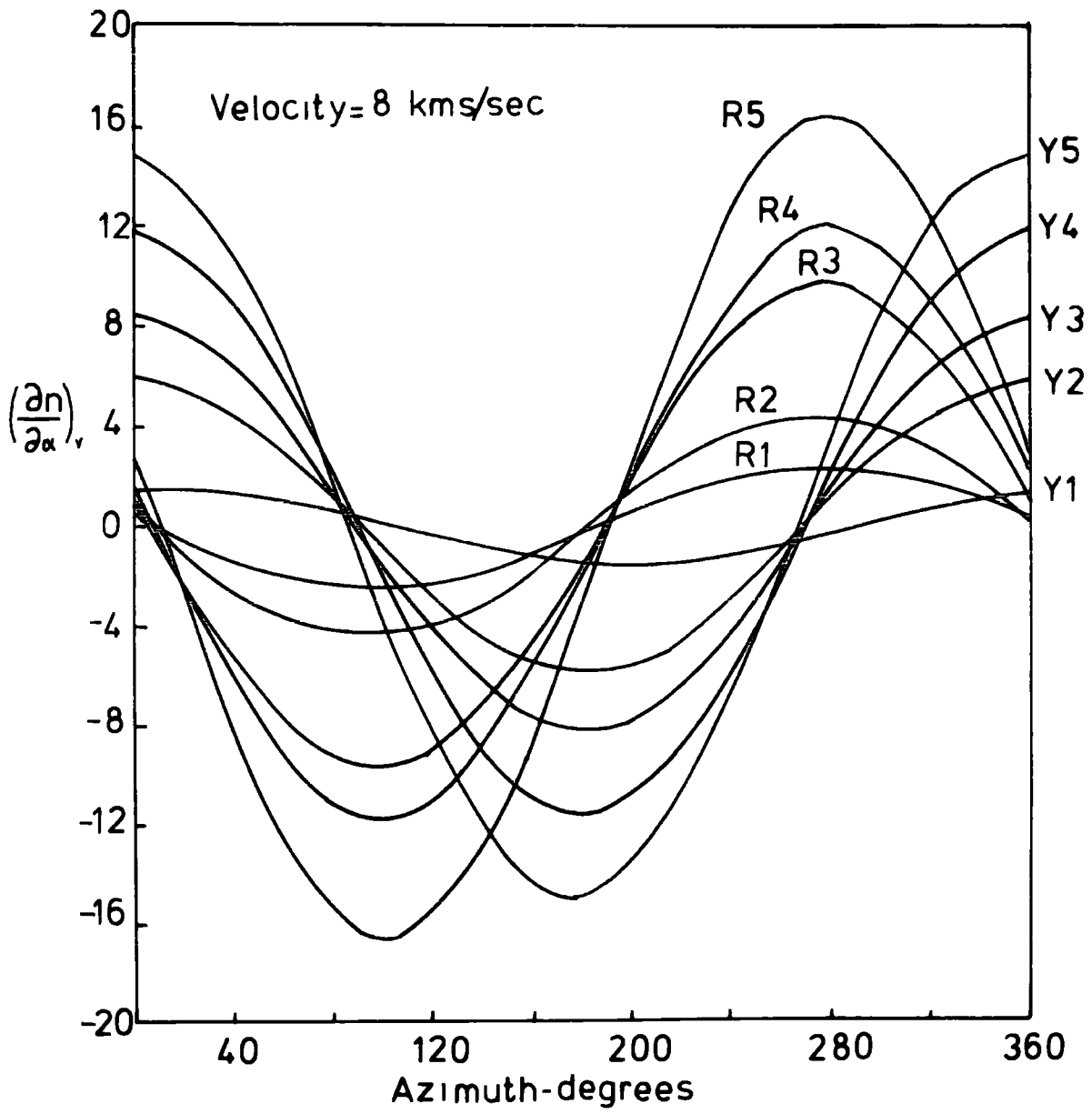
1.5

2.0

2.5

Figure 6.2

Plot of  $(\frac{\partial n}{\partial \alpha})_v$ , in the units of samples/radian, against azimuth for a velocity of 8 km/sec for the seismometers of the array.



north-east and south-west and most insensitive to arrivals from the north-west and south-east.

This method of describing the response of an array is of particular use in assessing the performance of a fairly remote temporary array such as Kaptagat where it is difficult to maintain the equipment to a high standard. Essentially, one is faced with an array whose properties are frequently varying and a fairly rapid method of determining the usefulness of a particular array configuration for a particular event is required. The two groups of curves may be generated and plotted very rapidly by computer and the relative importance of each seismometer assessed and thus the effect of the loss of given seismometers estimated.

The diagrams may also be used to determine a minimum sampling rate necessary to give a required resolution or to determine the maximum resolution given a maximum sampling rate assuming no interpolation between samples. For example, consider an arrival from  $180^{\circ}$  with velocity 8 km/sec; the gradients  $\left(\frac{\partial n}{\partial v}\right)_{\alpha}$  for each of the seismometers are shown in Table 6.1. for a variety of sampling rates. Since delays are applied only to the nearest sample, a sample number has to change by a whole unit before a new sample will on average be taken. If, as an approximation, the gradients are taken as linear, three seismometers will change their samples on going from 8 km/sec to 9 km/sec or from 7 km/sec to 8 km/sec for a sampling rate of 25 samples/second so that for a resolution of  $(8.0 \pm 1.0)$  km/sec the array is operating on three seismometers. At 50 samples/second the operation is on four seismometers, at 100 samples/second on 5 and at 500 samples/second on 7.

Table 6.1

values of  $(\partial n / \partial v)_\alpha$  at 2km/sec and  $100^\circ$  azimuth.

$(\partial n / \partial v)_\alpha = (\text{samples} / (\text{km} / \text{sec}))$

Seismometer	Sampling rate (samples/sec)			
	25	50	100	500
R1	0.30	0.60	1.20	6.0
R2	0.56	1.12	2.23	11.17
R3	1.20	2.41	4.81	24.06
R4	1.46	2.92	5.84	29.22
R5	2.03	4.06	8.12	40.62
Y1	-0.07	-0.14	-0.26	-1.33
Y2	0.00	0.00	0.00	0.00
Y3	-0.01	-0.02	-0.05	-0.23
Y4	0.00	0.01	0.02	0.09
Y5	0.10	0.20	0.39	1.95

6.4.2. The Array Response in the Presence of Incoherent Noise

The response of the array in the presence of incoherent noise is considered in Appendix C where it is shown that if an array consists of  $n$  seismometers the process of delaying and summing will on average improve the signal to noise ratio by a factor  $\sqrt{n}$ .

6.4.3. The Array Response in the Presence of Coherent Noise

If an array is tuned to velocity  $V$  and azimuth  $\alpha$ , denoted here by  $(V, \alpha)$ , then any signal  $(V', \alpha')$  may be defined as coherent noise. The effect of coherent noise has been analysed for various array geometries by Birtill and Whiteway (1965). They assume an array is tuned to an arrival  $(V, \alpha)$  and calculate how the array responds to an arrival  $(V', \alpha')$  and an array response diagram is calculated for the space defined by  $V'$  and  $\alpha'$ . It may be noted that the information contained in this analysis is exactly equivalent to that given in section 6.4.1. although in a different form. If a signal  $(V, \alpha)$  occurs in a region with a large variation of  $\left(\frac{\partial n}{\partial V}\right)_\alpha$  and  $\left(\frac{\partial n}{\partial \alpha}\right)_V$  the array will go rapidly out of tune with changes in  $V$  or  $\alpha$  (although this response is dependent only on the magnitude of the phase shift).

The array response depends on the method of correlation used; two techniques were considered and theoretical responses are derived in Appendix C and illustrated in Figs.6.3. and 6.4. for the Kaptagat array. Fig.6.3. shows the response of summing the red and yellow lines and squaring the resultant  $(\sum R + \sum Y)^2$  and Fig.6.4. shows the response of taking the product of the summed red and yellow lines  $(\sum R \sum Y)$ . The

Figure 6.3

Contoured plot of the response of the array, relative to unity for the in-phase condition, as a function of velocity and azimuth; the response is found by adding the summed red and yellow lines -  $(\sum R + \sum Y)$ . The radial component is linear in wavenumber and the numbers shown are the equivalent velocities (in km/sec) assuming a frequency of 4 Hz.

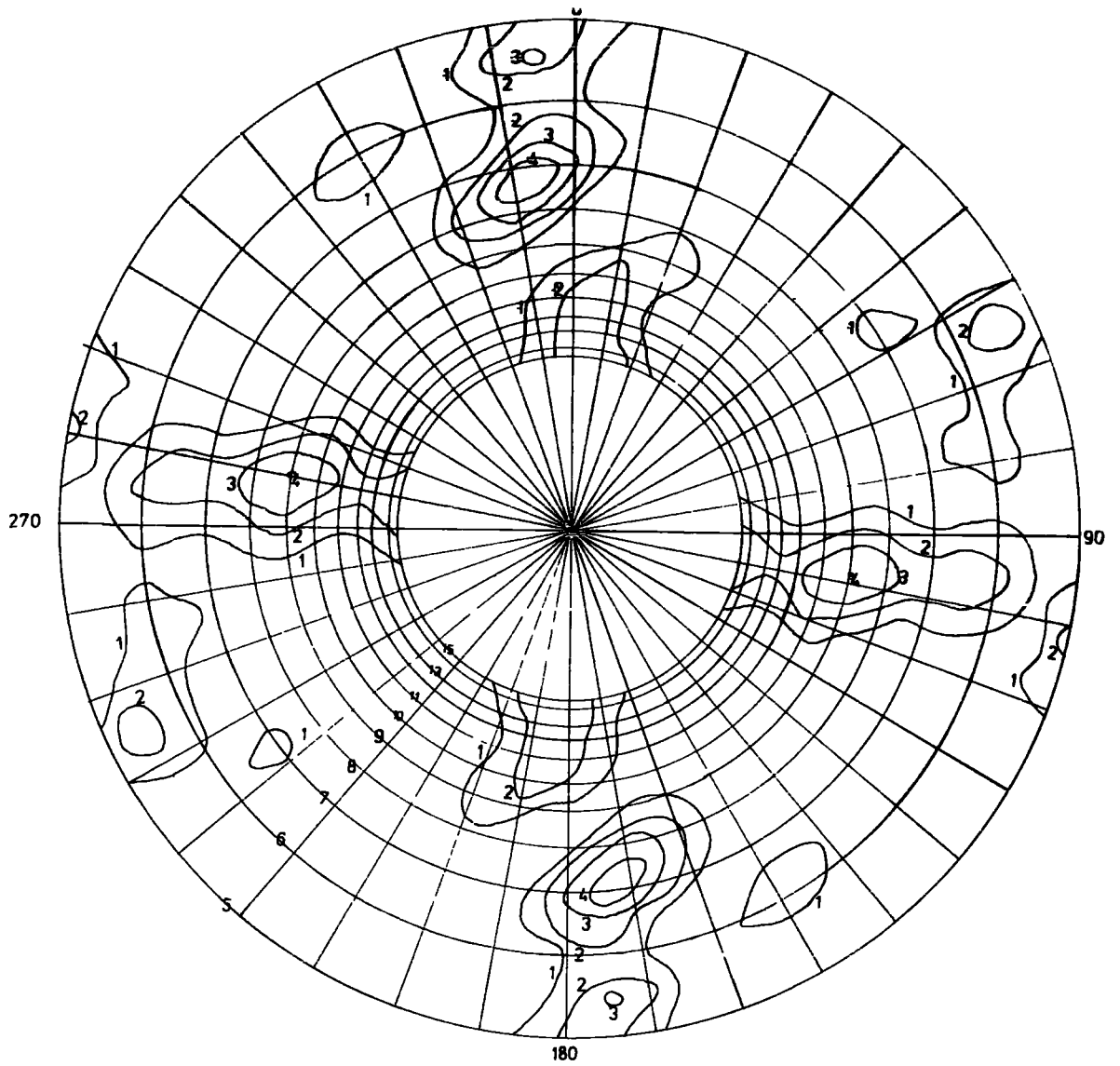
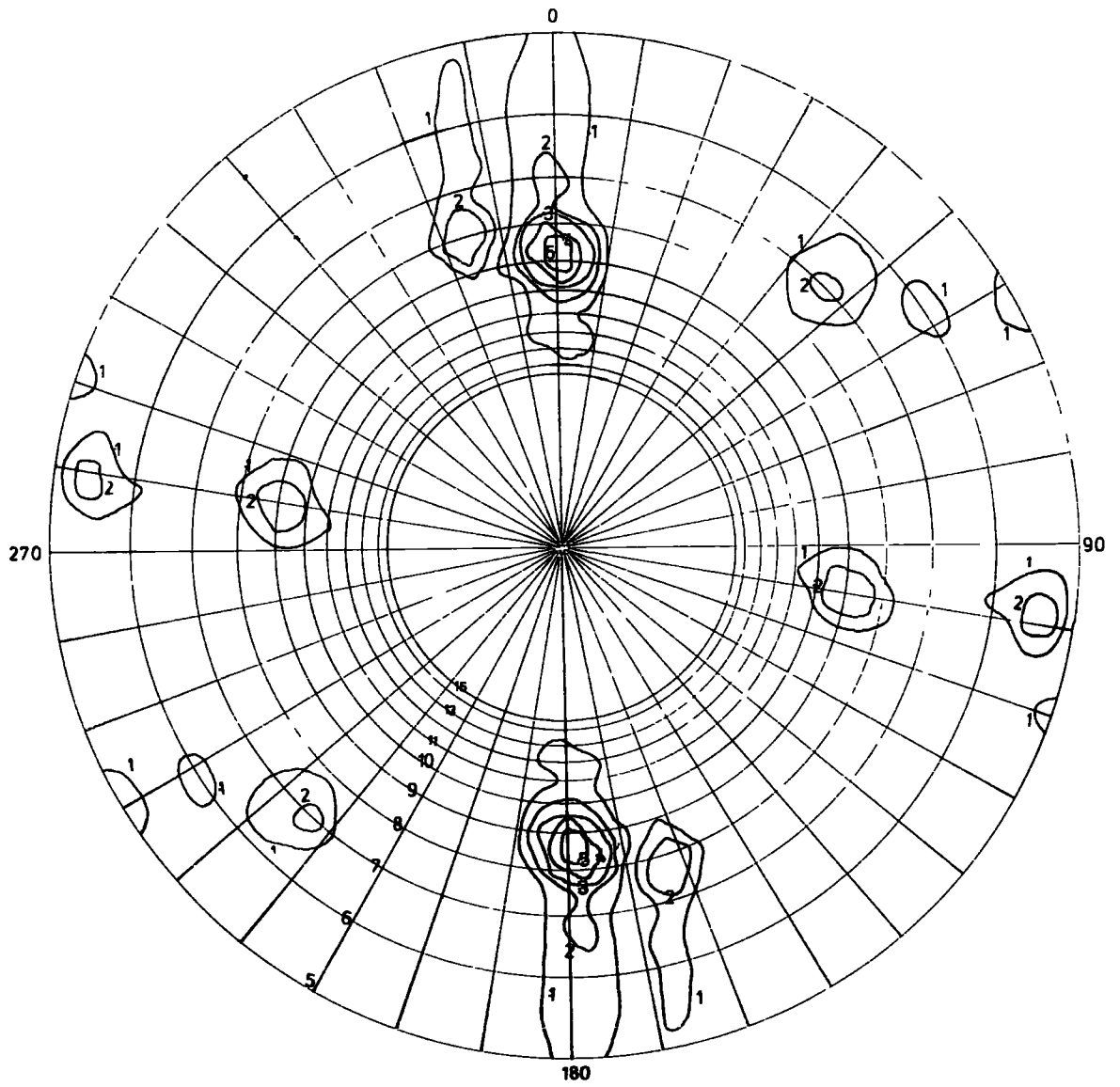


Figure 6.4

Contoured plot of the response of the array found by taking the product of the summed red and yellow lines -  $(\sum R \cdot \sum Y)$ . Details are as given in Fig. 6.3.



contours show the response relative to unity for the in phase condition (i.e. infinite velocity). The effect of coherent noise is most easily calculated by algebra in wavevector ( $\underline{K}$ ) space and the radial distance of the plot is thus linear in  $\underline{K}$  (details of this procedure are given in Appendix C). For a full representation of the response of the array it is necessary to include the dependence on frequency, effectively as a third dimension in the plot; in the present case the average frequency of local arrivals at Kaptagat was found to be approximately 4 Hz and this frequency was used to calculate the responses shown.

In comparison with the standard plots of Birtill and Whiteway these contours appear somewhat uneven but it must be remembered that these diagrams represent the response of a real array with seismometers not equally spaced or in exact geometric patterns. It can also be seen that in general the second correlation technique gives a lower response to coherent noise on average than the straight summation so that this technique was always used.

#### 5.4.4. Interference Problems

Maguire (1974) has investigated the expected density of arrivals at Kaptagat from local earthquakes using a synthetic seismogram program. He found that, for an event at distance 55 km, sixty arrivals occurred within the first 9.63 sec of record if amplitudes within three orders of magnitude are considered. The apparent velocities varied from 3.47 km/sec to 13.57 km/sec and P,S and mode conversions were considered. Consequently the problem of interference is quite serious after the first arrival. While a detailed

treatment of this problem requires a knowledge of the interfering wave forms and their arrival times, a very elementary and crude analysis will illustrate that interfering arrivals can produce anomalous results.

Consider two waves propagating across the array with the same angular frequency  $\omega$  but with two different wave vectors  $\underline{k}_1$  and  $\underline{k}_2$  with phase difference  $\phi$ ; to illustrate the principles of the problem they will be assumed to be represented by equal amplitude sinusoids. (Although arrivals will appear with differing frequency content due to path differences, the variation is small, in comparison with the variation in apparent velocity, hence interference effects in space are of more importance than those in time.) The displacements are given by

$$y_1 = a \cdot \sin (\omega t - \underline{k}_1 \cdot \underline{r} + \phi)$$

$$y_2 = a \cdot \sin (\omega t - \underline{k}_2 \cdot \underline{r})$$

and thus the resulting displacement,  $Y$ , is given by

$$\begin{aligned} Y &= y_1 + y_2 \\ &= 2a \cdot \sin \left( \omega t - \frac{1}{2}(\underline{k}_1 + \underline{k}_2) \cdot \underline{r} + \frac{\phi}{2} \right) \cdot \cos \left( -\frac{1}{2}(\underline{k}_1 - \underline{k}_2) \cdot \underline{r} + \frac{\phi}{2} \right) \end{aligned}$$

6-(iv)

If the most likely case of two waves with differing velocities but the same azimuth is considered then the first term in equation 6-(iv) represents a wave travelling in the same direction as the initial disturbances but with wave vector  $\underline{k}_3$  where

$$|\underline{k}_3| = \frac{1}{2} (|\underline{k}_1| + |\underline{k}_2|)$$

The second term represents the interference effect and is independent of time. If the wavelength of the interference pattern is large compared with the dimensions of the array

then its effect is negligible. Table 6.2. lists the wavelength of the interference pattern associated with the two given velocities and it can be seen that, for example, the interference of an arrival with velocity 15 km/sec with one of 5 km/sec produces an interference wavelength of 3.7 km. It is possible that the velocity filtering process could correlate the interference envelope rather than the individual arrivals and produce a high correlation at an anomalous velocity. However, since the interference pattern propagates in the same direction as that of the interfering waves this will not lead to an anomalous azimuth.

If two waves with differing velocities and azimuths are considered the resulting wavevector  $\underline{k}_3$  will be given by

$$\underline{k}_3 = \frac{1}{2} (\underline{k}_1 + \underline{k}_2)$$

and necessarily  $|\underline{k}_3| < \frac{1}{2} (|\underline{k}_1| + |\underline{k}_2|)$ . The resulting wave thus propagates with a new velocity and azimuth and moreover the second term means that the interference pattern is parallel to neither wavefront so that the effect described above could lead not only to a spurious velocity but also a spurious azimuth.

This analysis has been at a very simple level but has served to illustrate two important points. First, waves from the same azimuth can interfere and produce anomalous velocities but not anomalous azimuths. Secondly, waves arriving from different azimuths can lead to both spurious velocities and azimuths.

## .5. Event Selection and Processing Technique

### .5.1. Choice of Events

An analysis of seismicity associated with the Eastern and

Table 6.2

wavelength of the Interference Pattern by two waves  
with Velocities  $V_1$  and  $V_2$

		$V_1$ (km/sec)				
		5.0	6.5	8.0	10.0	15.0
$V_2$ (km/sec)	5.0	$\infty$	9.00	6.67	5.00	3.70
	6.5		$\infty$	16.67	7.09	3.36
	8.0			$\infty$	20.00	8.33
	10.0				$\infty$	14.29
	15.0					$\infty$

Western Rift has been carried out, at the same time as this study, by Arnold using the array at Kaptagat and Figs.6.5. and 6.6. indicate the locations of local earthquakes recorded at Kaptagat between 10.3.71 and 14.11.71. As the velocity and azimuth of these events had been previously obtained by onset time analysis, the events to be processed were chosen from these.

A preliminary examination of a number of events from various azimuths and distances using the methods described in section 6.5.2. was made to indicate the sort of correlations produced. It was found that events more distant than 100 km did not indicate any significant high velocity second arrivals at anomalous azimuths. The events from the Kavirondo Rift were selected for analysis for two reasons. First, the first arrivals are consistent with the crustal model for regions of normal crust proposed by Maguire and Long (1975) (Arnold - personal communication) and thus appear to have travelled through normal crust. Secondly, events from this region provide a reasonable variation of distance and azimuth and thus the interference effects described in section 6.4.4. may be expected to vary so that any consistently anomalous arrivals cannot be ascribed to interference.

On examining the records many of the events were rejected as unsuitable either because of a high noise level or more usually because of saturation throughout the relevant part of the record. Those which were suitable are listed in Table 6.3. and their locations shown in Fig.6.7. The distance and azimuth are determined to within a standard error of 2 km on epicentral distance and  $2^{\circ}$  on azimuth; focal depths where given or not queried, are accurate to within a standard

Figure 6.5

Locations of all earthquakes analysed at Kaptagat  
by Arnold.

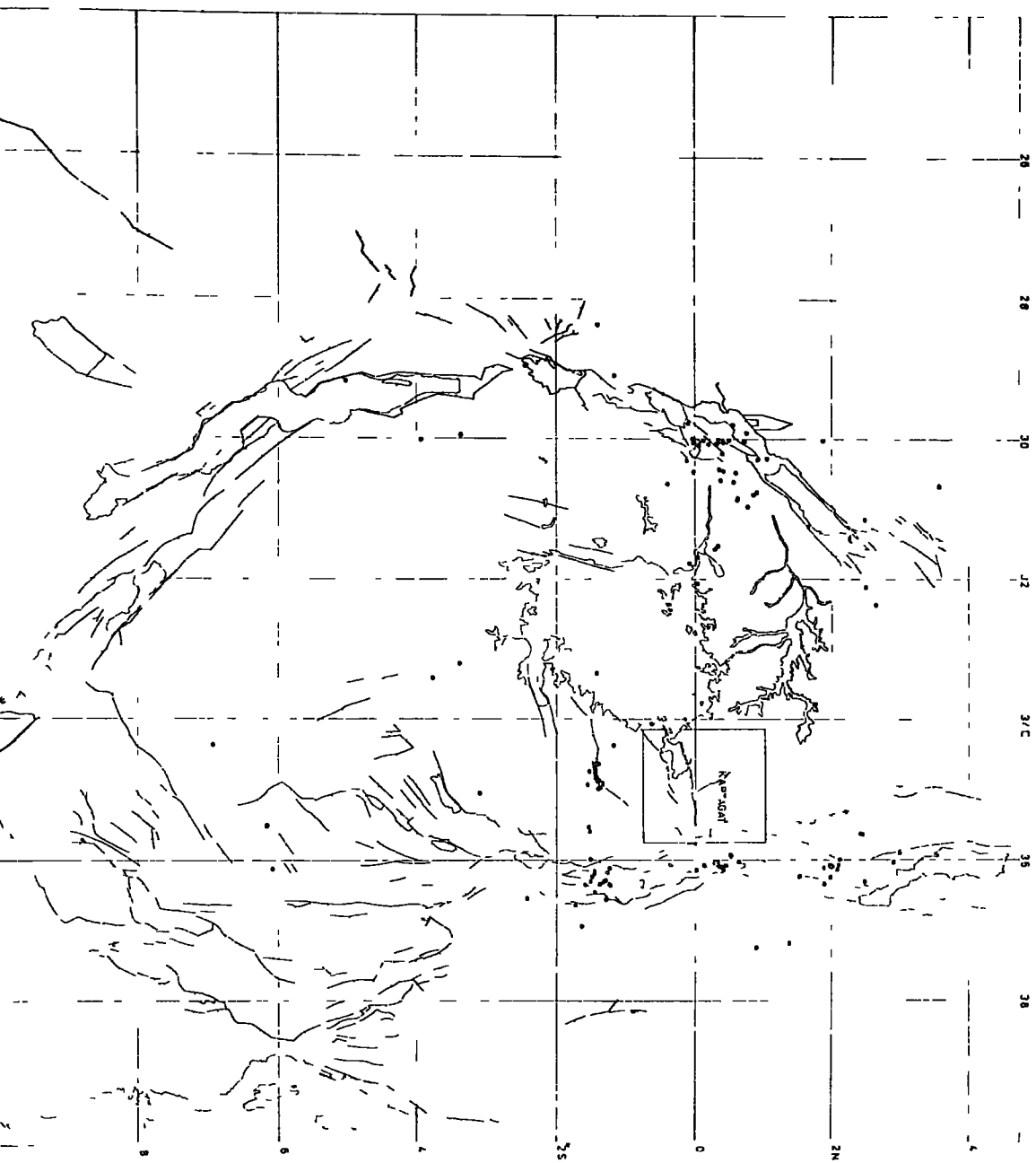


Figure 6.6

Locations of earthquakes from the region of the  
Kavironde Gulf analysed by Arnold.

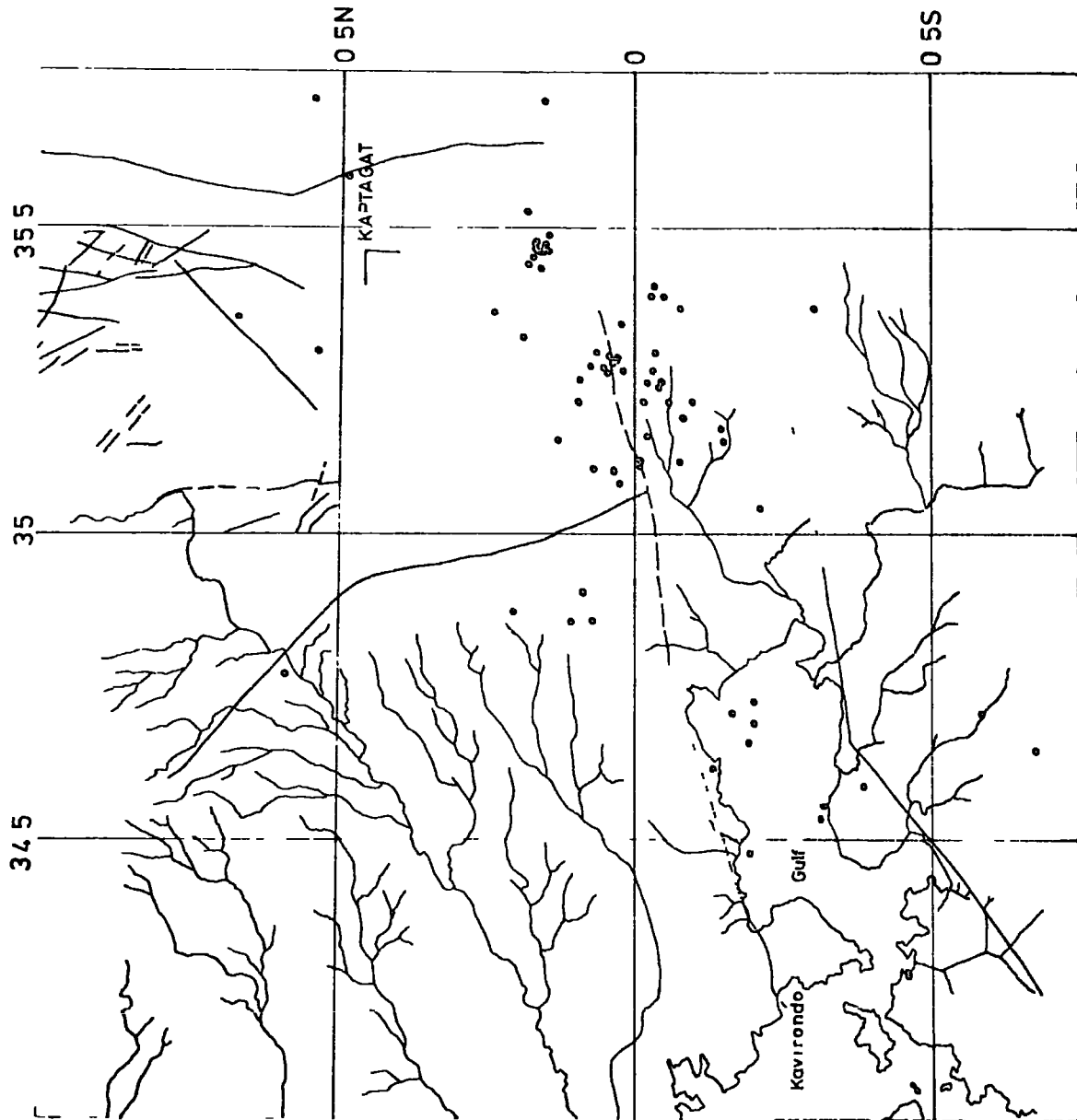


Figure 6.7

Locations of the twelve earthquakes analysed by  
velocity filtering techniques.

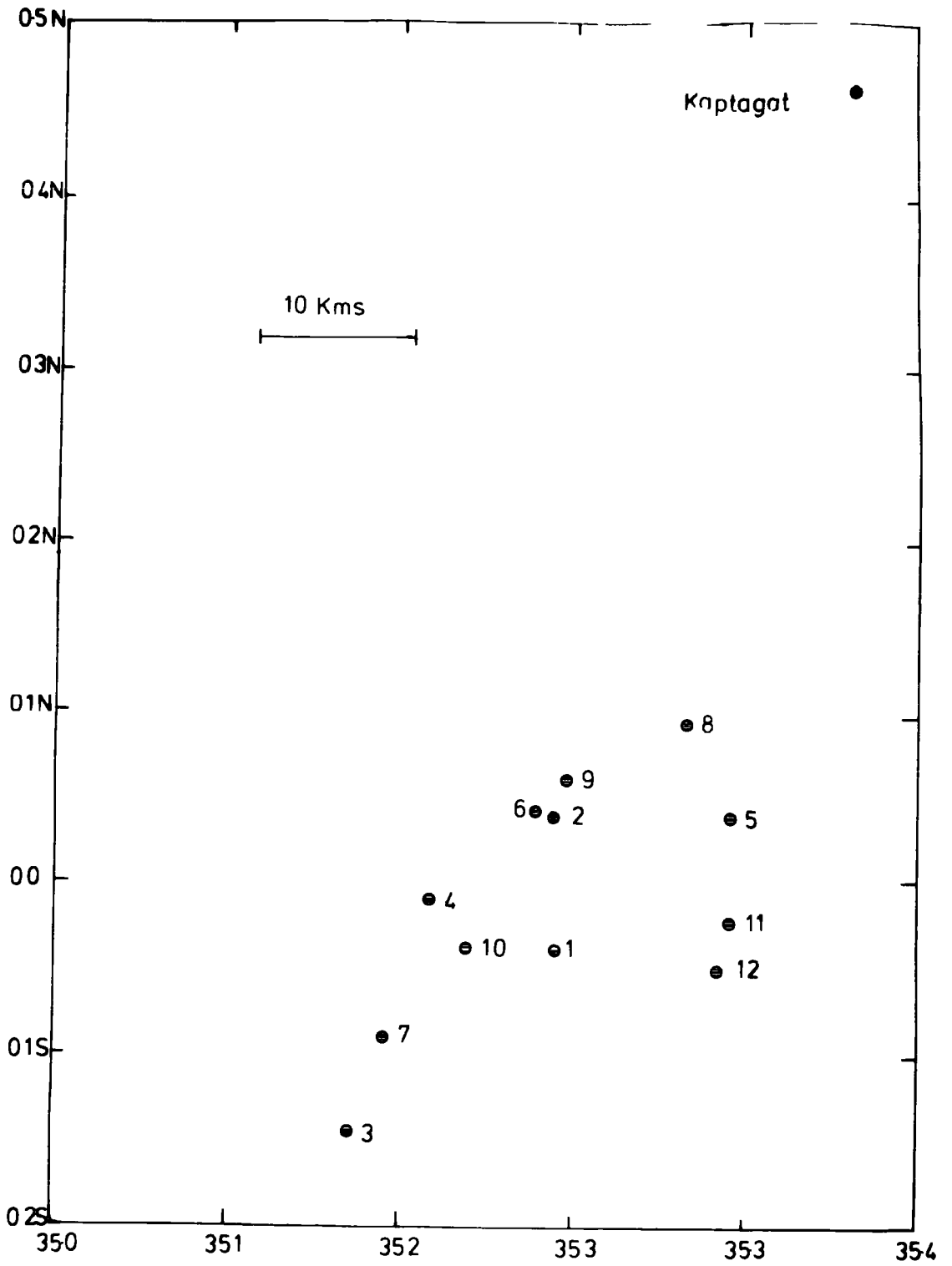


Table 6.3

Local earthquakes used in Second Arrival Analysis.

Event No.	First Arrival					
	Velocity (km/sec)	Azimuth (degrees)	Lat.	Long.	Distance (degrees)	Focal Depth (km)
1	6.32	198.7	0.035S	35.297E	57.1	5
2	6.48	202.5	0.030N	35.287E	50.7	5
3	6.42	205.9	0.145S	35.173E	75.6	5
4	6.12	207.2	0.017S	35.220E	58.5	5
5	6.47	196.7	0.027N	35.334E	49.3	18
6	6.47	203.8	0.040N	35.280E	50.0	?
7	5.46	205.0	0.092S	35.190E	67.1	0
8	6.49	203.1	0.094S	35.370E	45.1	?
9	7.00	205.0	0.066S	35.398E	47.1	?
10	6.36	204.4	0.040S	35.238E	59.9	5
11	6.60	182.7	0.025S	35.380E	53.5	18
12	7.08	188.3	0.051S	35.387E	57.1	25

error of 1 km (Arnold - personal communication). Generally, these events are well recorded and saturation is very slight although there are still quite considerable variations in the quality of the records.

#### 5.5.2. Processing Technique

The methods used will be illustrated with reference to event number one. Seven channels were operating when recorded and the seismograms and time code are illustrated in Fig.6.8.

Once an event had been selected for processing it was digitized at 25 samples/second and automatically captured onto disc with one second of noise before the first arrival. After checking that the digitization had been correct the event was permanently stored on tape. The process was repeated at digitization rates of 50 and 100 samples/second. If a seismometer channel was obviously not operating correctly the input was put to zero volts and thus all tape files consisted of the same format of ten channels plus one time code regardless of the number of channels operating. In cases where the noise level was significant the automatic capturing process was often triggered by noise in which case a very tight frequency filter was used on the test channel to exclude the noise although in all cases the unfiltered record was digitized and recorded.

The velocity filtering was performed using the program listed. Essentially the yellow and red line were delayed, summed and multiplied. The correlation was then integrated over a window of 0.2 sec; this corresponds to approximately a wavelength and was found by trial and error to give the

Figure 6.8

Seismograms of the seven operating seismometers for event number one; also shown is the binary time code indicating second markers.



sharpest response for second arrivals. The correlations were displayed using a Hewlett-Packard x-y plotter.

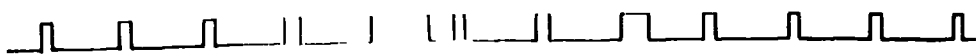
The correlation function was calculated for the event, using a sampling rate of 50 samples/second, at a velocity of 8 km/sec for azimuths between  $0^{\circ}$  and  $360^{\circ}$  in steps of  $2^{\circ}$  and displayed on the plotter. A short section of such a record is illustrated in Fig.6.9. The correlation function was then calculated and displayed for the first arrival azimuth (as calculated by onset time analysis) between velocities of 5.0 and 10.0 km/sec (Fig.6.10.) in order to compare the two techniques and ensure that the digital record is correct (Fig.6.11. shows the height of the first arrival correlation against velocity).

The azimuth sweep was then analysed; the maximum amplitude of the peak was used as the quality of the correlation (King et al, 1973) and thus the various correlations at anomalous azimuths were investigated. One example is shown in Fig.6.9. where the shaded portion is the arrival under consideration. Fig.6.12. shows the plot of correlation against azimuth and a clear peak is observed between  $120^{\circ}$  and  $140^{\circ}$ .

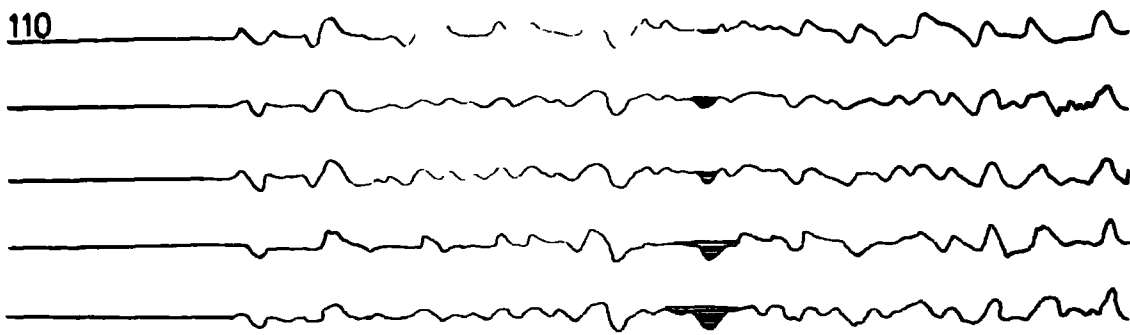
The records were now velocity filtered at this second arrival azimuth between velocities of 5.0 km/sec and 10.0 km/sec. On the vast majority of occasions these arrivals gave a high correlation at low velocities but occasionally the peak correlated at a high velocity as is shown for the peak illustrated in Fig.6.13.

Figure 6.9

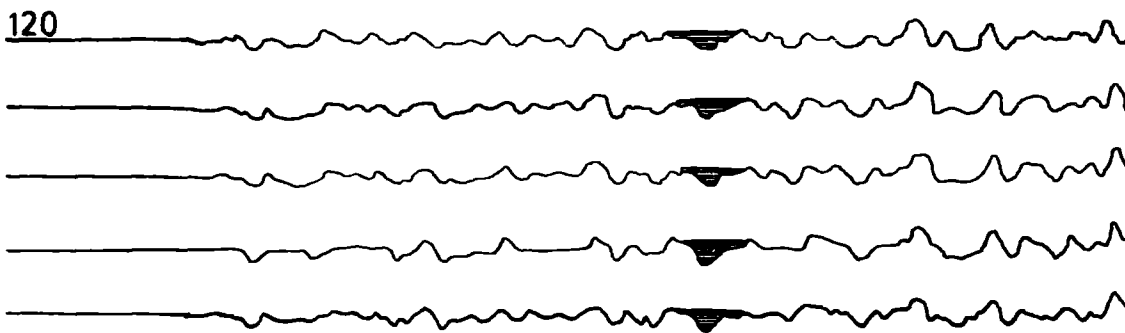
Correlation across the record as a function of azimuth at a velocity of 8 km/sec. The shaded region indicates a high correlation of the type analysed.



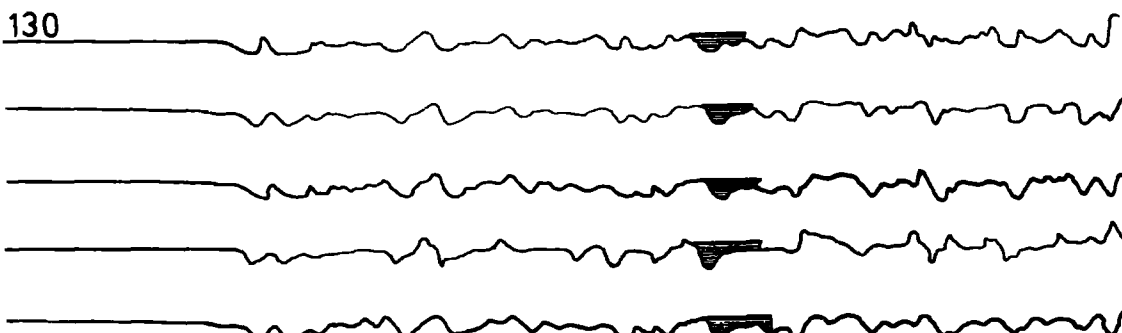
110



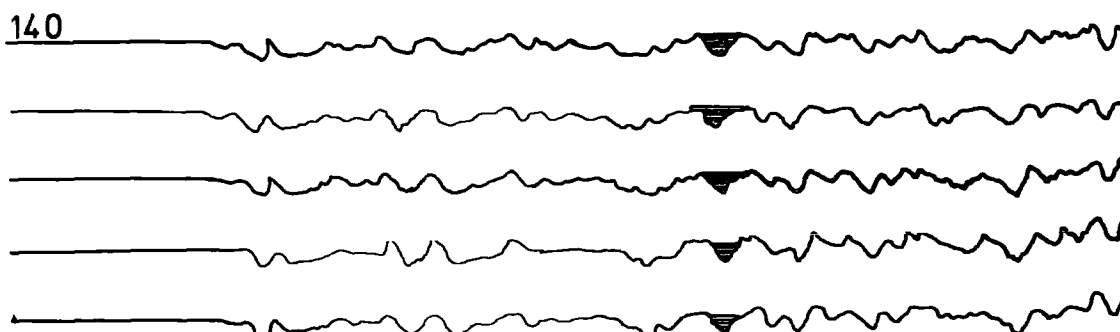
120



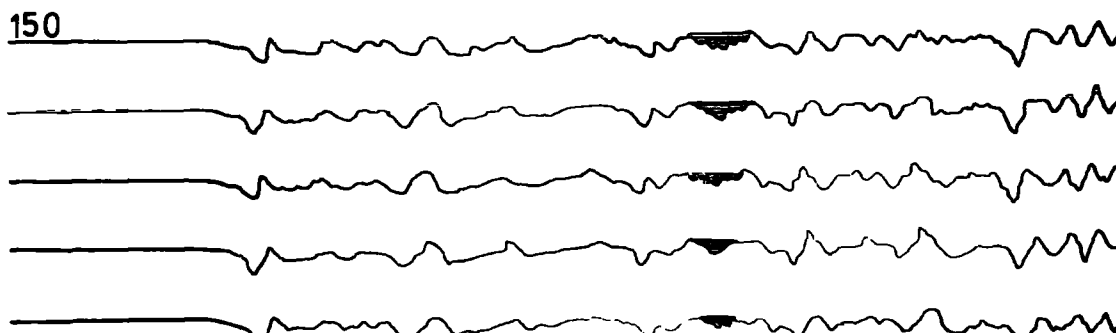
130



140



150

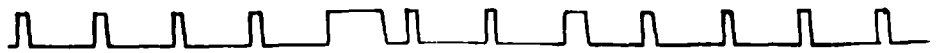


160

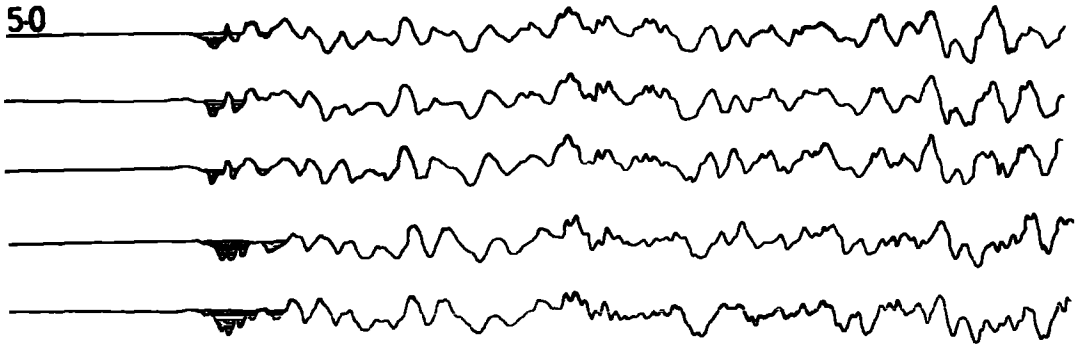


Figure 6.10

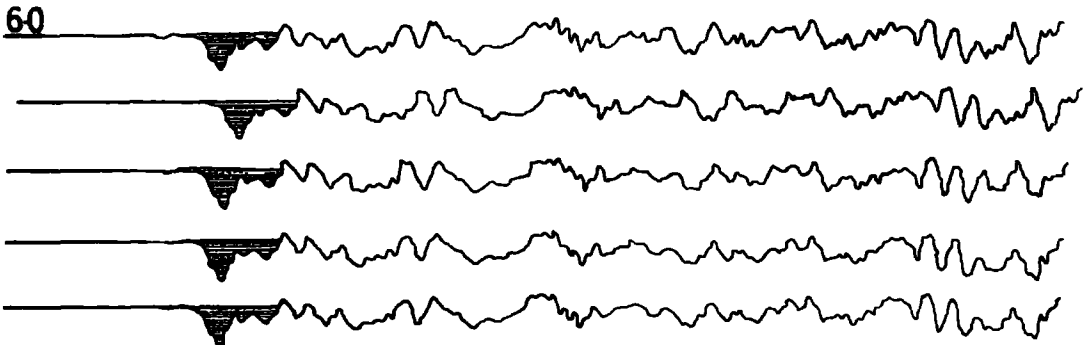
Correlation across the record as a function of velocity at the first arrival azimuth. Region shaded shows the correlation of the first arrival azimuth.



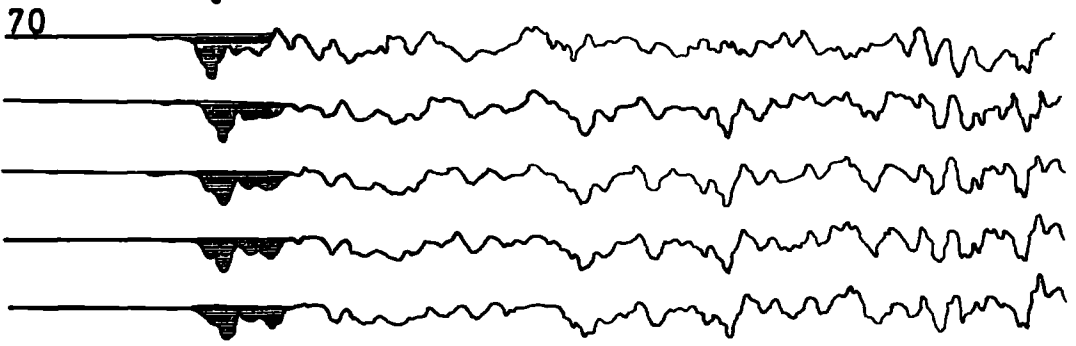
50



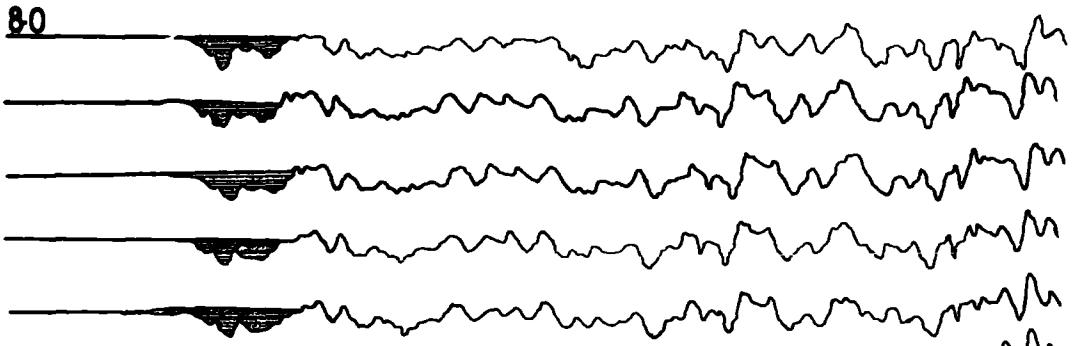
60



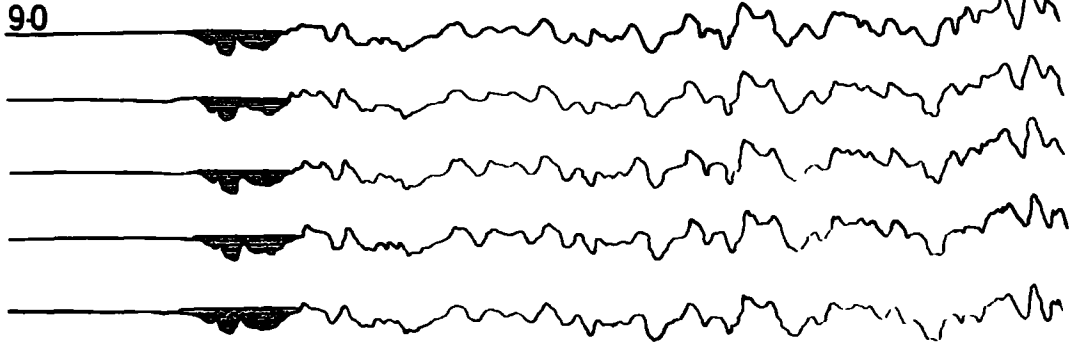
70



80



90



100

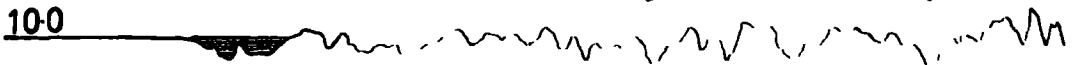


Figure 6.11

Plot of amplitude of correlation of first arrival  
against velocity - the correlation is shown in  
Fig. 6.10.

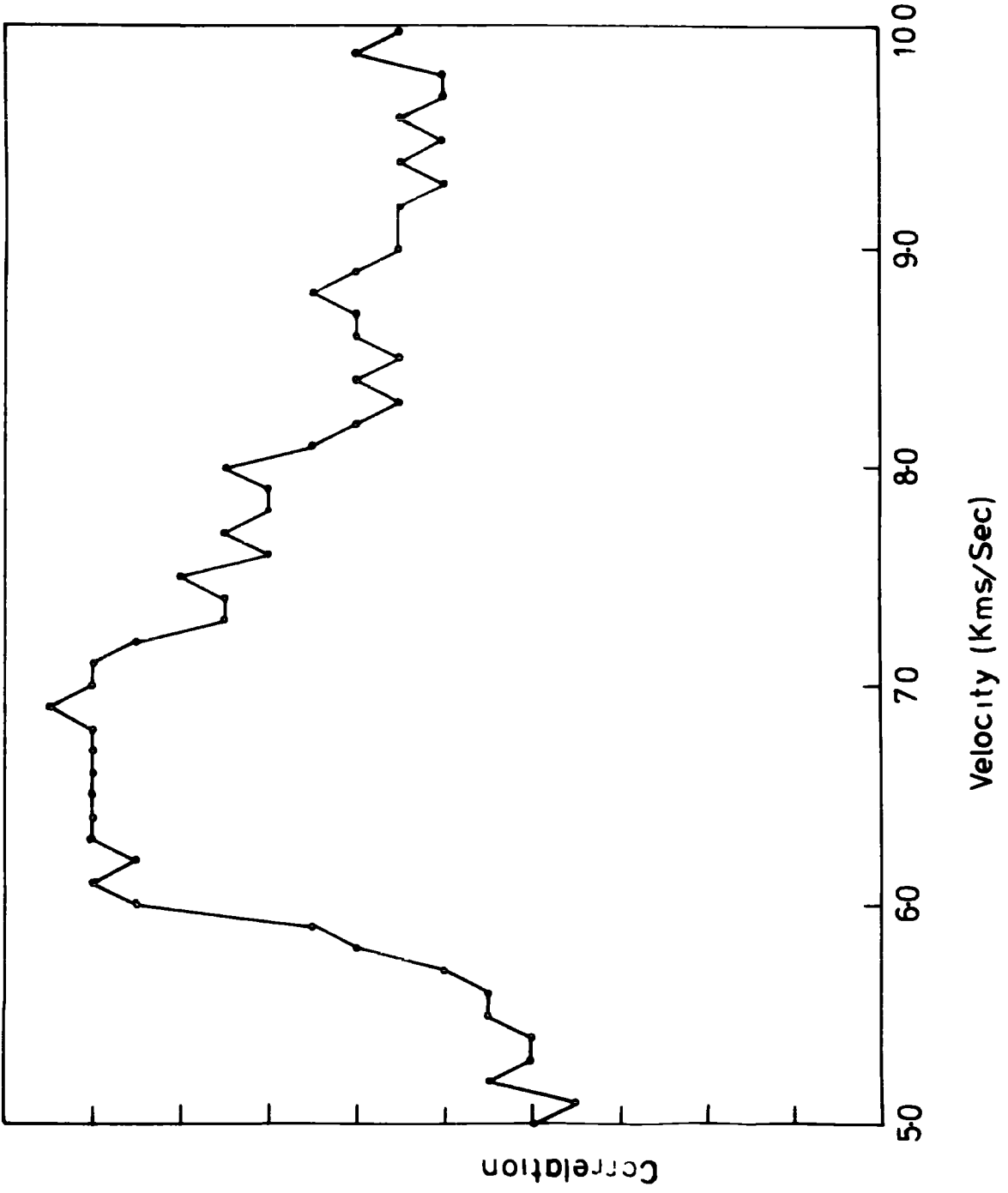


Figure 6.12

Plot of amplitude of correlation of second arrival  
shown in Fig. 6.9 against azimuth.

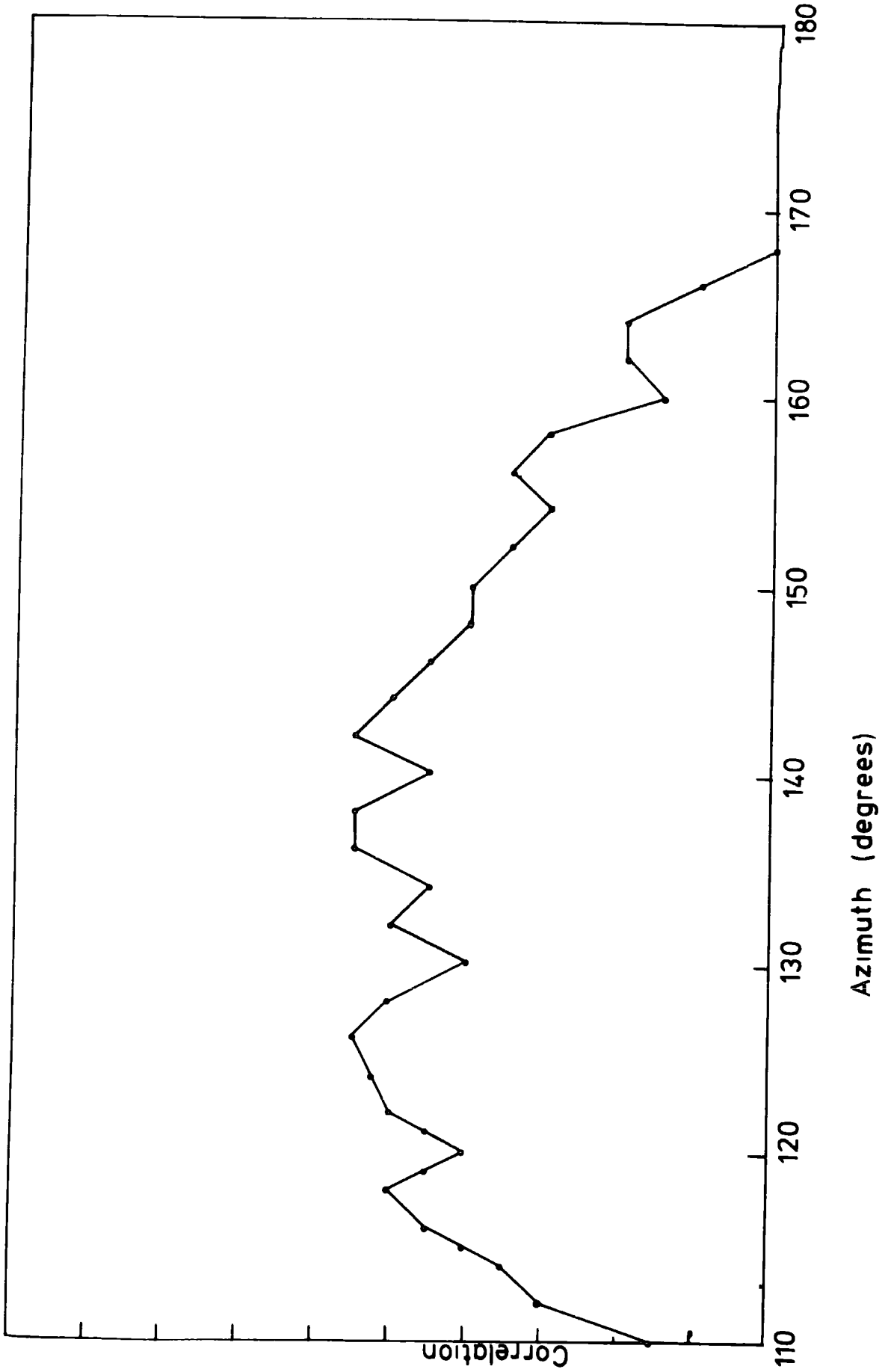
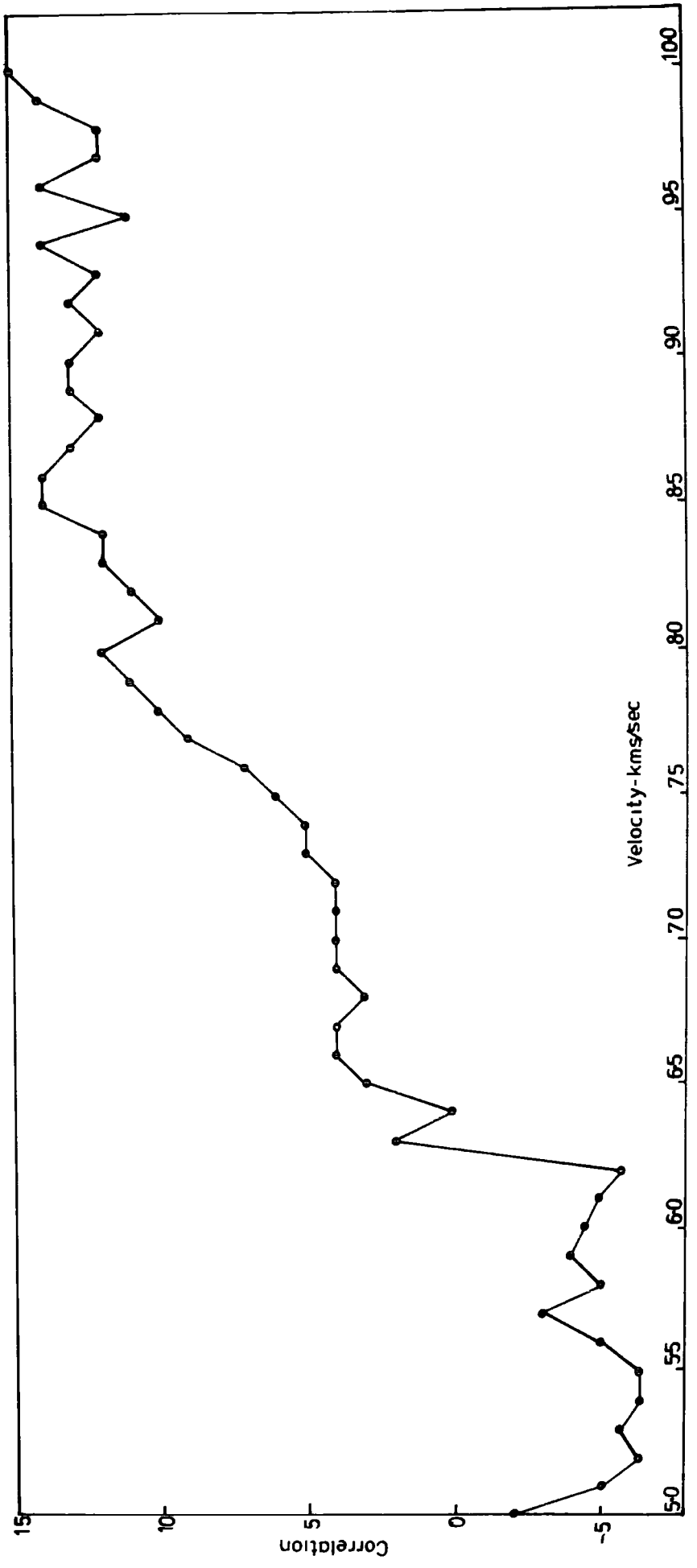


Figure 6.13

Plot of amplitude of second arrival correlation  
against velocity.



6.6.

### Results

The events listed in Table 6.3. were analysed using the method described in the previous section. Generally high correlations at azimuths significantly different from that of the first arrival were found to have low velocities. These arrivals are considered to be equivalent to those found at the Eskdalemuir array by Key (1968) and explained theoretically by Hudson (1968). A plane compressional wave reflected from a sharp boundary will be reflected, usually, as a compressional and shear wave but if the wave is incident at an irregular boundary surface waves, in addition to the compressional and shear waves, will be generated. If such a discontinuity occurs near the array surface waves may arrive within the P coda and will exhibit a low velocity and an anomalous azimuth. (It may be mentioned that these arrivals will complicate the interference effects already described even further.)

Occasionally, however, a well defined high velocity arrival was found as illustrated in the previous section. Usually the arrival correlated well at 8 km/sec and retained a high correlation for all higher velocities as would be expected from the earlier discussion of the control of the array resolution by the sampling rate.

The high velocity arrivals found in the group are summarized in Table 6.4. The events are classified as good, fair or poor; generally the quality refers to the signal to noise ratio found on the record and to saturation. Poor quality records are usually caused by saturation in part of the record; saturation seriously effected the quality of correlations at the first arrival azimuth throughout the record

Table 6.4

Event No.	Quality of record	Summary of high velocity second arrival data.
1	Good	Group of arrivals of high velocity ( 8.0) at 130° azimuth between 6.0 and 6.6 seconds after first arrival
2	Good	Second arrival of high velocity at 130° azimuth 6.0 seconds after first arrival
3	Good	Second arrival of high velocity at 110° azimuth 6.0 seconds after first arrival
4	Poor	No observed second arrivals.
5	Good	No observed second arrivals.
6	Poor	No observed second arrivals.
7	Poor-some saturation	No observed second arrivals.
8	Poor-some saturation	A high velocity arrival at 10° azimuth
9	Poor	No observed second arrival.
10	Fair	A high velocity arrival at 45° azimuth, 3.0 seconds after the first arrival.
11	Poor	A high velocity arrival at 54° azimuth at 2.6 seconds after first arrival.
12	Poor	No second arrival found.

and thus the arrivals for events 8 and 11 are considered dubious.

It can be seen that the only reliable events showing high velocity second arrivals are numbers 1, 2, 3 and 10 and only the first three can be taken as indicating a consistent arrival. It should be added that these events, together with number 5, were the clearest and least noisy of all those analysed and it is possible that the search for these anomalous phases failed simply because of the quality of the records available.

5.7.

### Discussion

Although the search for this arrival has not been successful it is important to try to determine what the arrivals in events 1, 2 and 3 are and to see if anything can be said of the structure in the absence of these arrivals.

It is possible that the anomalous arrivals of the first three events are not caused by a reflection off the surface but from other sources. One possibility is that they are produced as an interference effect between a normal second arrival and a locally generated surface wave or the anomalous arrival under consideration. Although this may account for events 8, 10 or 11 it is unlikely to have effected the three events in such a consistent manner when the variation in azimuth and distance are considered.

A second possibility is that these correlations are manifestations of a large amplitude second arrival at the first arrival azimuth which causes a side lobe response in the array at this particular velocity and azimuth. The expected second arrival sequence was calculated using the

crustal structure of Maguire and Long (1975) and the locations of Arnold (Table 6.3.). It is found that the Moho reflection,  $P_m$ , is expected at approximately six seconds after the first arrivals (for events, 1, 2 and 3 the times are 6.2, 6.7 and 7.1 seconds) and indeed a good correlation is found at this point in the record at the first arrival azimuth with a correlation amplitude somewhat less than that found for the first arrival. By using the array response diagram of Fig.6.8. the response of the array to the Moho arrival when tuned to the observed second arrival may be determined as described in Appendix C. ( $P_m$  arrives at 11.82, 11.40 and 9.05 km/sec for events 1, 2 and 3.) It is found that tuning to any velocity above 8 km/sec for azimuths between  $110^\circ$  and  $130^\circ$  (the observed azimuth) produces a maximum response to  $P_m$  of less than 0.2 relative to unity for the in phase condition. It is thus considered unlikely, though not impossible, for the observed correlations to be caused by the pure  $P_m$  phase.

The expected azimuths, arrival times and velocities expected from the optimum models of chapter four were calculated using the ray tracing techniques described in Appendix B. It will, however, be remembered that the structure is poorly defined in the region of interest as no reliable teleseisms occurred within this azimuth range; if the optimum models are extrapolated on the basis of the mathematical function (a procedure not supported by any data points) the intersection always occurred at depths in excess of 200 km and this phase would thus be expected within the true surface wave arrivals and would be difficult to observe; little importance is attached to this point however. Since

it is not possible to predict the intersection it is of use to see under what conditions a reflection of reasonable amplitude may be found. If it is assumed that the boundary between normal mantle and the anomalous structure is perfectly sharp then the conditions for a reasonable reflection will be the best obtainable; any gradations in the boundary will cause the reflected amplitude to be lower than predicted. The plane wave approximation is satisfactory for the present purposes and by demanding that the stress and displacement are continuous across the boundary it is possible (Bullen, 1965; Ewing et al, 1957) to calculate the amplitude of the reflected and refracted P and S waves. The normal mantle was assumed to have a P velocity of 8.1 km/sec, and S velocity of 4.7 km/sec and a density of 3.3 gms/cc. As an example of the possible extremes two sets of data for the anomalous body were taken. The density was taken as 3.2 gms/cc since this is the largest reasonable density contrast (see chapter seven); as a maximum P velocity 7.5 km/sec was taken and the corresponding S velocity of 4.3 km/sec was used. The amplitude of the reflected wave as a function of angle of incidence is shown in Fig.6.14. As a minimum velocity 6.8 km/sec was taken for P and a low S velocity of 3.3 km/sec was used and this amplitude is shown in Fig.6.15. (No attention is paid to phase changes in this plot.) The results are remarkably similar and it can be seen that under these circumstances the angle of incidence must be at least  $80^{\circ}$  before a reasonable amount of energy goes into the reflected phase. If we again take the most favourable circumstance and assume that intersection occurs just beneath the Moho then of all the events considered the maximum angle of incidence (in a horizontal layer) is  $64.3^{\circ}$  for event number 12. It is

Figure 6.14

Plot of amplitude of reflected P-Wave against angle of incidence. Medium 1 contains the incident and reflected waves and 2 is the refracting medium.

Compressional velocities ( $V_{p1}, V_{p2}$ ), shear velocities ( $V_{s1}, V_{s2}$ ) and densities ( $P_1, P_2$ ) are

$$V_{p1} = 8.1 \text{ km/sec} \quad V_{s1} = 4.7 \text{ km/sec} \quad = 3.3 \text{ gm/cc}$$

$$V_{p2} = 7.5 \text{ km/sec} \quad V_{s2} = 4.3 \text{ km/sec} \quad = 3.2 \text{ gm/cc}$$

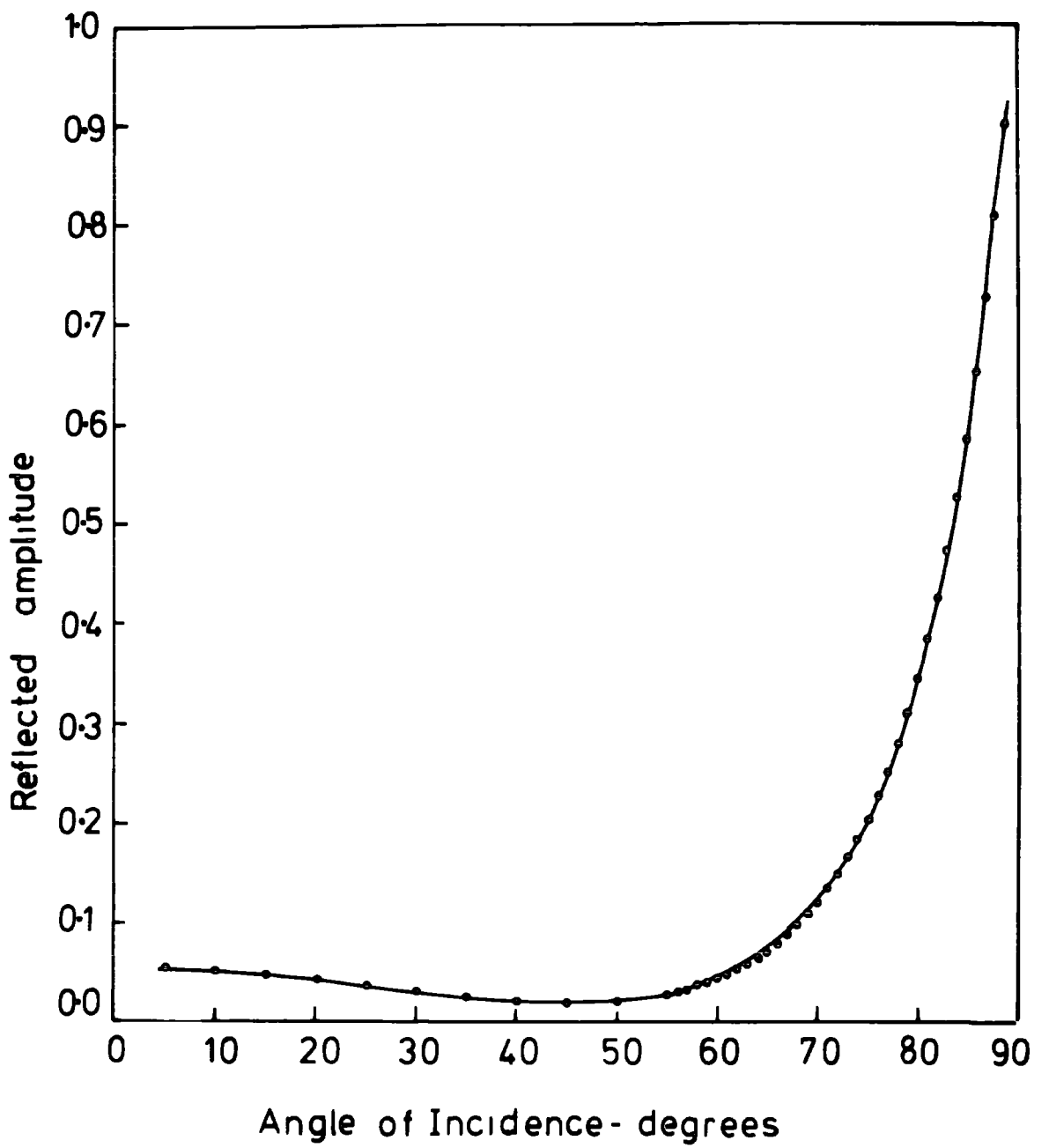
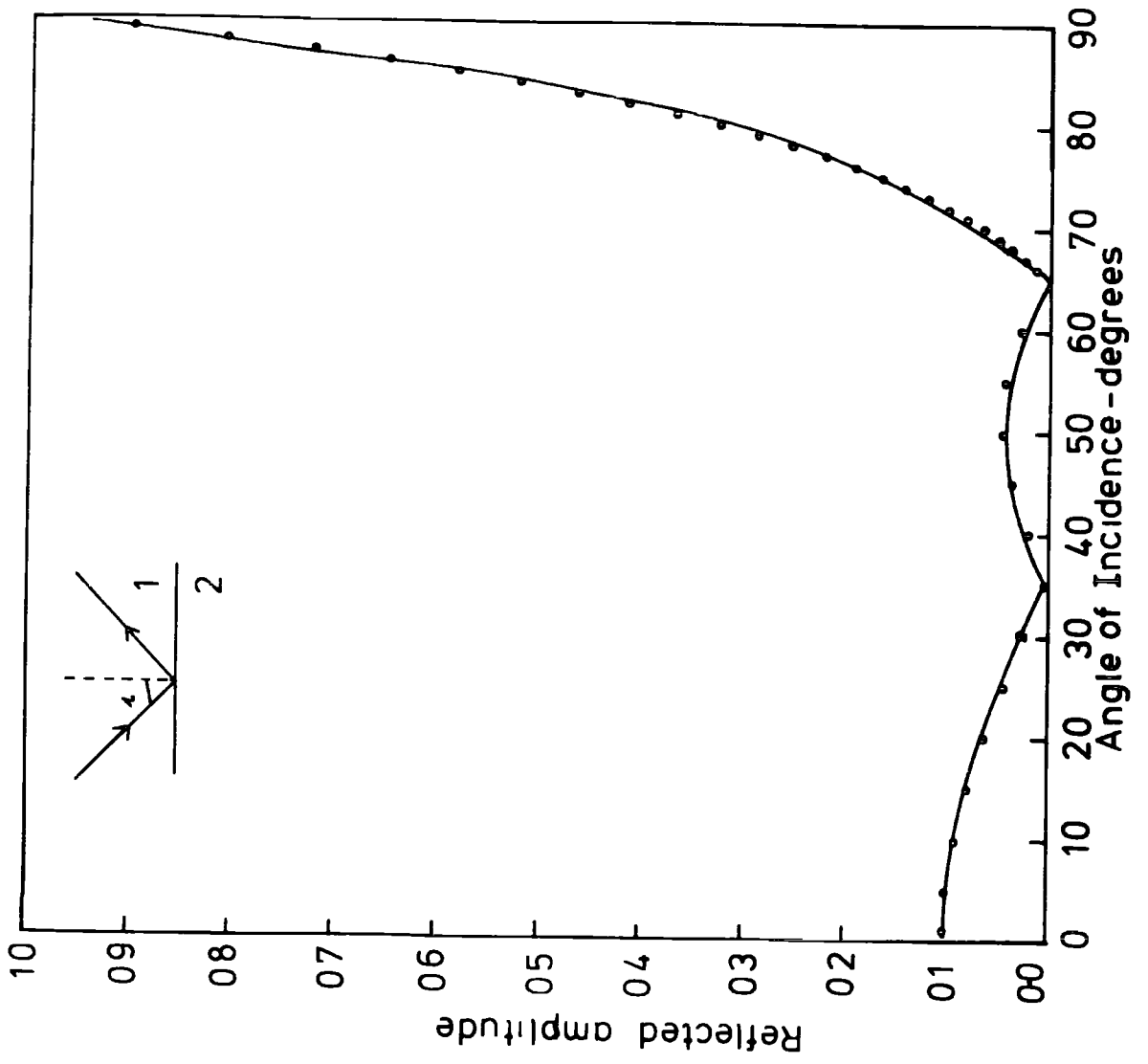


Figure 6.15

Plot of amplitude of reflected P-wave against angle  
of incidence for the following case

$$V_{p1} = 8.1 \text{ km/sec} \quad V_{s1} = 4.7 \text{ km/sec} \quad = 3.3 \text{ gm/cc}$$

$$V_{p2} = 6.8 \text{ km/sec} \quad V_{s2} = 3.3 \text{ km/sec} \quad = 3.2 \text{ gm/cc}$$



possible that the slope on the interface could be such as to increase the angle of incidence and without information on the shape of the structure this cannot be calculated. One possible indication comes from the work of Darracott et al (1972) who put forward a regional gravity map of the rift south of  $1^{\circ}\text{S}$ . This is illustrated in Fig.7.2. where it is discussed further but it may be taken as a rough indication of the anomalous upper mantle structure. It can be seen that the structure is apparently running north-south near the Kavirondo and thus the normal at the point of intersection is running east-west and thus not increasing the angle of incidence considerably (as would be the case with the normal running say north-west).

One final reason for a possible non-discovery may be mentioned and this concerns the assumption that the anomalous arrival appears at an azimuth significantly different from that of the first arrival. Of course, if the normal points in a direction not significantly different from the direction between the station and the event, the azimuthal anomaly will be small and will have escaped detection in this analysis. However, if this is the case then it is considered that this arrival simply could not be distinguished from the profusion of other high velocity arrivals.

The result is thus negative and, moreover, negative in an unsatisfactory manner in that no single cause can be ascribed to the non-discovery or the non-arrival of the anomalous phase. In spite of this it is considered that the effort involved was justified because of the potential value of such arrivals if found as they would have permitted the

analysis of the upper surface of the body with no interference from structure beneath; the analysis has also provided some idea of the problems involved in such a search and the resolution available using the techniques described.

CHAPTER 7

GRAVITY MODELS

7.1. Introduction

The proposed anomalous mantle structure will be reflected in the observed regional gravity field if its low velocity is related to a reduced density. It will be seen that there are considerable problems in correlating the regional Bouguer anomaly with the upper mantle structure which will cause the analysis to be at a semi-quantitative level.

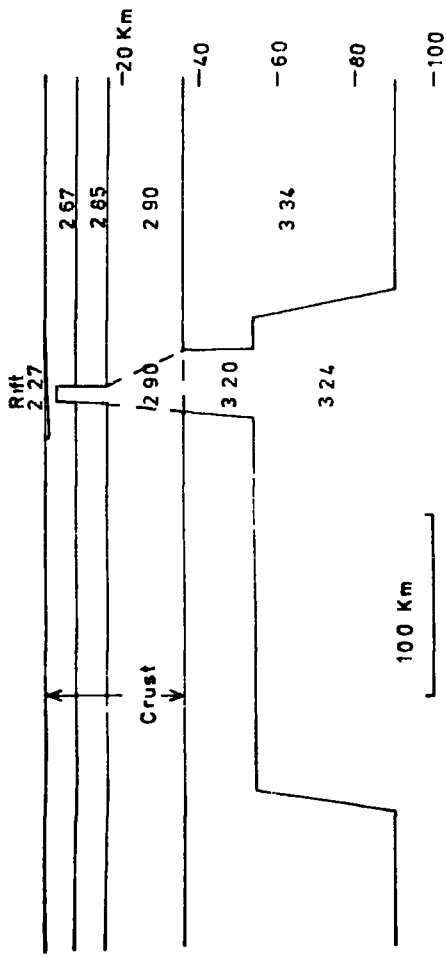
7.2. Previous Gravity Studies in East Africa

The practical problems of carrying out gravity field work in East Africa are considerable and have led to several investigations being restricted by both the quality and the quantity of the data. These problems are gradually being overcome thanks to extensive academic work and also the release of a considerable amount of data previously kept confidential by the oil companies.

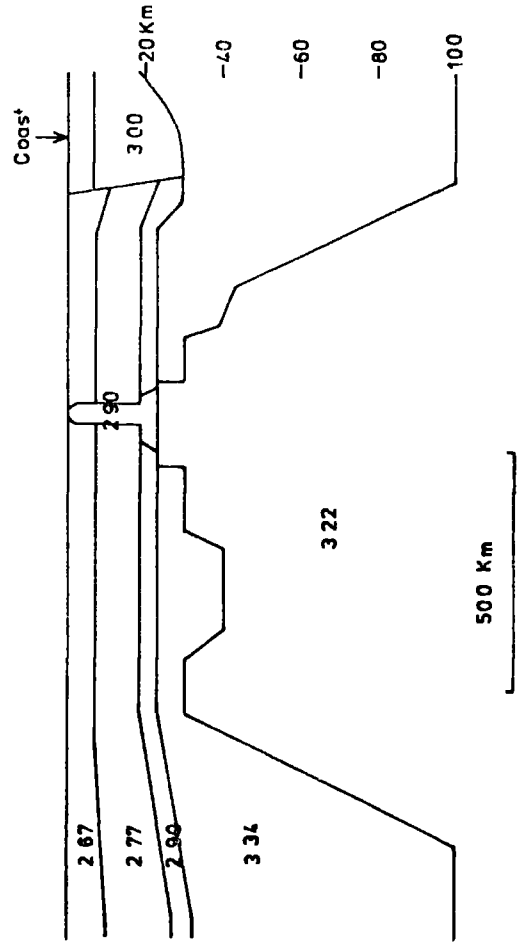
Because of these problems the accuracy of some of the profiles calculated and the interpretations subsequently produced are open to question; for example four recent interpretations are shown in Fig.7.1. and it can be seen that the proposed structures exhibit considerable variation although it must be realized that all four models represent different cross sections across the rift. The basic solution of the anomaly is the same in all cases in that the long wavelength negative anomaly is explained by the presence of anomalously low density material in the mantle which intrudes into the crust, with or without modification, to cause a positive anomaly. Beyond this point however the models diverge, the

Figure 7.1

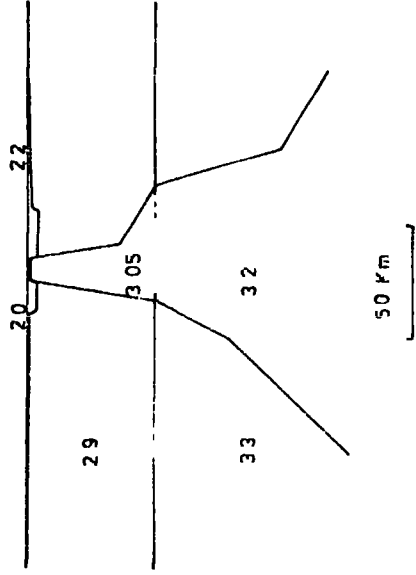
A summary of four recent gravity interpretations.



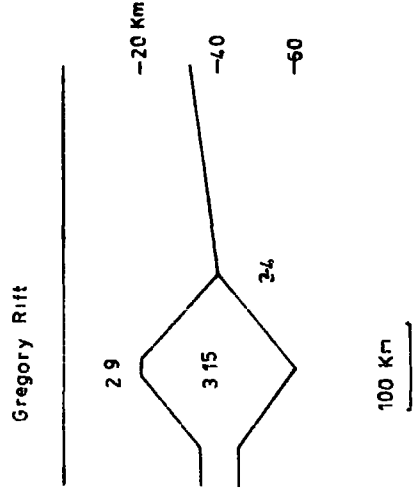
Darracott et alia 1972  
Latitude 16°S



Fairhead and Girdler 1972  
Latitude 00



Baker and Wohlenberg 1971



Khan and Mansfield 1971

models of Fairhead and Girdler (1972) and Darracott et al (1972) bear no relation to the models proposed earlier while the shape of the structure of Khan and Mansfield (1971) is very similar to that proposed by Backhouse (1972). The gravity model of Baker and Wohlenberg (1971) is the only one to relate satisfactorily to the seismic structure proposed.

It appears that the interpretations differ for two reasons. First, the large thickness of low density volcanics within, and on the flanks of, the rift exert a strong, but unknown, influence on the shape of the curve (Baker and Wohlenberg, 1971) most especially near the short wavelength positive anomaly. Secondly, in order to compute the mantle structure the regional Bouguer anomaly must be used and this is liable to considerable error when the data is distributed sparsely. Moreover, although the high frequency anomalies observed in the Bouguer map may be ascribed to shallow structure it is difficult to estimate the effect of long wavelength anomalies produced in the crust. Thus, in the case under consideration the effect of Mount Elgon on the regional anomaly, computed on the basis of frequency content of the Bouguer anomaly, will be considerable, making a direct correlation with the anomalous mantle incorrect.

At the present time extensive gravity measurements are being carried out by C.J. Swain of Leicester University and work is proceeding on the compilation of this data with all other gravity measurements made in East Africa which have been catalogued by Searle and Darracott (1971) and these are being used to produce a much more detailed Bouguer anomaly map of Kenya than is at present available. I am grateful to Dr. M.A. Khan for permission to use unpublished provisional

maps of this work (which unfortunately do not contain Swain's measurements) and the publication of the final maps is awaited with interest. The sections of the maps showing the region of the Kenyan domal uplift are shown in Figs.7.2. and 7.3; Fig.7.2. shows the Bouguer anomaly map and Fig.7.3. shows the derived regional anomaly map. The part of the map of direct relevance to the proposed seismic structure is between latitudes  $1^{\circ}\text{N}$  to  $4^{\circ}\text{N}$  and longitudes  $34^{\circ}\text{E}$  to  $35^{\circ}\text{E}$  and in this region the locations of the actual measurements are shown.

Fig.7.4. shows a regional Bouguer anomaly map compiled by Darracott et al (1972) and effectively extends the gravity coverage to the whole of the Kenya dome. A comparison of the two maps in the region they overlap shows the problems involved in this process and it is for this reason that the final work from Leicester is desirable.

7.3.

### Relation Between Density and Seismic Velocity

Before proceeding to compare the seismic structure with the observed anomalies it is necessary to consider the relation between the velocities derived earlier and the densities appropriate to the structure.

It is now generally accepted that the low velocity zone in the upper mantle is caused by a degree of partial melting (e.g. Anderson, 1967). It is therefore reasonable to postulate that this is also the cause for the much lower velocities proposed for the structure under discussion. Bott (1965) has argued for this point of view in a discussion of the upper mantle beneath Iceland. Here the anomalous upper mantle was shown by Bath (1960) to have a velocity of 7.4 km/sec and Tryggvasson (1964) has suggested that this

Figure 7.2

A Bouger anomaly map of part of the Kenya Rift taken from Khan and Swain (1974). Dots indicate the location of the measurements made to compile the map between  $1^{\circ}\text{N}$  -  $4^{\circ}\text{N}$  and  $34^{\circ}\text{E}$  -  $35^{\circ}\text{E}$ . The dashed line indicates the section compared with the seismic model.

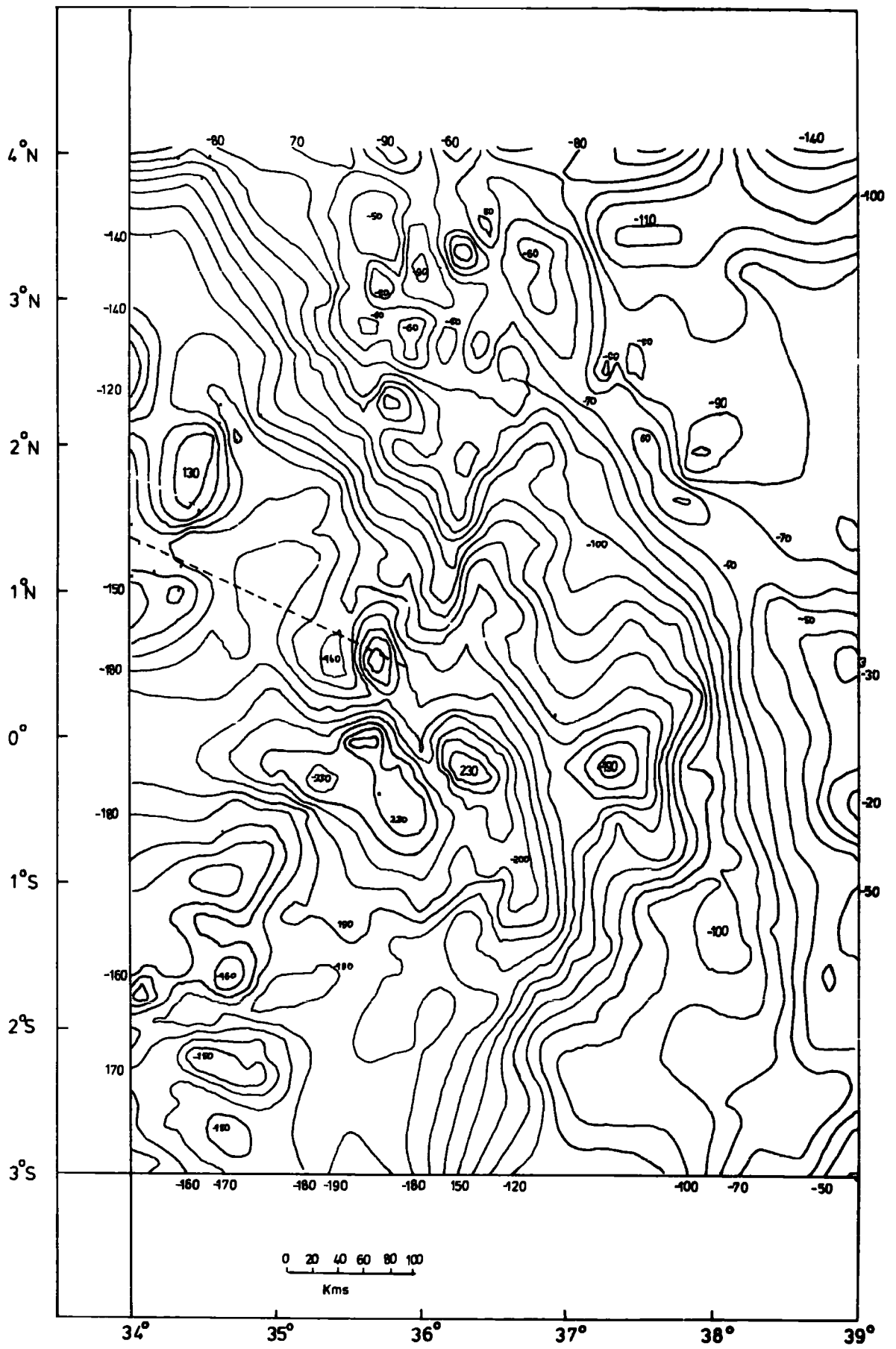


Figure 7.3

A regional gravity anomaly map; from Khan and Swain (1974).

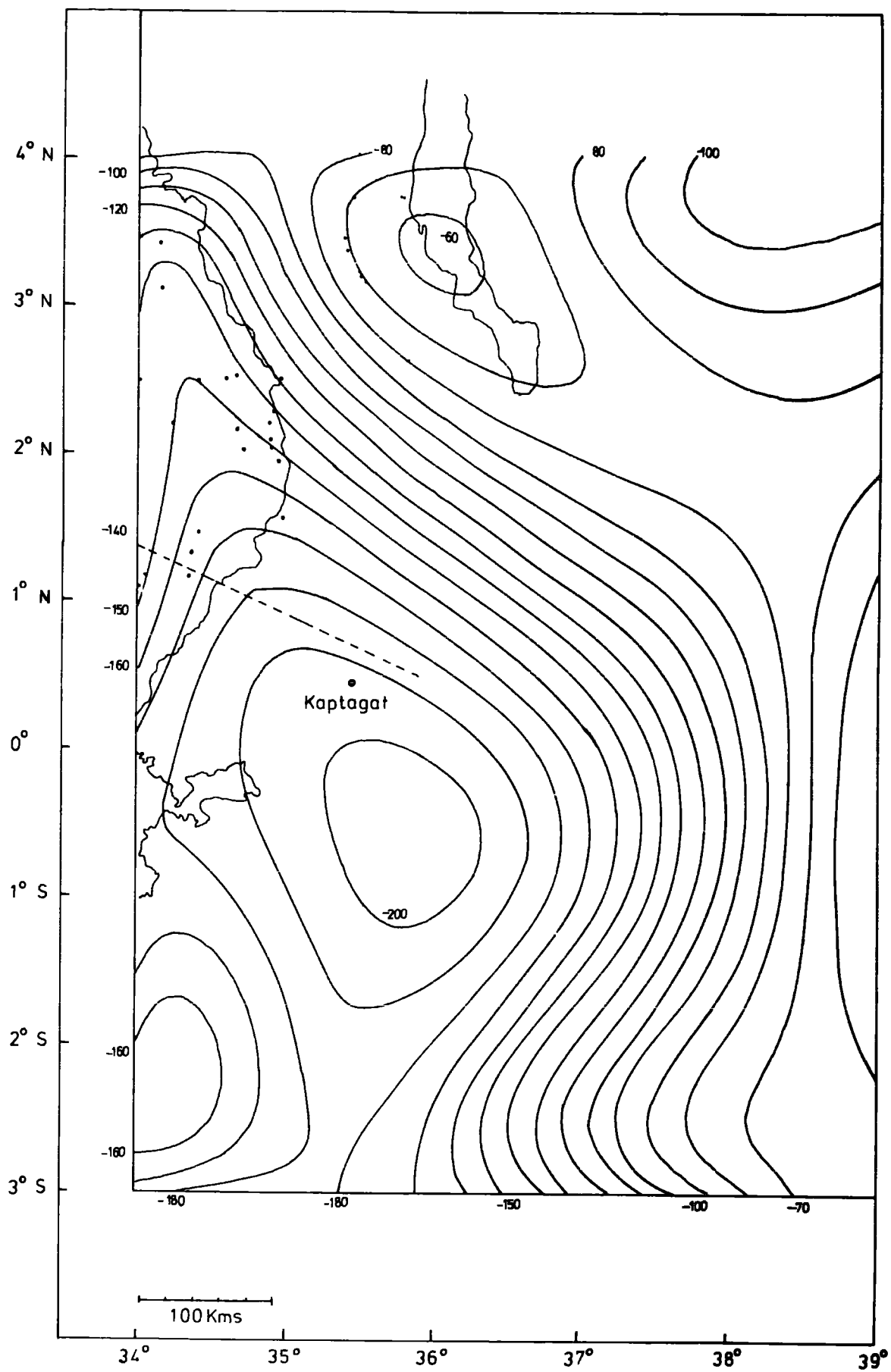
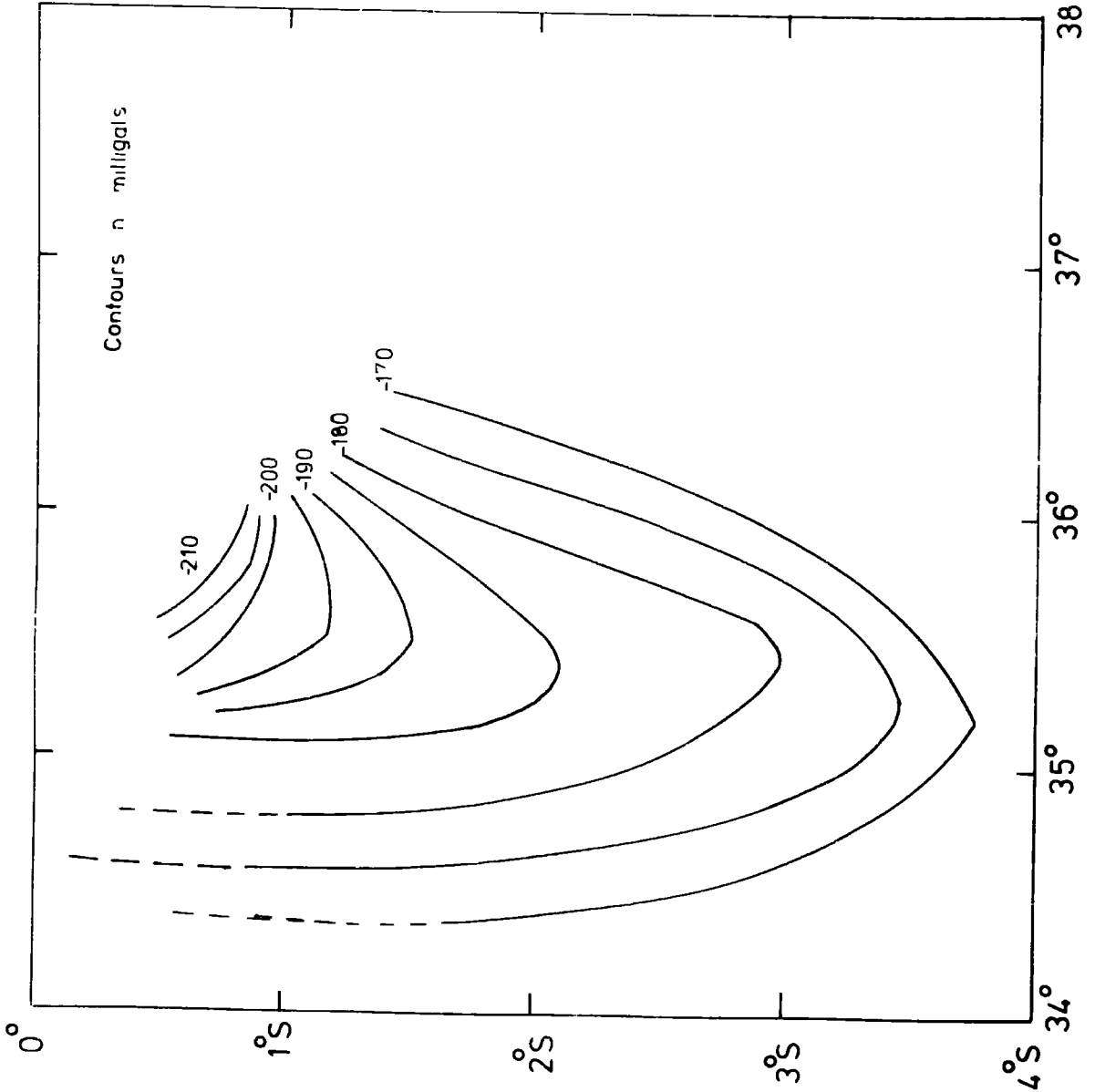


Figure 7.4

A contour map of the regional gravity anomaly for the Kenya rift south of the equator - from Darracott et al (1974).



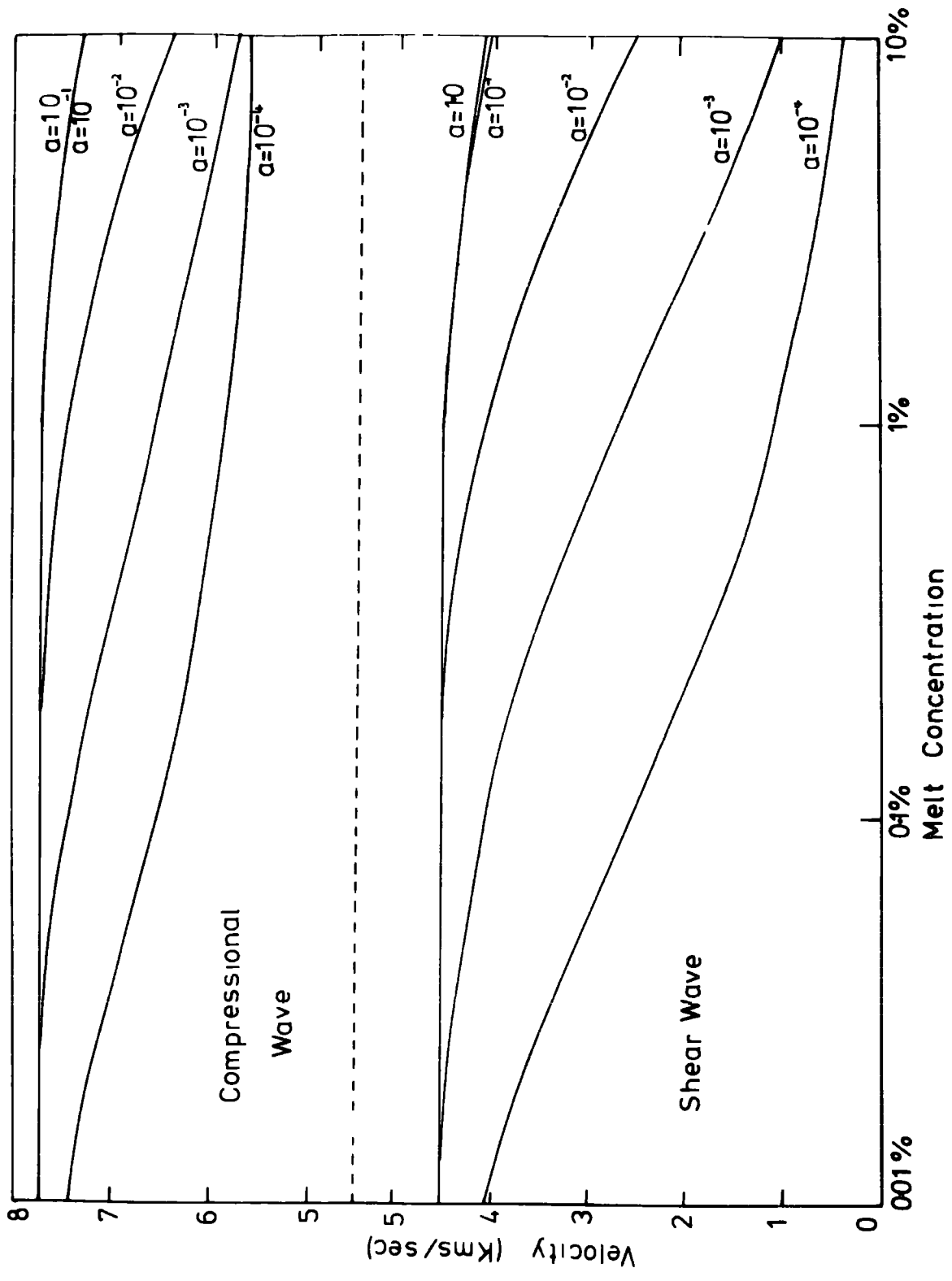
extends to a depth of 240 km. Bott showed that if such a reduction in velocity were to occur for a normal rock type a density contrast of more than 0.1 gms/cc would be expected between normal and anomalous upper mantle and this is in contradiction to the observed gravity anomalies. The most simple solution is to postulate the existence of a partial melt which can cause a considerable reduction in the compressional wave velocity, the reduction to almost zero of the shear wave velocity with a relatively small change in density. (Bott suggested a contrast of 0.03 gms/cc for the above case.)

Attempts to correlate the degree of partial melting with the reduction in velocity have been hindered because so little is known of the mechanism for the melting process. Attempts have been made to simulate the problem using ice-brine systems (Spetzler and Anderson, 1968) but some of the most conclusive results have come from the theoretical work of Walsh (e.g. Walsh, 1969) who has shown that if the melt occurs as randomly oriented ellipsoidal inclusions then the P and S velocities depend critically on the 'aspect ratio' and which is the ratio of the thickness to the length of the inclusion. Fig.7.5. shows how both the degree of melt and the aspect ratio critically effect the problem and it can be seen that an aspect ratio of  $10^{-4}$  could cause a reduction in P wave velocity to approximately 6 km/sec with only 1% of partial melt.

This discussion has shown that at the present time it is not possible to correlate degrees of partial melting, and thus density contrasts, with a reduction in P or S velocities and that a large decrease in seismic velocity is not inconsistent with a relatively small reduction in density.

Figure 7.5

Dependence of P- and S-wave velocities on the melt concentration and aspect ratio  $a$  - see section 7.3 - according to Walsh (1969) - from Anderson and Spetzler (1970).



7.4.

Correlation Between Seismic Models and Regional Gravity Field

First the qualitative features of the regional gravity maps of Khan and Swain (1974) (Fig.7.2.) and Darracott et al (1972) will be considered. In Fig.7.2. the area which may be directly compared with the seismic structure influenced by three unfortunate features. First, in any process which filters out the high frequency components the regions around the borders will be somewhat inaccurate due to edge effects. Secondly, the data coverage in this area is rather sparse, and this will again contribute to the inaccuracy of the regional and, thirdly, the effect of Mount Elgon between  $1^{\circ} - 2^{\circ}\text{N}$  and  $34^{\circ} - 35^{\circ}\text{E}$  makes it difficult to extract the contribution of the upper mantle to the anomaly. In addition, the gradient of the anomaly is remarkably asymmetric about the rift. If measurements are taken from the centre -200 mgal contour then the field increases by only 40 mgals in 200 km in north-westerly and south-westerly directions yet increases by 100 and 110 mgals in similar distances to the north-east and south-east. No such severe asymmetry is present in the field of Darracott et al (1972) or in the traverse of Baker and Wohlenberg (1971). Because of these points it was not possible to use the regional anomaly presented here as a quantitative test for the seismic models put forward.

If the behaviour of the anomaly to the east of the rift is considered it can be seen that, in a qualitative manner, the gravity anomaly behaves in a way very similar to the structure put forward for the north-west quadrant of the rift. The gravity anomaly, and presumably the mantle structure, pinches into the rift as it runs into the Ethiopian dome and as the rift dies out toward the south; the outward movement

of the contours toward the extreme south is somewhat disturbing but it is possible that this is again an edge effect of the map.

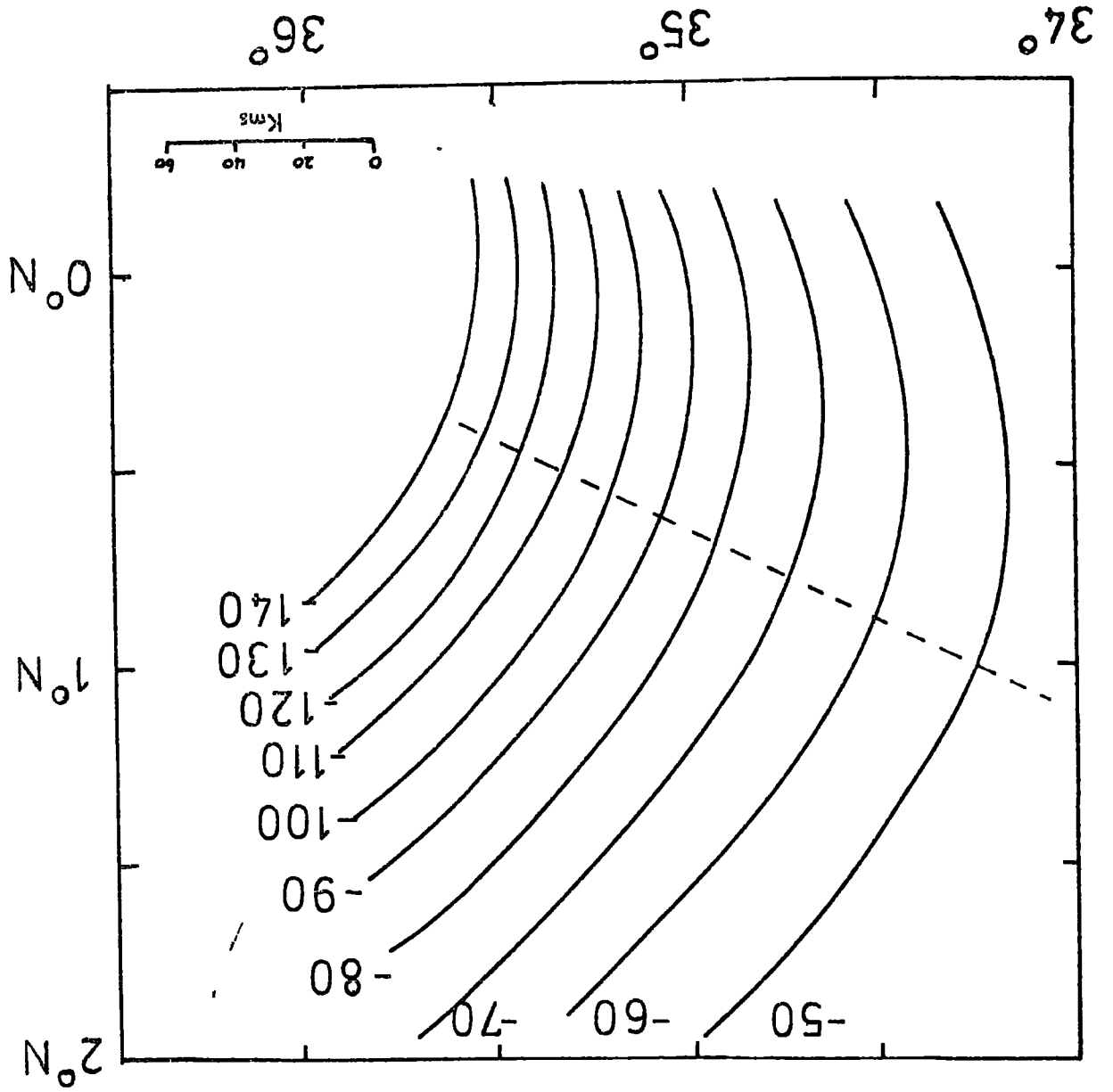
Consequently the traverse of Baker and Wohlenberg (1971) is used as a comparison. Unfortunately this line crosses the rift at approximately the equator and runs in a direction ENE - WSW; also, their traverse does not extend as far west from the rift as the seismic interpretation or the gravity maps of Khan and Swain (1974). Lines 1 and 2 of Fig.7.7. show sections of the regional and Bouguer anomaly maps of Khan and Swain; their position is indicated by the lines on Figs.7.2. and 7.3. Line 3 illustrates the Bouguer anomaly used by Baker and Wohlenberg (1974) in the region where the influence of the short wavelength positive anomaly has been removed. Because both lines refer to different regions of the rift an exact comparison is not possible but the difference in the scale of the gradient is quite obvious.

The optimum seismic model at 6.8 km/sec was taken (Fig.4.7) and as an extreme example a depth to the bottom of the interface of 250 km is assumed. A density contrast of 0.1 gms/cc is assumed to a depth of 80 km beneath which a density contrast of 0.03 gms/cc is assumed. Thus the anomalous mantle is considered to merge into the asthenosphere as the depth increases as postulated for the mantle beneath the mid-Atlantic ridge (Oxburgh and Turcotte, 1968; Solomon and Julian, 1974). The resulting contour map over the surface covered by the seismic structure is shown in Fig.7.6. and the corresponding section is shown as line 3 in Fig.7.7.

Figure 7.6

Gravity map produced from the seismic model assuming a P-wave velocity of  $6.8$  km/sec and a depth of 250 km. A density contrast of 0.1 gm/cc down to 80 km is assumed beneath which a contrast of 0.03 gm/cc is taken. The line indicates the location of the cross-section shown in Fig. 7.7.

Contours in milligals



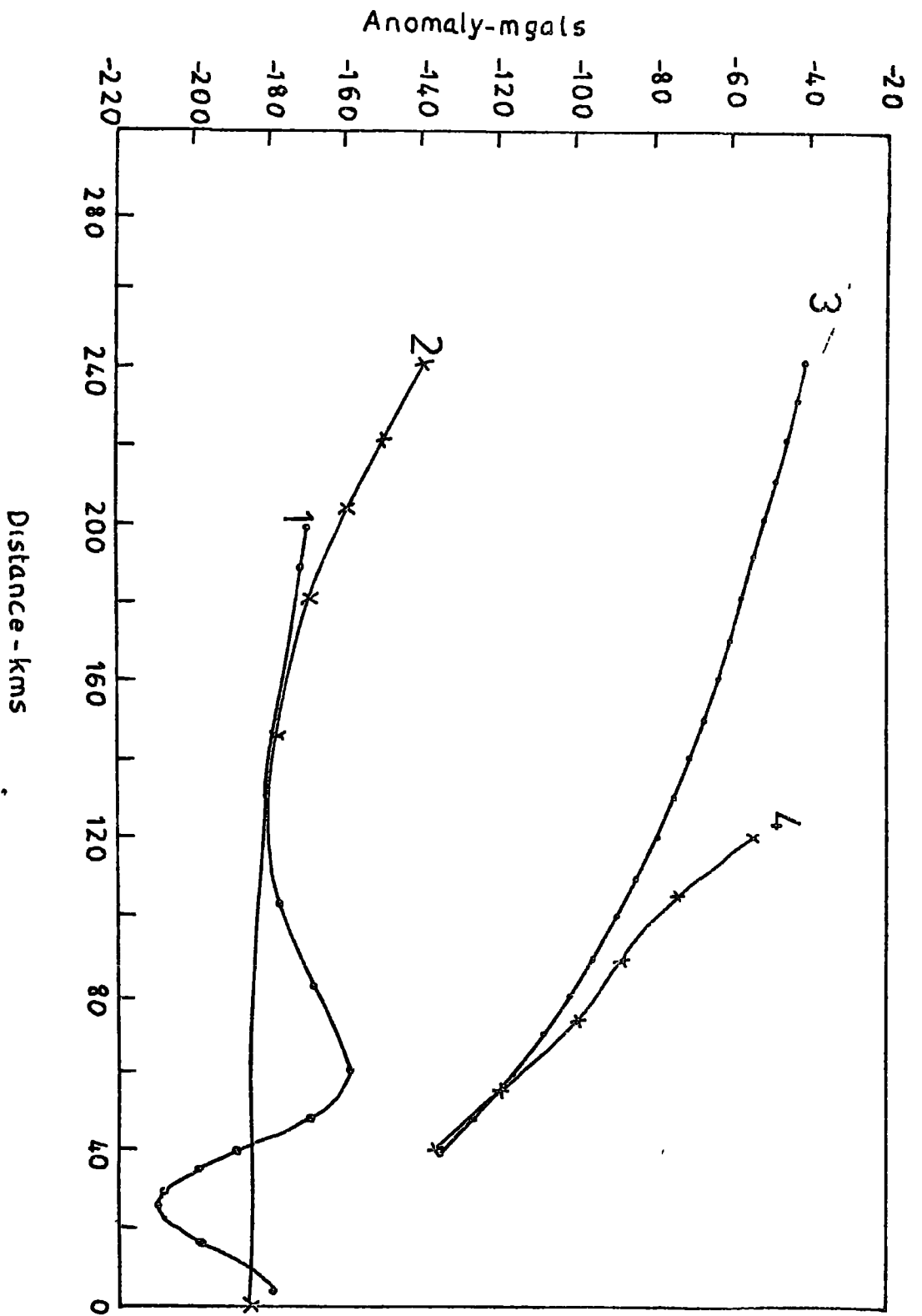


Figure 7.7

Comparison between various anomalies:

1. Bouguer anomaly according to Khan and Swain (1974)
2. Regional anomaly according to Khan and Swain (1974)
3. Anomaly derived from seismic structure.
4. A typical anomaly from Baker and Vohlenberg (1971)

While this cannot be taken as confirming any model it does show that the seismic model proposed is not incompatible with the observed regional gravity fields either in the magnitude or the gradients observed.

## CHAPTER 8

### DISCUSSION AND CONCLUSIONS

#### 3.1. Discussion of Seismic Models Presented

A model has been presented which satisfies the teleseismic slowness and azimuth anomalies measured at the Kaptagat array (Fig.4.7.), if it is assumed that the anomalous upper mantle may be represented as having an average velocity of 6.8 km/sec. Other models may be produced if higher velocities are assumed but any velocity above 7.0 km/sec produces a much poorer fit to the observed data and the maximum possible average velocity, assuming that the observed anomaly is caused by a single interface, has been shown to be less than 7.5 km/sec.

In the model presented for an anomalous velocity of 6.8 km/sec control on the depth of the structure is considered to be good down to approximately 150 km beyond which data is very sparse and often with large errors. If higher velocities are assumed the dips on the structure increase and the depth range covered by the data is consequently expanded.

The models show that the interface between normal and anomalous mantle dips sharply westward to the west of the rift and that further north from the array the structure exhibits a shallower dip with the strike of the surface having a more easterly component indicating a closure of the structure as the rift approaches Ethiopia. Similar effects are observed in the north east sector of the rift in the provisional regional gravity map of Swain and Khan (1974) where the strike of the gravity anomaly, and presumably the surface, has a considerable westerly component.

Relative delay time measurements between Kaptagat and Bulawayo have been interpreted on the basis of the above model. Although the scatter on the data is large, it was shown that the general azimuthal behaviour of the data was consistent with the above model with the most notable feature being that the small variation of delay time with azimuth is consistent with the proposed steeply dipping interface. If a maximum velocity of 7.5 km/sec is assumed then a depth to the bottom of the anomaly of between 300 and 350 km is found (any further restriction on the depth is considered to be unrealistic on consideration of the quality of the delay time data) and if the preferred velocity of 6.8 km/sec is assumed then a depth to the bottom of the anomaly of between 150 and 200 km is found.

A search for reflections from the top surface of the anomaly was made using velocity filtering techniques but was unsuccessful as no arrivals could be identified with confidence; moreover no single explanation could be offered for the fact that this arrival was not observed and on considering all the possibilities this negative result must be considered the most likely outcome of this part of the project.

Finally, the correlation between the observed regional Bouguer anomaly and the postulated seismic model was briefly explored in the last chapter. At the present time it is felt that a satisfactory regional Bouguer anomaly map of the part of the domal uplift sampled by the seismic data is not available; work at present being undertaken by Leicester University is likely to improve this situation considerably and when this is available some very interesting possibilities

are apparent.

3.2. The Relation of the Anomalous Mantle to Various Features

So far there has been very little discussion of the implications of the models presented it being considered better to present, uninterrupted, the line of reasoning which led to the structures proposed.

3.2.1. The Anomalous Mantle as the Cause of the Domal Uplift

The structure proposed is consistent with the theory developed by Gass to describe the development of continental rifting. (This theory and its implications are described and developed most fully in Gass (1970) although a useful summary is also given in Gass (1972).) It is suggested that the initial cause of the process is a localized region of the mantle hotter than its surroundings. The experimental studies of Elder (1966) are cited for the spatial development of such systems; the term 'penetrative convection' is used to describe the convective process involving both heat and mass transfer. The thermal activity produces quantities of magma and the increase in the thermal gradient leads to the transition of the high pressure-low temperature mineral forms to their less dense low pressure-high temperature forms. The resulting increase in volume is most easily accommodated by vertical movement and this is postulated as the cause of the region of domal uplift. The system is envisaged as developing to produce crustal penetration and finally separation.

A model of this process is shown in Fig.8.1. (after Gass (1972)) and it can be seen that stage (b) is very similar to the models proposed here. The major discrepancy

Figure 8.1

Schematic representation of magma genetic and tectonic stages in transcontinental rupture

- a) Perturbation in asthenosphere, development of tabular magmatic body, doming of surface and eruption of alkalic undersaturated basalts.
- b) Concentration of magmatic activity along major rift zone, attenuation of lithosphere beneath rift and eruption of transitional basalts within rift.
- c) Continuing magmatic activity in rift zone elevates the mantle isotherms so that magma can equilibrate at very shallow depths. With continued intrusion of basaltic dykes along the fracture the once contiguous lithosphere plates are separated.
- d) Idealized three dimensional diagram to show how the magma genetic zone in c) is elongate and exists all along the rift zone.

(Gass, 1972.)

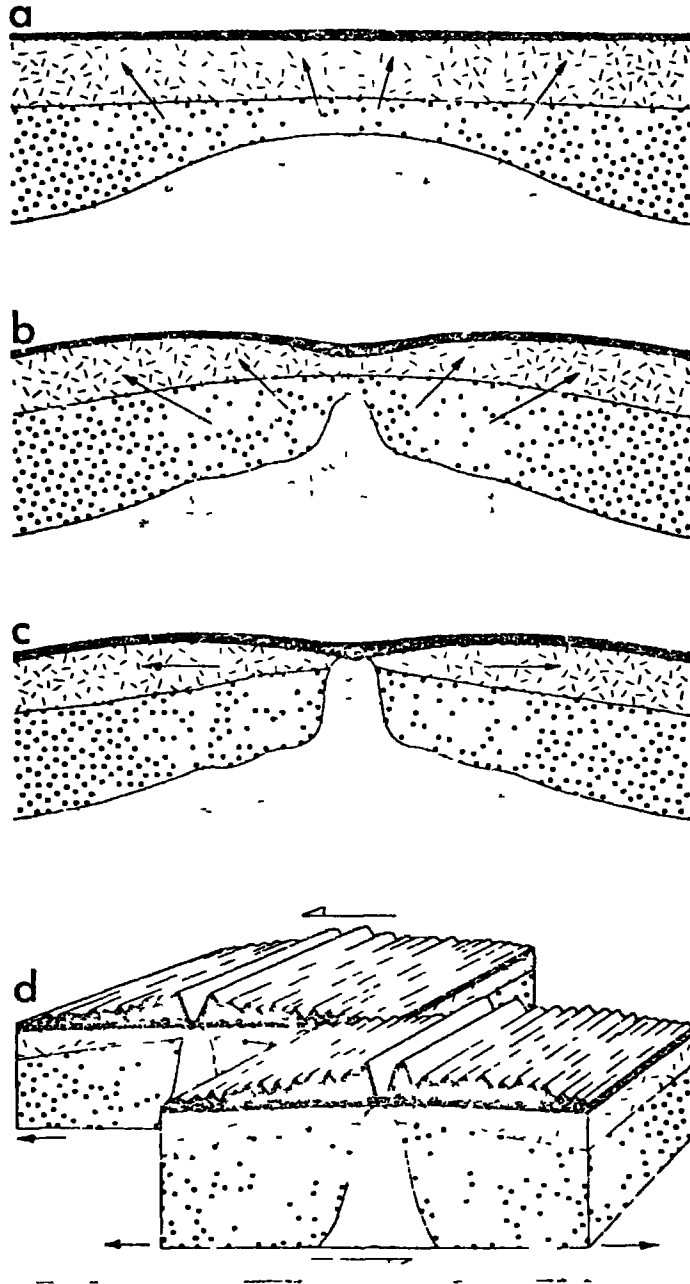


Fig. 1

between the two structures is that here Gass envisages the thermal disturbance being located at the lithosphere-asthenosphere boundary put at a depth of 100 km. No reason is given for this choice and in the more detailed work cited above (Gass, 1970) the 'lithothermal system' is projected to a depth in excess of 150 km.

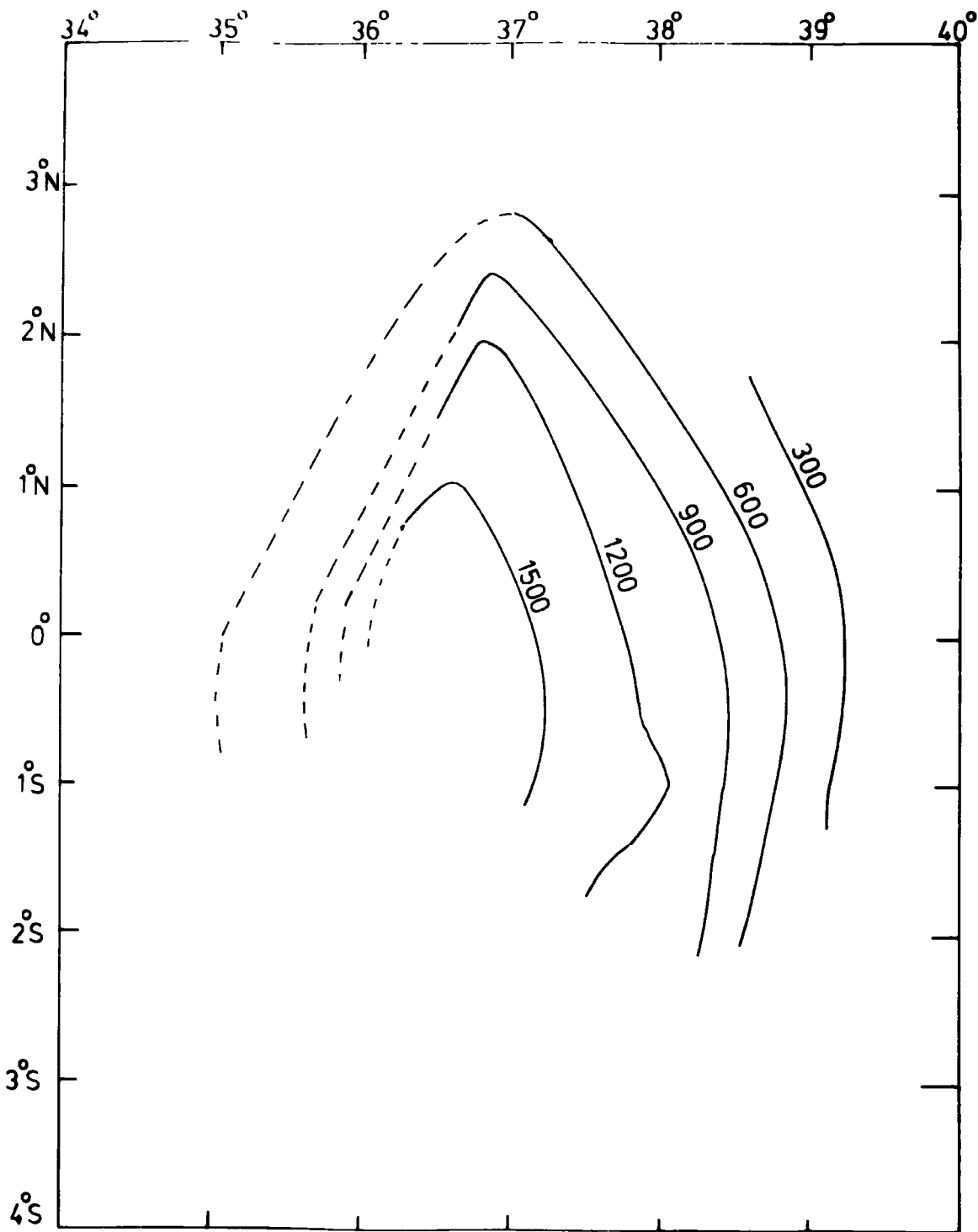
In quantitative terms Magnitsky and Kalashnikova (1970) have shown that a density change of 0.2 gms/cc over a region of some 35 km would produce an uplift of approximately three kilometres and thus in the present model a much smaller density change over a much larger region would cause a similar effect.

If this theory is valid it is reasonable to compare the observed domal uplift with the proposed mantle structure. In order to do this satisfactorily the dynamic development of the upper mantle must be considered and the resulting topographic structure calculated. An attempt is being made to solve this problem in association with D.J. Woodward; it is hoped to be able to calculate both densities and temperatures within the upper mantle for various heat sources and to consider the development, in time, of both the upper mantle and surface topography.

Although the results of these calculations are not available at the present time the qualitative features of the correlation may be seen in Fig.8.2. where the topographic contours of the Kenya dome are illustrated. Unfortunately the region which could be correlated directly is strongly influenced by the rift faulting and Mount Elgon and the contours to the east of the rift have been used to extrapolate the

Figure 8.2

Topography of the Kenya dome to the east of the Gregory Rift, dashed lines indicate that the contours have been extrapolated and the effects of faulting have been neglected. The actual contours are from Baker et al (1972).



structure to the north west quadrant. It can be seen that the strike of both the upper mantle anomaly and the surface topograph are very similar although detailed comparisons of gradients must await further analysis.

.2.2. The Relation of the Ethiopian and Kenyan Domal Uplifts

Le Bas (1971) has suggested that the two structures are essentially independent and considers that they do not represent an early stage in the development of an oceanic rift as is the natural conclusion of the theory of Gass. While it is agreed that the two structures did develop independently, and this work would support the concept that any contact between the two structures is at a considerable depth within the asthenosphere, it is considered that this is not an obstacle to the theory of Gass for the following reasons.

If the development of the rift system is considered two points are apparent. First, the rift has developed, both in Kenya and Ethiopia, in a sporadic fashion. Saggerson and Baker (1965) show that there were three main periods of uplift which were interspersed with long periods of quiescence and secondly, the history of both systems shows that the Kenyan uplift is at an earlier stage of development than the Ethiopian structure (see section 1.1.2. for details). Gass considers that continental rifting occurs when these isolated disturbances join together. Clearly, this stage has not been reached but this is not to say that the process has stopped rather that it is in another quiescent stage. In this light, any tensional process envisaged for continental rifting, for example that of Oxburgh and Turcotte (1974), is

likely to cause intermittent movements in its early stages, rather the apparently continuous movements of oceanic rifting and the present theories of plate movements may only be applicable when rifting has occurred along the whole length of the African plate.

Thus the rift system may indeed be the beginning stages of oceanic rifting but the development to the complete oceanic form could take a great deal longer than expected and we are observing the early stages of a long process.

### 2.3. The East African Rift and Other Continental Rifts

The seismic refraction line of Griffiths et al (1972) has indicated a 20 km thick layer with velocity 6.4 km/sec overlying material with an apparent velocity of 7.5 km/sec. This latter has been ascribed to the top surface of the anomalous body under discussion. Refraction studies indicate that the upper mantle, or at least the top surface of it, beneath other continental rifts have somewhat similar low velocities; 7.1 - 7.5 km/sec for the Baikal Rift (Artemjev and Artyushkov, 1971) and 7.2 - 7.7 km/sec for the Rhine Graben (Mueller et al, 1969). Baker and Wohlenberg (1971) show that the uplift surrounding the Grefory Rift has reached 1.7 km since mid-Tertiary and similar uplifts are observed in the continental rifts already mentioned (Illies, 1969).

### 2.4. The East African Rifts and Oceanic Rifts

Of rather more interest is the comparison with the mid-oceanic rifts, as within the last twenty years a vast amount of effort has been spent on elucidating their structure.

The structure of the crust and upper mantle beneath Iceland shows a remarkable similarity with that derived for

beneath the rift. Bath (1960) found a 6.71 km/sec layer to a depth of 17.8 km with a velocity of 7.38 km/sec beneath; Tryggvason (1964) showed that relative delays between Kiruna (Sweden) and Reykjavik implied a thickness of approximately 240 km for an anomaly with this velocity.

The deep structure of the submerged mid-ocean ridges has been investigated using seismic refraction and gravity studies. Velocities of 7.3 - 7.4 km/sec have been found for the upper mantle beneath the mid-Atlantic ridge (Ewing and Ewing, 1959; Le Pichon et al, 1965) and 7.3 - 7.6 km/sec for the East Pacific Rise (Le Pichon et al, 1965) while Fig.8.3. shows a gravity interpretation of the mid-Atlantic Ridge from Talwani et al (1965).

In total the general structure beneath the mid-ocean ridges is very similar to that postulated for beneath the rift. However, the details of the structures are not known and cannot be used as a control for the East African models.

Some indications of these are given from theoretical studies of the mid-ocean ridges. One of the most interesting calculations is that of Oxburgh and Turcotte (1968) who investigated the thermal regime of an ascending plume of hot material beneath the ridge. Fig.8.4. shows a model taken from this paper which indicates the zone of fusion and the numbers indicate the zones within which the temperature exceeds the olivine-tholeiite fusion temperature by the number of degrees centigrade indicated. While it is obviously difficult to transfer the scale of this structure directly to the mantle beneath East Africa it is of interest that the structure is similar to that being put forward. It will be noted that quite a considerable degree of partial melting is

Figure 8.3

Crust and upper mantle model for the mid-Atlantic Ridge  
from gravity interpretation (Talwani et al, 1965).

Densities are in gm/cc.

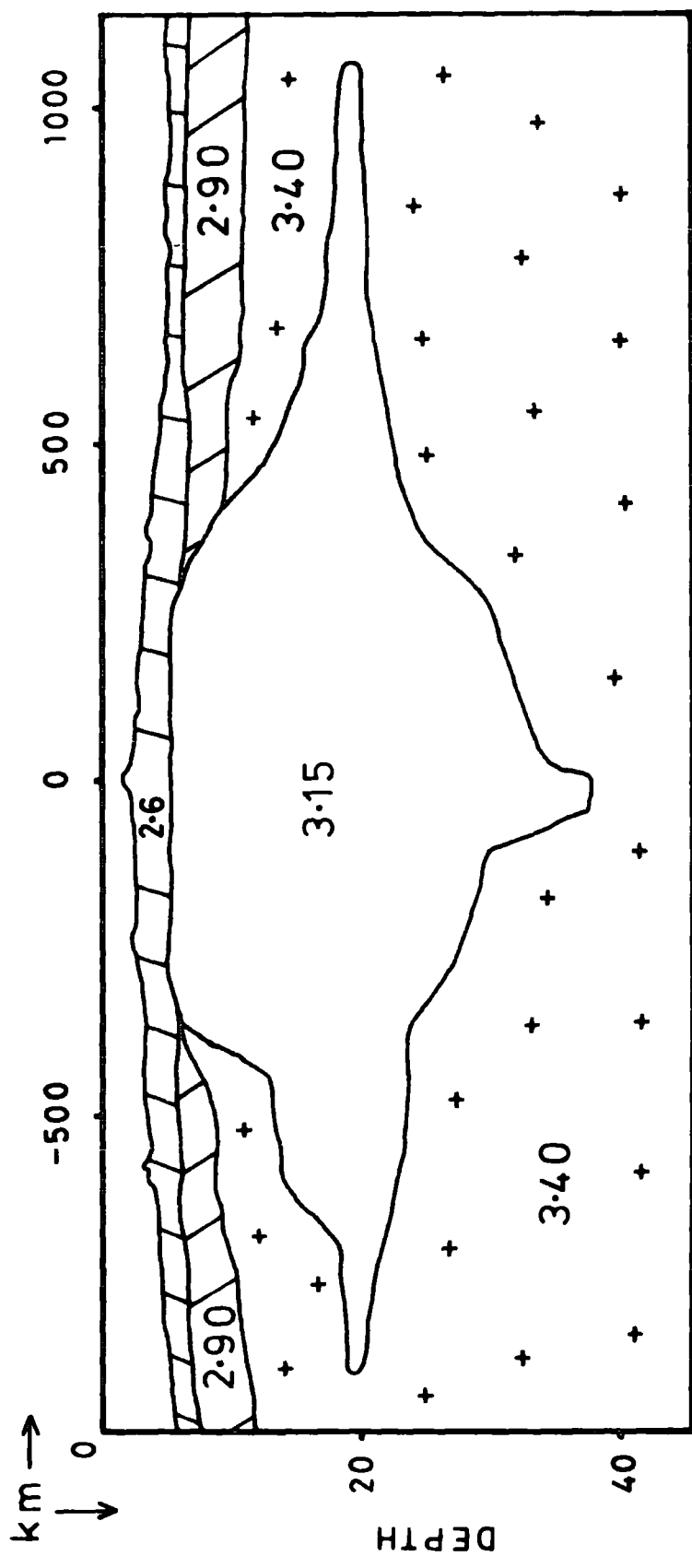
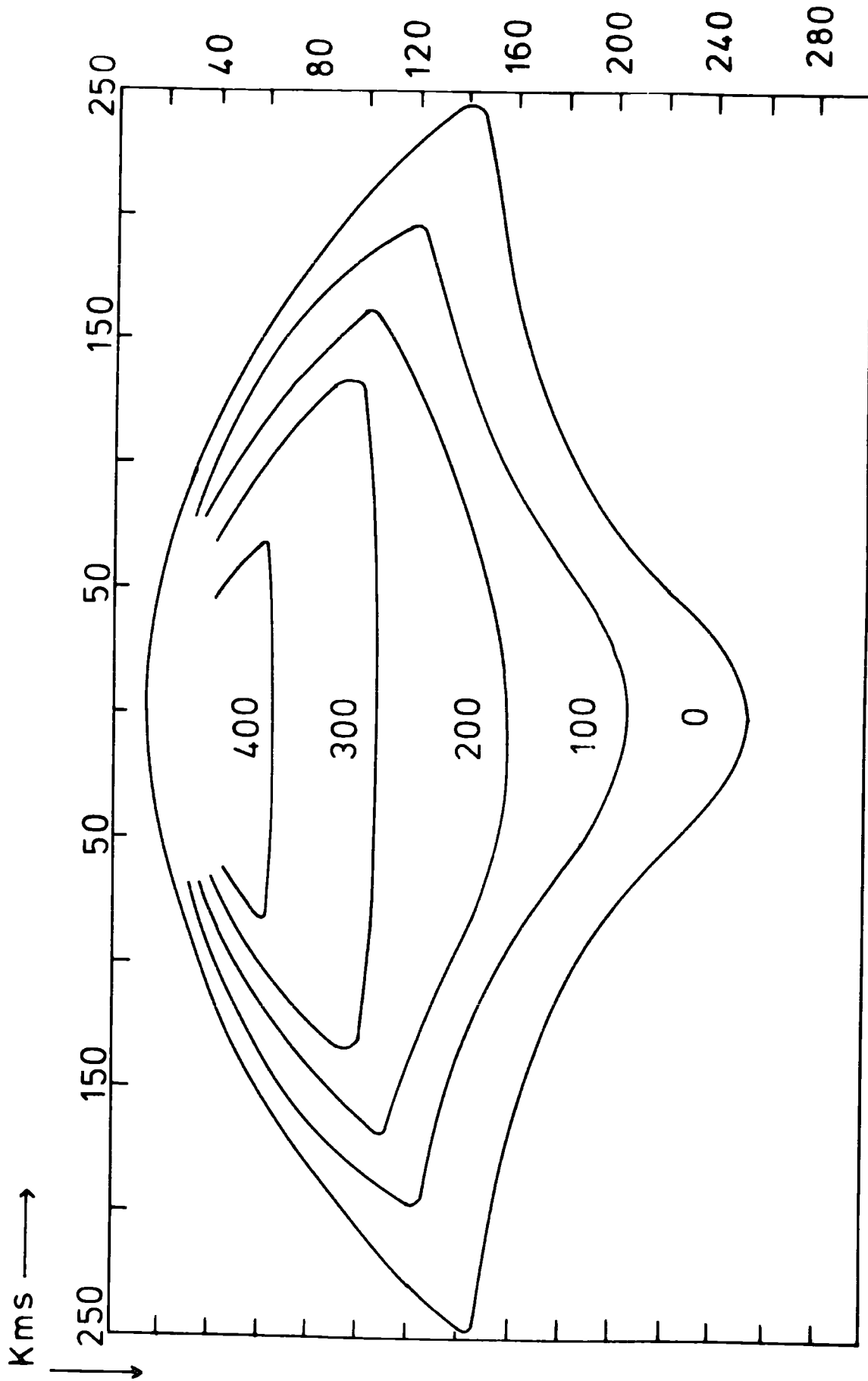


Figure 8.4

Structure of the upper mantle beneath mid-ocean ridges from Oxburgh and Turcotte (1968). Numbers indicate the number of degrees centigrade by which the predicted temperature exceeds the olivine-tholeiite fusion temperature.



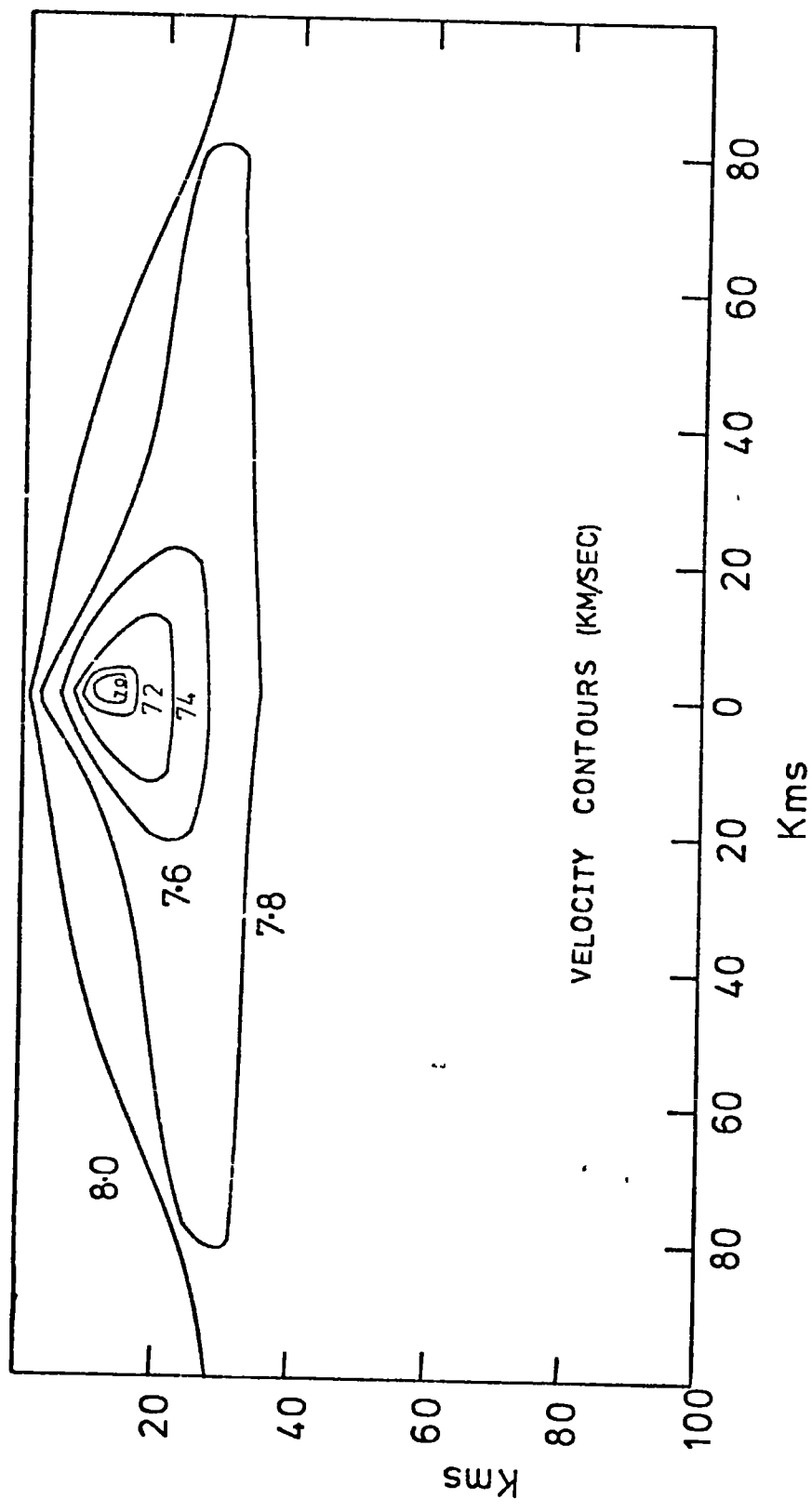
predicted and that from the discussion of section 7.3. there will be a considerable velocity gradient both vertically and laterally within the structure. Fig.8.5. shows a diagram from the work of Solomon and Julian (1974) with a similar purpose but from a different viewpoint. By assuming a temperature field in the crust and mantle, composition and a velocity-density model it is possible to predict the velocity distribution beneath the ridge. The shape of the structure is similar to that of Oxburgh and Turcotte (1968) although the scale is smaller. The model again has considerable velocity structure down to a minimum of 7.0 km/sec. The details of this model are considered suspect and, in particular, the conversion from a degree of partial melt to velocity is fraught with difficulties (for a fuller discussion see section 7.3.) and the work of Oxburgh and Turcotte (1968) is considered a more useful guide. This paper does, however, make two interesting points. It is suggested that the effects of refraction through the interfaces shown will cause the rays to be deviated and as a result the earthquake fault plane solution will exhibit non-orthogonal nodal planes. By studying the orientation they suggest that information on the structure at source may be found. They also conclude that the variation of delay time with azimuth is also insensitive to the geometry of the structure.

### 3. Velocity Determination and the Shape of the Structure

The entire analysis presented in this thesis has rested on two assumptions. First, that the anomaly can be interpreted on the basis of a single interface and secondly that the concept of an average velocity is meaningful in this context. The justification for these assumptions is now discussed.

Figure 8.5

Contours of constant P-wave velocity for the mantle  
beneath the mid-ocean ridge - from Solomon and  
Julian (1974).



The theoretical work of Oxburgh and Turcotte (1968) and Solomon and Julian (1974) provides welcome support for the assumption that the anomaly is most strongly influenced by the upper interface. Thus in Fig.8.4. the regions with the highest degrees of partial melting have an almost flat bottom surface and will thus cause negligible slowness anomalies and it is only at the lower degrees of partial melting that an appreciable dip occurs on the lower interface. It must be remembered that the situation at the oceanic ridge is dynamic compared with the almost static case of the continental rift. It is envisaged rather that the litho-thermal disturbance causing the upwelling gradually subsides with depth until it merges with normal asthenosphere so that density and velocity contrasts slowly change to zero. Fig.8.5. is even more encouraging from this point of view in that nearly the whole anomaly would be caused by the top interface.

The second point concerns the velocity and is rather more difficult to deal with; the two models already quoted indicate that velocity structure within the anomaly is considerable. Moreover, it will be realized that the 'average' velocity so far discussed is an immensely complicated quantity depending on the weighted travel paths for all the events. One further complication is that the average velocity as defined by an azimuth anomaly differs from the average velocity defined by the slowness anomalies in a structure with a velocity gradient. Unless the gradient is severe this effect is not significant but it does indicate the complexity of the problem. Certainly because of these problems detailed conclusions about the exact shape of the body cannot be drawn but the general size and structure is considered to be well

controlled by the data.

The question of the most suitable average velocity is uncertain. Optimum models were reached at velocities between 6.8 and 7.0 km/sec although further reduction in the velocity reduced the minimum value of the function slightly. However, since the top of the structure is believed to have an approximate velocity of 7.5 km/sec an average velocity of 6.8 km/sec implies an extremely low minimum velocity. Fig.7.5. shows that a huge degree of partial melt in the most favourable circumstances cannot reduce the P wave velocity much below 6.0 km/sec. Although it is not certain, a mean P wave velocity of approximately 7.0 km/sec is preferred which implies a thickness of some 200 km before normal asthenosphere occurs.

#### 4. Conclusions

The analysis of teleseismic signals arriving at the Kaptagat array station suggests that the mantle beneath the Gregory Rift of East Africa consists of a low velocity body with steeply dipping sides near the rift which become gentler as the structure deepens. The structure has been shown to be truly three dimensional in that it deepens on going north and west from Kaptagat and any connection with the assumed similar body beneath the Ethiopian dome must be at a considerable depth. The optimum average compressional velocity is found to be between 6.8 km/sec and 7.0 km/sec implying a depth to the 'bottom' of the anomaly of some 200 km.

These results have provided the basis to undertake a further stage in the analysis of the upper mantle structure beneath the rift and at the time of writing a new experiment

is starting. The emphasis in this experiment has changed from array stations to the use of fairly closely grouped stations consisting of three component sets. With the processing techniques developed, and in process of development, at Durham, it is hoped to derive the angle of approach of locals and teleseisms at each three component set and thus derive considerably more information of the type used in the present analysis; consequently, it is hoped that considerably more of the upper mantle can be mapped.

In addition it is considered that much useful information can be derived from using the resulting seismic models in a region where the gravity control is better but this must await the publication of the Leicester gravity study being undertaken.

Appendix A Calculation of the Normal to a Refracting Surface.

Vectors  $\hat{\underline{I}}$  and  $\hat{\underline{T}}$  are derived from the measured and theoretical velocities as described in section 3.5.

$\hat{\underline{N}}$  represents the normal to the surface causing refraction.

By Snell's Law  $\hat{\underline{I}}$ ,  $\hat{\underline{N}}$  and  $\hat{\underline{T}}$  are co-planar and this is expressed by the condition

$$\begin{vmatrix} n_1 & n_2 & n_3 \\ i_1 & i_2 & i_3 \\ t_1 & t_2 & t_3 \end{vmatrix} = 0$$

which may be written

$$n_1 \cdot (i_2 \cdot t_3 - i_3 \cdot t_2) + n_2 \cdot (i_3 \cdot t_1 - i_1 \cdot t_3) + n_3 \cdot (i_1 \cdot t_2 - i_2 \cdot t_1) = 0 \quad A-(1)$$

(This may be shown as follows: define the normal to the plane  $\Pi$  containing  $\hat{\underline{I}}$ ,  $\hat{\underline{N}}$  and  $\hat{\underline{T}}$  as  $\hat{\underline{N}}'$  then

$$\begin{aligned} \hat{\underline{N}}' \cdot \hat{\underline{N}} &= 0 \\ \hat{\underline{N}}' \cdot \hat{\underline{I}} &= 0 \\ \hat{\underline{N}}' \cdot \hat{\underline{T}} &= 0 \end{aligned}$$

then

$$\begin{aligned} n_1' \cdot n_1 + n_2' \cdot n_2 + n_3' \cdot n_3 &= 0 \\ n_1' \cdot i_1 + n_2' \cdot i_2 + n_3' \cdot i_3 &= 0 \\ n_1' \cdot t_1 + n_2' \cdot t_2 + n_3' \cdot t_3 &= 0 \end{aligned}$$

which for a non-trivial solution requires the determinant to be zero.)

If the refracted angle, which is taken as the angle within normal mantle material, is  $\phi$  then

$$\hat{\underline{N}} \cdot \hat{\underline{I}} = \cos \phi$$

$$n_1 \cdot i_1 + n_2 \cdot i_2 + n_3 \cdot i_3 = \cos \phi \quad \text{A-(11)}$$

and the properties of the direction cosines requires

$$n_1^2 + n_2^2 + n_3^2 = 1 \quad \text{A-(111)}$$

Equations A-(1), A-(11) and A-(111) may be solved simultaneously to give two solutions which correspond to the normal being between the obtuse or reflex angle between  $\hat{\underline{I}}$  and  $\hat{\underline{T}}$ . These correspond to a reflection and refraction and the refraction is chosen. The angle of incidence is steadily increased and the behaviour tested against Snell's Second Law. By an iterative process a solution of any required accuracy may be found. This procedure was carried out in the computer program listed NORMAL.

Appendix B Ray Tracing Procedures.

B.1. Calculation of reflection and refraction in three dimensions.

Consider a ray originating from  $\underline{S} (s_1, s_2, s_3)$  and incident upon a surface  $\phi(x_1, x_2, x_3) = 0$  at  $\underline{P} (p_1, p_2, p_3)$  where  $(x_1, x_2, x_3)$  is a right handed co-ordinate system as shown (Fig.B.1.)

In the present work  $\phi$  is described by

$$\phi(x_1, x_2, x_3) = ax_1^2 + bx_2^2 + cx_3^2 - 1 = 0 \quad \text{B-(1)}$$

which may be written more compactly as

$$X^T A X = 1 \quad \text{B-(11)}$$

where

$$A = \begin{pmatrix} a & 0 & 0 \\ 0 & b & 0 \\ 0 & 0 & c \end{pmatrix}$$

and

$$X = \begin{pmatrix} x_1 \\ x_2 \\ x_3 \end{pmatrix}$$

and  $X^T$  is the transpose of  $X$ .

If  $\hat{\underline{I}} (i_1, i_2, i_3)$  are the direction cosines of the ray from  $\underline{S}$  to  $\underline{P}$  and its length is  $L$  then

$$\underline{P} = \underline{S} + L \cdot \hat{\underline{I}} \quad \text{B-(111)}$$

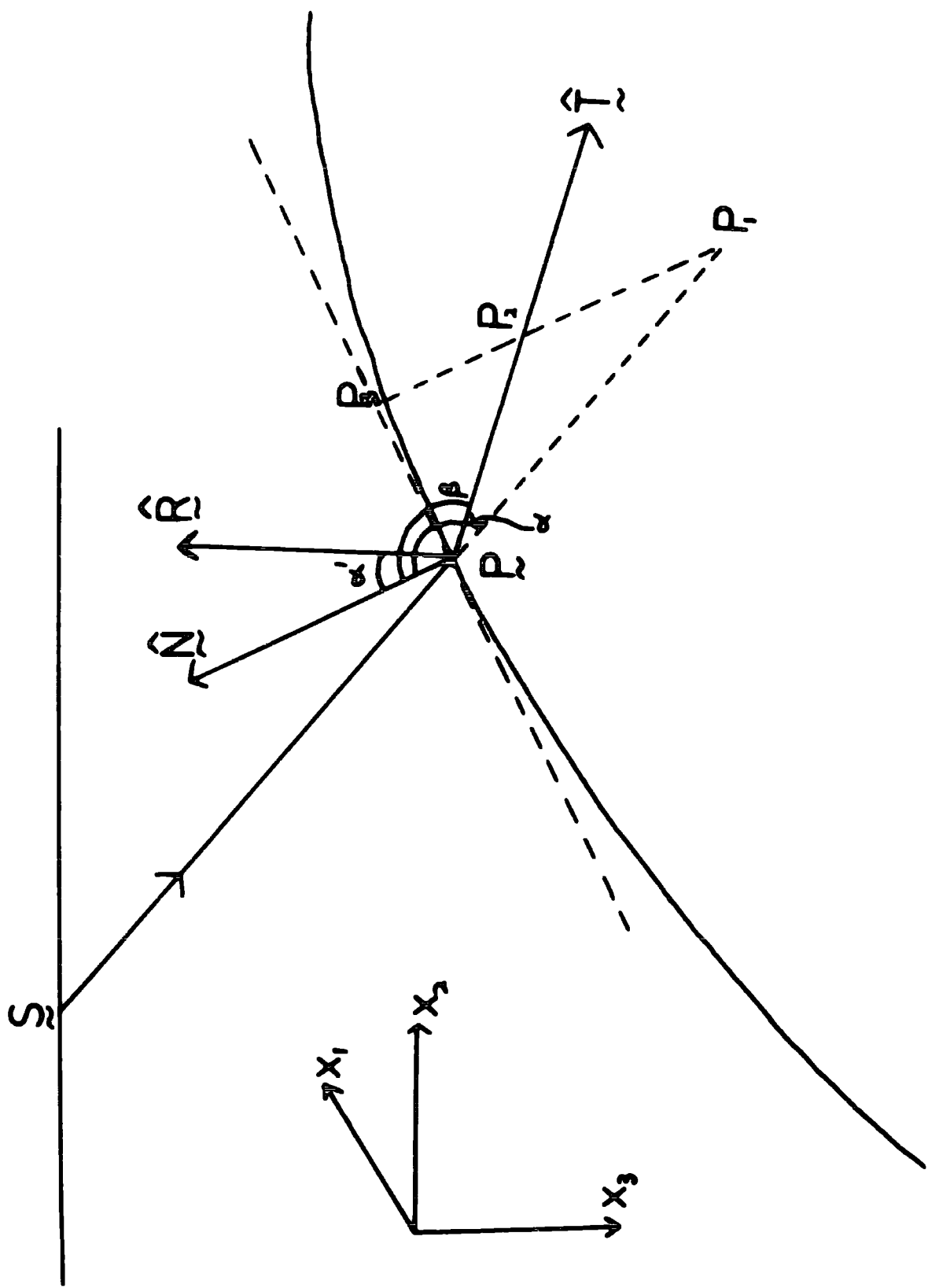
Now  $\underline{P}$  lies on the surface  $\phi = 0$  and so must satisfy B-(1)

so that

$$\begin{aligned} \underline{P}^T \cdot A \cdot \underline{P} &= 1 \\ (\underline{S}^T + L \cdot \hat{\underline{I}}^T) \cdot A \cdot (\underline{S} + L \cdot \hat{\underline{I}}) &= 1 \end{aligned}$$

Figure 3.1

Diagram to illustrate ray tracing procedures.



$$L^2.(\hat{\underline{I}}^T.A.\hat{\underline{I}}) + L.(\underline{S}^T.A.\hat{\underline{I}} + \hat{\underline{I}}^T.A.\underline{S}) + \underline{S}^T.A.\underline{S} = 1 \quad B-(1v)$$

This quadratic in L may be solved to give, in general, two solutions and the required root must be chosen. Once the value of L has been calculated P may be determined from B-(111).

In order to calculate the reflected and refracted rays the normal  $\hat{\underline{N}} (n_1, n_2, n_3)$  at  $\underline{P}$  must be calculated. The direction of the normal to the junction is given by

$$\nabla\phi = \hat{\underline{i}} \frac{\partial\phi}{\partial x_1} + \hat{\underline{j}} \frac{\partial\phi}{\partial x_2} + \hat{\underline{k}} \frac{\partial\phi}{\partial x_3}$$

(where  $(\hat{\underline{i}}, \hat{\underline{j}}, \hat{\underline{k}})$  are unit vectors in the direction of the axes) and the direction cosines of the normal are given by

$$\hat{\underline{N}} = \frac{\nabla\phi}{(\nabla\phi^T \nabla\phi)^{1/2}} \quad B-(v)$$

By Snell's First Law the incident ray, the normal and the transmitted ray ( $\hat{\underline{T}}$ ) all lie in the same plane and thus  $\hat{\underline{T}}$  may be written

$$\hat{\underline{T}} = c_1 \hat{\underline{I}} + c_2 \hat{\underline{N}}$$

and from Fig.B.1. it may be seen that

$$PP_2.\hat{\underline{T}} = PP_1.\hat{\underline{I}} + P_1P_2.\hat{\underline{N}} \quad B-(v1)$$

The velocity of the incident, transmitted and refracted rays are denoted  $V_1$ ,  $V_t$ , and  $V_r$  respectively.

The angle of incidence,  $\alpha$ , is given by

$$\cos \alpha = \hat{\underline{I}}.\hat{\underline{N}}$$

where  $\alpha > \frac{\pi}{2}$  for a downgoing ray since  $n_3 < 0$ . Snell's Second Law now gives

$$\frac{\sin \alpha}{V_1} = \frac{\sin \beta}{V_t} \quad B-(v11)$$

Where for the downgoing ray  $\beta > \frac{\pi}{2}$

From plane trigonometry

$$PP_3 = PP_1 \cdot \sin(\pi - \alpha) = PP_1 \cdot \sin \alpha \quad B-(v_{111})$$

and

$$PP_2 = \frac{PP_3}{\sin(\pi - \beta)} = PP_1 \cdot \frac{\sin \alpha}{\sin \beta} \quad B-(1x)$$

and

$$P_1P_3 = PP_1 \cdot \cos(\pi - \alpha) = -PP_1 \cdot \cos \alpha$$

$$P_2P_3 = PP_2 \cdot \cos(\pi - \beta) = -PP_2 \cdot \cos \beta = -PP_1 \cdot \sin \alpha \cdot \cot \beta$$

so that

$$\begin{aligned} P_1P_2 &= P_1P_3 - P_2P_3 \\ &= -PP_1 \cdot \cos \alpha + PP_1 \cdot \sin \alpha \cdot \cot \alpha \\ &= \frac{PP_1 \cdot \sin(\alpha - \beta)}{\sin \beta} \quad B-(x) \end{aligned}$$

Inserting equations B-(1x) and B-(x) into B-(v1)

$$P_1P_2 \hat{\underline{I}} + PP_1 \cdot \frac{\sin(\alpha - \beta)}{\sin \beta} \cdot \hat{\underline{N}} = PP_1 \cdot \frac{\sin \alpha}{\sin \beta} \cdot \hat{\underline{T}}$$

$$T = \frac{\sin \beta}{\sin \alpha} \cdot \hat{\underline{I}} + \frac{\sin(\alpha - \beta)}{\sin \alpha} \cdot \hat{\underline{N}} \quad B-(xi)$$

and by B-(v11)

$$\hat{\underline{T}} = \frac{V_t}{V_1} \hat{\underline{I}} + (\cos \beta - \cos \alpha \cdot \frac{V_t}{V_1}) \cdot \hat{\underline{N}} \quad B-(x_{11})$$

The reflected ray  $\hat{\underline{R}}$  is most easily calculated by replacing  $\beta$  by  $\alpha'$  and  $V_t$  by  $V_r$ . Thus from B-(x<sub>11</sub>)

$$\hat{\underline{R}} = \frac{V_r}{V_1} \hat{\underline{I}} + (\cos \alpha' - \frac{V_t}{V_1} \cdot \cos \alpha) \cdot \hat{\underline{N}}$$

and for the particular case considered in chapter 6 when incident P and reflected P only are considered

$V_r = V_1$  and  $\alpha + \alpha' = \pi$  the equation simplifies to

$$\begin{aligned} \hat{\underline{R}} &= \hat{\underline{I}} + (\cos(\pi - \alpha) - \cos \alpha) \cdot \hat{\underline{N}} \\ &= \hat{\underline{I}} - 2 \cdot \cos \alpha \cdot \hat{\underline{N}} \quad B-(x_{111}) \end{aligned}$$

B.2. Ray Tracing through Plane Parallel Structures.

Consider the ray  $\hat{\underline{I}} (i_1, i_2, i_3)$  incident at the plane boundary  $x_3 + c = 0$  so that  $\hat{\underline{N}} = (0, 0, -1)$ . The angle of incidence  $\alpha$  is given by

$$\cos \alpha = \hat{\underline{N}} \cdot \hat{\underline{I}} = -i_3 \quad \text{B-(xiv)}$$

The direction cosines of the transmitted ray are now given by B-(xiii)

$$t_1 = \frac{v_t \cdot i_1}{v_1}$$

$$t_2 = \frac{v_t \cdot i_2}{v_1}$$

$$t_3 = -\cos \beta$$

$$(t_1, t_2, t_3) = \left( \frac{v_t \cdot i_1}{v_1}, \frac{v_t \cdot i_2}{v_1}, -\cos \beta \right) \quad \text{B-(xv)}$$

B.3. The Dip and Strike of  $(x_1, x_2, x_3) = 0$ .

The direction cosines of the incident and transmitted rays are related to the measured and theoretical velocity and azimuth (denoted  $v_m, \theta_m, v_{th}, \theta_{th}$ ) by the relations

$$\begin{aligned} t_1 &= \cos \theta_{th} \cdot \frac{v_t}{v_{th}} & i_1 &= \cos \theta_m \cdot \frac{v_1}{v_m} \\ t_2 &= \sin \theta_{th} \cdot \frac{v_t}{v_{th}} & i_2 &= \sin \theta_m \cdot \frac{v_1}{v_m} \\ t_3 &= \left( 1 - \frac{v_t^2}{v_{th}^2} \right)^{\frac{1}{2}} & i_3 &= \left( 1 - \frac{v_1^2}{v_m^2} \right)^{\frac{1}{2}} \end{aligned}$$

(equations 3-(1), 3-(11) and 3-(111) )

If the strike of the normal is  $\gamma$  then

$$\tan \gamma = \frac{n_2}{n_1}$$

and by equation B-(x11)

$$\begin{aligned} \tan \gamma &= \frac{t_2 \cdot (V_1/V_t)^{-1_2}}{t_1 \cdot (V_1/V_t)^{-1_1}} = \frac{(t_2 \cdot V_1^{-1_2} \cdot V_t)}{(t_1 \cdot V_1^{-1_1} \cdot V_t)} \\ &= \frac{\sin \theta_{th} \cdot \frac{V_t \cdot V_1}{V_{th}} - \sin \theta_m \cdot \frac{V_1 \cdot V_t}{V_m}}{\cos \theta_{th} \cdot \frac{V_t \cdot V_1}{V_{th}} - \cos \theta_m \cdot \frac{V_1 \cdot V_t}{V_m}} \\ &= \frac{\frac{\sin \theta_{th}}{V_{th}} - \frac{\sin \theta_m}{V_m}}{\frac{\cos \theta_{th}}{V_{th}} - \frac{\cos \theta_m}{V_m}} \end{aligned} \quad \text{B-(xv1)}$$

It can be seen that the strike component of the surface depends only on the measured and theoretical velocities and the azimuths and not on the velocities of the media.

If the dip of the normal is  $\alpha$  then

$$\cos \alpha = n_3 = \frac{(t_3 \cdot V_1 - 1_3 V_t)}{(V_1 \cdot \cos \beta - V_t \cdot \cos \alpha)}$$

and thus substituting for  $1_3$  and  $t_3$

$$\cos \alpha = \frac{(1 - \frac{V_t^2}{V_{th}^2})^{\frac{1}{2}} \cdot V_1 - (1 - \frac{V_1^2}{V_m^2})^{\frac{1}{2}} \cdot V_t}{V_1 \cdot \cos \beta - V_t \cdot \cos \alpha}$$

and since

$$\cos \alpha = \hat{N} \cdot \hat{I} = n_1 \cdot 1_1 + n_2 \cdot 1_2 + n_3 \cdot 1_3$$

$$\cos \beta = \hat{N} \cdot \hat{T} = n_1 \cdot t_1 + n_2 \cdot t_2 + n_3 \cdot t_3$$

and it can be seen that the dip of the normal depends not only on the measured and theoretical velocities and azimuths but also on the velocities of the media,  $V_1$  and  $V_t$ .

Appendix C. The Array Response to Coherent and Incoherent Noise.

C.1. Coherent Noise.

Consider a wavefront crossing an array with velocity  $V$  and apparent wavelength  $\lambda$ . The array consists of  $n$  seismometers and the  $r$ th seismometer at  $Q$  is at distance  $a_r$  and azimuth  $\alpha_r$  from an origin  $O$  (Fig.A1). The wave incident at azimuth  $\theta$  travels a distance  $d_r \cos(\theta - \alpha_r)$  between crossing  $Q$  and  $P$  and the phase difference between  $Q$  and  $P$  is thus

$$\beta_r = 2\pi \frac{d_r}{\lambda} \cos(\theta - \alpha_r) \tag{C-(1)}$$

If all the seismometers are summed without any delay then the summed output is given by  $A_n$  with a phase lag relative to  $O$  of  $\alpha_n$ , the phase shifts may be added vectorially to give

$$A_n \cos \gamma_n = \sum_{r=1}^n a_r \cos \beta_r \tag{C-(11)}$$

$$A_n \sin \gamma_n = \sum_{r=1}^n a_r \sin \beta_r \tag{C-(111)}$$

where  $a_r$  is the amplitude at the  $r$ th seismometer.

These equations may be solved to give

$$A_n^2 = \left[ \left( \sum_{r=1}^n a_r \cos \beta_r \right)^2 + \left( \sum_{r=1}^n a_r \sin \beta_r \right)^2 \right] \tag{C-(1v)}$$

and 
$$\gamma_n = \tan^{-1} \left[ \left( \sum_{r=1}^n a_r \sin \beta_r \right) / \left( \sum_{r=1}^n a_r \cos \beta_r \right) \right] \tag{C-(v)}$$

If the amplitude of the wave remains constant over the array at a C-(1v) may be simplified to give

$$A_n^2 = a^2 \left[ \left( \sum_{r=1}^n \cos \beta_r \right)^2 + \left( \sum_{r=1}^n \sin \beta_r \right)^2 \right] \tag{C-(v1)}$$

If all the waves are in phase then the amplitude

$A_n$  is given by

$$A_n' = \sum_{r=1}^n a = na$$

and an amplitude  $E_n$  which corresponds to the amplitude normalized to unity for the in phase condition may be written

$$E_n^2 = \frac{A_n^2}{A_n'^2} = \frac{\left[ \left( \sum_{r=1}^n \cos \beta_r \right)^2 + \left( \sum_{r=1}^n \sin \beta_r \right)^2 \right]}{n^2} \quad C-(v111)$$

As explained in section 6.3 it is more usual to sum the red and yellow lines individually and then multiply them together. If the red line corresponds to the seismometers 1 to  $\frac{n}{2}$  and the yellow line to seismometers  $\frac{n}{2} + 1$  to  $n$  then two subsidiary amplitudes are given by

$$A_R = a \left[ \left( \sum_{r=1}^{\frac{n}{2}} \cos \beta_r \right)^2 + \left( \sum_{r=1}^{\frac{n}{2}} \sin \beta_r \right)^2 \right]^{\frac{1}{2}}$$

and

$$A_Y = a \left[ \left( \sum_{r=\frac{n}{2}+1}^n \cos \beta_r \right)^2 + \left( \sum_{r=\frac{n}{2}+1}^n \sin \beta_r \right)^2 \right]^{\frac{1}{2}}$$

and so  $A = A_R \cdot A_Y$

$$A = a^2 \left[ \left( \sum_{r=1}^{\frac{n}{2}} \cos \beta_r \right)^2 + \left( \sum_{r=1}^{\frac{n}{2}} \sin \beta_r \right)^2 \right]^{\frac{1}{2}} \left[ \left( \sum_{r=\frac{n}{2}+1}^n \cos \beta_r \right)^2 + \left( \sum_{r=\frac{n}{2}+1}^n \sin \beta_r \right)^2 \right]^{\frac{1}{2}}$$

The corresponding in phase response is

$$A = \frac{n}{2}a \cdot \frac{n}{2}a = \frac{n^2 a^2}{4}$$

so that the normalized response is

$$E = \frac{4}{n^2} \left[ \left( \sum_{r=1}^{\frac{n}{2}} \cos \beta_r \right)^2 + \left( \sum_{r=1}^{\frac{n}{2}} \sin \beta_r \right)^2 \right]^{\frac{1}{2}} \left[ \left( \sum_{r=\frac{n}{2}+1}^n \cos \beta_r \right)^2 + \left( \sum_{r=\frac{n}{2}+1}^n \sin \beta_r \right)^2 \right]^{\frac{1}{2}} \quad C-(v111)$$

Usually the delays are adjusted so that the in phase condition corresponds to a given velocity and azimuth ( $V_1, \theta_1$ ) in which case the relevant phase shift at  $Q$  for a signal ( $V, \theta$ ) is

$$\beta_r = 2\pi \frac{d_r}{D} \frac{D}{\lambda} \cos(\theta - \alpha_r) - 2\pi \frac{d_r}{D} \frac{D}{\lambda} \cos(\theta_1 - \alpha_r)$$

$$= 2\pi \frac{d_r}{D} \left[ \frac{D}{\lambda} \cos \theta \cos \alpha_r + \frac{D}{\lambda} \sin \theta \sin \alpha_r - \frac{D}{\lambda_1} \cos \theta_1 \cos \alpha_r - \frac{D}{\lambda_1} \sin \theta_1 \sin \alpha_r \right]$$

$$= 2\pi \frac{dr}{D} \left[ \cos \alpha_r \left( \frac{D}{\lambda} \cos \theta - \frac{D}{\lambda_1} \cos \theta_1 \right) + \sin \alpha_r \left( \frac{D}{\lambda} \sin \theta - \frac{D}{\lambda_1} \sin \theta_1 \right) \right]$$

$$= 2\pi \frac{dr}{D} \frac{D}{\lambda'} \cos(\theta' - \alpha_r) \quad C-(1x)$$

where  $\frac{D}{\lambda'} \cos \theta' = \frac{D}{\lambda} \cos \theta - \frac{D}{\lambda_1} \cos \theta_1$   
 and  $\frac{D}{\lambda'} \sin \theta' = \frac{D}{\lambda} \sin \theta - \frac{D}{\lambda_1} \sin \theta_1$

and thus the phase shift produced is equivalent to a signal with azimuth  $\theta'$  and wavelength  $\lambda'$  which is the difference between the vectors  $(D/\lambda, \theta)$  and  $(D/\lambda_1, \theta_1)$ . The response as a function of  $(V, \theta)$  is thus determined by placing the origin at  $(\frac{D}{\lambda_1}, \theta_1 + \pi)$ .

This analysis may be developed to include waves of varying frequency but the variation in frequency of the waves from local earthquakes arriving at Kaptagat is such as to make this unnecessary.

The responses for a frequency of 4 Hz defined by C-(v11) and C-(1x) are calculated and illustrated in Figs. 6.3 and 6.4

C.2. Incoherent Noise.

If the noise is considered white the amplitude  $a$  at each seismometer will be constant but the phase will be random. If the phase angle at the  $r$ th seismometer is  $\alpha_r$  then in analogy to C-(11) and C-(111) the resultant  $R_n$  and phase angle  $\gamma$  may be written

$$R_n \cos \gamma = a \sum_{r=1}^n \cos \alpha_r$$

$$R_n \sin \gamma = a \sum_{r=1}^n \sin \alpha_r$$

so that

$$R_n^2 = a^2 \left[ \left( \sum_{r=1}^n \cos \alpha_r \right)^2 + \left( \sum_{r=1}^n \sin \alpha_r \right)^2 \right]$$

$$= a^2 \left\{ \left[ \sum_{r=1}^n \cos^2 \alpha_r + \sum_{\substack{r=1 \\ r \neq j}}^n \cos \alpha_r \sum_{r=1}^n \cos \alpha_j \right] + \left[ \sum_{r=1}^n \sin^2 \alpha_r + \sum_{\substack{r=1 \\ r \neq j}}^n \sin \alpha_r \sum_{r=1}^n \sin \alpha_j \right] \right\}$$

but  $\alpha_r$  is random so that the average value of  $\cos \alpha_r$  and  $\sin \alpha_r$  is zero and the average value of  $\sin^2 \alpha_r$  and  $\cos^2 \alpha_r$  is  $\frac{1}{2}$

$$R_n^2 = a^2 \cdot \left( \frac{1}{2}n + \frac{1}{2}n \right) = na^2$$

For signal of amplitude  $a$  at each of the seismometers the summed output for the in phase condition is

$$R_s = na$$

Thus without using the array the signal to noise ratio is unity but on using the array the new signal to noise ratio is

$$\frac{R_s}{R_n} = \frac{na}{\sqrt{n} \cdot a} = \sqrt{n}$$

so that the signal to noise ratio has been increased by  $\sqrt{n}$ .

My thanks are due to P.D. Marshall for illustrating this proof.

REFERENCES

- Aki, K. (1973) Scattering of P waves under the Montana LASA. J. Geophys. Res., 78, 1334-1346.
- Al-Chalabi, M. (1971) Reliability of the rotation pole in continental fitting. Earth Planet. Sci. Letters., 11, 257-262.
- Anderson, D.L., and Spetzler, H. (1970) Partial melting and the low velocity zone. Phys. Earth. Planet. Interiors, 4, 62-64.
- Artemjev, M.E., and Artyushkov, E.V. Structure and isostasy of the Baikal Rift and the mechanism of rifting. J. Geophys. Res., 69, 1103-1111.
- Artyushkov, E.V. (1973) Stresses in the lithosphere caused by crustal thickness inhomogeneities J. Geophys. Res., 78, 7675-7708.
- Backhouse, R.W. (1972) Upper mantle structure using P-wave data from an East African array station. Ph. D. thesis, University of Durham.
- Baker, B.H. (1969) Structural evolution of the rift zones of the Middle East - a comment. Nature, 224, 359-360.
- Baker, B.H., and Wohlenberg, J. (1971) Structure and evolution of the Kenya Rift Valley. Nature, 229, 538-542.
- Baker, B.H., Mohr, P.A., and Williams, L.A.J. (1972) Geology of the Eastern Rift System of Africa. Geol. Soc. Am. Pap., 136.
- Banks, R.J., and Ottey, P. (1974) Geomagnetic deep sounding in and around the Kenya Rift valley. Geophys. J. Roy. Astr. Soc., 36, 321-335.
- Bath, M. (1960) Crustal structure of Iceland. J. Geophys. Res., 65, 1793-1807.
- Berteussen, K.A. (1975) Crustal structure and P-wave travel time anomalies at NORSAR. J. Geophys., 41, 71-84.
- Birtill, J.W., and Whiteway, F.E. (1965) The application of phased arrays to the analysis of seismic body waves. Phil. Trans. Roy. Soc. Lond., Series A., 258, 421-443.

- Block, S., Hales, A.L., and Landisman, M. (1969) Velocities in the crust and upper mantle of southern Africa from multi-mode surface wave dispersion. Bull. Seism. Soc. Am., 59, 1599-1629.
- Bolt, B.A., and Nuttli, O. (1966) P-wave residuals as a function of azimuth 1. Observations. J. Geophys. Res., 71, 5977-5985.
- Bott, M.H.P. (1965) Formation of oceanic ridges. Nature, 207, 840-843.
- Bullard, E.C. (1936) Gravity measurements in East Africa. Phil. Trans. Roy. Soc. Lond. Series A., 235, 445-531.
- Bullard, E.C., and McKenzie, D.P. (1971) Remarks on uncertainties in poles of rotation in continental fitting. Earth Plan. Sci. Letters, 11, 263-264.
- Bullen, K.E. (1956) Encyclopaedia of Physics. Vol. XLVII. Springer-Verlag.
- Bullen, K.E. (1965) Introduction to the theory of seismology, Cambridge.
- Burke, K., and Wilson, J.T. (1972) Is the African plate stationary? Nature, 239, 387-390.
- Capon, J. (1974) Characterization of crust and upper mantle structure under LASA as a random medium. Bull. Seism. Soc. Am., 64, 235-266.
- Capon, J., Greenfield, R.J., and Kolker, R.J. Multidimensional maximum-likelihood processing of a large aperture seismic array. Proc. I.E.E.E., 55, 192-211.
- Carpenter, E.W. (1966) Onset time analysis. AWRE Blacknest Note PA4/AG, 66.
- Chapman, D.S., and Pollack, H.N. (1975) Heat flow and incipient rifting in the central African plateau. Nature, 256, 28-30.
- Chernov, L.A. (1960) Wave propagation in a random medium. McGraw-Hill, New York.
- Cleary, J., and Hales, A.L. (1966) An analysis of the travel times of P-waves to North American stations in the distance range  $32^{\circ}$ - $100^{\circ}$ . Bull. Seism. Soc. Am., 56, 467-489.
- Cleary, J., Wright, C., and Muirhead, K.J. (1968) The effects of local structure upon measurements of the travel time gradient at the Warramunga seismic array. Geophys. J. Roy. Astr. Soc., 16, 21-29.

- Colley, G.R. (1973) Measurement of relative teleseismic P-wave delay times between Nairobi and Kaptagat (Kenya). M.Sc. Dissertation, University of Durham.
- Corbishley, D.J. (1969) Measurements of the derivative of the P-wave travel time curve by means of an array network. Ph. D. thesis University of Durham.
- Corbishley, D.J. (1970) Structure under seismic arrays. Geophys. J. Roy. Astr. Soc., 21, 415-425.
- Darracott, B.W., Fairhead, J.D., and Girdler, R.W. (1972) Gravity and magnetic surveys in Northern Tanzania and Southern Kenya Tectonophysics, 15, 131-141.
- Davidon, W.C. (1968) Variance algorithm for minimization. Comp. J. 10, 406-410.
- Davies, D., and McKenzie, D.P. (1969) Seismic travel time residuals and plates. Geophys. J. Roy. Astr. Soc., 18, 51-63.
- Davies, D., Kelly, E.J., and Filson, J.R. (1971) Vespa process for the analysis of seismic signals. Nature Phys. Sci., 232, 8-13.
- Davies, D., and Sheppard, R.M. (1972) Lateral heterogeneity in the earth's mantle. Nature, 239, 318-323.
- Der, Z., Masse, R., and Landisman, M. (1970) Effects of observational errors on the resolution of surface waves at intermediate distances. J. Geophys. Res., 69, 3027-3031.
- Dixey, F. (1956) The East African rift system. Bull. Colon. Geol. Mineral Resources Suppl.
- Douglas, A. (1967) Joint Epicentre Determination. Nature, 215, 47-48.
- Douglas, A. (1967) A special purpose least squares program. AWRE Blacknest Report No. O-54/66.
- Elder, J.W. (1966) Penetrative convection; its role in volcanism. Bull. Vulc., 29, 327-343.
- Evernden, J.F. (1953) Direction of approach of Rayleigh waves and related problems. Bull. Seism. Soc. Am., 43, 335-374.

- Ewing, W.M.,  
Jardetzky, W.S., and  
Press, F. (1957) Elastic waves in layered media.  
McGraw-Hill, New York.
- Ewing, J., and  
Ewing, M. (1959) Seismic refraction measurements in  
the Atlantic Ocean basins, in the  
Mediterranean Sea, on the Mid-  
Atlantic Ridge, and in the  
Norwegian Sea.  
Bull. Geol. Soc. Am., 70, 291-318.
- Fairhead, J.D. (1968) The seismicity of the East African  
rift system 1955-1968.  
M. Sc. Dissertation, University of  
Newcastle-upon-Tyne.
- Fairhead, J.D., and  
Girdler, R.W. (1969) How far does the rift system extend  
through Africa?  
Nature, 221, 1018-1020.
- Fairhead, J.D., and  
Girdler, R.W. (1971) The seismicity of Africa.  
Geophys. J. Roy. Astr. Soc., 24,  
610-631.
- Fairhead, J.D., and  
Girdler, R.W. (1972) The seismicity of the East African  
rift system.  
Tectonophysics, 15(1/2), 115-122.
- Frazier, S.B. (1970) Adjacent structure to Ethiopia:  
that portion of the Red Sea coast  
including Dahlak Kebir Island and  
the Gulf of Zula.  
Phil. Trans. Roy. Soc. Lond.,  
Series A, 267, 131-141.
- Freund, R. (1970) Plate tectonics of the Red Sea and  
East Africa.  
Nature, 228, 453.
- Gass, I.G. (1970) Tectonic and magmatic evolution of  
the Afro-Arabian dome.  
In 'African Magmatism and Tectonics'  
285-297, Oliver and Boyd.
- Gass, I.G. (1972) The role of magmatic processes in  
continental rifting and sea-floor  
spreading.  
Fourth Tomkeieff Memorial Lecture,  
University of Newcastle-upon-Tyne.
- Gass, I.G., and  
Gibson, I.L. (1969) Structural evolution of the rift  
zones of the Middle East.  
Nature, 221, 926-930.
- Girdler, R.W. (1958) The relationship of the Red Sea to  
the East African rift system.  
Quart. J. Geol. Soc. Lond., 114,  
79-105.

- Girdler, R.W. (1964) Geophysical studies of Rift Valleys. Physics and Chemistry of the Earth, 5, 121-156.
- Girdler, R.W., and Darracott, B.W. (1972) African poles of rotation. Comm. Earth. Sci. Geophys., 2, 131-138.
- Girdler, R.W., and Styles, P. Two stage Red Sea floor spreading. Nature, 247, 7-11.
- Grasty, R., Miller, J.A., and Mohr, P.A. (1963) Preliminary results of potassium-argon age determinations on some Ethiopian Trap Series basalts. Bull. Geophys. Obs. Addis Ababa, 6, 97-102.
- Green, T.H., Green, D.H., and Ringwood, A.E. (1967) The origin of high alumina basalts and their relation to quartz tholeiites and alkali basalts. Earth and Planetary Sci. Letters, 2, 41-51.
- Greenfield, R.J., and Sheppard, R.M. (1969) The Moho depth variations under the LASA and their effect on dT/d measurements. Bull. Seism. Soc. Am., 59, 409-420.
- Gregory, J.W. (1921) The rift valleys and geology of East Africa. Seeley and Service Co. Ltd., London.
- Griffiths, D.W. (1972) Some comments on the results of a seismic refraction experiment in the Kenya rift. Tectonophysics, 15(1/2), 151-156.
- Griffiths, D.H., King, R.F., Khan, M.A., and Blundell, D.J. (1971) Seismic refraction line in the Gregory rift. Nature, 229, 69-71.
- Gumper, F., and Pomeroy, P.W. (1970) Seismic wave velocities and earth structure on the African continent. Bull. Seism. Soc. Am., 60, 651-668.
- Harris, P.G. (1969) Basalt type and rift valley tectonism. Tectonophysics, 8, 427-436.
- Heiskanen, W.A., and Vening Meinesz, F.A. (1958) The earth and its gravity field. McGraw-Hill, New York.
- Herrin, E., and Taggart, J. (1968) Regional variations in P travel times. Bull. Seism. Soc. Am., 58, 1325-1337.
- Herrin, E., Arnold, E.P., Bolt, B.A., Clawson, G.E., Engdahl, E.R., Gordon, D.W., Hales, D.W., Kales, A.L., Lobbell, J.L., Nuttli, O., Romney, C., Taggart, J., and Tucker, W. (1968) Seismological tables for P-phases. Bull. Seism. Soc. Am., 58, 1193-1241.

- Husebys, E.S.,  
Berteussen, E.S.,  
Christofferson, A., and  
Dahle, A. (1975) Wave scattering theory in the  
analysis of P-wave anomalies at  
NORSAR and LASA.  
Geophys. J. Roy. Astr. Soc., 42,  
403-417.
- Illies, J.H. (1969) An intercontinental belt of the  
world rift system.  
Tectonophysics, 8, 5-29.
- James, F. (1968) Monte Carlo for Particle physicists.  
Proceedings of 1968 Hercig-Novik  
School.
- James, F., and  
Roos, M. (1969) CERN computer 6000 series program  
library D506.
- Jeffreys, H., and  
Bullen, K.E. (1940) Seismological Tables.  
Brit. Assn. Gray-Milne Trust.
- Jennings, D.J. (1964) Geology of the Kapsabet Plateau area  
Geol. Surv. Kenya. Report No. 63.
- Kanestrom, R. (1969) The dip of Moho under NORSAR.  
Scientific report No. 3,  
Seismological Observatory, University  
of Bergen, Bergen, Norway.
- Kelly, E.J. (1964) Limited network processing of  
seismic signals.  
M.I.T. Lincoln Lab. Group Report 44.
- Key, F.A. (1968) Some observations and analyses of  
signal generated noise.  
Geophys. J. Roy. Astr. Soc., 15,  
377-392.
- Khan, M.A., and  
Mansfield, J. (1971) Gravity measurements in the Gregory  
Rift.  
Nature, 229, 72-75.
- King, B.C. (1970) Volcanicity and rift tectonics in  
East Africa.  
In 'African magmatism and tectonics'  
263-283, Oliver and Boyd.
- King, D.W., Mereu, R.F.,  
and Muirhead, K.J. (1973) The measurement of apparent velocity  
and azimuth using adaptive processing  
techniques on data from the  
Warramunga Seismic Array.  
Geophys. J. Roy. Astr. Soc., 35,  
137-167.
- Knopoff, L., and  
Schlue, J.W. (1972) Rayleigh wave phase velocities for  
the path Addis-Ababa - Nairobi.  
Tectonophysics, 15(1/2), 157-163.
- Laughton, A.S. (1966) The Gulf of Aden.  
Roy. Soc. Lond. Philos. Trans.,  
Series A, 259, 150-171.

- Le Bas, M.J. (1971) Per-alkaline volcanism, crustal swelling and rifting. Nature Phys. Sci., 230, 85-87.
- Le Pichon, X. (1968) Sea-floor spreading and continental drift. J. Geophys. Res., 73, 3661-3697.
- Le Pichon, X., Houtz, R.E., Drake, C.L., and Nafe, J.F. (1965) Crustal structure of the mid-ocean ridges (1) Seismic refraction measurements. J. Geophys. Res., 70, 319-340.
- Lehmann, I. (1967) Low velocity layers. In 'The Earth's Mantle', 41-61, Academic Press, London and New York.
- Lilwall, R.C., and Douglas, A. (1970) Estimation of P-wave travel times using the Joint Epicentre Method. Geophys. J. Roy. Astr. Soc., 19, 165-181.
- Logatchev, N.A., Belousov, V.V., and Milanovsky, E.F. (1972) East African Rift development. Tectonophysics, 15(1/2), 71-81.
- Long, R.E. (1968) Temporary seismic array stations. Geophys. J. Roy. Astr. Soc., 16, 37-45.
- Long, R.E., and Mitchell, M.G. (1970) Teleseismic P-wave delay in Iceland. Geophys. J. Roy. Astr. Soc., 20, 41-48.
- Long, R.E., Backhouse, R.W., Maguire, P.K.H., and Sundaralingham, K. (1972) The structure of East Africa using surface wave dispersion and Durham seismic array data. Tectonophysics, 15(1/2), 165-178.
- Magnitsky, V.A., and Kalashnikova, I.V. (1970) Problem of phase transitions in the upper mantle and its connection with the earth's crustal structure. J. Geophys. Res., 75, 877-885.
- Maguire, P.K.H., and Long, R.E. (1975) The crustal structure on the western flank of the Gregory rift (Kenya). In the press.
- McCamy, K., and Meyer, R.P. (1964) A correlation method of apparent velocity measurement. J. Geophys. Res., 69, 691-699.
- McConnell, R.B. (1970) Evolution of rifting in Africa. Nature, 227, 699.
- McKenzie, D.P., and Parker, R.L. (1967) The north Pacific; an example of tectonics on a sphere. Nature, 216, 1276-1280.

- McKenzie, D.P.,  
Davies, D., and  
Molnar, P. (1970) Plate tectonics of the Red Sea and East Africa.  
Nature, 226, 243-248.
- Merla, G. (1963) Missione geologica nell 'Ethiopia meridionale del C.N.R. 1959-1960. Notizie geomorfologiche: G. Geol. Bologna, 31, 1-56.
- Mitchell, M.G. (1969) The crust and upper mantle beneath Iceland.  
Ph. D. thesis, University of Durham.
- Mohr, P.A. (1970) Plate tectonics of the Red Sea and East Africa.  
Nature, 228, 547-548.
- Mohr, P.A. (1963) The Ethiopian Cainozoic lavas - a preliminary study of some trends; spatial, temporal and chemical.  
Bull. Geophys. Obs. Addis Ababa, 6, 103-144.
- Mohr, P.A. (1967) Review of the geology of the Simien mountains.  
Bull. Geophys. Obs. Addis Ababa, 10, 79-93.
- Molnar, P., and  
Oliver, J. (1969) Lateral variations of attenuation in the upper mantle and discontinuities in the lithosphere.  
J. Geophys. Res., 74, 2648-2682.
- Morgan, W.J. (1968) Rises, trenches, great faults and crustal blocks.  
J. Geophys. Res., 73, 1959-1982.
- Mueller, St.,  
Peterschmitt, E.,  
Fuchs, K., and  
Ansorge, J. (1969) Crustal structure beneath the Rhine Graben from seismic refraction and reflection measurements.  
Tectonophysics, 8, 529-542.
- Murray, C.G. (1970) Magma genesis and heat flow, differences between mid-oceanic ridges and African rift valleys.  
Earth Planet. Sci. Letters, 9, 34-38.
- Niazi, M. (1966) Corrections to apparent azimuths and travel-time gradients for a dipping Mohorovicic discontinuity.  
Bull. Seism. Soc. Am., 56, 491-509.
- Nuttli, O., and  
Bolt, B.A. (1969) P-wave residuals as a function of azimuth (2) Undulations of the mantle low velocity layer as an explanation.  
J. Geophys. Res., 74, 6594-6602.

- Osmaston, M.F. (1971) Genesis of ocean ridge median valleys and continental rift valleys. *Tectonophysics*, 11, 387-405.
- Otsuka, M. (1966) Azimuth and slowness anomalies of seismic waves measured on the central Californian Seismographic array. Part 1, Observations. *Bull. Seism. Soc. Am.*, 56, 223-239.
- Otsuka, M. (1966) Azimuth and slowness anomalies of seismic waves measured on the central Californian Seismographic array. Part 2, Interpretation. *Bull. Seism. Soc. Am.*, 56, 655-675.
- Oxburgh, E.R., and Turcotte, D.L. (1968) Mid-ocean ridges and geotherm distribution during mantle convection. *J. Geophys. Res.*, 73, 2643-2661.
- Oxburgh, E.R., and Turcotte, D.L. (1974) Membrane tectonics and the East African rift. *Earth Plan. Sci. Letters*, 22, 133-140.
- Powell, C. (1975) Evidence for mantle heterogeneity from two large seismic arrays. *Nature*, 254, 40-42.
- Powell, J.D. (1964) An efficient method for finding the minimum of a function of several variables without calculating derivatives. *Comp. J.*, 7, 155.
- Roberts, D.G. (1969) Structural evolution of the rift zones in the Middle East. *Nature*, 223, 55-57.
- Rosenbrock, H.H. (1960) An automatic method for finding the greatest and least value of a function. *Comp. J.*, 3, 175-184.
- Saggerson, E.P., and Baker, B.H. (1965) Post-Jurassic erosion surfaces in eastern Kenya and their deformation in relation to rift structure. *Geol. Soc. London. Quart. Jour.*, 121, 51-72.
- Sattlegger, J. (1965) A method of computing true interval velocities from expanding spread data in the case of arbitrarily long spreads and arbitrarily dipping plane interfaces. *Geophys. Prosp.*, 13, 306-318.

- Searle, R.C., and Darracott, B.W. (1971) A catalogue of gravity data from Kenya. Newcastle University.
- Shah, P.M. (1973) Ray tracing in three dimensions. *Geophysics*, 38, 600-604.
- Solomon, S.C., and Julian, B.R. (1974) Seismic constraints on ocean-ridge mantle structure; anomalous fault plane solutions from first motions. *Geophys. J. Roy. Astr. Soc.*, 38, 265-285.
- Sorrels, G.G., Crowley, J.R., and Veith, K.F. (1971) Methods for computing raypaths in complex geological structures. *Bull. Seism. Soc. Am.*, 61, 27-53.
- Spetzler, H., and Anderson, D.L. (1968) The effect of temperature and partial melting on velocity and attenuation in a simple binary mixture. *J. Geophys. Res.*, 73, 6051-6060.
- Stefansson, R. (1967) Some problems of studies on the mid-Atlantic ridge, Iceland and the mid-ocean ridges. *Soc. Sci. Islandica 'Rit'*, 38, 80-90.
- Sundaralingham, K. (1971) Seismic investigation of the crust and upper mantle of East Africa. Ph. D. thesis, University of Durham.
- Swain, C.J., and Khan, M.A. (1974) A gravity map of Kenya at 1:2,000,000. Provisional version, Leicester University.
- Sykes, L.R., and Landisman, M. (1964) The seismicity of East Africa, the Gulf of Aden and the Arabian and Red Seas. *Bull. Seism. Soc. Am.*, 54, 1927-1940.
- Talwani, M., Le Pichon, X., and Ewing, M. (1965) Crustal structure of the mid-ocean ridges (2) Computed model from gravity and seismic refraction data. *J. Geophys. Res.*, 70, 341-352.
- Tramontini, C., and Davies, D. (1969) A seismic refraction survey in the Red Sea. *Geophys. J.*, 17, 225-241.
- Tryggvason, E. (1964) Arrival times of P waves and upper mantle structure. *Bull. Seism. Soc. Am.*, 54, 727-736.
- Turcotte, D.L. (1974) Membrane Tectonics. *Geophys. J. Roy. Astr. Soc.*, 36, 33-42.

- Turcotte, D.L., and  
Oxburgh, E.R. (1973) Mid-plate tectonics.  
Nature, 244, 337-339.
- Underwood, R., and  
Lilwall, R.C. (1969) The systematic error in seismic  
location.  
Geophys. J. Roy. Astr. Soc., 17,  
521-526.
- Wayland, E.J. (1930) Rift valleys and Lake Victoria.  
C.R. Int. Geol. Congr. 15(6), 323.
- Whiteway, F.E. (1965) The recording and analysis of  
seismic body waves using linear  
cross arrays.  
Radio and Electronic Engineer, 29,  
33-46.
- Willis, B. (1936) East African Plateaus and Rift  
Valleys.  
Carnegie Inst. Washington Pub.  
No. 470, 358p.
- Wohlenberg, J. (1970) On the seismicity of the East  
African Rift system.  
In 'Graben Problems'. I.U.M.P.,  
Report No. 27, 289-295.
- Young, J.B., and  
Gibbs, P.B. (1968) GEDESS: A series of computer  
programs for deriving information  
at selected seismic recording  
sites, for signals from known  
hypocentres.  
AWRE Blacknest Report No. O 54/68.

Velocity Filtering Program

```

49;
;
SPR;
VELOCITY,
ASK;
ADD,159;104;
SPR;
FILEN,
ASK,

CALL;36,

LINK;;;14.;
INS;F;159;
INP,F;;;1,2,3,4,5,6,7,8,9,10,11,1,2,3,4,5,6,7,8,9,10,11,
WEI;11,.1;54;
OUT;;;1,2,3,4,5,6;50,51,53,54,61,62;
IGOTO;9;

14DO,A,B,D,2.6,2.6,1.0;0.01,0.01,0.4,2.8,2.8,9.0;
INS;C,159;

CALL,36;

INPUT,C;;;1,2,3,4,5,6,7,8,9,10;1,2,3,4,5,6,7,8,9,10;
STACK;1,2,3,4,5;E;A,50;
STACK,6,7,8,9,10,E,B;51;
MUL;50,51,50;
    60,60,51,
    50,51,71;
IF;C(.71,0) 0;
SUB;71,70;71;
SQRT,71;71;
SUB;71;70;12,
GOTO;28,
DLSE;
SQRT,71;12;
INT,12;.2;52;
WEI,52;.05;53;
ADD;53,103;54;
ADD;62,63;62;
OUT;0;1.2,3,4,5,6,50,51,53,54,61,62;
IGOTO,17;
CONT;

GOTO;1,

36SET;50,51,52,53,60,61,62,63,70;0,0,0,0,.1,10,0,.01,0;

DO;90,0;.01;1;
SET;11;;
SET;1,2,3,4,5,6,7,8,9,10,,,,,,,,,;
INP;;;1;91;
OUT;;;1,2,3,4,5,6;50,51,53,54,61,62;
IGOTO,37,

CONT;

SET;61,-10;
RETURN,
END;

```

Subroutine LVZSUB

```

C PRGAM LVZSUB IS A SUBROUTINE FOR THE OPTIMIZING PROCEDURES DESCRIBED
C IN CHAPTER FOUR. THE MAIN PROGRAM IS STOPPED UNDER FILE TOTQ-MIN. THE SUB-
C ROUTINE AND MAIN PROGRAM CALCULATE THE MINIMUM OF THE FUNCTION DEFINED BY
C THE SEVEN VARIABLES A,R,C,THETA,X,Y AND VELOCITY FOR WEIGHTED SLOWNESS AND
C AZIMUTH ANOMALIES AND FOR GROUP WEIGHTS APPLIED TO THE SLOWNESS AND AZIMUTH
C DATA.

```

```

      SUBROUTINE FCN(N,G,F,VAR,IFLAC)
      REAL LENGTH,LI,KCS
      DIMENSION DEPTH(150),VEL(160),SINJ(160),EVFNT(70),A7(70),AZN(70),A
      LZH(70),DJD(70),DIDN(70),DIDP(70),ANOMP(70),ANOMAZ(70),FUNCT(70),
      IDZ(70),DZH(70),DZN(70),DNOM(70),C(N),VAR(N),WAITP(70),WAITA7(70)

```

```

      IF (IFLAC.FQ.7) GO TO 1000
      IF (IFLAC.NE.1) GO TO 1001
      READ(5,92) WTP,WTAZ
      READ(5,83) NEVENT
      READ(5,94) (EVENT(I),DJD(I),DIDN(I),DIDP(I),AZH(I),WAITA7(I),WAITD(I)
      I),I=1,NEVENT)

```

```

      READ(5,85) (DEPTH(I),VEL(I),I=1,76)
C AZIMUTH VALUES ARE INPUTED IN DEGREES,AS IS THE ORIENTATION, BUT THE
C FUNCTION VALUE IS CALCULATED FOR THE RESIDUALS IN DEGREES.

```

```

      DO 433 KK=1,NEVENT
      AZ(KK)=A7(KK)/57.2956
      A7H(KK)=AZH(KK)/57.2956
433 CONTINUE
      92 FORMAT(2F5.2)
      83 FORMAT(13)
      84 FORMAT(7F10.2)
      85 FORMAT(F5.2,F7.2)

```

```

C STRUCTURE PARAMETERS ARE SFT AS VARIABLES.
      I=1 A=VAR(1)
      RO=VAR(2)
      CO=VAR(3)
      VLZ=VAR(4)
      ORIENT=VAR(5)/57.2956

```

```

YT = VAS(6)
XTQ = JAR(7)
ZTQ = 0.0
C STRUCTURE PARAMETERS ARE CONVERTED TO CONVENIENT FORM,
A = 1.0/(AO*AO)
R = 1.0/(RO*RO)
C = -1.0/(CO*CO)
ON 432 JJ=1, NEVFMT
C FAY IS TRACED THROUGH EACH LAYER IN TURN.
YT = XTQ
YT = YTO
ZT = ZTQ
SINI(1) = VFL(1) * DTD(JJ) * 0.00899
AI = CCS(AZ(JJ) - CRIFNT) * SINI(1)
AM = SIN(AZ(1) - CRIFNT) * SINI(1)
AP = SQRT(1.0 - SINI(1) * SINI(1))
LENGTH = (DEPTH(2) - DEPTH(1)) / AN
XR = YT + (LENGTH * AI)
YR = YT + (LENGTH * AM)
ZR = DEPTH(2)
DC(1) JD = 2, 75
ID = JC + 1
KD = JC - 1
XT = XB
YT = YR
ZT = ZP
SINT(JD) = SINI(KD) * VEL(JC) / VEL(KD)
C TESTING FOR TOTAL INTERNAL REFLECTION.
IF (SINI(JD) * CT > 1.0) GO TO 103
AL = SINI(JD) * CCS(AZ(JJ) - CRIFNT)
AM = SINI(JD) * SIN(AZ(JJ) - ORIFMT)
AN = SQRT(1.0 - SINI(JD) * SINI(1))
LENGTH = (DEPTH(2) - DEPTH(1)) / AN
XR = XT + LENGTH * AI

```

```

Y2=YT+LENGTH*AM
Z9=DEPTH(10)
IF (Z9-00.0) 102,103,103
C IF INTERSECTION DOES NOT OCCUR BY 400 Y* IT IS ASSUMED NOT TO OCCUR.
C INTERSECTION WITH THE STRUCTURE IS NOW CALCULATED.
1,2 AP=A*AL*AL+P*AM*AM+C*AN*AN
HP=(A*XT+AI+B*YT-AM+C*ZT*AN)*2.0
CP=(A*XT+YT+R*YT+VT+C*ZT*ZT)-1.0
PCCT=BP+RP-4.*AR*CR
IF (PCCT) 10,11,11
11 DPOS=(-RR+SQRT(PCCT))/(2.0*AP)
DNEG=(-RR-SQRT(PCCT))/(2.0*AP)
IF (DPOS*DNEG) 13,14,14
13 D=DPCS
IF (DNEG.GT.DPOS) D=[NEG
GO TO 15
14 IF (DPCS.LT.0.0) GO TO 10
D=DPCS
IF (DNEG.LT.DPOS) D=DNEG
XTINT=XT+D*AL
YTINT=YT+D*AM
ZTINT=ZT+D*AN
IF (ZTINT.LE.ZB.AND.ZTINT.GE.ZT) (C TO 17
10 CONTINUE
IF (JD.EG.75) GO TO 103
17 FACTOR=SQRT(A*XTINT*XTINT+B*RYTINT*YTINT+C*ZTINT*ZTINT)
C NORMAL TO THE SURFACE AT THE POINT OF INTERSECTION IS CALCULATED.
ALN=A*XTINT/FACTOR
AMN=B*YTINT/FACTOR
ANN=C*ZTINT/FACTOR
IF (ANN.LT.C.) GO TO 16
ALN=-ALN
AMN=-AMN
ANN=-ANN

```

```

16 CCSI=AL*ALN+AM*AMN+AN*ANN
   SNI=SQRT(1.-CCSI*CCSI)
   SINR=VLVZ*SMI/VEL(JD)
   IF (SINR.GT.1.0) GO TO 32
   CCSR=-SQRT(1.0-SINR*SINR)
C TRANSMITTED RAY IS NOW CALCULATED.
   ALTI=VLV7*AL/VEL(JD)-((VLV7*CCSI/VEL(JD))-CCSP)*ALN
   AMTI=VLVZ*AM/VEL(JD)-((VLVZ*CSI/VEL(JD))-CCSD)*AMN
   ANTI=VLVZ*AN/VEL(JD)-((VLVZ*CSI/VEL(JD))-CCSP)*ANN
   FACTOR=SQRT(ALTI*ALTI+AMTI*AMTI+ANTI*ANTI)
   ALTI=ALTI/FACTOR
   AMTI=AMTI/FACTOR
   ANTI=ANTI/FACTOR
   IF (ANTI.GT.0.0) GO TO 39
   ALTI=-ALTI
   AMTI=-AMTI
   ANTI=-ANTI
39 OTDN(JJ)=(6371.*ZINTI*SORT(1.-ANTI*ANTI))/(VLV7*57.2954)
C REFRACTION AND SIGNNESS ARE CALCULATED.
   KCS=APCCS(ALTI/SQRT(1.0-ANTI*ANTI))
   IF (ALTI.GT.0.0.AND.AMTI.GT.0.0) AZN(JJ)=KCS
   IF (ALTI.LT.0.0.AND.AMTI.GT.0.0) AZN(JJ)=KDS
   IF (ALTI.LT.0.0.AND.AMTI.LT.0.0) AZN(JJ)=6.2832-KDS
   IF (ALTI.GT.0.0.AND.AMTI.LT.0.0) AZN(JJ)=6.2832-KCS
   AZN(JJ)=AZN(JJ)+ORIENT
   ANCMP(JJ)=OTDN(JJ)-OTDN(JJ)
   ANDMA7(JJ)=AZH(JJ)-AZN(JJ)
   TE=ABS(ANDMAZ(JJ)).GT.1.5708) ANDMA7(JJ)=6.2832-ABS(ANDMAZ(JJ))
   GO TO 42
32 ANOMP(JJ)=10.0
   ANCMZ(JJ)=10.0
   GO TO 432

```

```

34 ANCMP(JJ)=10.1
ANOMAZ(JJ)=10.1
GO TO 432
103 ANCMZ(JJ)=AZH(JJ)-AZ(JJ)
IF (ABS(ANOMAZ(JJ)).GT.1.5708) ANOMAZ(JJ)=6.2832-ABS(ANOMAZ(JJ))
ANCMP(JJ)=DTH(JJ)-DTH(JJ)
432 CONTINUE
C FUNCTION VALUE IS CALCULATED.
F=0.0
DO I=7 JJ=1,NEVENT
F=F+(WTP+ANGMP(JJ)*ANGMP(JJ)+WAITP(JJ)*WAITP(JJ))+{WTAZ*ANOMAZ(JJ)
1*ANCMZ(JJ)+WAITAZ(JJ)*WAITAZ(I)}
FUNCT(JJ)=F
107 CONTINUE
GO TO 102
C DATAOUTPUT SECTION.
1000 WRITE(6,108)
DO I=12 N=1,NEVENT
DNOMAZ(N)=ANOMAZ(N)*57.2956
DZH(N)=AZH(N)*57.2956
DZ(N)=AZ(N)*57.2956
CZN(N)=AZN(N)*57.2956
112 CONTINUE
108 FORMAT('1',EVENT,10X,'A/JMUTH ANOMALY',10X,'PARAMETER P ANOMALY',
1,10X,'FUNCTION VALUE')
WRITE(6,100) (FVENT(IJ),ANOMAZ(IJ),FUNCT(IJ),IJ=1,NEVENT)
1)
109 FORMAT('1',F8.2,15X,F7.2,20X,F5.2,20X,F7.2)
WRITE(6,110)
110 FORMAT('1',5X,'DTH',6X,'DTDN',6X,'AZH',6X,'AZN',6X,'DTH',6X,'DZ',
WRITE(6,111) (DTH(IJ),DTDN(IJ),DZH(IJ),DZN(IJ),DTH(IJ),DZ(IJ),IJ=1,NEVENT)
1,NEVENT)
111 FORMAT(6F11.2)
1002 PFTURN
END

```

Program NORMAL

```

C PROGRAM NORMAL CALCULATES THE DIRECTION OF THE NORMAL WHICH CAUSES
C A RAY WITH GIVEN VELOCITY AND AZIMUTH TO BE DEVIATED TO ANOTHER
C VELOCITY AND AZIMUTH ASSUMING BOTH VELOCITIES ARE KNOWN.
C DIMENSION PATSIN(20), ANGLE(20), DVEXP(150), DAZEXP(150), DVMEAS(150),
C ICANGLE(150), DIP(150), DCOSAZ(150), DELTA(150), DN1(20), DN2(20), DN3(2
C 0), DZMFAS(150), EVENT(150)
C REAL I1, I2, I3, N1PLUS, N2PLUS, N3PLUS, N1MINS, N2MINS, N3MINS, LCANG
C
C INPUT DATA
C 1) DEPTH THIS IS FOR INFORMATION ONLY AND INDICATES THE
C DEPTH RANGE APPROPRIATE TO THE U.M. VELOCITY.
C 2) VELOC. VELOCITY IN NORMAL U.M.
C 3) NEVENT: NUMBER OF EVENTS CONSIDERED.
C 4) IFULL: IF IFULL IS 1 CONDENSED OUTPUT IS GIVEN.
C 5) IFLOT: IF IPLOT IS 1 PLOTTING ROUTINES ARE CALLED.
C 6) DVEXP(I)--VELOCITY EXPECTED
C 7) AZEXP(I)--AZIMUTH EXPECTED
C 8) VMFAS(I)--VELOCITY MEASURED
C 9) ZMFAS(I)--AZIMUTH MEASURED
C 10) EVENT(I)--EVENT CODE
C 11) DELTA(I)--DISTANCE IN DEGREES
C
C READ(5, 10) DEPTH
C 10 FORMAT(2F10.0)
C READ(5, 11) VELLVZ
C 11 FORMAT (F10.0)
C READ(5, 12) NEVENT
C READ(5, 12) IFULL
C READ(5, 12) IPLOT
C 12 FORMAT(I3)
C READ(7, 13) (DVEXP(I), DAZEXP(I), DVMEAS(I), DZMEAS(I), EVENT(I), DELTA(
C I), I=1, NEVENT)
C 13 FORMAT(6F10.0)

```

```

C DATA INPUT CHECK
WRITE(6,20) DEPTH,VELAB
20 FORMAT (' ', 'NORMAL STRUCTURE: DEPTH=',F7.2,'KMS. VELOCITY',F7.
12,'KMS/SEC')
WRITE(6,21) VELLVZ
21 FORMAT (' ', 'LOW VELOCITY ZONE',F7.2,'KMS./SEC')
DC 9.11 I1=1,NEVENT
VFXP=DVEXP(I1)
VMFAS=DVMEAS(I1)
AZEXP=FAZEXP(I1)
A7MEAS=D7MFAS(I1)
IF (IFULL.FG.1) GO TO 42
WRITE(6,1000) EVENT(I1)
1000 FORMAT (' ', '*****') EVENT NO.,F8.2)
C
C (CONVERSION OF AZIMUTH AND VELOCITY TO DIRECTION CCSINFS
42 INDIR=)
AZEXP=AZEXP/57.2958
AZMEAS=AZMEAS/57.2956
IF (VELAR.GT.VMEAS) GO TO 899
IF (VELLVZ.GT.VEXP) GO TO 800
SINAB=VELAR/VMEAS
COSAR=SQRT(1.0-SINAB*SINAB)
I1=COS(A7MEAS)*SINAB
I2=SIN(A7MEAS)*SINAB
I3=CCSAR
SINBFL=VELLVZ/VEXP
COSBREL=SQRT(1.0-SINBFL*SINBFL)
T1=COS(AZEXP)*SINBFL
T2=SIN(AZEXP)*SINRFL
T3=CCSREL
C
C NORMALITY CONDITION PARAMETERS

```

```
A1=I2*I3-I3*I2
A2=I3*I1-I1*I3
A3=I1*I2-I2*I1
```

```
C
C SURPARAMETERS IN SIMULTANEOUS EQUATIONS
```

```
ALPD=1.0
146 DO 150 J=1,1C
ALPD=9.0*FLCAT(J)
```

```
C
C IF INDIC=0 THEN INCIDENT ANGLE INCREASES BY 9 DEGRFES.
C IF INDIC=1 THEN INCIDENT ANGLE INCREASES BY 1 DEGRFE.
IF (INDIC.FO.) GO TO 177
```

```
ALPD=1.0*FLOAT(J)+LOANG-1.0
17C K=21-J
```

```
ANGLE(I)=ALPD
ANGLE(K)=ALPD
ALF=ALPD/57.2956
B2=(A3*COS(ALP))/(I2*A3-I3*A2)
C2=(A1*I3-A3*I1)/(A3*I2-A2*I3)
B3=(A2*COS(ALP))/(A2*I3-A3*I2)
C4=(A1*I2-A2*I1)/(A2*I3-A3*I2)
```

```
C
C PARAMETERS IN QUADRATIC
```

```
D1=(1.0+C2*(C2+C3*(3)
D2=2.0*(B2+C2+B3*(C2)
D3=B2*B2+B3*B3-1.0)
```

```
C
C SOLUTION OF QUADRATIC
```

```
ROOT=(D2*D2-4.0*D1*D3)
IF (ROOT.LT.0.0) GO TO 160
N1PLUS=(-D2+SQRT(ROOT))/(2.0*D1)
N1MINS=(-D2-SQRT(ROOT))/(2.0*D1)
N2PLUS=(-A1*N1PLUS+I3-A3*COS(ALP)+I1*N1PLUS*A3)/(A2*I3-A3*I2)
N2MINS=(-A1*N1MINS+I3-A3*COS(ALP)+I1*N1MINS*A3)/(A2*I3-A3*I2)
N3PLUS=(A2*COS(ALP)-I1*N1PLUS*A2+A1*N1PLUS*I2)/(A2*I3-A3*I2)
```

```

N3MINS=(A2*CCS(ALP)-I1*N1MINS+A2+41*N1MINS*I2)/(A2=I3-A3+I2)
IF (N3PLUS.GT.P.C) GO TO 110
N1PLUS=-N1PLUS
N2PLUS=-N2PLUS
N3PLUS=-N3PLUS
110 IF (N3MINS.GT.0.0) GO TO 120
N1MINS=-N1MINS
N2MINS=-N2MINS
N3MINS=-N3MINS

C CALCULATION OF REFRACTION AND TESTING
120 RATIC=VELAR/VFLV7
COSPP=T1*N1PLUS+T2*N2PLUS+T3*N3PLUS
COSRM=T1*N1MINS+T2*N2MINS+T3*N3MINS

C FOR SMALL ANGLE OF INCIDENCE ROUNDING OFF EPROPS CAN CAUSE
C CCSFP AND COSRM TO OVERFLOW UNITY.
IF (COSRP.GT.1.0) COSPP=1.0
IF (COSRM.GT.1.0) COSRM=1.0
SINFP=SQRT(1.0-COSPP*CCSPP)
SINRM=SQRT(1.0-COSRM*COSRM)

C FOR SMALL ANGLES PHYSICALLY UNACCEPTABLE SOLUTIONS OCCUR:
C THESE ARE REJECTED
IF (SINRP.LT.0.0001) GO TO 151
IF (SINRM.LT.0.0001) GO TO 152
RATSIP=SIN(ALP)/SINPP
PATSIM=SIN(ALP)/SINPM
RATSIN(K)=RATSIM
RATSIN(J)=RATSIP
GO TO 153
151 PATSIN(J)=131.070
GO TO 153
152 PATSIN(K)=131.070

```

```

153 (N)(K)=N1MINS
    DN2(L)=N2MINS
    DN3(K)=N3MINS
    CN1(I)=N1PLUS
    DN2(J)=N2PLUS
    DN3(J)=N3PLUS
    GO TO 150
154 WRITE(6,140)
140 FORMAT('C', 'ROOTS IMAGINARY')
150 CONTINUE
C
C CHOICE OF SOLUTION AND CONSEQUENT ITERATIONS
DO 160 I=1,19
  K=J+1
C
C SOLUTIONS DESCRIBED ABOVE ARE EXCLUDED
  IF (J.FQ.10) GO TO 1
  IF (ANGLE(J).LT.25.0) GO TO 160
  IF (ANGLE(K).LT.25.0) GO TO 160
  IF (RATSIN(K).EQ.131.079) GO TO 160
  IF (RATSIN(J).EQ.131.079) GO TO 160
C
C SOLUTIONS ARE TESTED IF THEY PASS THE PREVIOUS TESTS.
200 IF (PATSIN(J).CT.PATIO.AND.PATSIN(K).LT.RATIO) GO TO 161
  IF (RATSIN(J).LT.RATIO.AND.PATSIN(K).CT.PATIO) GO TO 161
160 CONTINUE
161 IF (INDIC.EQ.0) GO TO 167
  DANGLE(I)=ANGLE(I)
  IF (IFULL.EQ.1) GO TO 167
C
C DETAILS OF SOLUTION ARE GIVEN
  WRITE(6,162) ANGLE(J),PATSIN(J),DN1(J),DN2(J),DN3(J)
162 FORMAT(' ', 'ANGLE', F7.2, 'RATIO', F7.2, 'DCS', 3F8.2)
  WRITE(6,162) ANGLE(K),RATSIN(K),DN1(K),DN2(K),DN3(K)

```

```

167 IF (ANGLE(I).GT .ANGLE(K)) GO TO 163
10ANG=ANGLE(J)
GO TO 164
163 LOANG=ANGLE(K)
164 IF (INCIC.EQ.1) GO TO 800
INDIC=1
GO TO 166

C
C TRANSFORMATICN PACK TO AZIMUTH AND DIP REPRESENTATION
R(1) AVN1=(DN1(K)+DN1(J))/2.0
AVN2=(DN2(K)+DN2(J))/2.0
AVN3=(DN3(K)+DN3(J))/2.0
SINMP=SQRT(1.0-AVN3*AVN3)
DIP=(AP SIN(SINMP))*57.2956
COSAZ=(ARCCOS(AVN1/SINMP))*57.2956
DDIP(11)=DIP
DCCSAZ(11)=COSAZ
IF (IFULL.EQ.1) GO TO 900
WRITE(6,801) DIP,COSAZ
801 FORMAT('0', 'DIP OF NORMAL', F10.2, 'AZIMUTH OF NORMAL', F10.2)
GO TO 900
899 WRITE(6,898) EVENT(11)
900 CONTINUE
IF (IFULL.EQ.0) GO TO 41
WRITE(4,43)
43 FORMAT (' ', 'EVENT NO.', 4X, 'DIP OF NORMAL', 4X, 'AZIMUTH', 6X, 'INCIDE
INT ANGLE', 6X, 'DELTA')
WRITE(6,45) (EVENT(M), DDIP(M), DCCSAZ(M), DANGLE(M), DELTA(M), N=
11, NEVENT)
45 FORMAT (' ', 2X, F7.2, 9X, F5.2, 11X, F5.1, 11X, F4.1, 13X, F4.1)
IF (IPLOT.EQ.0) GO TO 41
CALL PAXIS (0.5,0.5, 'DELTA-DEGREES', 13, 10.0, 0.0, 0.0, 1.0, 1.0)
CALL PAXIS (0.5,0.5, 'DIP-DEGREES', 11, 10.0, 90.0, 0.0, 10.0, 1.0)

```

```
CALL PLTFFS (0.0,10.0,0.0,0.10,0.0,0.5,0.5)
CALL PLTNE (DELTA,DDIP,NVEENT,1,-1,11,1)
CALL PPSYMR (1.0,1.0,-0.25,'DCP G1',0.0,6)
CALL PLTFEND
CALL EXIT
41 STOP
END
```

Program DELAY

```

C
C PROGRAM DELAY CALCULATES THE DELAY APPROPRIATE TO A WAVE ARRIVING
C AT A STATION WITH GIVEN VELOCITY AND AZIMUTH AFTER PASSING THROUGH
C A STRUCTURE OF THE FORM ASSUMED
C
C PARAMETERS USED AS INPUT
C A1,B1,C1 - STRUCTURE PARAMETERS
C XTO,YTO,ZTO - COORDINATES OF STATION
C PIEN1 - ORIENTATION OF COORDINATE SYSTEM (DEGREES)
C VLVZ - ANOMALOUS VELOCITY (KMS/SEC)
C BCTTM,VFREL,IC - DEPTH TO BOTTOM OF STRUCTURE;
C VELOCITY BENEATH STRUCTURE;
C AN INTEGER CONTROLLING NUMBER OF LAYERS TO BE USED
C IN CALCULATING NORMAL TRAVEL PATH.
C
C AZINIT,AZINC,NAZINC - INITIAL AZIMUTH (DEGREES);
C AZIMUTH INCREASE;
C NUMBER OF INCREMENTS.
C FINIT,FINC,NFINC - INITIAL SLOWNESS (SEC/DEG);
C SLOWNESS INCREASE;
C NUMBER OF INCREMENTS.
C DEPTH(1),VEL(I),I=1,76 - VELOCITY - DEPTH STRUCTURE ACCORDING TO
C HERPIN ET AL (1968) TO 400 KMS.
C DELTA(I),P(I),I=1,160 - STANCAPO SLOWNESS VALUES ACCORDING TO HERPIN
C ET AL (1968).
C DIMENSION DEPTH(30),VEL(80),DELTA(200),P(200),SINI(80),TIME1(90)
C DIMENSION TIME2(30)
C REAL LENGTH,KOS
C REAC(5,20) AO,RO,CO
C RFAD(5,20) XTO,YTO,ZTO
C REAP(5,21) RIEN1
C REAC(5,21) VLVZ
C REAP(5,22) BCTTM,VELREL,IC
C REAC(5,22) AZINIT,AZINC,NAZINC

```

```

READ(5,22) P,INIT,PINC,NPINC
READ(7,23) (DEPTH(I),VEL(I),I=1,76)
READ(8,24) (DELTA(I),P(I),I=1,160)
20 FORMAT (3F11.2)
21 FORMAT (F10.2)
22 FORMAT (2F10.2,F5)
23 FORMAT(F5.2,F7.2)
24 FORMAT (F5.2,F11.2)
C DATA INPUT CHECK.
WRITE(6,70) A0,B0,C0
70 FORMAT (' ','STRUCTURE PARAMETERS',3F10.2)
WRITE(6,71) XTC,YTC,ZTC
71 FORMAT ('0','STATION COORDINATES',3F10.2)
WRITE(6,72) RIENT
72 FORMAT (' ','ORIENTATION(DEGREES)',F11.2)
WRITE(6,73) VLVZ
73 FORMAT ('0','LCM VELOCITY ZONE',F10.2)
WRITE(6,121)
121 FORMAT ('0',3X,'AZ',4X,'A1N DTD DTDN TIM1 TIM2 TIM3 T
THETA PHI X',10X,'TOTAL CPLAY')
C STRUCTURE PARAMETERS CONVERTED TO CONVENIENT FORM
A=1.0/A0^A0
B=1.0/B0^B0
C=-1.0/C0^C0
DO 1000 IAZ=1,NAZINC
UP AZIMUTH LOOP.
AZZ=AZINIT+(FLOAT(IAZ)-1.0)*AZINC
C SET UP SLCWNESS LCCP.
DO 1001 IP=1,NPINC
C TIME COUNTING ARRAYS SET TO ZERO.
DO 6, I=1,76
TIME1(I)=0.0
TIME2(I)=0.0
60 CONTINUE

```

C FAY JTD=PINI+(FLUAT(IP)-1.0)\*PING  
TPACING THROUGH FIRST LAYER; TIME IS CALCULATED IN TIME(I).

XT=XT0  
YT=YT0  
ZT=ZT0  
AZ=AZZ/57.2956  
CRIFNT=RIENT/57.2956  
SINI(1)=VFL(1)\*LTD\*0.0089  
AI=COS(AZ-ORIENT)\*SINI(1)  
AM=SIN(AZ-ORIENT)\*SINI(1)  
AN=SQR(1.0-SINI(1)\*SINI(1))  
LENGTH=(DEPTH(2)-DEPTH(1))/AN  
XR=XT+(LENGTH\*AL)  
YR=YT+(LENGTH\*AM)  
ZR=DEPTH(2)

TIME(1)=LENGTH/VEL(1)  
C RAY TPACING THROUGH EACH LAYER IN TURN.

C I TO JD=2.75  
ID=JD+1  
KD=JD-1  
XT=XB  
YT=YH  
ZT=ZR

SINI(JD)=SINI(KD)\*VEL(JD)/VEL(KD)  
C TEST FOR TOTAL INTERNAL REFLECTION.  
IF (SINI(JD).GT.1.0) GO TO 103  
AL=SINI(JD)\*COS(AZ-ORIENT)  
AM=SINI(JD)\*SIN(AZ-ORIENT)  
AN=SQR(1.0-SINI(JD)\*SINI(JD))  
LENGTH=(DEPTH(ID)-DEPTH(JD))/AN  
TIME(JD)=LENGTH/VFL(JD)  
XR=XT+LENGTH\*AL  
YR=YT+LENGTH\*AM  
ZR=DEPTH(JD)

```

C IF NO INTERSECTION IS FOUND BY A DEPTH OF 400 KMS IT IS ASSUMED NOT
C TO OCCUR.
  IF (ZP-400.0) 102,103,103
C INTERSECTIONS WITH STRUCTURE CALCULATED AND CHOSEN.
102 AR=A*AL+B*AL+B*AM*AN+C*AN*AN
  BR=(A*XT*AL+R*YT*AM+C*ZT*AN)*2.0
  CR=(A*XT*XT+B*YT*YT+C*ZT*ZT)-1.0
  RCOT=BR*BP-1.0*AR*CR
  IF (RCOT) 10,11,11
11 DPOS=(-BR+SGRT(ROOT))/(2.0*AR)
  DNEG=(-BR-SGRT(ROOT))/(2.0*AR)
  IF (DPCS*DNEG) 13,14,14
13 D=DPOS
  IF (DNEG*CT.DPOS) D=DNEG
  GO TO 15
14 IF (DPOS.LT.0.0) GO TO 10
  D=DPCS
  IF (DNEG.LT.DPOS) D=DNEG
15 XTINT=XT+D*AL
  YTINT=YT+D*AM
  ZTINT=ZT+D*AN
  IF (ZTINT.LE.ZB.AND.ZTINT.GE.ZT) GO TO 17
10 CONTINUE
  IF (ID.EQ.75) GO TO 103
C DIRECTION COSINES OF NORMAL AT POINT OF INTERSECTION CALCULATED.
17 FACTOR=SGRT(A*A*XT*INT+P*RYT*INT*YT*INT+C*C*ZT*INT*ZT*INT)
  ALN=A*XT*INT/FACTOR
  AMN=R*YT*INT/FACTOR
  ANN=C*ZT*INT/FACTOR
  IF (ANN.LT.0.0) GO TO 16
  ALN=-ALN
  AMN=-AMN
  ANN=-ANN

```

```

C ANGLES OF INCIDENCE AND REFRACTION CALCULATED, TEST FOR TOTAL INTERNAL
C REFLECTION.
15 CCSI=AL*ALN+AM*AMN+AN*ANN
SNI=SQRT(1.-CCSI*CCSI)
SINP=VLVZ*SNI/VFL(JD)
IF (SINP.GT.1.0) GO TO 103
COSP=-SQRT(1.0-SINP*SINP)
C DIRECTION COSINES OF TRANSMITTED RAY CALCULATED.
A1T1=VLVZ*AL/VFL(JD)-((VLVZ*COSI/VFL(JD))-COSR)*ALN
AMT1=VLVZ*AM/VFL(JD)-((VLVZ*COSI/VFL(JD))-COSR)*AMN
ANT1=VLVZ*AN/VFL(JD)-((VLVZ*COSI/VFL(JD))-COSR)*ANN
FACTOR=SQRT(A1T1*A1T1+AMT1*AMT1+ANT1*ANT1)
A1T1=A1T1/FACTOR
AMT1=AMT1/FACTOR
ANT1=ANT1/FACTOR
IF (AMT1.GT.0.0) GO TO 35
ALT1=-ALT1
AMT1=-AMT1
ANT1=-ANT1
C FAY TRACED THROUGH STRUCTURE AND NEW AZIMUTH AND SLOWNESS CALCULATED.
30 LFRIGHTH=(ZTINT-DEPTH(JD))/AN
TIME1(IC)=LENGTH/VFL(JD)
LFGTH=(BCTTCM-ZTINT)/ANT1
TIME1(JD+1)=LFGTH/VLVZ
JDI=JD+1
XT=XTINT+LENGTH*ALT1
YT=YTINT+LFGTH*AMT1
ZT=ZTINT+LFGTH*ANT1
ALT2=ALT1*VELBFL/VLVZ
AMT2=AMT1*VELBEI/VLVZ
COSI=ARCCOS(ANT1)
SNI=SIN(COSI)
SINP=VEL(IC)*SNI/VLVZ
SINI(IC)=SINR

```

```

AMT2=CCS(ARSIN(SINR))
DTDN=(111.2+SQRT(1.0-AMT2+AMT2))/(VELBEL)
KDS=ARCCS(ALT2/SQRT(1.0-AMT2-AMT2))
C CORRECT QUADRANT FOR AZIMUTH CHOSEN.
IF (ALT2.GT.0.0.AND.AMT2.GT.0.0) AZN=KDS
IF (ALT2.LT.0.0.AND.AMT2.GT.0.0) AZN=KDS
IF (ALT2.LT.0.0.AND.AMT2.LT.0.0) AZN=6.2832-KDS
IF (ALT2.GT.0.0.AND.AMT2.LT.0.0) AZN=0.2832-KDS
TIM1=0.0
C TRAVEL TIME CALCULATED.
DO 105 I=1,76
IF (ABS(TIME1(I)).LT.0.00000001) GO TO 103
TIM1=TIM1+TIME1(I)
105 CONTINUE
103 TIM1=TIM1
SINI(IC)=VEL(IC)*DTDN:0.0089
C RAY RETRACED THROUGH NORMAL STRUCTURE AND TRAVEL TIME TIME2(I) CALCULATED.
IC1=IC-1
DO 40 I=1,IC1
TD=IC-I
XB=XT
YB=YT
ZB=ZT
SINI(ID)=SINI(ID+1)+VEL(ID)/VEL(ID+1)
AL=COS(AZN)*SINI(ID)
AM=SIN(AZN)*SINI(ID)
AN=SQRT(1.0-SINI(ID)*SINI(ID))
LNGTH=(DEPTH(IC+1)-DEPTH(ID))/AN
TIME2(ID)=LENGTH/VEL(ID)
XT=XB-LENGTH*AL
YT=YB-LENGTH*AM
ZT=ZB-LENGTH*AN
40 CONTINUE
TIM2=0.0

```

```

TC1=IC-1
DC 42 J=1,IC1
TIM2=TIM2+TIME2(J)
42 CONTINUE
C TRAVEL TIME CUE TC DEVIATION (ALCULATED).
THETA=(ATAN((YTN-VT)/(XTJ-XT)))*57.2956
IF (XT.LT.XT0) THETA=THETA+180.)
IF (YT.ST.XT0.AND.YT.LT.YT0) THETA=THETA+360.*
PHI=(AZ-ORIENT)+57.2956
IF (PHI.LT.0.0) PHI=PHI+360.0
X=SQRT(((XT-XT')*(XT-XT'))+((YT-VT')*(YT-VT'))))
DEL=-X*ABS(COS((THETA-PHI)/57.2956))
TEST=ABS(THETA-PHI)
IF (TEST.GT.90.*.AND.FEST.LT.270.*.) DEL=-DEL
DELAY3=FFL*DTDN/111.2
AZP=AZ#57.2956
AZNR=AZN#57.2956
TDEL=TTM1-TIM2+DELAY3
WRITE(6,12') AZP,AZNR,ITD,ETCN,TTM1,TIM2,DELAY3,THETA,PHI,X
1,TFEL
122 FORMAT(' ',2F7.1,3F6.1,2F7.1,F9.1,2F9.1,3X,F10.2)
1001 CONTINUE
1002 CONTINUE
STOP
END

```

25/11/70